Medical Radiology
Diagnostic Imaging
A.L. Baert
M.F. Reiser
H. Hricak
M. Knauth

Thorsten R.C. Johnson
Christian Fink
Stefan O. Schönberg
Maximilian F. Reiser
Editors

Dual Energy CT in Clinical Practice

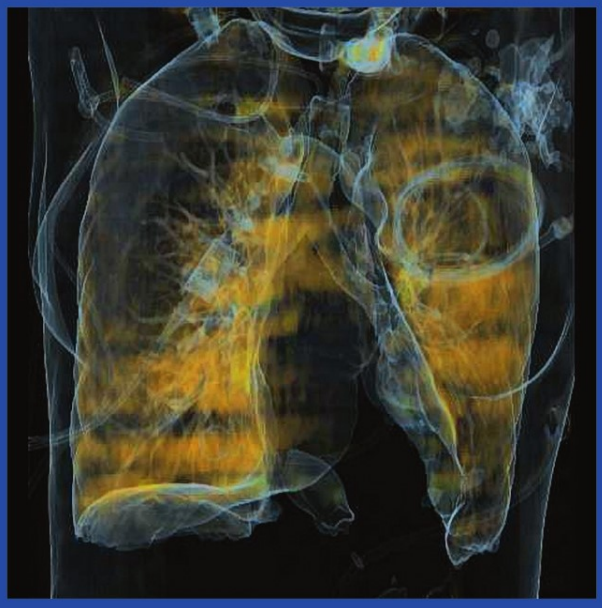

Springer

Medical Radiology

Diagnostic Imaging

Series Editors

For further volumes:
http:/www.springer.com/series/4354

Medical Radiology

Diagnostic Imaging

Editorial Board

Thorsten R.C. Johnson • Christian Fink •
Stefan O. Schönberg • Maximilian F. Reiser
(Eds.)

Dual Energy CT in Clinical Practice

Foreword by
M.F. Reiser

Springer

Editors
Priv. Doz. Dr. med. Thorsten R. C. Johnson
Institut für Klinische Radiologie
Klinikum der Universität München
Campus Großhadern
Marchioninistr. 15
81377 München
Germany
thorsten.johnson@med.uni-muenchen.de

Prof. Dr. med. Stefan O. Schönberg
Institut für Klinische Radiologie und
Nuklearmedizin
Universitätsmedizin Mannheim
Theodor-Kutzer-Ufer 1-3
68167 Mannheim
Germany
stefan.schoenberg@umm.de

Prof. Dr. med. Christian Fink
Institut für Klinische Radiologie und
Nuklearmedizin
Universitätsmedizin Mannheim
Theodor-Kutzer-Ufer 1-3
68167 Mannheim
Germany
christian.fink@umm.de

Prof. Dr. med. Dr. h.c. Maximilian F. Reiser,
FACR, FRCR
Institut für Klinische Radiologie
Klinikum der Universität München
Campus Großhadern
Marchioninistr. 15
81377 München
Germany
maximilian.reiser@med.uni-muenchen.de

ISSN: 0942-5373

ISBN: 978-3-642-01739-1 e-ISBN: 978-3-642-01740-7

DOI: 10.1007/978-3-642-01740-7

Springer Heidelberg Dordrecht London New York

Library of Congress Control Number: 2010937236

Cover design: eStudio Calamar, Figueres/Berlin

Printed on acid-free paper

Springer is part of Springer Science+Business Media (www.springer.com)

Foreword

It is a great pleasure to introduce this new volume of the Diagnostic Imaging series on Dual Energy CT in Clinical Practice. It is amazing how rapidly this emerging technology is gaining importance and diagnostic value for daily clinical practice, and it is great to see how many aspects are already covered in this textbook.

With the development of Multi Detector Row CT, image quality, scan speed, and diagnostic utility of CT have greatly improved. Moreover, new applications such as cardiac imaging, CT angiography, and CT urography have become viable clinical diagnostic methods. Functional tests such as perfusion scanning added valuable information to the high resolution display of morphology provided by CT. With Dual Energy CT, another dimension has opened up: The spectral differentiation of molecular substances makes an identification and characterization of pathologic substances or tissue feasible and allows to directly visualize the substrate of disease. Dual Energy CT also offers means to reduce the radiation exposure of patients by replacing multiphase exams with more specific single acquisitions. This work represents a comprehensive, up-to-date compilation of all technical and clinical aspects of this fascinating new imaging modality.

I am greatly indebted to the other editors of this volume, T. R. C. Johnson, C. Fink, and S.O. Schoenberg, for their dedication and effort in composing and editing the chapters in a very brief period of time. I would also like to take this opportunity to thank the contributing authors – all renowned experts on CT technology or CT in clinical radiology – for sharing their knowledge and providing comprehensive practical advice in their area of exceptional expertise.

This book will help the readers to rapidly grasp the technical background, it will provide technicians with a reference for suitable settings and parameters and it will support radiologists with advice on practical clinical interpretation. I am confident that this volume will fulfil the expectations of the readers and meet the same success as other volumes of this series.

M.F. Reiser

Preface

Dual Energy Computed Tomography is one of the most exciting evolving fields in radiology. The possibility to acquire CT scans with different x-ray spectra to enhance material differentiation had already been realized and tested in the 1970s. However, only since the introduction of Dual Source CT in 2006 the method has achieved clinical significance and widespread application. Nowadays, several CT vendors have implemented Dual Energy CT with different technical approaches, and the integration and the clinical applications are continuously making progress. The editors have been among the first radiologists to explore this new technology and want to share their experience and enthusiasm with others.

This book has several aims. First, it wants to inform about the physical background and the different approaches of technical implementation. To cover this aspect, there is one chapter giving a general physical introduction, three chapters elucidating the different CT vendors' approaches, and another chapter explaining how to post-process CT data to obtain spectral information. A second main aim is to provide practical advice for clinical application. In this respect, there are 15 chapters presenting different clinical applications. Each chapter describes the substrate being imaged and the concept how this helps to characterize a certain disease. Tables provide scan protocol settings for practical utilization. A third aim of this book is to give account of unbiased scientific data on the clinical value of the different applications. Most of the authors of the clinical chapters are scientists who have published several articles in peer-reviewed scientific literature. They were asked to give account of their scientific evidence and to also include data from other groups working in the respective field. Thus, the reader should get an impression of the actual clinical value of each application.

We would like to take this opportunity to express our sincere gratitude to all the authors who have contributed to this book. We are proud and thankful that we have been able to obtain contributions from the CT development departments of the three CT vendors that have implemented Dual Energy CT. Renowned CT physicists have contributed chapters on physical background and post-processing. And clinical colleagues, mainly radiologists and experienced scientists, have compiled an impressing and helpful combination of practical advice and scientific evidence.

We hope that this book will provide a sufficient and comprehensive physical and technical background to a medical reader and that the practical advice and scientific evidence in the clinical chapters are helpful for clinical application and interpretation.

Munich and Mannheim
April 2010

T.R.C. Johnson, C. Fink
S.O. Schoenberg, M.F. Reiser

Contents

Part I

Physical Implementation

Physical Background

Thorsten R.C. Johnson and Willi A. Kalender

Contents

Abstract

- There had been attempts to utilize spectral information for tissue characterization soon after the invention of Computed Tomography, but only recently Dual Energy CT has achieved a significant role in clinical radiology.
- To perform Dual Energy CT, it is necessary to generate x-rays with different energies, mostly as polychromatic spectra. On the other hand, the detector has to be capable to differentiate x-ray quanta of different energies. There are four technical approaches to meet these requirements, of which the Dual Source CT, the rapid voltage switching and the layer detector technology are available or being implemented.
- To obtain relevant diagnostic information, there have to be substances with spectral properties which reflect the pathology by their presence or distribution. Most important is the photoelectric effect of elements like uric acid, iron, calcium, iodine or xenon gas, which are present in pathological structures or can be administered as contrast material. The identification and quantification of these elements can be used to diagnose several diseases.

T.R.C. Johnson (✉)
Department of Clinical Radiology, University of Munich,
Grosshadern Hospital, Marchioninistrasse 15,
81377 Munich, Germany
e-mail: thorsten.Johnson@med.uni-muenchen.de

W.A. Kalender
Institute of Medical Physics, University of Erlangen,
Henkestrasse 91, 91052 Erlangen, Germany

1 History

First attempts to use spectral information in computed tomography date back to the late 1970s (Millner et al. 1979; Avrin et al. 1978; Chiro et al. 1979; Genant and Boyd 1977). At that time, two separate scans were acquired and either projection data or reconstructed

T.R.C. Johnson et al. (eds.), *Dual Energy CT in Clinical Practice*, Medical Radiology,
DOI: 10.1007/174_2010_43

data were postprocessed. However, the lacking stability of the CT density values, the long scan times which often caused patient motion between scans, the limited spatial resolution, and the difficulty of postprocessing were the main reasons why the method never achieved broad clinical acceptance (Kelcz et al. 1979). With the necessity to acquire both scans separately, the use of contrast material and its differentiation by dual-energy or spectral analysis was impossible. Since 2006, dual-energy CT has experienced a revival and success in clinical application. The main reason was the introduction of dual-source CT that made it possible to acquire two spiral scans simultaneously with different X-ray spectra by running the two X-ray sources at different tube voltages (Flohr et al. 2006; Johnson et al. 2007a). Today, there are several technical approaches to dual-energy CT.

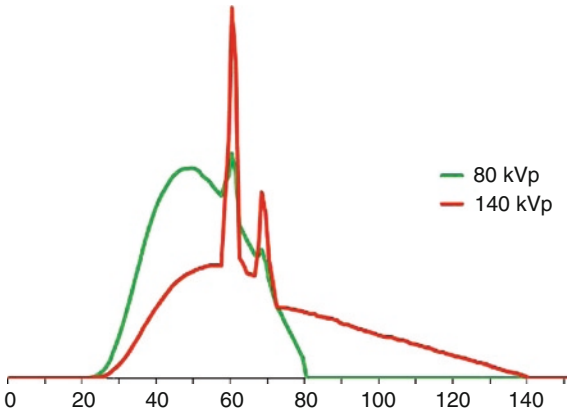

Fig. 1 Spectra of the Straton tube at 140 and 80 kV potential. The *peaks* represent the characteristic lines of the tungsten anode and the continuous spectrum is a result of Bremsstrahlung. The mean photon energies are 53 and 71 keV, respectively

2 X-ray Spectra

Generally, there are three requirements for spectral CT imaging: First, X-ray sources providing X-ray quanta with different energies are necessary. Obviously, this can be achieved optimally when using two separate X-ray sources emitting different photon energies. However, this criterion is basically also met by single X-ray sources, because they generally provide polychromatic spectra. The X-ray spectrum of a normal tube with a tungsten anode consists of a continuous part, the Bremsstrahlung, and discrete peaks according to the energy levels of the electrons in the shell of the tungsten atoms. Figure 1 shows the X-ray spectra that are obtained from an X-ray tube operated at 140 and 80 kV. Obviously, the area under the curve for equivalent tube currents differs by a factor of about 4–5, and the tube current needs to be adapted to obtain a similar output of quanta from both tubes. The higher energy spectrum is dominated by the characteristic lines of the tungsten anode, while the lower energy spectrum mainly consists of Bremsstrahlung. In this case, the mean photon energies are 71 and 53 keV, respectively, for the primary spectra. It is desirable to have as little overlap as possible between the spectra; therefore, the lowest and highest potentials offered by the respective CT scanner are always used for dual-energy acquisitions. A tube voltage lower than 80 kV is not useful because too much of the quanta would be absorbed by the human body; values higher than 140 kV are generally not available and would result in very low soft tissue contrast that likely would contribute very little to tissue differentiation. Obviously, it is not possible to obtain monochromatic X-rays with today's tube technology; monochromatic X-ray sources so far do not provide a sufficient output of quanta for clinical applications. An exception is monochromatic synchrotron radiation that can be used for experimental setups. As synchrotrons are far too large for use in a rotating gantry, the object has to be rotated between the source and the detector, i.e., it is not possible to use them for clinical imaging.

3 Detector Technology

The second requirement is that the detector has to be able to differentiate quanta of different energies. With technologies in use in clinical CT today, this is not directly possible with a single detector. The detector integrates the fluorescent light intensities of all photons detected during a single readout interval, but does not give account of their energy. Current approaches either rely on entirely separate X-ray sources and corresponding separate detectors, on reading out the projection data at different time points, or on using a two-layer or "sandwich" detector with different spectral sensitivities. In the near future, cadmium-based materials such as CdZnTe may serve as semiconductors for

photon-counting detectors that resolve the energy of each individual photon. However, this detector technology cannot yet cope with the high photon flux required for clinical CT.

These first two requirements define the spectra of the X-ray sources and the corresponding detectors, representing the sensitivity of the systems for photons, detectors of different energies. The more these spectra differ, the stronger the contrast-to-noise ratio of the resulting spectral information, as long as both sufficient transmission and attenuation can be achieved in the human body at these photon energies.

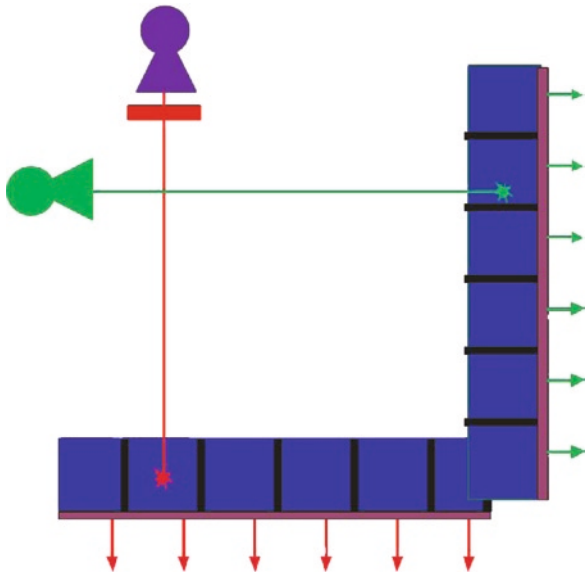

Fig. 2 Sketch of a dual-source CT system. Two tubes and detectors are mounted orthogonally. To obtain dual-energy datasets, the tubes are operated at different tube voltages, e.g., 80 and 140 kV (*green* and *violet*). Additionally, a filter (indicated in *red*) can be applied to harden the high-energy spectrum

4 Tissue Properties

The third requirement is a sufficient difference in spectral properties of the materials under investigation. The attenuation that is quantified in CT to characterize different body tissues is caused by three physical processes. Compton scatter is the largest component of attenuation. It is related to the electron density and not to the protons in the atomic core that would allow a material differentiation (McCullough 1975). Rayleigh scatter also is related to the electrons and not to the atomic core, but contributes only a negligible amount. The third process, the photoelectric effect, is strongly related to the atomic number, Z, of the material, i.e., to the number of protons of the atomic core (Fig. 2). Therefore, only elements with a considerable difference in Z values will be distinguishable by their spectral properties. This difference can be characterized with the so-called dual-energy index (DEI):

$$DEI = \frac{x_{80} - x_{140}}{x_{80} + x_{140} + 2000},$$

where $x80$ is the CT value in HU at 80 kV tube potential and $x140$ the value of the respective voxel at 140 kV (Johnson et al. 2007a).

According to Alvarez and Macovski (1976), the photoelectric interaction with the K shell is proportional to the third power of the atomic number (Z). Therefore, high values apply for Z values of 53 (iodine) or 54 (xenon). The elements of which the human body consists, i.e., hydrogen ($Z=1$), oxygen ($Z=8$), carbon ($Z=6$) and nitrogen (7), have low Z numbers and hence do not show a sufficient photo effect and spectral behavior that would allow a differentiation (Michael 1992). Bone with its high content in calcium ($Z=20$) and fat, which only consists of hydrogen and carbon, represent tissues that differ from other body tissues significantly, which also explains their good differentiation in standard CT. This feature has also been employed in approaches for the quantification of obesity or for the identification of calcifications in pulmonary nodules (Cann et al. 1982; Svendsen et al. 1993). The most clinically useful application of dual-energy CT can be expected for the differentiation of iodine (Kruger et al. 1977; Riederer and Mistretta 1977; Nakayama et al. 2005), which is generally used in CT as a contrast agent and the distribution of which can be masked by the underlying tissue.

5 Dual-Source CT

At present, there are three different approaches to clinical dual-energy CT commercially available or under investigation. The most straightforward approach is dual-source CT with two X-ray sources running at different voltages with two corresponding detectors

(Fig. 2). Additionally, a filter can be used to further harden the higher energy spectrum, i.e., to rid the spectrum of low-energy quanta. This setup has several advantages. First, established X-ray sources and detector materials can be used. Also, the image reconstruction can rely on established methods. But the most important benefit of this technology is that the tube voltage and current can be adjusted freely to obtain the largest possible difference in photon energies with similar total amounts of quanta from both tubes. A disadvantage of this approach is the considerable hardware effort, making the system expensive. Also, the space in the CT gantry is only sufficient for a smaller second detector so that the field of view of the dual-energy scans is restricted. The acquired projection data primarily have to be reconstructed by standard filtered backprojection, separately for the two simultaneously acquired spiral datasets. The fact that the acquired projection data have an offset of 90° at equal z-axis positions means that a primary postprocessing of projection data is impossible because there are no equivalent projections. Still, data at equivalent z-positions are sampled simultaneously, so the angular offset does not imply a temporal offset between the acquisitions. A problem is posed by the cross-scatter that is oriented perpendicular to the primary course of beam, thus hitting the second detector and contaminating its data. However, comparative Monte Carlo simulations show a good spectral separation with dual-source CT (Fig. 3) (Kappler et al. 2009).

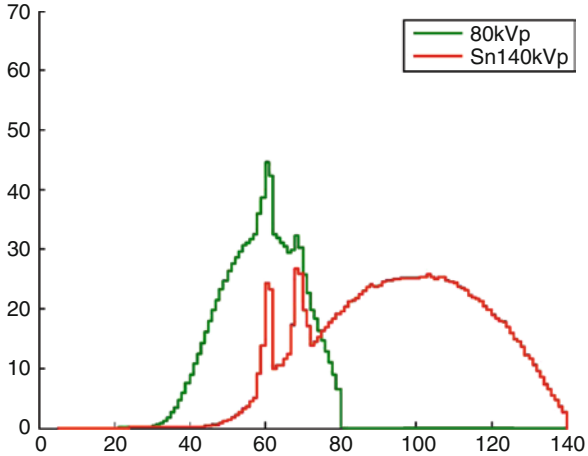

Fig. 3 X-ray spectra of the two tubes running at 80 and 140 kV with 0.9 mm titanium and 3.5 mm aluminum filters on both and an additional 0.4 mm tin filter on the high-energy tube

6 Rapid Voltage Switching

Another approach that requires less hardware effort is rapid voltage switching. With this method, the tube voltage follows a pulsed curve, and projection data is collected twice for every projection, one at high and one at low tube voltage (Fig. 4). Optimally, the tube current should be modulated at least inversely to the voltage so that the difference in the number of photons is kept as small as possible (Grasruck et al. 2009). The major advantage of this approach is that it can be realized at considerably lower cost, because no major additional hardware is required. Limitations include the slow acquisition, because the rotation time has to be reduced to less than half to allow the collection of the additional projections. Also, the course of the tube current and voltage retain a non-rectangular, curved shape so that the resulting spectral difference does not correspond to the nominal tube voltages. The adaptation of the current also has limitations so that there is generally a far lower signal at low energy than at high energy. Figure 5 shows the resulting spectra with a rather large difference in size.

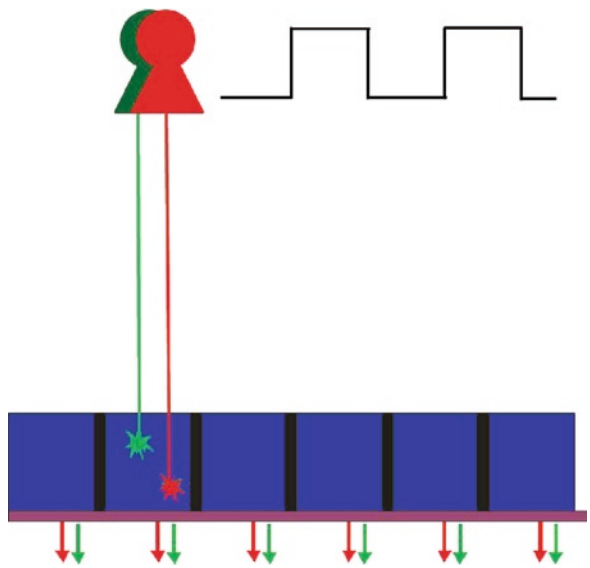

Fig. 4 Sketch of a rapid kV switching system. There is only one tube and detector, but the tube voltage is switched rapidly between two levels. Optimally, the current is adjusted at least inversely

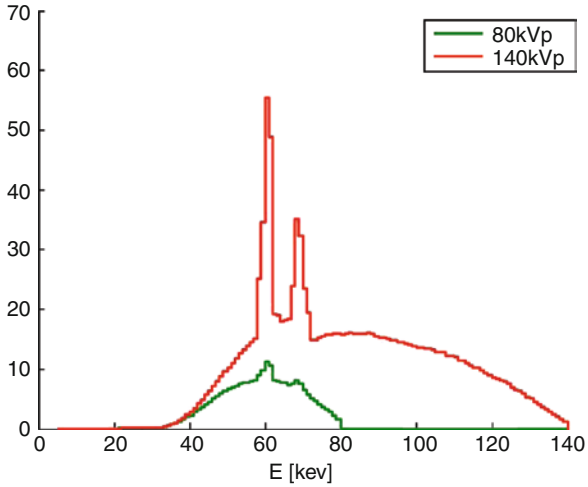

Fig. 5 There is an obvious difference in the total number of photons in the spectra because the output of quanta is smaller at low tube voltages, and this difference cannot be compensated fully by adjusting the current

7 Layer Detector

A third approach is not to generate different photon spectra but to work with two detector layers that have their maximum sensitivity for different photon energies (Fig. 6). The sensitivity is determined by the scintillator material, e.g., consisting of ZnSe or CsI in the top and Gd_2O_2S in the bottom layer. This setup has the advantage that only one standard tube is required. Disadvantages include the hardware effort for the layer detector and the lower dose efficiency of such a setup. Also, the obtainable spectral difference is rather low so that the contrast of the spectral information is limited or requires additional dose. Figure 7 shows the sensitivity profile of a layer detector with ZnSe and Gd_2O_2S scintillators.

8 Sequential Acquisition

Another approach that is not being implemented currently is sequential filtering or voltage switching, i.e., two subsequent rotations are acquired in a sequence mode at the same table position with different tube voltages and optionally an additional filter. This would imply a rather minor hardware effort and may be a viable option especially for systems with broad

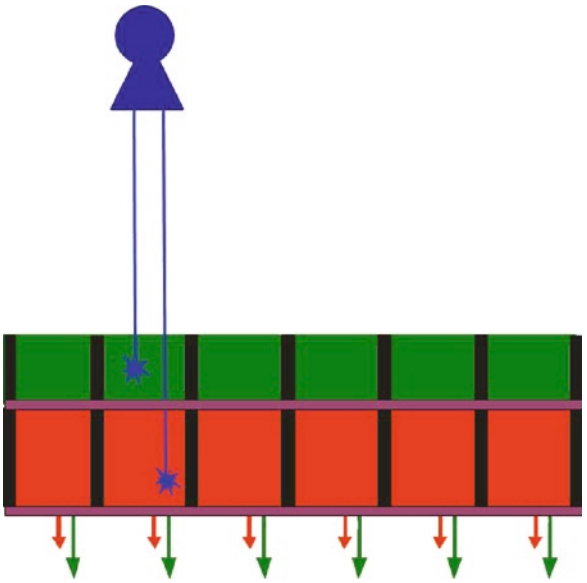

Fig. 6 Sketch of a layer detector system. There is only one X-ray tube running at constant voltage. The dual-energy information is derived from two layers of the detector with different sensitivity profiles. The *top layer* may, e.g., use CsI or ZnSe as the scintillator so that it is more sensitive to low-energy quanta, while the *bottom layer* may consist of Gd_2O_2S as the standard material

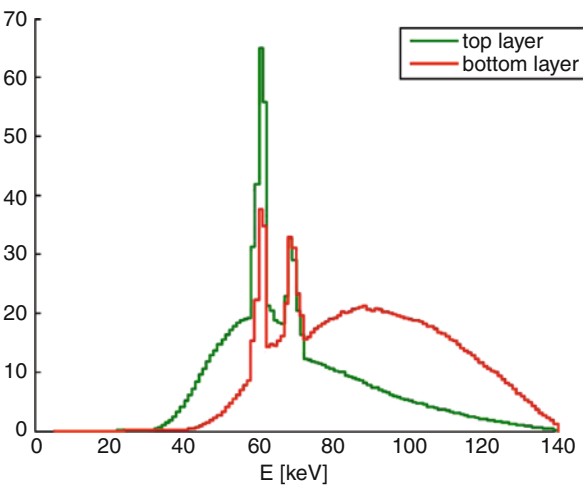

Fig. 7 The sensitivity spectra of the two layers indicate a similar overall sensitivity for high- and low-energy quanta, but a considerable overlap which limits spectral contrast

detectors and a rather high number of simultaneously acquired slices. An obvious disadvantage is the rather long delay between both acquisitions, which is too long to preclude artifacts from cardiac or respiratory motion or changes in contrast material opacification.

9 Radiation Exposure

Regarding radiation exposure, dual-energy CT based on dual-source CT acquisitions does not require a higher patient dose than a routine CT scan of the same body region. It is possible to tailor the tube current such that the dose from both tubes matches that of a routine single-source CT protocol (Johnson et al. 2007a). Recent comparative phantom studies with external validation have proven that dual-energy acquisitions can provide similar or even improved contrast-to-noise ratios at equivalent dose (Schenzle et al. 2010). This is in contrast to investigations by Ho et al. 2009 who observed two to three times higher doses for dual-energy CT. However, their setup was based on a single-source system using rapid voltage switching and contained neither a normalization of image noise nor of dose, so the lower energy spectrum was obtained with the same tube current time product as the single energy scan. In another study with normalization to equivalent low-contrast detectability (Li et al. 2010), Li et al. observed an additional dose of 14% in the body and 22% in the head with rapid kV switching. Specific clinical studies comparing the dose efficiency of different dual-energy CT systems are lacking, but it is evident that dual-energy CT does not necessarily imply an increased dose.

10 Clinical Applications

Meanwhile there are numerous clinical applications of dual-energy CT. Among these are bone removal from the carotid (Morhard et al. 2009) or peripheral runoff (Sommer et al. 2009) CT angiography datasets, the reconstruction of virtual noncontrast images or quantification of iodine enhancement in lesions of solid organs (Graser et al. 2009), the depiction of iodine (Thieme et al. 2008; 2009) or xenon gas (Chae et al. 2008) distribution in the lung and the differentiation of kidney stones (Graser et al. 2008), or the identification of gout tophi (Johnson et al. 2007b). Also, image quality and display can be optimized, e.g., by generating monoenergetic images (Voit et al. 2009), or images with optimized contrast (Holmes et al. 2008). As this more specific or functional additional information can be obtained without an additional dose, it should be exploited whenever diagnostically useful.

11 Summary

In summary, dual-energy CT offers the possibility to exploit spectral information for diagnostic purposes. There are different technical approaches that all have inherent advantages and disadvantages. Some systems are commercially available, and there is already quite a number of well-established clinical applications.

References

Alvarez RE, Macovski A (1976) Energy-selective reconstructions in X-ray computerized tomography. Phys Med Biol 21:733–744

Avrin DE, Macovski A, Zatz LE (1978) Clinical application of Compton and photo-electric reconstruction in computed tomography: preliminary results. Invest Radiol 13:217–222

Cann CE, Gamsu G, Birnberg FA, Webb WR (1982) Quantification of calcium in solitary pulmonary nodules using single- and dual-energy CT. Radiology 145:493–496

Chae EJ, Seo JB, Goo HW et al (2008) Xenon ventilation CT with a dual-energy technique of dual-source CT: initial experience. Radiology 248:615–624

Chiro GD, Brooks RA, Kessler RM et al (1979) Tissue signatures with dual-energy computed tomography. Radiology 131:521–523

Flohr TG, McCollough CH, Bruder H et al (2006) First performance evaluation of a dual-source CT (DSCT) system. Eur Radiol 16:256–268

Genant HK, Boyd D (1977) Quantitative bone mineral analysis using dual energy computed tomography. Invest Radiol 12:545–551

Graser A, Johnson TR, Bader M et al (2008) Dual energy CT characterization of urinary calculi: initial in vitro and clinical experience. Invest Radiol 43:112–119

Graser A, Johnson TR, Hecht EM et al (2009) Dual-energy CT in patients suspected of having renal masses: can virtual nonenhanced images replace true nonenhanced images? Radiology 252:433–440

Grasruck M, Kappler S, Reinwand M, Stierstorfer K (2009) Dual energy with dual source CT and kVp switching with single source CT: a comparison of dual energy performance. Proc SPIE 7258:72583R

Ho LM, Yoshizumi TT, Hurwitz LM et al (2009) Dual energy versus single energy MDCT: measurement of radiation dose using adult abdominal imaging protocols. Acad Radiol 16:1400–1407

Holmes DR III, Fletcher JG, Apel A et al (2008) Evaluation of non-linear blending in dual-energy computed tomography. Eur J Radiol 68:409–413

Johnson TR, Krauss B, Sedlmair M et al (2007a) Material differentiation by dual energy CT: initial experience. Eur Radiol 17:1510–1517

Johnson TR, Weckbach S, Kellner H, Reiser MF, Becker CR (2007b) Clinical image: dual-energy computed tomographic molecular imaging of gout. Arthritis Rheum 56:2809

Kappler S, Grasruck M, Niederloehner D, Strassburg M, Wirth S (2009) Dual-energy performance of dual kVp in comparison to dual-layer and quantum-counting CT system concepts. Proc SPIE 7258:725842

Kelcz F, Joseph PM, Hilal SK (1979) Noise considerations in dual energy CT scanning. Med Phys 6:418–425

Kruger RA, Riederer SJ, Mistretta CA (1977) Relative properties of tomography, K-edge imaging, and K-edge tomography. Med Phys 4:244–249

Li B, Yadava G, Hsieh J (2010) Head and body CTDIw of dual energy x-ray CT with fast-kVp switching. In: SPIE Medical Imaging, San Diego, CA, paper 7622–7669

McCullough EC (1975) Photon attenuation in computed tomography. Med Phys 2:307–320

Michael GJ (1992) Tissue analysis using dual energy CT. Australas Phys Eng Sci Med 15:75–87

Millner MR, McDavid WD, Waggener RG, Dennis MJ, Payne WH, Sank VJ (1979) Extraction of information from CT scans at different energies. Med Phys 6:70–71

Morhard D, Fink C, Graser A, Reiser MF, Becker C, Johnson TR (2009) Cervical and cranial computed tomographic angiography with automated bone removal: dual energy computed tomography versus standard computed tomography. Invest Radiol 44:293–297

Nakayama Y, Awai K, Funama Y et al (2005) Abdominal CT with low tube voltage: preliminary observations about radiation dose, contrast enhancement, image quality, and noise. Radiology 237:945–951

Riederer SJ, Mistretta CA (1977) Selective iodine imaging using K-edge energies in computerized x-ray tomography. Med Phys 4:474–481

Schenzle JC, Sommer WH, Neumaier K et al (2010) Dual energy CT of the chest: how about the dose? Invest Radiol 45:347–353

Sommer WH, Johnson TR, Becker CR et al (2009) The value of dual-energy bone removal in maximum intensity projections of lower extremity computed tomography angiography. Invest Radiol 44:285–292

Svendsen OL, Hassager C, Bergmann I, Christiansen C (1993) Measurement of abdominal and intra-abdominal fat in postmenopausal women by dual energy X-ray absorptiometry and anthropometry: comparison with computerized tomography. Int J Obes Relat Metab Disord 17:45–51

Thieme SF, Becker CR, Hacker M, Nikolaou K, Reiser MF, Johnson TR (2008) Dual energy CT for the assessment of lung perfusion–correlation to scintigraphy. Eur J Radiol 68:369–374

Thieme SF, Johnson TR, Lee C et al (2009) Dual-energy CT for the assessment of contrast material distribution in the pulmonary parenchyma. AJR Am J Roentgenol 193:144–149

Voit H, Krauss B, Heinrich MC et al (2009) Dual-source CT: in vitro characterization of gallstones using dual energy analysis. Rofo 181:367–373

Dual Source CT

Bernhard Krauss, Bernhard Schmidt,
and Thomas G. Flohr

Contents

Abstract

- At the moment, there are two clinical, commercially available Dual Source CT (DSCT) scanners: the SOMATOM Definition and the SOMATOM Definition Flash (both by Siemens AG, Forchheim, Germany). Each of them contains two X-ray tubes and two detectors which are mounted so that the X-ray beams are approximately perpendicular to each other.
- For dual energy scan modes, the SOMATOM Definition is operated at 80 kV/140 kV, while the SOMATOM Definition Flash has an additional tin filter (Sn) and is typically used at 100 kV/Sn140 kV. This allows for high-quality DE scans also in the case of lager patient diameters, where 80 kV typically cannot be applied.
- The commercially available software syngo Dual Energy (Siemens AG) accompanies the scanners and uses image-based dual-energy analysis to perform, for example, automatic bone removal, monoenergetic imaging, lung perfusion imaging, or virtual noncontrast imaging. Due to the extremely fast scanning speed and simultaneous data acquisition at full dose modulation, Dual Source, Dual Energy CT (DECT) is fully applicable in routine use.

B. Krauss (✉), B. Schmidt, and T.G. Flohr
Siemens AG, Healthcare Sector, 91301 Forchheim, Germany
e-mail: bernhard.krauss@siemens.com

T.R.C. Johnson et al. (eds.), *Dual Energy CT in Clinical Practice*, Medical Radiology,
DOI: 10.1007/174_2010_44

1 Dual Source Dual Energy Scanning

1.1 Introduction

The first clinical Dual Source scanner (SOMATOM Definition, Siemens AG, Forchheim, Germany) was introduced in 2006; it consists of two separate third-generation CT acquisition systems mounted in one gantry (Petersilka et al. 2008). Each system has its own tube, generator, detector, and control devices, while for example cooling and the image reconstruction system are shared.

Dual Source CT (DSCT) scanning has four distinctive advantages over single source scanning: First, the two perpendicular X-ray beams image the same slice of the patient at the same time. This allows for robust cardiac imaging at high temporal resolution because already a quarter rotation is sufficient to reconstruct an image, while the apparent disadvantages of multisegment approaches (Halliburton et al. 2003) are avoided. With a gantry rotation time of 0.33 s, DSCT has a temporal resolution of only 83 ms, which is especially beneficial for improving image quality and reducing dose in cardiac CT scans.

Secondly, high-pitch modes are available, in which approximately the scan speed of a single source scanner with twice the number of slices is achieved, while maintaining the temporal resolution of DSCT.

Thirdly, the projection data from both detectors can be added, so that the SOMATOM Definition behaves like a single source scanner with double X-ray tube power.

Fourthly, for Dual Energy CT (DECT), the two tubes can simultaneously be operated at different voltages and the image sets are reconstructed independently (Johnson et al. 2006). Typically, 80 and 140 kV are chosen to maximize the difference of the spectra and the images are then analyzed with dedicated software (syngo Dual Energy; Siemens AG, Forchheim, Germany) to take advantage of the additional information. Fast image acquisition allows for dual-energy applications, like bone removal (Direct Angio) or lung perfusion imaging, that require short gantry rotation times and fast volume coverage.

In 2008, the second-generation DSCT "SOMATOM Definition Flash" was introduced. It features even faster gantry rotation (0.28 s), twice the number of detector slices and a larger field of view (332 mm) as well as a special spectral filter for dual-energy imaging.

1.2 Scanner Design

1.2.1 SOMATOM Definition

The SOMATOM Definition has two X-ray tubes which offer voltages between 80 and 140 kV in steps of 20 kV. The maximum tube current is 550 mA at 80 kV, 650 mA at 100 kV, and 500 mA at 140 kV. In dual-energy mode, the combination of 140 kV on system A and 80 kV on system B is used for all scans except for cardio scans (100 kV on system B).

To reduce patient dose, the tube current on both systems can be modulated independently as a function of patient diameter and tube angle by using CAREDose4D. The modulation amplitude is larger with 80 kV than with 140 kV due to the higher absorption by body materials at lower photon energies.

The mean energy of the 80(140) kV photon spectrum behind the bow-tie filter at its center is 52(69) keV; the detector is an integrating UFC scintillation detector, which means that the high-energy photons dominate and the mean energy of the power spectrum is 54(76) keV.

For both tube voltages, the photon spectrum (Fig. 1) is rather broad and ranges roughly from 35 keV to

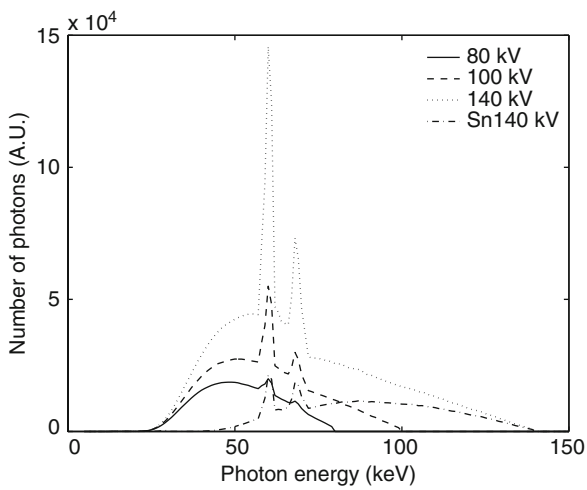

Fig. 1 X-ray spectra of the SOMATOM Definition Flash: Rays through the isocenter were simulated with DRASIM; the tube current was the same for all spectra

electron charge *e* times the tube voltage (kV). The photon energy is thus clearly above the K-edge of all common atoms in the human body (the K-edge of iodine is at 33 keV). The characteristic line spectrum of the tungsten anode is more pronounced at 140 kV than at 80 kV and systematically lowers the mean energy of the 140 kV spectrum.

Each X-ray detector has two different readout modes: as there are 32 readout channels for each detector column, it is either possible to choose a detector collimation of 64 × 0.6 mm by using only the central 32 slices and z-Sharp technology or 24 × 1.2 mm by using, in addition, the outer 8 thick detector slices, while binning the central slices. For DECT, one special mode is 14 × 1.2 mm; in this mode, the central 28 slices are illuminated by the X-ray-beam, but the whole detector is read out, which allows to measure the scatter signal in the shadow of the collimator.

While the first detector (A) has 672 columns, the second detector (B) has only 352 columns; consequently the field of view is 500 mm (A) or 268 mm (B). The different field of view is dictated by the required temporal resolution for cardiac scanning and the allowed dimensions of the gantry due to room height and centripetal force. In order to reconstruct images for system B, the sinogram outside the B field of view is filled with data from system A. Outside the B field of view, the B-image is clipped and only the 140 kV image is available.

If A images and B images are reconstructed separately, the temporal resolution is identical to the corresponding single source scan. For the SOMATOM Definition a 180° reconstruction results in simultaneously acquired images of the same *z*-position with a temporal resolution of 165 ms. This is the only meaningful quantity to characterize temporal resolution of a CT scan and it is at least by a factor of two faster than kV-switching on a single source scanner at same tube load, because two tubes deliver twice the power of a single quickly switching tube; in addition, rotation time with fast kV-switching is further limited by the finite switching time. Furthermore, as image-based dual-energy analysis is applied, there is, for example, no need of measuring along the same trajectory twice within a short time interval, because there is no danger of projection data inconsistencies as encountered with raw data-based methods (Kalender et al. 1986).

1.2.2 SOMATOM Definition Flash

The generators of the SOMATOM Definition Flash provide the same voltages as the SOMATOM Definition, while the additional tin filter (selective photon shield) on system B is denoted by the new voltage label "Sn140 kV." The mean energy of the Sn140 kV spectrum behind the bow-tie filter (Fig. 1) is 89 keV; the mean detected energy in the detector is 92 keV.

The tin filter has two benefits:

- Increase of spectral separation between the low and the high-energy spectrum
- Narrowing of the 140 kV spectrum (which entails better dose efficiency and less beam-hardening artifacts)

A comparison of different dual-energy acquisition methods shows that, by the use of the tin filter, spectral separation at same dose is superior to kV-switching and dual-layer techniques, while quantum counting devices currently achieve a similar performance at much lower count rates (Kappler et al. 2009; Grasruck et al. 2009).

The tin filter reduces dose by more than a factor of three with respect to 140 kV without filter. In order to provide enough power, the maximum current at Sn140 kV can be increased up to 700 mA. For dual energy scanning on the SOMATOM Definition Flash, three different voltage combinations are available: The most dose-efficient mode for typical European or North American patient diameters is the voltage combination 100 kV/Sn140 kV. Best spectral separation is achieved with 80 kV/Sn140 kV. For reasons of compatibility with the SOMATOM Definition, the mode 80 kV/140 kV is also available.

The SOMATOM Definition Flash offers three different shaped filters to achieve optimum dose and spectral distributions across the scan field of view for imaging of different body regions.

The two detectors have 64 physical slices, which in combination with the z-Sharp leads to 128 measured slices per rotation. While the larger detector (A) has 736 columns, the smaller detector (B) has 480 columns; this is equivalent to a field of view of 500 mm (332 mm) for detector A(B). The field of view of detector B was increased by increasing the angle between tube A and tube B to 95° (compare Fig. 2). With this improvement, all relevant anatomy fits into the FOV of the B system. The impact of this change on temporal

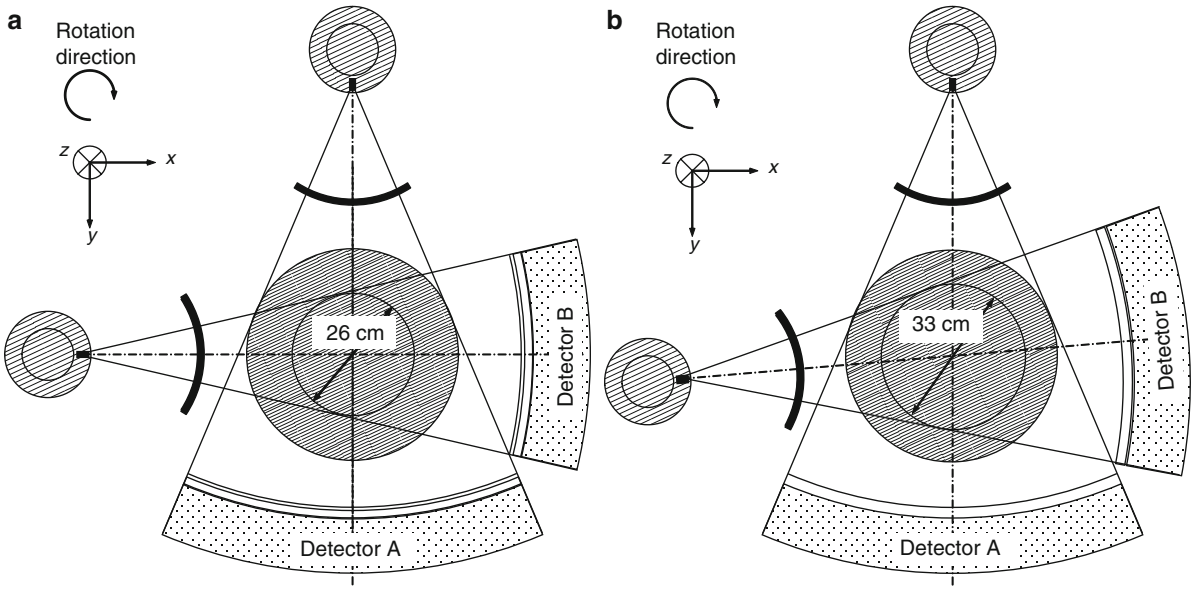

Fig. 2 Schematic drawings of the SOMATOM Definition (**a**) and the SOMATOM Definition Flash (**b**). The larger second detector in the SOMATOM Definition Flash became possible, because of a larger angle between the two fan-beams

resolution in case of a cardiac dual source scan is, however, negligible (75 ms instead of 71 ms).

Four different collimations are available: 128×0.6 mm (z-Sharp), 64×0.6 mm (z-Sharp), 32×0.6 mm (no z-Sharp), and 40×0.6 mm (z-Sharp).

Each detector is also equipped with additional sensors, placed on both sides of the detector along the *z*-direction. They allow for measuring and subsequent correction of cross-scattered radiation even with the widest detector collimation.

Standard temporal resolution for dual energy cardiac scanning with separate reconstruction of the data sets is 143 ms. In addition, the same data can be used to reconstruct merged images with an even higher temporal resolution of 75 ms, while the iodine enhancement of the 100 kV scan is maintained.

1.3 Data Acquisition

The available voltage combinations were tailored to provide optimum dose performance: For each patient diameter, there is an optimum voltage for which image noise in a single energy scan is best at a given dose; for the typical abdomen of average-sized patients in Europe and North America, it is approximately 120 kV. Hence, in DECT the mixed image, which is a linear combination of the two acquired images stacks, should have similar noise and contrast enhancement properties compared to an image of a dose-equivalent single energy CT scan at 120 kV. In clinical routine, a dose-efficient low noise mixed image is as important as good spectral resolution. As a consequence, the voltage combination 100 kV/Sn140 kV is better suited for average to larger patient diameters, while the voltage combination 80 kV/140 kV or 80 kV/Sn140 kV is better suited for small patient diameters. A combination of 60 and 180 kV would have good spectral separation, but very poor dose efficiency for the mixed image; similarly, the tin filter may not be too thick. In order to obtain maximum dose efficiency, it is also important to keep an appropriate current ratio between the two tubes. At 100 kV/Sn140 kV the suggested ratio of the quality reference mAs varies between 1.0 and 1.3 depending on the body region. For typical patients, the obtained effective mAs are identical to the quality reference mAs which enter the automatic exposure control, while for larger patient diameters the ratio of the obtained effective mAs is more than 1.3 to optimize dose efficiency.

For the 80 kV/140 kV voltage combination, 140 kV are assigned to the A-system, because it will always have good image quality and sufficient iodine enhancement. In the mode 100 kV/Sn140 kV the situation is reversed:

Although the Sn140 kV image would have very good image quality, iodine enhancement would be rather low, so that the 100 kV were assigned to system A.

With dual source scanners, special attention has to be paid to cross-scattered radiation. Cross-scattered radiation originates from the X-ray tube of the other acquisition system and enters the detector due to Compton scattering at the surface of the patient.

With dual energy scanning, cross scatter can be more pronounced than with dual source cardiac scanning. Since the high kV X-ray quanta have a higher mean energy than the low kV X-ray quanta, the low kV image will receive a relatively larger amount of cross scatter from the high kV tube than vice versa. It is therefore desirable to optimize scan protocols also with respect to cross-scattered radiation.

Since the amount of cross scatter is roughly proportional to the z-opening of the collimator, narrow collimations provide best quality for quantitative imaging.

Angular dose modulation is another important way of reducing cross-scattered radiation by reducing the tube output where it is not needed, while tube output on the other tube is simultaneously increased.

In addition to reducing cross-scattered radiation, it finally has to be corrected for by either measuring the scatter signal in the shadow of the collimator (Definition, Definition Flash) or by subtracting a model distribution (Definition only). Narrow collimations are again advantageous, as the cross-scattering signal has fewer variations along the *z*-direction. The default scan protocols try to minimize cross-scattering in order to achieve extremely stable CT values and maximize dose efficiency.

The dose of dual energy scans is not increased compared to standard single energy scans if the proper combination of spectra is used. Figure 3 shows a comparison between a 30-cm water phantom scanned at 120 kV with a standard body angio protocol on a standard 64 slice scanner (SOMATOM Definition, single source mode) and the standard dual-energy body angio protocol for bone removal with 100 kV/Sn140 kV on the Definition Flash (128 slices, same reconstruction parameters) adjusted to the same total dose. Noise in the DE-mixed image is actually slightly lower than in the single energy image. This has been verified in a comparison between several Definition and Definition Flash scanners.

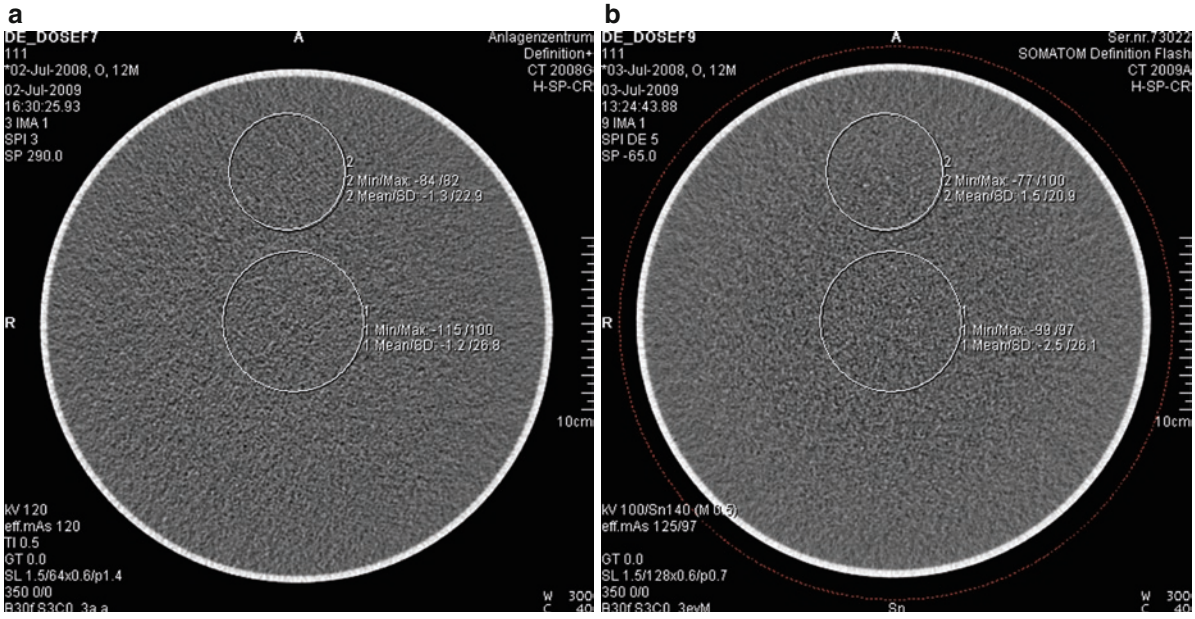

Fig. 3 Noise comparison between single and Dual Energy CT (DECT): a 30 cm cylindrical water phantom was scanned on the SOMATOM Definition with the default single energy protocol for body angios (**a**) at $CTDI_{vol} = 8.64$ mGy. The scan was repeated on the SOMATOM Definition Flash with the fast dual-energy body angio protocol (**b**) at $CTDI_{vol} = 8.66$ mGy and similar iodine enhancement in the mixed image. With the same reconstruction kernel, image noise in the dual-energy image is slightly lower for both shown ROIs. This result was confirmed in a comparison between 4 SOMATOM Definition scanners and 7 SOMATOM Definition Flash scanners

As illustrated in this case, the dose of the dual energy scan protocols is usually driven by the diagnostically needed quality of the mixed images rather than the dual-energy evaluation.

2 Image-Based DECT Analysis

2.1 Introduction

Image-based analysis of DECT data has a long history (Zatz 1976). On the one hand, it has advantages in clinical routine as the reconstructed CT images can directly be interpreted by any radiologist, while on the other hand, its precision relative to raw data-based approaches has sometimes been questioned (Marshall et al. 1981). To assess this issue, it is important to distinguish between the theoretical accuracy for arbitrary scanned objects and the clinically relevant application, which only deals with realistic patient cross-sections. In clinical routine electronics noise, scanner calibration, stability of emitted spectra, cone beam effects, and scattered radiation can have a larger impact on the obtained results than the analysis method.

Modern CT scanners are calibrated such that the CT value of an object that only contains water with arbitrary densities is theoretically correct. Proteins are chemically very similar to dense water, while body fat has only a slightly lower effective atomic number, which means that most components of the human body have well-defined CT values. On the other hand, heavy atoms like Calcium or Iodine have a CT value that is not a unique function of their atomic density; instead, the CT value depends on the surrounding object and the exact X-ray spectrum.

In reality, the CT value is at least semiquantitative as long as these intrinsic limitations are observed.

2.2 The Thin Absorber Case

Image-based dual-energy analysis works best under the following conditions: The scanner must be equipped with a shaped filter of sufficient beam-hardening and the approximately cylindrical patient cross-section has to be centered within the scan field of view of the scanner. Clearly, patients do not have a strictly cylindrical cross-section, but in practice also elliptical cross-sections fulfill the prerequisite, while, for example, a triangular shape – which is not seen in reality – would cause artifacts. In addition to the geometrical requirements, the scanner must perform a beam-hardening correction that is optimized for water.

All this ensures that neither the CT value of water nor the CT value of a small iodine sample depends on its position inside the scanned object. However, the CT value of iodine still depends on the patient diameter. This is shown for the SOMATOM Definition and cylindrical water phantoms in Fig. 4; for elliptical phantoms (or more complex shapes), an equivalent water diameter can be defined. Usually, the diameter dependence has not been taken into account for image-based processing in the published literature. This explains the better performance of the present approach with dual source, dual energy scanners.

Finally, image-based processing only works if the product of the absorption of the sample $\mu(E)$ for all energies E contained in the spectrum and the maximum thickness d of the sample along any measured direction is small compared to one attenuation length. Only under this condition it is valid to assume a linear dependence of the additional nonwater-like attenuation by the

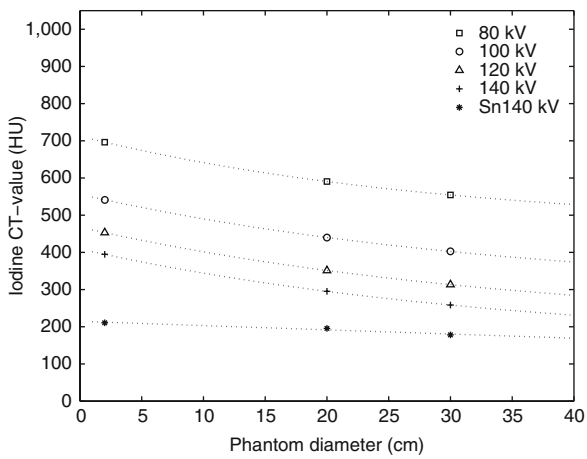

Fig. 4 Iodine enhancement as a function of phantom diameter: A small sample of iodine (diameter 2 cm, 15 mg mL^{-1} iodine) was scanned in air and cylindrical water phantoms of 20 and 30 cm diameter on a SOMATOM Definition Flash using all available spectra. The CT value with tin filter is very stable which indicates low beam-hardening of this spectrum

sample on the product $\mu(E)\times d$, which is the basic requirement for image-based processing. Clearly, this requirement is not exactly fulfilled for all energies in the detected spectrum, but the value of μ averaged over the detected spectrum is a useful scale. For water, this is approximately 0.2 cm^{-1}, such that the thin absorber approximation is expected to break down for iodine samples with more than 5,000 HUcm. In practice, negligible deviations were found for iodine absorption thickness products of 1,000 HUcm, which corresponds to the clinical situation of 33 cm of liver with an iodine enhancement of 30 HU. For the same product of absorption and thickness, bone has a sizable water-like component and is therefore less critical.

All the above is typically fulfilled in the case of DSCT systems and many clinical scenarios.

2.3 Mixed Image, Monoenergetic Image, Dual Energy Index

The mixed image is the diagnostic image that is obtained by linear weighting of the CT value for the two spectra:

$$x = w \times x_{low} + (1-w) \times x_{high}, \qquad (1)$$

where w is the "dual energy composition," x denotes the CT value in the mixed image, and x_{low} and x_{high} are the CT values of the low and high kV image, respectively.

As the CT value of iodine drops monotonously with increasing voltage, the mixed image has an iodine enhancement that is the same as at some intermediate voltage. In addition, two-material decomposition predicts (Alvarez and Macovski 1976) that also all other materials have the correct CT value corresponding to this voltage. The mixed image is therefore largely equivalent to a standard CT image.

Within the thin absorber model, the calculation of monoenergetic images is straightforward: An image is equivalent to a certain monoenergetic image if the measured iodine enhancement is the same. This means that the low kV image as well as the high kV image is equivalent to a certain energy (59 keV for 80 kV and 79 keV for 140 kV at 20 cm diameter), and the mixed image corresponds to an intermediate energy. Monoenergetic images corresponding to energies outside this range can be obtained by calculating water and iodine concentrations, multiplying them with the predicted CT value per concentration, and summing up the two contributions. As the monoenergetic image is synthetic, so are its noise properties. Hence, noise increases strongly for very low and very high energies (Alvarez and Seppi 1979).

Finally, in order to quantify the general dual-energy behavior of test samples, the dual energy index (DEI) is useful (Fig. 5). For a material in air (not dissolved in water), it is defined as

$$DEI = \frac{x_{low} - x_{high}}{x_{low} + x_{high} + 2{,}000\,HU}, \qquad (2)$$

with x_{low} and x_{high} being the HU values of image pixels at low energy and high energy, respectively. The DEI is zero for water, negative for light atoms, and positive for all heavy atoms that are typically encountered in the human body. The DEI of a mixture of materials is between the DEIs of the original two materials. In contrast to the effective atomic number (which is usually calculated as the root of a weighted sum of the contained atomic numbers (Hawkes and Jackson 1980)), the DEI does not rely on a claimed behavior of the photoelectric cross-section and is also meaningful for mixtures of light atoms with elements heavier than iodine.

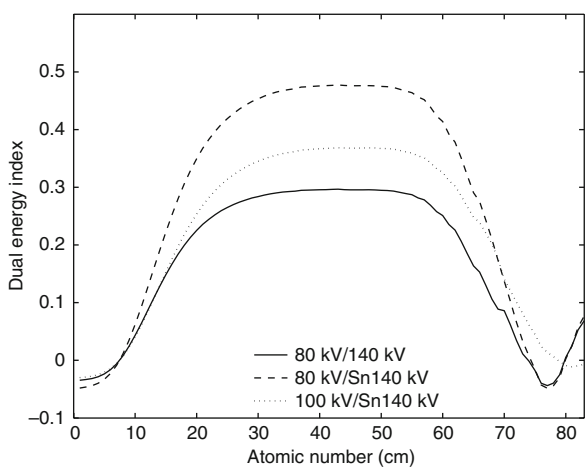

Fig. 5 Simulation of dual energy index (DEI) vs. atomic number: The DEI of thin pure material samples was simulated for all available combinations of spectra with the SOMATOM Definition Flash. The magnitude of the DEI is considerably increased with tin filter, while the shape of the curves is very similar

2.4 Material Decomposition Analysis

The software package syngo Dual Energy, which is optionally available on the two dual-source dual-energy scanners, uses two main approaches for image analysis. The first one is material decomposition, while the second is material labeling. Both methods are best understood in the CT-value diagram (x_{low} vs. x_{high}) as shown in Fig. 6.

Material decomposition into two materials of arbitrary density has been known for a longer time (Hawkes et al. 1986). Decomposition into three materials of known density was proposed in 1990 (van Kuijk et al. 1990). The present method for subtracting iodine from a DECT image is a modification of this approach: Instead of a decomposition into three fixed points in the x_{low}/x_{high} plane, syngo Dual Energy uses two body material data points (fat and soft tissue) and the slope of the iodine enhancement vector. This is possible as the infinitesimal addition of iodine to both body tissues leads to a similar and measurable enhancement vector for both tissues, while the CT value of pure iodine contrast agent is much more difficult to determine.

Subtraction of the iodine corresponds to a parallel projection in the CT-value diagram or the solution of a linear equation. Image noise is inflated during decomposition and it is also possible to calculate the image noise in the result images. Especially if spectral resolution is bad, noise will increase dramatically. Under the assumptions of identical image noise in both images, an enhancement ratio of 2.0 for iodine, air and water as second and third materials, and a suitable dual-energy composition of 0.5, image noise is inflated by a factor of 4 relative to the mixed image. This challenge requires dedicated noise-reducing filtering as it is implemented in syngo Dual Energy or, for example, suggested in (Kalender 1988).

If various spectra are used alternatively, like on the Definition Flash, it is possible to transform the CT values of all materials by knowledge of the CT values of iodine for the old and the new combination of spectra. For the CT values of soft body tissues, changes are almost negligible.

In syngo Dual Energy, this kind of material decomposition analysis is used to highlight iodine vs. hemorrhage in the brain (Brain Hemorrhage, Ferda J et al (2009)), to visualize perfusion defects in the lung (see chapters LungPBV; Lung Perfusion), to isolate the iodine signal in a liver with fatty infiltrations or necrosis (see chapters LiverVNC; Neurological Applications, Liver Imaging, Kidney Imaging), to visualize perfusion defects in the myocardium (see chapters HeartPBV; Myocardial Perfusion), and to visualize the iodine uptake of lung nodules (see chapters LungNodules; Pulmonary Nodules and Lung Cancer).

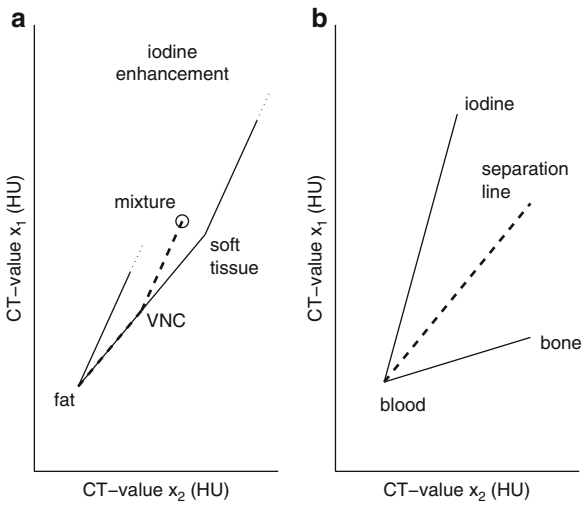

Fig. 6 Material decomposition (**a**) and material labeling (**b**): While material decomposition yields two CT images containing different materials (iodine and VNC image), material labeling distinguishes two possible material mixtures that are above or below the separation line

2.5 Material Labeling and Highlighting

General material highlighting is possible with DECT by mapping each position in the CT-value diagram to some displayed color and intensity. As this requires a number of distinct materials of unique chemical composition and density, this approach is only useful for very specific clinical questions, like the highlighting of tendons and ligaments (see chapter Kidney Stones).

In clinical applications, the more common case is that the materials of interest are embedded or mixed with a common matrix material like blood or soft tissue. In the CT-value diagram, mixtures of two noninteracting materials are always located on straight lines between the pure materials. For example, in the case of dual-energy bone removal (Fig. 6), the pure materials iodine or bone mineral of arbitrary concentration mix with the common matrix material blood/soft tissue. The most general approach to separate the two potential

material mixture lines is to use a separation line that goes through the common matrix material; the slope of the separation line is close to the bisector between the two material mixture lines. However, the ideal choice also depends on image noise and typical iodine and bone concentrations. It is therefore not possible to define an exact transformation for the slope when changing the combination of spectra and empirical corrections are used for example when changing the combination of spectra on the SOMATOM Definition Flash.

Material mixtures that contain mainly the matrix material are difficult to classify. It is therefore useful to introduce a minimum threshold on the CT value in the mixed image. Only voxels above this threshold are then, for example, labeled with two different colors, which reflect if they are above or below the separation line.

Material labeling has a finite spatial resolution that is typically less than that of the CT image, especially if voxels are close to the minimum threshold. Hence, dedicated filter algorithms are used to improve noise and/or spatial resolution.

Interestingly, the apparent boundary between two adjacent differently labeled materials in the image depends on the choice of the separation line as well as the concentrations of the two materials. In this sense, the separation line concept in itself does not eliminate the "blooming" effect that is known from single energy CT; moreover, in a clinical case with realistic patient dose mainly the filter algorithm is responsible for the exact behavior at these boundaries.

In syngo Dual Energy, material labeling with separation lines is used for bone subtraction in CT angiographic data sets (see chapters Bone Removal; Head and Neck, Aorta, Peripheral Arteries) to visualize the composition of kidney stones (see chapters Kidney Stones; Pancreas), the iodine content of extremely small lung vessels (see chapter Lung Vessels, Krissak R et al (2010)), and Gout vs. deposition of Calcium (see chapters Gout; Tendons and Ligaments).

3 Outlook

Due to the additional tin filter, which is to our knowledge only possible on dual tube systems, the SOMATOM Definition Flash has considerably higher spectral separation capabilities than classical dual energy scanners, which use 80 and 140 kV or dual-layer CT systems. Its increased field of view and faster volume coverage make it an ideal dual energy scanner for CT angiography and thoracic imaging. Together with the improved dose performance and the ability to apply established dose reduction techniques like CAREDose4D, this ensures that the scanner can be used in daily routine to gain additional diagnostic information. The capability to simultaneously acquire high and low kV data at the highest rotation time (0.28 s) in cardiac dual-energy mode allows both reading from CTA images with a temporal resolution of 75 ms and dual-energy postprocessing based on a second reconstruction.

The first scientific publications based on this scanner have just become available and it can be expected that many more will follow.

In the future, DSCT may also profit from other developments in CT technology: With increasing X-ray tube power, additional filters may be added in both X-ray beams. This would increase spectral separation as well as dose efficiency even further and reduce beam-hardening effects at the same time.

In terms of postprocessing, DSCT may benefit from iterative reconstruction: This method allows for raw data-based processing with nonmatching X-ray projections for the two spectra. Thus, Dual Source DECT has plenty of potential to evolve in the future.

Acknowledgment We would like to thank Dr. Martin Petersilka for his contributions.

References

Alvarez RE, Macovski A (1976) Energy-selective reconstructions in X-ray computerized tomography. Phys Med Biol 21(5):733–744

Alvarez R, Seppi E (1979) A comparison of noise and dose in conventional and energy selective computed tomography. IEEE Trans Nucl Sci 26(2):2853–2856

Ferda J et al (2009) The assessment of intracranial bleeding with virtual unenhanced imaging by means of dual-energy CT angiography. Eur Radiol 19(10):2518–2522

Grasruck M et al (2009) Dual energy with dual source CT and kVp switching with single source CT: a comparison of dual energy performance. Proc SPIE 7258(2):72583R

Halliburton SS et al (2003) Do segmented reconstruction algorithms for cardiac multi-slice computed tomography improve image quality? Herz 28(1):20–31

Hawkes DJ, Jackson DF (1980) An accurate parametrisation of the X-ray attenuation coefficient. Phys Med Biol 25(6): 1167–1171

Hawkes DJ, Jackson DF, Parker RP (1986) Tissue analysis by dual-energy computed tomography. Br J Radiol 59:537–542

Johnson TR et al (2006) Material differentiation by dual energy CT: initial experience. Eur Radiol 17(6):1510–1517

Kalender WA (1988) An algorithm for noise suppression in dual energy CT material density images. IEEE Trans Med Imaging 7(3):218–224

Kalender WA et al (1986) Evaluation of a prototype dual-energy computed tomographic apparatus. I. Phantom studies. Med Phys 13(3):334–339

Kappler S et al (2009) Dual-energy performance of dual kVp in comparison to dual-layer and quantum-counting CT system concepts. Proc SPIE 7258(3):725842

Krissak R et al (2010) Enhanced visualization of lung vessels for diagnosis of pulmonary embolism using dual energy CT angiography. Invest Radiol 45(6), 341–346

Marshall WH Jr, Alvarez RE, Macovski A (1981) Initial results with prereconstruction dual-energy computed tomography (PREDECT). Radiology 140:421–430

Petersilka M et al (2008) Technical principles of dual source CT. Eur J Radiol 68(3):362–368

van Kuijk C et al (1990) Evaluation of postprocessing dual-energy methods in quantitative computed tomography. Invest Radiol 25(8):876–881

Zatz LM (1976) The effect of the kVp level on EMI values. Selective imaging of various materials with different kVp settings. Radiology 119:683–688

Dual Layer CT

Alain Vlassenbroek

Contents

Abstract

› Dual-energy CT enables improvement of material and possibly tissue separation when compared to regular CT. Philips Healthcare has been successfully operating a dual-layer detector system in a modified Brilliance 64 CT scanner installed since 2005 in Hadassah University Medical Center, Israel. The dual-layer detector acquires single x-ray source CT data using two scintillation layers on top of each other with which two energy datasets are acquired simultaneously. The results of the two reconstructions are mapped into a plane created from the Hounsfield units (HU) of the upper-layer image versus the HU of the lower-layer image. We find that different materials end up in different definable regions in the HU-plane, so material separation can be performed. Application of a special correction on the reconstructed images achieves stability on the HU-plane despite beam-hardening effects on this image-based dual energy CT. We describe the material separation capabilities and algorithms with such a configuration and conclude that the combination of the dual-layer CT with the classification analysis in the HU-plane is a practical and robust method that may improve clinical applications, in particular those involving Iodine-Calcium.

A. Vlassenbroek
CT Clinical Science and Applications, Europe
Philips Healthcare, Rue des Deux Gares 80,
1070 Brussels, Belgium
e-mail: Alain.Vlassenbroek@Philips.com

T.R.C. Johnson et al. (eds.), *Dual Energy CT in Clinical Practice*, Medical Radiology,
DOI: 10.1007/174_2010_56

1 Introduction

Recent developments in detector technology and modern clinical requirements, like quantitative Computed Tomography and the need for tissue classification, have revived interest in spectral Computed Tomography. Research work on the separation of the x-ray beam into multiple energy windows shows great promise to further enhance the diagnostic capabilities of CT scanning (Shlomka et al. 2008). The most advanced form of spectral CT is enabled by photon counting detectors; highly efficient "low dose" detectors which count each individual incident x-ray and measure the energy of each photon. Photon counting uses narrow selectable subranges (or bins) of the spectrum which can be used for example to detect and classify spectral "k-edge" patterns of clinical relevant materials at very low concentrations (Roessl and Proksa 2007). Early results are extremely promising. However, to count photons in multiple energy bins at rates required for diagnostic use in humans remains a significant hurdle. Clinical photon counting would require 100 times faster detectors than currently available to go into clinical use. The CT rotation speed and x-ray tube current of existing prototypes is very low, the net effect being long scan time; the goal of sub-second scanning is still elusive. But faster counting detectors and electronics are envisioned that may open the door to a new window on the human body and bring molecular imaging to CT.

Rather than using the "energy resolving" photon counting detectors, today's clinical spectral CT scanners use the traditional integrating detectors which show a much better counting rate performance, adequate for clinical use. This detector technology has the crucial disadvantage that the detected photons are simply integrated, irrespective of their energy and thus not taking into account the abundant spectral information of the polychromatic x-ray spectrum passing through the imaged object. As a consequence, the current clinical spectral CT scanners do not have full spectral capability and should be named dual energy CT scanners (DECT) since they enable separation into two different overlapping energy windows. Still, they enable the discrimination between different materials based on the differential x-ray attenuation properties in two "energy bands" of the spectrum, instead of averaging the entire polychromatic beam like conventional CT does. In other words, the spectral dependencies of the net x-ray attenuation can be imaged and analyzed as a material characteristic and can be used to discriminate materials. With clinical DECT, this additional information can be obtained using several data acquisition methods: (1) Single x-ray source, Dual kVp Spin (Philips), (2) Single x-ray source, Dual kVp Switch (General Electric), (3) Dual x-ray source (Siemens) and (4) Single x-ray source, Dual-Layer Detector (Philips).

The present chapter will be dedicated to the last method which uses one single x-ray source and detects the radiation using innovative, dual-layer detectors that separate the x-ray beam into two components (i.e., polychromatic x-ray detection).

2 Physical Background

In a single source, dual-layer detector scanner configuration, one x-ray tube is used to expose a detector consisting of two layers of scintillators (Fig. 1). The two

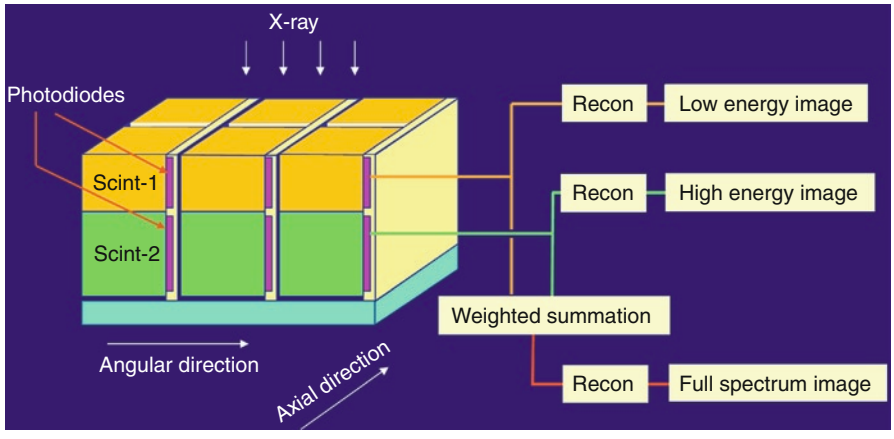

Fig. 1 A schematic illustration of the dual-layer detection system (only a few detector elements are shown). The photodiodes are parallel to the x-ray direction, attached to the sides of the two types of scintillator elements

layers are directly on top of one another. A single CT scan is performed at a high kVp (e.g., 120 or 140 kVp). The first layer encountered by the x-ray photons absorbs most of the low-energy spectrum (by design approximately 50% of the beam), while the bottom detector layer absorbs the remaining higher energy photons. Images are reconstructed separately from the data of the upper and lower layers.

In contrast to other approaches of dual energy CT, there is no need to redundantly expose materials with both low and high energy x-rays. Furthermore, since the spectral energy separation is intrinsic to the detection system, rather than sequentially generated at the x-ray source, this approach eliminates the time lag of sequential techniques, making it ideal for imaging moving organs (see Fig. 2). In other words, the dual-layer technique is fully registered both spatially and temporarily. It has no spatial shift or dead time such as in dual kVp or dual tube techniques. The low- and high-energy spectral images can be easily combined on a voxel-to-voxel basis into a conventional "full spectrum" CT image without the need to compensate for warping and shifting due to the time lags. The use of a single source also obviates the cross scatter limitation of dual source techniques (Engel et al. 2008). Furthermore, this approach allows full 50 cm FOV imaging so it can be used for both fast and wide MDCT imaging and spectral imaging.

We also want to emphasize the advantage which results from the obtained radiation spectra of the two energy windows, especially for objects with high radiation attenuation such as abdomen, pelvis and large patients in general. The dual-layer detectors have typical absorbed spectra as shown in Fig. 3. As can be seen, the low energy spectrum (of the upper scintillation layer) has energy components which continue up to the maximal energy determined by the applied tube voltage. In addition, the high energy spectrum (recorded by the lower layer) is very hard (i.e., with little low energy components) due to the strong "filtration" by the first layer. Overall, the energy separation between the two windows is appropriate for material separation while the two spectra are significantly harder compared to the other dual kVp methods (e.g. 80 and 140 kV). The hard spectrum shape of the high energy window of the dual-layer detector cannot be achieved by strongly filtering the emitted x-ray radiation (e.g., by using a metal filter immediately after the x-ray tube) since such strong filtration would produce significant forward scattered radiation from the filter sheet and would degrade significantly the image quality (Carmi et al. 2008). In the dual-layer technique such problem is eliminated since the filtrating first layer is closely adjacent to the second layer. For body regions with high radiation attenuation, dual kVp techniques suffer from an inferior image quality since the low voltage

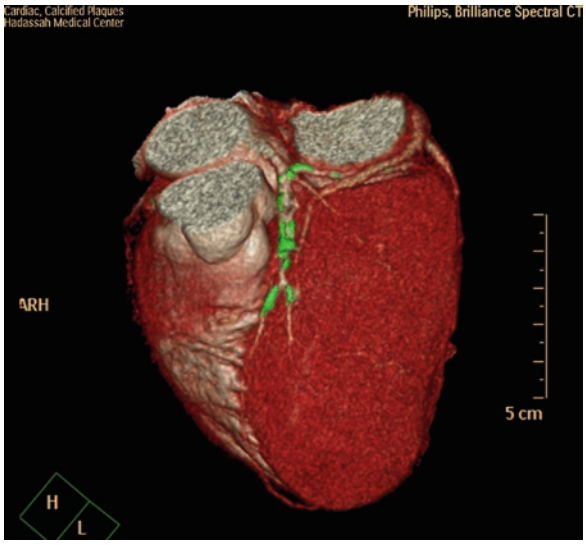

Fig. 2 In a single source, dual-layer detector scanner configuration, the spectral energy separation is intrinsic to the detection system, rather than at the x-ray source. This approach eliminates the time lag of sequential techniques, making it ideal for imaging moving organs, such as the heart. Dual energy material separation then enables to identify selected material as the coronary calcifications (highlighted in *green*) which can be separated from the iodinated blood pool

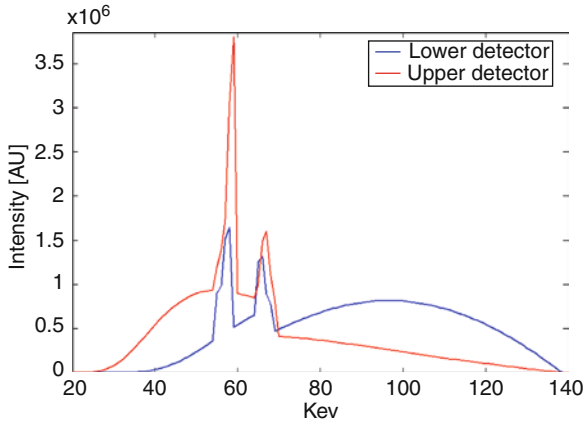

Fig. 3 The absorption spectra of the dual-layer CT with a tube voltage of 140 kVp

scan (usually 80 or 90 kV) produces very low signal at the CT detectors (due to the too soft radiation with such voltage).

3 System Design

The Dual-Layer CT prototype scanner from Philips HealthCare is a modified Brilliance 64-slice scanner (B64) used as a 32-slice dual-layer scanner with 64 electronic channels (2 per each dual-layer detector element). All the scanner hardware elements are identical to those of the B64 except the detection system which contains the same number of detectors in the scan plane XY (672 detector elements per detector row) with full field of view (= 50 cm) scan capability but only 32 detectors rows along the patient axes *Z*, with a minimal slice thickness of 0.625 mm at isocenter.

4 Image Reconstruction

4.1 Image Reconstruction and Energy Map

Images are reconstructed separately from the data of the upper (low-energy E1) and lower (high energy E2) layers using a full three-dimensional filtered back projection algorithm (Feldkamp et al. 1984). By combining the raw data of the two layers, standard CT images obtained from the full energy spectrum are also reconstructed and are used by the radiologists for routine diagnostic imaging. With this image-based DECT, the raw data sets of the upper and lower layers are treated independently till after the reconstruction. The reconstructed E1 and E2 image datasets can then be combined to obtain material specific images using a post-processing software, as will be discussed in Sect. 5.

A major difference between image-based and raw data based DECT is in the beam-hardening correction. Raw data-based DECT is passing the raw data through a decomposition function followed by image reconstruction. Raw data-based decomposition is exact and the final image will not show beam hardening artifacts. However, raw data-based decomposition requires consistent raw data sets (Baer et al. 2009). Image-based decomposition does not have this advantage. However, as will be discussed in detail in Sect. 4.3, special post-processing corrections can be applied to achieve stability on the HU-plane and this approach provides a practical way to improve image-based DECT without changing the scanner software or hardware.

Figure 4 shows an example of the three datasets obtained after reconstruction of a spiral neck scan performed at 140 kVp. Additional spectral information can then be obtained after mapping the data from the E1 and E2 images into a plane created from the HU of the upper-layer image vs. HU of the lower-layer image. At every image position, this HU plot displays the (E1, E2) values of every image voxel located in the reconstructed field of view. The resulting HU plot or "Energy Map" is also presented in Fig. 4.

If a voxel contains only one material, its position on the Energy Map will be located in a region centered on the expected HU values (E1, E2) for this material and with a size which depends on the noise in both the E1 and E2 images. For example, a voxel containing pure water should be located in a cloud centered at (0,0) HU, the width of the cloud being dependent on the noise in the dual-energy CT images. If a voxel contains two materials, its place on the plot is on a line between these two composing materials. In particular, different concentrations of a material in water appear on a line emanating from the water point, where the low concentration is closer to the water and the high concentration is further away. This forms a "hands-of-a watch" impression in which different materials relevant for human body CT lie on different "hours." In principle, if noise is not too high and beam-hardening effects are overcome, a straight line is sufficient to separate the different materials that cannot be separated by a regular CT. Figure 5 shows the full spectrum CT image (Fig. 5a) and the corresponding Energy Map (Fig. 5b) of a water phantom containing eight identical tubes, four containing solutions of $CaCl_2$ and four containing solutions of iodine in water at decreasing concentrations. The respective relative concentrations are: 1.0 (tubes 1 and 2: CT# = 879 HU), 0.54 (tubes 3 and 4: CT# = 477 HU), 0.29 (tubes 5 and 6: CT# = 252 HU) and 0.16 (tubes 7 and 8: CT# = 140 HU) in both the calcium and iodine tubes and the CT# are measured on the full spectrum CT images. We note that a material classification (calcium or iodine) cannot be performed based on the HU values measured on the "full spectrum" CT image since the HU values were chosen identical on purpose. However,

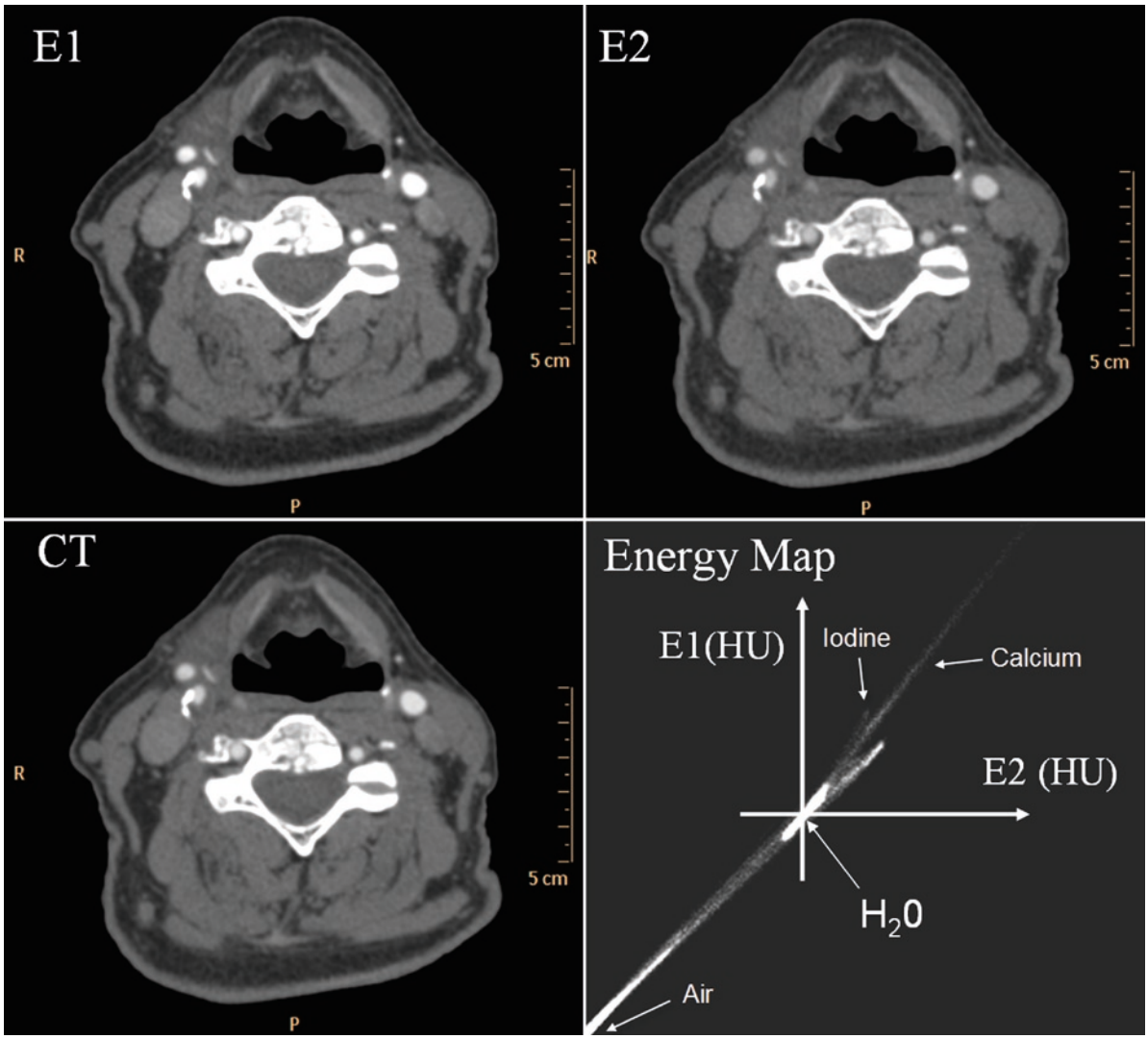

Fig. 4 The three datasets obtained after reconstruction of a spiral neck scan performed at 140 kVp. Additional spectral information is then obtained after mapping the data from the E1 and E2 images into a plane created from the HU of the upper-layer image vs. HU of the lower-layer image. At every slice position, the HU plot displays the (E1, E2) values of every voxel located in the reconstructed field of view. In the energy map: iodine, calcium, air and soft tissue voxels are easily identified. The calcium line extends far in the upper right corner due to the high attenuation of the bone and calcified structures

in the energy map, each tube can be tagged according to its position in the energy map and a single line (Fig. 5d) enables to separate the calcium and iodine tubes. The voxels located above the separation line are displayed in blue and classified as "iodine" voxels while the voxels located below the separation line are displayed in yellow and classified as "calcium" (Fig. 5c). A threshold is also used for the voxel classification which defines the lower limit for the CT values that should be separated as "iodine" or "calcium."

4.2 Material Separation and Noise

Figure 6 shows the Energy Maps of the water phantom described in previous paragraph at different dose levels. We see that the diameter of the clouds generated in the Energy Map by each calcium and iodine tube increase with decreasing dose and that the separation performance drops down, especially at lower concentrations where the calcium and iodine clouds increasingly mix with one another (Coulon et al. 2007b). The middle row

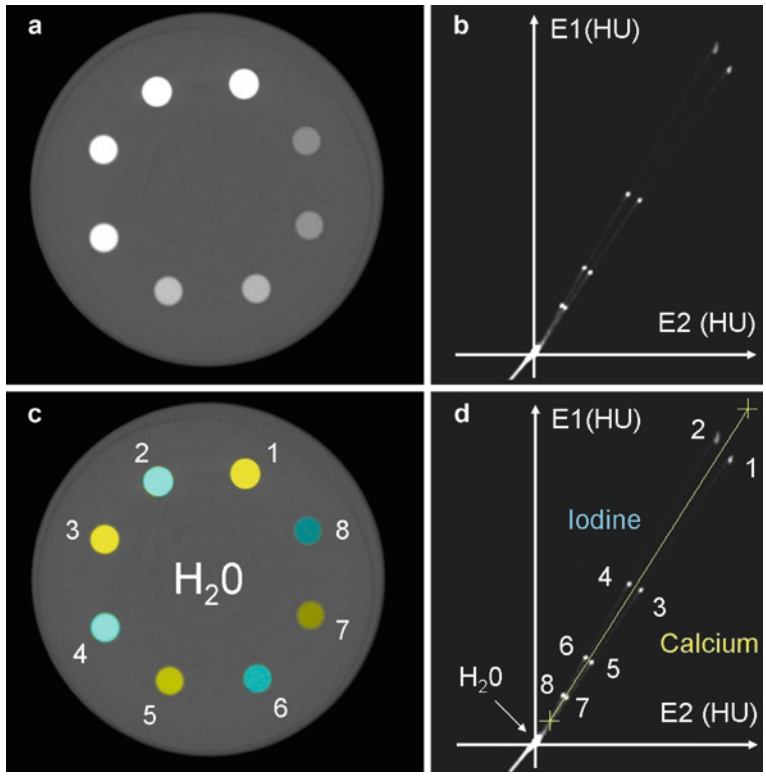

Fig. 5 (**a**) The combined CT image and (**b**) the corresponding Energy Map of a water phantom containing eight identical tubes, four containing solutions of $CaCl_2$ and four containing solutions of iodine in water in decreasing concentrations such that the HU# of corresponding tubes are equal. (**d**) A single line drawn in the Energy Map enables to separate the calcium and iodine tubes. A threshold is used for the voxel classification which defines the lower limit for the CT values that should be separated as "iodine" or "calcium." This threshold is defined by the lower end of the separation line (yellow cross). (**c**) The voxels located above the separation line are displayed in *blue* and classified as "iodine" voxels while the voxels located below the separation line are displayed in *yellow* and classified as "calcium"

scan was performed with a dose such that the standard deviation of the measured voxel HU# (noise) was on the average 15.5 HU on the phantom cross-sectional water background. This corresponds to the noise of a typical abdominal CT scan on an average size patient, reconstructed with a slice width of 3 mm and scanned with a $CTDI_w$ around 13 mGy. On the upper row, the average standard deviation was 4.2 HU corresponding to a very high dose scan (approximately 14 times the dose of the middle row) and on the lower row , it was 29.8 HU corresponding to a low dose scan (approximately a quarter of the dose of the middle row). Figure 7 shows a plot of the calcium classification efficiency as a function of the calcium concentration in the tube. Similar results are obtained for iodine. The calcium classification efficiency or equivalently the separation efficiency is defined as the percentage of the tube volume with the calcium correctly classified, the reference volume being chosen as the one measured on the calcium tube with the highest concentration and at the highest dose. With this definition, a separation efficiency of 50% means a bad separation performance since it corresponds to 50% of misclassified voxels in the tube. At a typical abdominal dose, we see that the separation performance based on dual energy classification is only 70% at the lowest concentration (corresponding to calcium @ 140 HU in the full spectrum CT image).

The material separation performance at a given x-ray dose of any DECT scanner increases with the angular separation between the material axes in the Energy Map. To compare the angular separation of the dual-layer CT scanner and the one obtained with a Dual kVp scan on a regular Brilliance 64 CT scanner (Philips HealthCare), the angular separation between the iodine and calcium lines were measured in the Energy Map after scanning the water phantom described above. The scans were performed at 140 kVp on the dual-layer CT and successively at 140 and 80 kVp on the Brilliance 64 CT scanner. There was 21% increase in the angle between the iodine and calcium lines with the dual-layer CT compared to the Dual kVp technique. In other words, the bad material separation performance at low concentration and at typical abdominal dose is not a specificity of the dual-layer detector and is even worse with a Dual kVp DECT scanner.

The material separation performance on a Dual kVp DECT or Dual Source DECT scanner can be improved by hardening the spectrum of the high energy window.

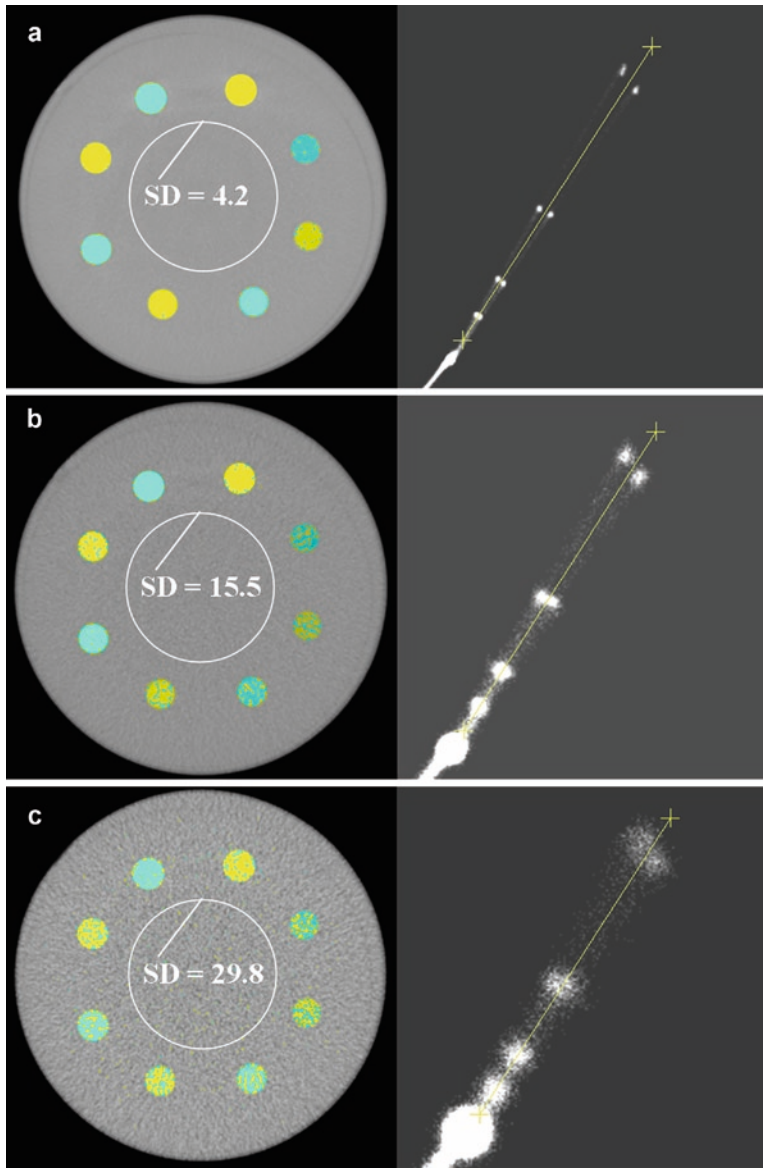

Fig. 6 The Energy Maps of the water phantom described in Fig. 5 scanned at different dose levels. The diameter of the cloud generated in the Energy Map by each calcium and iodine tube increases with decreasing dose and the separation performance drops down, especially at lower concentrations where the calcium and iodine clouds increasingly mix with one another. The middle row scan (**b**) is performed with a dose such that the standard deviation of the measured voxel HU# (noise) is 15.5 HU on the phantom cross-sectional water background. On the upper (**a**) and lower rows (**c**), the average standard deviations are 4.2 and 29.8 HU respectively

This can be achieved by strongly filtering the emitted x-ray radiation using a metal filter. As already mentioned, such a strong filtration would produce significant forward scattered radiation from the filter sheet and would significantly degrade the image quality (Carmi et al. 2008).

4.3 Polychromatic Correction

In an x-ray CT system the HU of a specific material may have different values depending on the size and composition of the scanned object due to beam-hardening effects. Usually, a pre-processing polychromatic correction and an additional iterative bone correction are applied in order to correct accurately the HU of water. Our separation method is most successful if the location of a specific material on the HU-plane is stable despite beam-hardening effects. We apply a special post-processing image correction in order to achieve stability in the HU-plane (Carmi et al. 2005). The values of the two image sets prior to the mapping into the HU-plane are corrected in a two step process. The first step is to create a special attenuation map for

the images (Fig. 8). This map contains for each pixel in the image a value that characterizes the average beam hardening on that pixel calculated by the summation of all projections (line integrals on the HU values) through that pixel. The second step is to use the attenuation map to correct the HU values of the original image (Fig. 9). We use the transformation:

$$V_{ij}^{c} = (V_{ij} - HU_{Water}) \times (1 + F \times A_{ij}) + HU_{Water} \qquad (1)$$

V_{ij} – pixel values in the original image.

V_{ij}^{c} – pixel values in the corrected image.

A_{ij} – pixel values in the attenuation map.

F – a constant empirical factor that gives the average optimal correction for the relevant set of materials (e.g., Iodine and calcium).

i,j – pixel indices.

Note that the equation above keeps the water unchanged. The correction function above is applied separately on each one of the two energy windows images. The factor – F can be different for each energy window. It is important to emphasize that for the suggested technique of material separation it is not required that a given material has the "physically true" HU value. The corrected HU value should only be confined inside the predefined region for that particular material.

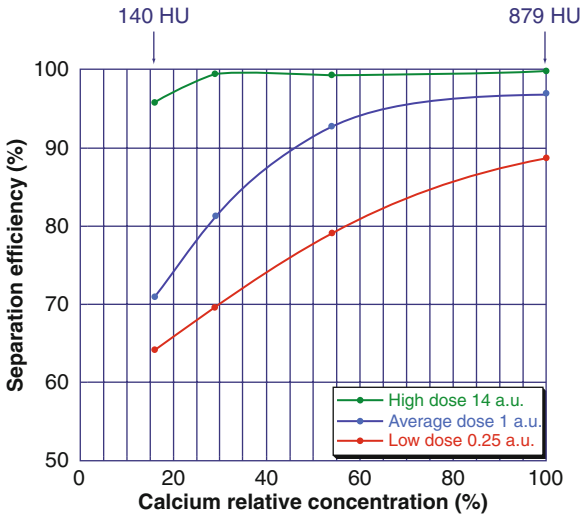

Fig. 7 The separation efficiency as a function of the relative calcium concentration in the tubes

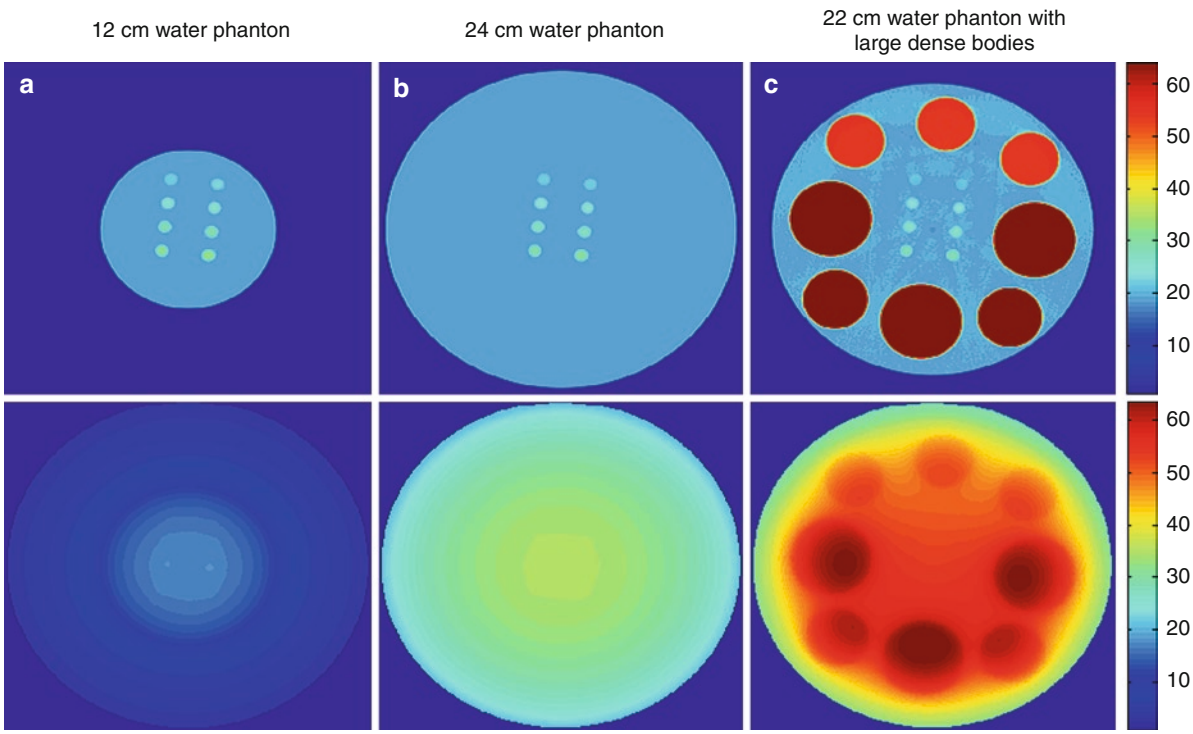

Fig. 8 A simulation example of three different phantoms (three upper images) and their associated attenuation maps (three lower images) used for the post-processing polychromatic correction. The simulated phantoms include several 8 mm diameter cylinders with different concentrations of Iodine and Calcium inside (**a**) 12 cm diameter water cylinder, (**b**) 24 cm diameter water cylinder, (**c**) 22 cm diameter water cylinder with several large cylinders of highly dense materials. The phantom images and the attenuation maps are shown with arbitrary color scales

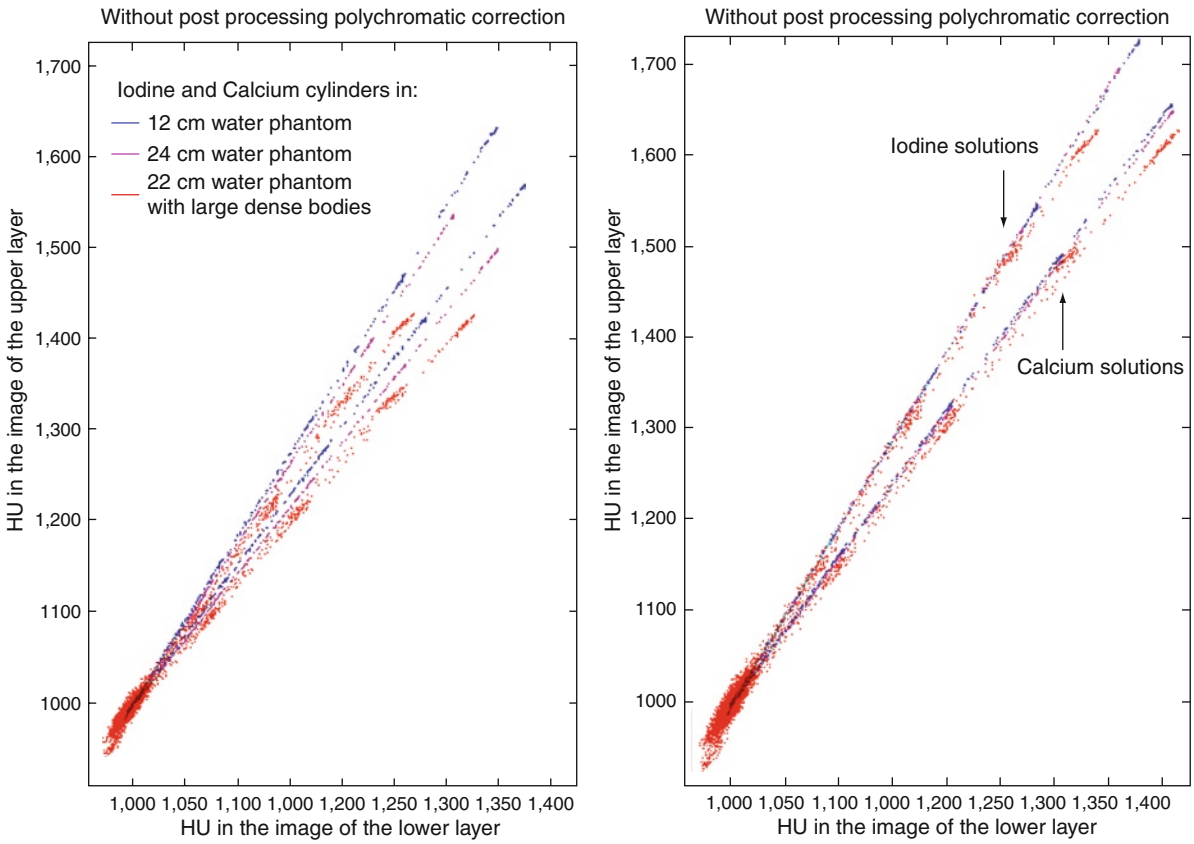

Fig. 9 The Iodine/Calcium separation results of the three phantom cases of Fig. 8. In both diagrams ordinary pre-processing polychromatic correction for water is applied. The right diagram shows the results after the additional post processing polychromatic correction. It can be seen that the additional correction brings the Iodine and the Calcium solutions to be approximately aligned with two constant lines

The material classification analysis on the HU-plane and the additional polychromatic correction described above can be used with other dual energy detection methods as well, such as the aforementioned dual tube-voltage technique and dual energy method with passive radiation filter.

5 Post-processing

Section 4 describes a simple separation technique which consists of drawing a separation line between the material specific axes with a lower separation threshold defined by the lower end of the separation line. With this binary approach, a voxel can be classified as one material OR another material. More sophisticated separation techniques, which enable mixed voxel separation, exist. Two additional algorithms are available at the Philips EBW workstation: the vectorial separation and the probability separation.

5.1 The Vectorial Separation

This method of separating materials assumes that the CT value of each voxel may be analyzed as a composition of two materials. The CT value of each voxel is seen as a vector summation of two vectors along the corresponding material axes in the Energy Map (see Fig. 10). The coordinates α and β of the two vectors along those basic directions represent the concentration of each material in the corresponding voxel. The material specific images are obtained by displaying the corresponding α or β value of each voxel belonging to the image. Figure 11 shows a full spectrum cross-sectional CT image (Fig. 11a) and the corresponding

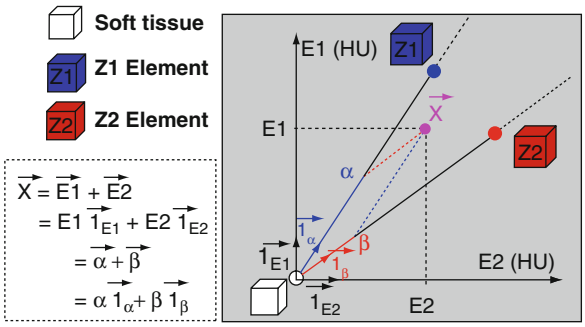

Fig. 10 With the vectorial separation, the CT value of each voxel is seen as a vector summation of two vectors along the corresponding material axes in the Energy Map. The coordinates α and β of the two vectors along those basic directions represent the concentration of each material in the corresponding voxel

Energy Map (Fig. 11b) of a water phantom containing 8 identical tubes, four of them containing solutions of pure $CaCl_2$ and iodine at various concentrations in water (relative concentrations ~1.0 and 0.5), the other four tubes containing mixtures of these solutions (ratio ~50–50%, 75–25%). The corresponding iodine- and calcium-selective images are obtained from the projections along the iodine and calcium axes respectively (Fig. 11c–d). A measure of the iodine concentration in regions of interest placed within each tube on the iodine-specific images shows that the results are highly correlated (R = 0.99) with the known iodine concentrations (Vlassenbroek et al. 2007).

A limitation of the vectorial separation technique is that the noise in the E1 and E2 images is amplified in the material specific images as a result of the projection on the material axes (Rebuffel and Dinten 2007). The resulting material-specific images obtained at commonly used radiation doses are extremely noisy, especially in body regions with high radiation attenuation such as abdomen, pelvis and in large patients in general. Kalender et al. (1988) showed that the noise in these material specific images is anticorrelated, so additional post processing of the images can be applied to extract the required information (Warp and Dobbins 2003).

5.2 The Probability Separation

Variations between the two sets of dual energy images contribute important information about different materials. As we have seen in previous sections, each material has a unique attenuation spectral response on an image-based energy map. However, in practice, in moderate and low radiation doses this spectral information is very noisy and further post-processing analysis is needed to extract the information (see Sect. 5.1). The probabilistic separation algorithm obviates this limitation by using a statistical model to separate between the two materials (Goshen et al. 2008; Vlassenbroek et al. 2007). This approach is based on a probability mixture model taking into consideration the spectral response of the materials, the noise characteristics and fundamental morphological considerations. We assume that the noise has a Gaussian distribution which is justified according to the physical analysis of the scanner. The output of this method is an estimate of the probability that each voxel is either material 1 or material 2. Figure 12 shows an example of a calcium-iodine separation using this algorithm.

The above analysis can be used to generate virtually non-contrasted images (VNC) of high quality (see Figs. 12e and 13). A complementary algorithm uses the estimated probabilities and the material response vectors to replace the iodine Hounsfield unit enhancement by the original soft tissue texture. This algorithm has the potential to eliminate the need for an initial non-contrast scan in multi-phasic MDCT clinical procedures, leading to reduced radiation exposure and fully registered studies.

5.3 3D Rendering

The Dual Energy capability opened a window for new important applications. Those applications may have a significant added value to anatomical visualization overcoming the "Hounsfield Barrier." The results may strongly depend on the quality of technology, such as energy separation, noise and dose.

A segmentation based on the voxel classification obtained with the material separation techniques described in the above sections can be performed. The corresponding 3D models of the various materials can then be displayed with a chosen opacity at the EBW workstation and can be superimposed, for example, on a 3D volume rendered anatomical image, close to the macroscopical pathological view. Among the applications with high impact, the following are

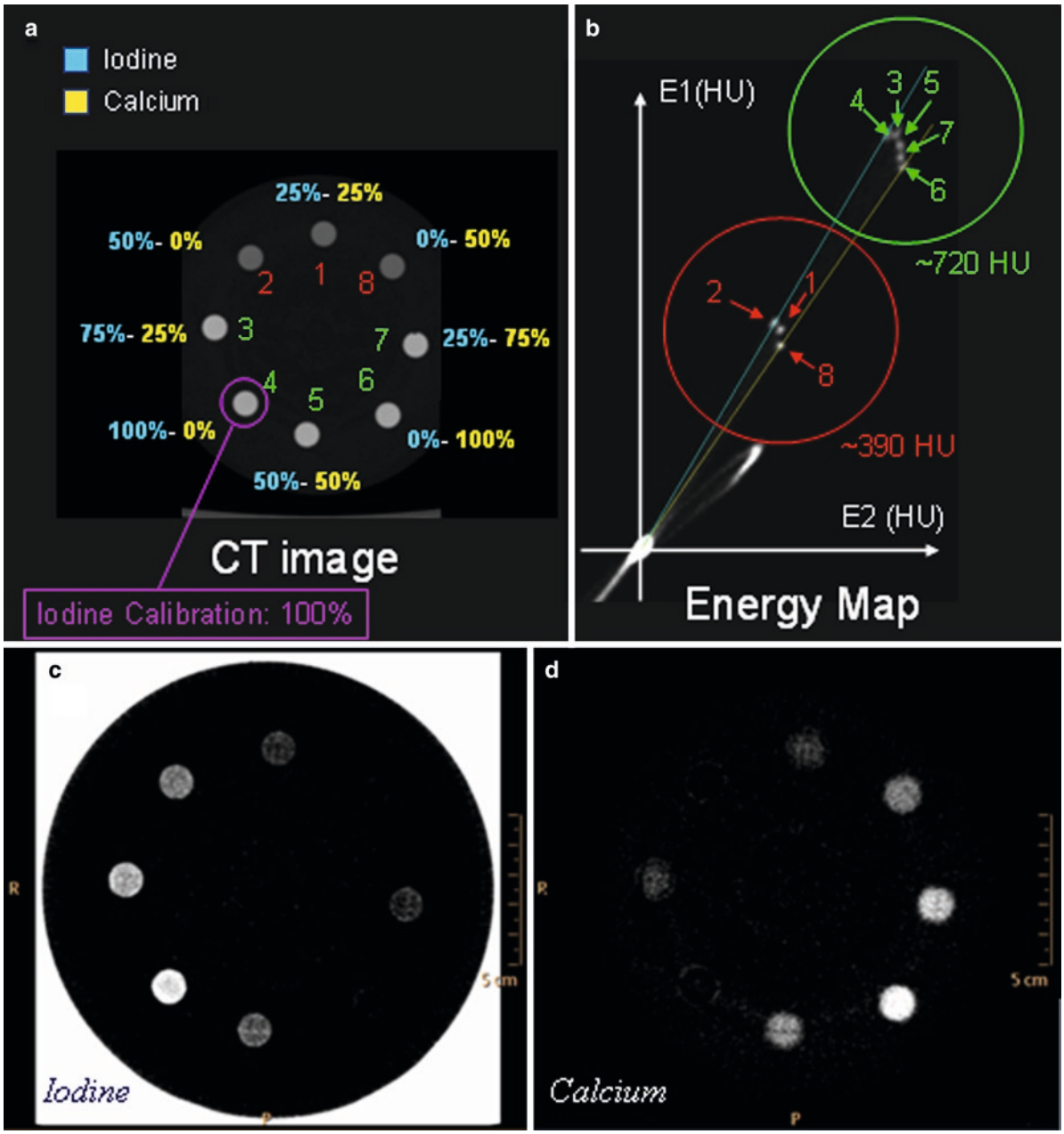

Fig. 11 (**a**) The full spectrum cross-sectional CT image and (**b**) the corresponding Energy Map of a water phantom containing eight identical tubes, four of them containing solutions of pure $CaCl_2$ and iodine at various concentrations in water (relative concentrations ~1.0 and 0.5), the other four tubes containing mixtures of these solutions (ratio ~50–50%, 75–25%). The corresponding (**c**) iodine- and (**d**) calcium-selective images are obtained from the projections along the iodine and calcium axes respectively

included: plaque quantification and characterization (Carmi et al. 2010), prepless virtual colonoscopy (Carmi et al. 2008), kidney stones characterization (Coulon et al. 2007a), direct CTA bone removal, cardiac perfusion, lung perfusion and pulmonary embolus (PE) detection (Bogot et al. 2007; Fingerle et al. 2010) etc. Figure 14 shows some examples of such 3D rendering images which can be used in a variety of clinical applications to enhance or remove specific materials.

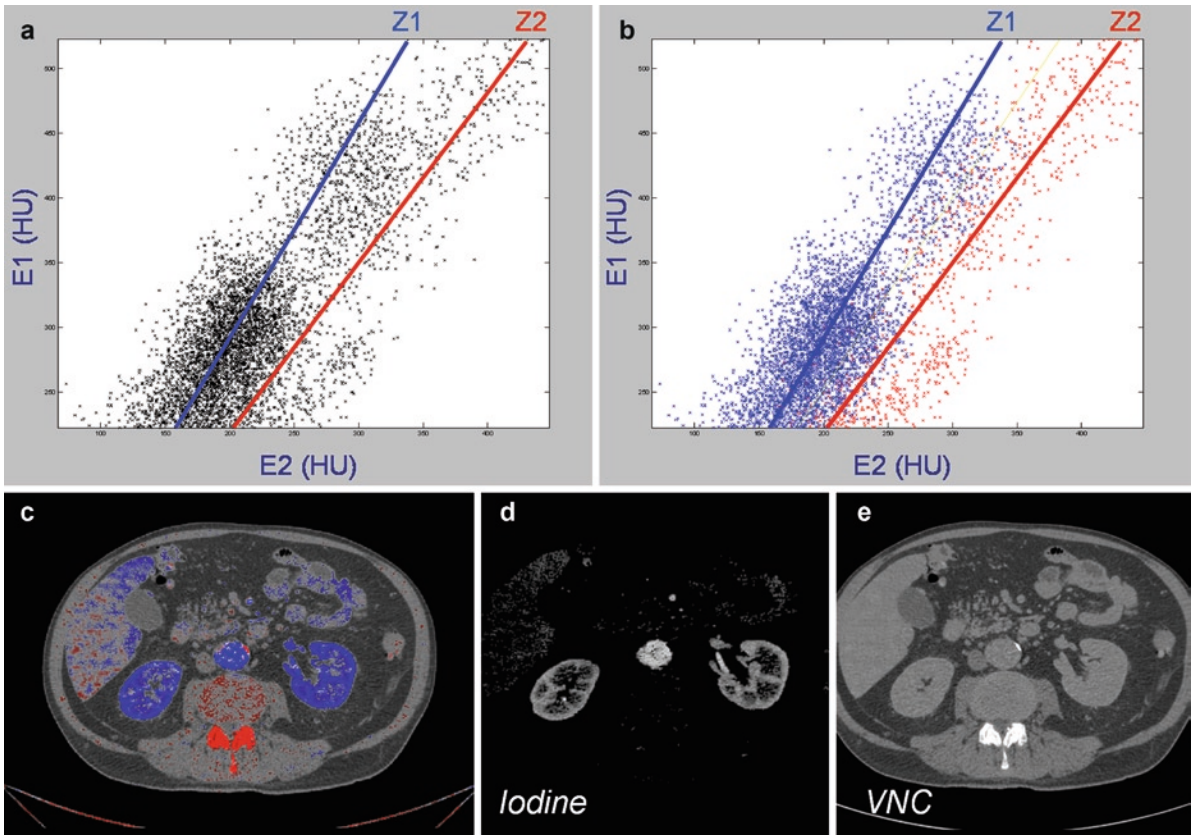

Fig. 12 Example of a clinical abdomen scanned with a typical radiation dose. (**a**) The energy map with the iodine- (*blue*) and calcium-axes (*red*). (**b**) The energy map with the points colored according to their dominant probability, i.e., blue and red for iodine and calcium respectively. (**c**) The original image with color layout in which the saturation of the pixel color was set in proportional to its corresponding probabilities. (**d**) The corresponding iodine map (**d**) and high quality virtually non-contrasted image (**e**) obtained by the algorithm

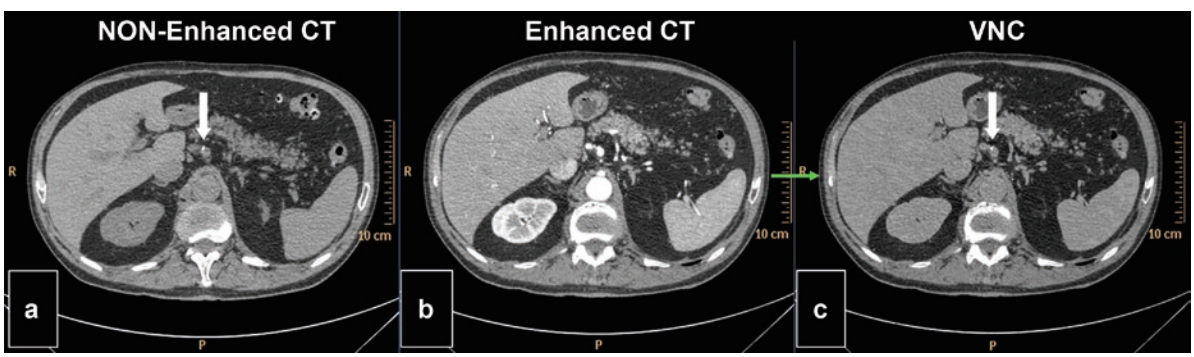

Fig. 13 (**a**) Non enhanced CT scan of the upper abdomen performed with the dual-layer detector, (**b**) contrast enhanced CT scan of the upper abdomen of the same patient and (**c**) high quality virtually non-contrasted image obtained from the contrast enhanced scan using the probability separation algorithm. A small calcified plaque in the mesenteric artery (*arrow*) is successfully separated from the iodinated blood pool

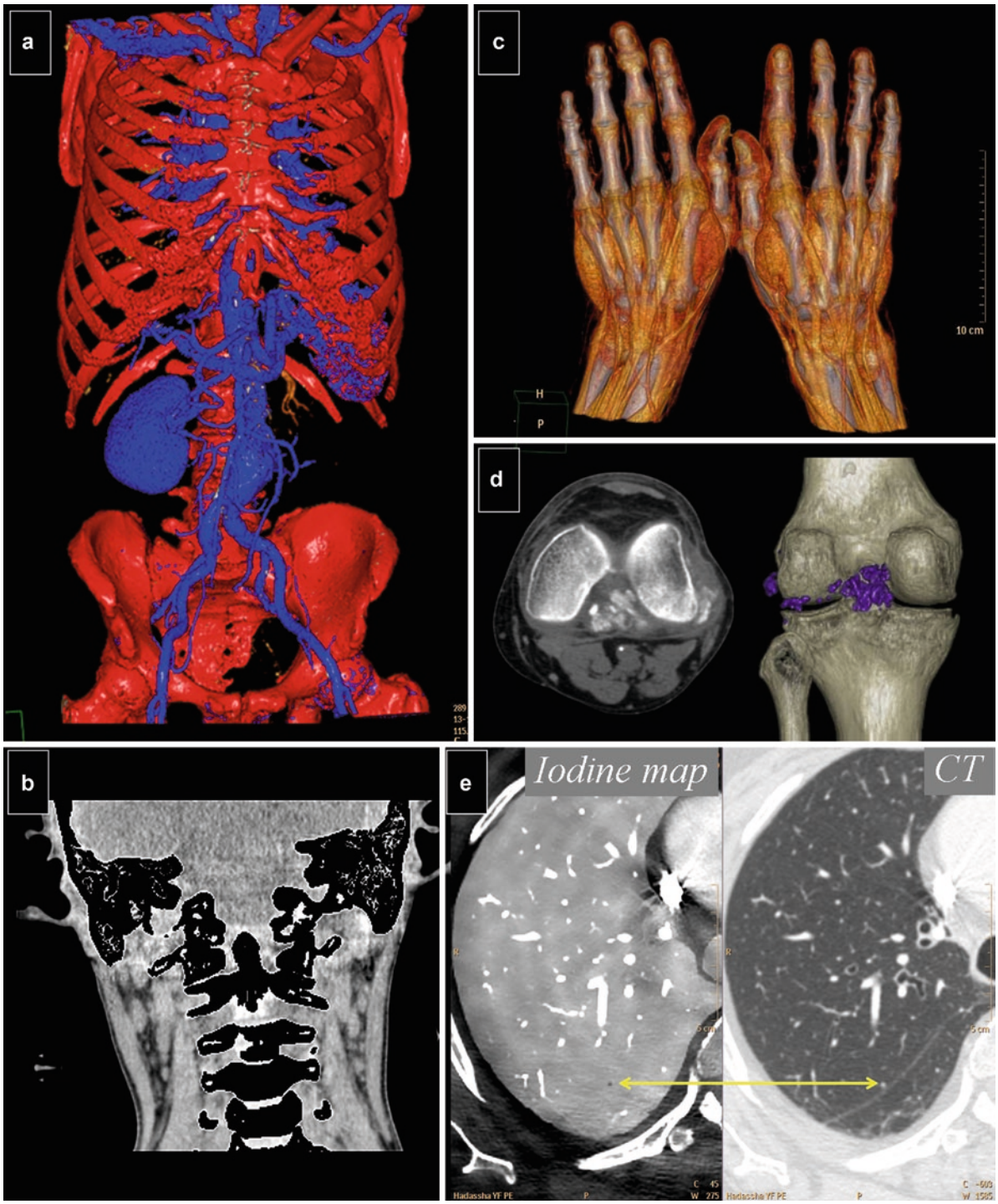

Fig. 14 A few examples of 3D volume rendered images obtained with dual energy material separation. (**a**) Calcium-iodine separation which can be used for (**b**) bone removal in CT angiography, (**c**) improved visualization of the tendons and ligaments, (**d**) uric acid detection and quantification in gout disease and (**e**) iodine map extraction obtained from a contrast enhanced CT scan of the lung, enabling a detailed perfusion analysis of the lung parenchyma. In this example, an improved visualization of a small lung nodule

Acknowledgements I would like to thank my colleagues from Philips HealthCare: Raz Carmi from the Global Research and Advanced Development group, Galit Kafri from the Clinical Solutions group, Philippe Coulon and Leon de Vries from the Clinical Science and Applications group, for taking the time to assess this manuscript. Their advice for some final corrections were greatly appreciated.

Research studies with the dual-layer detector have been made possible under guidance of a clinical team led by Prof. Jacob Sosna, Director of CT and Director of Research and Imaging Laboratories at HUMC. All phantom and clinical images presented in this chapter are courtesy of HUMC.

References

Baer M, Maaß C, Kalender WA, Kachelrieß M (2009) Image-based dual energy CT using optimized precorrection functions: a practical new approach to material decomposition in the image domain. Springer, Berlin, pp 205–208

Bogot NR, Shaham D, Nissenbaum I, Amin-Spector S, Libson E, Sosna J (2007) Single source dual energy MDCT: impact on attenuation in pulmonary CT angiography, RSNA SSG21–06, Book of Abstracts p 426

Carmi R, Naveh G, Altman A (2005) Material separation with dual-layer CT. IEEE Nucl Sci Symp Conference Record, vol.4 pp 1876–1878

Carmi R, Kafri G, Goshen L, Steinberg A, Amin-Spector S, Altman A, Sosna J (2008) A unique noncathartic CT colonography approach by using two-layer dual-energy MDCT and a special algorithmic colon cleansing method. IEEE Nucl Sci Symp Conference Record pp. 3868–3870

Carmi R, Kafri G, Altman A, Goshen L, Planer D, Sosna J (2010) Arterial double-contrast dual-energy MDCT: in-vivo rabbit atherosclerosis with iodinated nanoparticles and gadolinium agents. SPIE Conference paper 7626–7651

Coulon P, Vlassenbroek A, Amin-Spector S, Sosna J, Defasque E, Lemaitre LG (2007a) Renal stone composition analysis with simultaneous multi-energy MDCT. RSNA LL-GU2175-L02, Book of Abstracts p 809

Coulon P, Vlassenbroek A, Amin-Spector S, Bar Y, Delso G (2007b) Calcium-iodine separation and quantification with simultaneous multi-energy MDCT and material specific base projection method. RSNA SSC14–02, Book of Abstracts p 317

Engel KJ, Herrmann C, Zeitler G (2008) X-ray scattering in single and dual-source CT. Med Phys 35(1):318–332

Feldkamp LA, Davis L, Kress J (1984) Practical cone-beam algorithm. J Opt Soc Am 1:612–619

Fingerle AA, Bogot NR, Kafri G, Sosna J (2010) Dual-layer dual-energy MDCT: initial experience with iodine distribution maps of the entire chest in imaging of pulmonary embolism. ECR B-395, Book of Abstracts 1(Suppl 1):218

Goshen L, Sosna J, Carmi R, Kafri G, Iancu I, Altman A (2008) An iodine-calcium separation analysis and virtually non-contrasted image generation obtained with single source dual energy MDCT. IEEE Nucl Sci Symp Conference Record pp 3868–3870

Kalender WA, Klotz E, Kostaridou L (1988) An algorithm for noise suppression in dual energy CT material density images. IEEE Trans Med Imaging 7:218–224

Rebuffel V, Dinten JM (2007) Dual-energy X-ray imaging: benefits and limits. Insight 49(10):572–609

Roessl E, Proksa R (2007) K-edge imaging in X-ray computed tomography using multi-bin photon counting detectors. Phys Med Biol 52(15):4679–4696

Shlomka JP, Roessl E, Dorsheid R, Dill S, Martens G, Istel T, Bäumer C, Hermann C, Steadman R, Zeitler G, Livne A, Proksa R (2008) Experimental feasibility of multi-energy photon counting K-edge imaging in pre-clinical computed tomography. Phys Med Biol 53:4031–4047

Vlassenbroek A, Coulon P, Bar Y, Goshen L, Carmi R, Delso G (2007) Improved calcium and iodine spectral decomposition with multi-energy MDCT using a probability mixture model. RSNA SSC14–04, Book of Abstracts p 318

Warp RJ, Dobbins JT (2003) Quantitative evaluation of noise reduction strategies in dual-energy imaging. Med Phys 30(2):190–198

Gemstone Detector: Dual Energy Imaging via Fast kVp Switching

Naveen Chandra and David A. Langan

Contents

Abstract

› This chapter provides an overview of the GE Discovery CT750HD dual energy imaging capability known as *gemstone spectral imaging* (*GSI*). The CT750HD is a single X-ray source system that employs fast kVp switching for dual energy acquisitions. This acquisition method enables precise temporal registration of the dual-energy sinograms, projection-based material decomposition, and delivers a full 50 cm material decomposition scan field of view. The subsystem technologies employed to achieve the dual energy acquisitions are detailed in the discussion of system design. Calibration of fast kVp switching data, material decomposition, and visualization of the resulting images are covered in the image reconstruction and post processing sections. The chapter closes with GSI implementation in the context of challenging diagnostic applications.

1 Physical Background

The application of Dual energy in CT has been proposed since the 1970s and it has been extensively studied over the past several decades (Alvarez and Macovski 1976; Kalender et al. 1986). However due to various technical challenges, only recently has dual energy imaging become a reality in medical CT imaging. Relative to conventional single kVp imaging, dual energy imaging has the capability to enhance material differentiation and reduce beam hardening artifacts. In addition, fast kVp switching, where the kVp alternates

N. Chandra (✉)
GE Healthcare, Waukesha, WI, USA
e-mail: Naveen.chandra@ge.com

D.A. Langan
GE Global Research, Niskayuna, NY, USA
e-mail: langan@ge.com

T.R.C. Johnson et al. (eds.), *Dual Energy CT in Clinical Practice*, Medical Radiology,
DOI: 10.1007/174_2010_35

between low and high kVp, every view has several benefits including fine temporal view registration, helical and axial acquisitions, and full field of view. It also presents some implementation challenges.

System design must enable rapid kVp rise/fall[1] achieving sufficient energy separation and angular view sampling within the constraints of medical diagnostic rotation speeds. Detector primary decay and afterglow performance are critical to avoiding spectral blurring between views. Concurrently, there needs to be a strategy for dose efficiency through balancing the flux between the two spectrums and noise reduction processing.

Gemstone spectral imaging (GSI) is based on projection-based material decomposition. The mixed kVp sinogram is transformed into view aligned low and high kVp sinograms. Material basis decomposition is performed on the paired kVp measurements accounting for the tube spectrum, bowtie filter, and beam hardening properties of the basis materials. The noise correlation of the resulting material density images is well understood and employed in noise reduction processing (Alvarez and Seppi 1979).

Post processing and visualization of dual energy data for medical diagnostic imaging is an emerging field and active research area. The goal is to provide diagnostic information beyond that found in conventional imaging, in a manner consistent with workflow, and that increases the efficiency of clinical reads. The GSI Viewer provides a mix of basic capability for routine clinical readings, and advanced research capabilities for exploring applications.

The chapter closes with discussion on future research/applications in the clinical context of cardiac imaging with GSI.

2 System Design

The fundamental principle behind fast kVp switching, is the acquisition of two different kVps alternating on a view-by-view basis between low and high kVp in a single rotation. This enables precise temporal registration of views, thereby freezing motion as the alternating spectrums penetrate the patient, thereby significantly reducing artifact. For decades, the barrier preventing successful clinical introduction has been the limitations in the acquisition and detection system.

The advancements in system components comprising the Discovery CT750 HD make GSI possible. Both high and low energy data sets are acquired simultaneously for axial and helical acquisitions at the full 50 cm field of view.

The generator and tube are capable of reliably switching between 80 and 140 kVp targets, and have the capability to support sampling as quickly as every 150 microseconds.

The Gemstone detector is a key contributor to fast kVp switching acquisitions through its scintillator and data acquisition system (DAS).

GE Healthcare's (GEHC) scintillator material, referred to as *Gemstone*, is a complex rare earth based oxide, which has a chemically replicated garnet crystal structure. This lends itself to imaging that requires high light output, fast primary speed, very low afterglow[2], and almost undetectable radiation damage.

Gemstone has a primary decay time of only 30 ns, making it 100 times faster than GOS (Gd_2O_2S), while also having afterglow levels that reach only 25% of GOS levels making it ideal for fast sampling. The capabilities of the scintillator are matched with a fast sampling capability DAS, enabling simultaneous acquisition of low and high kVp sinograms at customary rotation speeds.

In order to combat the traditional flux issues that have challenged fast kV switching, low kVp and high kVp acquisitions are flux balanced through advances in the DAS, which allow for dynamically changing view integration times. Additional time is allocated to the low kVp acquisition relative to the high kV acquisition in order to reduce photon starvation conditions. Coupled with the appropriate rotation speed, a more balanced flux condition between the two kVp scans is achieved and serves to minimize patient dose.

Fast kV switching scans have been designed to minimize the additional dose relative to single energy

[1]Since the kVp rise and fall are incorporated into the view measurements, a fast switching generator is required, and any remaining low level nonidealities are accounted for in the spectral calibration of the data.

[2]Afterglow refers to a secondary decay of light emitting from the scintillator for several milliseconds after the X-ray source is turned off. It carries a part of the signal from one view to the next during a scan, thereby smearing the information, and potentially causing unwanted spectral decomposition artifact.

scans. In a recent dose and low contrast detectability (LCD) comparison (Li et al. 2010), the effectiveness of this sampling scheme with respect to dose was demonstrated by matching the LCD at a slice thickness equal to 5 mm and object size of 3 mm.

3 Image Reconstruction

Following the acquisition, calibration corrections are applied to the data. Spectral calibration is complicated by the nonideal kVp rise/fall making it difficult to find a fixed kVp having precisely the same spectral response as an actual fast kV switching energy spectrum. As a result, the spectrum is fitted to a linear combination of single kVp spectra. The overall spectrum is decomposed into a superposition of several known kVp spectra through the measurement of the detector response to the bowtie attenuation.

$$S_p(E) = \sum_k^{N_k} \alpha_k S_k(E)$$

Where $S_k(E)$ are the basis spectra of the fixed kVps, N_k is the total number of the basis spectra, and α_k are the weights of the basis spectra.

The self-normalized detector response to this spectrum can be written as:

$$R(d) = \frac{\sum_k \alpha_k G_k(d)}{\sum_d \sum_k \alpha_k G_k(d)}$$

by letting

$$G_k(d) = \int_E S_k(E) E[1 - e^{-\mu_d(E) t_d}] e^{-\sum_b \mu_b(E,d) I_b(d)} \, dE$$

in which, $\mu_d(E)$ is the linear attenuation coefficient of the detectors, t_d is detector thickness, $\mu_b(E,d)$ and $I_b(d)$ are respectively the linear attenuation coefficient and the thickness of bowtie material b corresponding to detector channel d. $R(d)$ can be measured through a fast switching air scan, and $G_k(d)$ can be calculated based on the system geometry. The problem now becomes to find α_k by solving for $R(d)$ which is over determined and can be easily solved by a least square fitting. Once the calibration corrections have been applied to the low and high kVp data sets, they are aligned in projection space, transformed into a material basis pair projection (such as water and iodine), and then reconstructed. These material density images[3] may be combined to create a monochromatic image at any specific keV level. A pictorial flow is presented in Fig. 1.

4 Projection-Based Material Decomposition

Dual energy material decomposition is based upon the mass attenuation coefficient across the medical diagnostic imaging spectrum being a function of two independent variables: photoelectric effect and Compton scatter (Alvarez and Macovski 1976). Through a mathematical change of basis one can express the energy dependent attenuation observed in two kVp measurements in terms of two basis materials:

$$\begin{aligned} p_{low} &= -\ln\left(\frac{I}{I_o}\right)_{low} \\ &= -\ln\left[\left\{\int S_{low}(E)\exp\{-[m_1\mu_1(E) \right.\right. \\ &\quad \left.\left. + m_2\mu_2(E)]\}dE\right\} / \left\{\int S_{low}(E)dE\right\}\right] \\ p_{high} &= -\ln\left(\frac{I}{I_o}\right)_{high} \\ &= -\ln\left[\left\{\int S_{high}(E)\exp\{-[m_1\mu_1(E) \right.\right. \\ &\quad \left.\left. + m_2\mu_2(E)]\}dE\right\} / \left\{\int S_{high}(E)dE\right\}\right] \end{aligned}$$

where $\mu_1(E)$ and $\mu_2(E)$ represent the mass attenuation coefficients of the basis materials, and, m_1 and m_2 are their respective effective densities. $S_{\text{low}}(E)$, and $S_{\text{high}}(E)$ are defined by the source spectrum, source filtration, and detector performance. The solution for the densities of the basis materials, m_1 and m_2, accounts for spectral variation over the field of view due to the bowtie filter, and multimaterial beam hardening. As a

[3]Material density images represent of the effective density for the material necessary to create the observed dkVp measurements. In other words, pure water appears as 1,000 mg/mL in a water image, 20 mg/mL of dilute iodine is labeled as such an iodine image, etc.

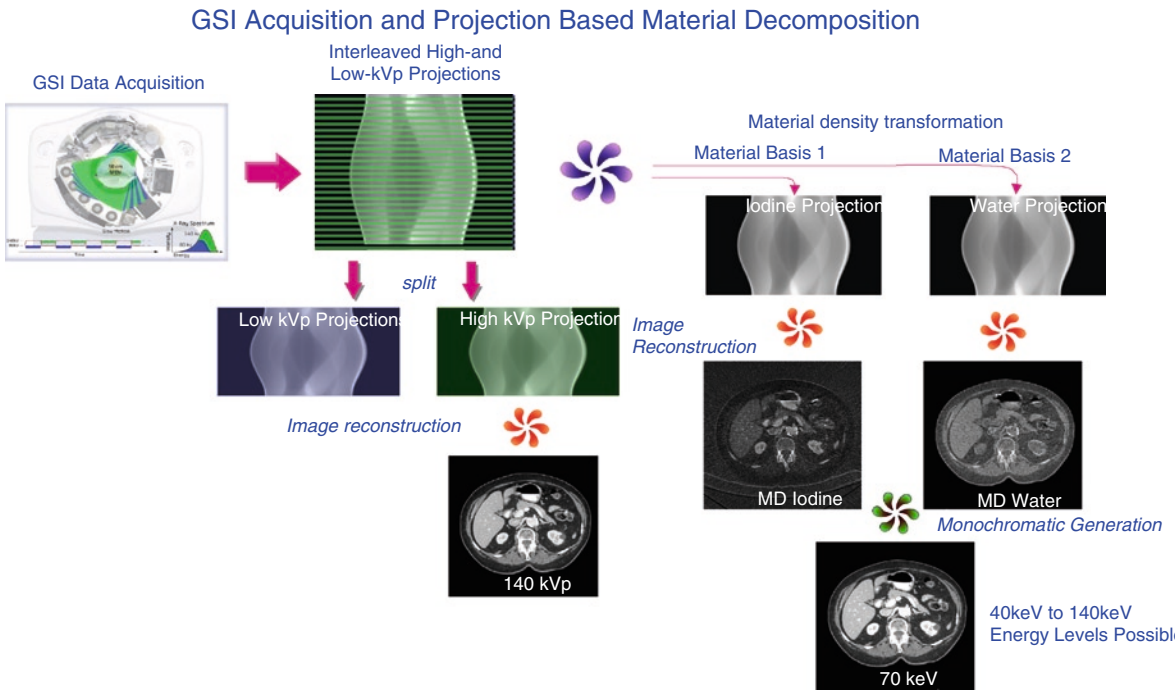

Fig. 1 GSI material decomposition processing

consequence, projection based material decomposition provides the opportunity for more quantitative precision than may be achieved with single kVp imaging.

$$p = -\ln\left(\frac{I}{I_o}\right) = m_1\mu_1(E) + m_2\mu_2(E)$$

Given the material basis density images, one can compute attenuation data that would be measured with a mono-energetic X-ray source.

For consistency with the Hounsfield Unit, one can normalize the attenuation measurement with respect to water.

5 Post Processing

5.1 Noise Suppression

Noise suppression is automatically applied to GSI imaging, and is used on the material density images in order to enhance the quality of the image without shifting the mean values. This allows for a quantitative material density image with good image quality.

The noise suppression itself leverages the statistical iterative reconstruction approach taken by ASIR[4] (Fan et al. 2010) while simultaneously leveraging well known noise correlation properties of the projection space material decomposition process (Alvarez and Seppi 1979).

Figure 2 shows the results of the unique integration of these two approaches. The leftmost image displayed for reference is that of a monochromatic 75 keV, the central image is that of its corresponding iodine density, and the rightmost image shows the corresponding water density image.

5.2 GSI Viewer

Dual energy CT provides the opportunity to view and quantify data in a number of ways. The diagnostic application and visualization of dual energy data is

[4]ASIR focuses on the statistical modeling of the noise properties of the system in conjunction with the properties of the scanned object. As a result, it provides significant benefit for those examinations that may experience limitations due to noise in the reconstructed images. In the case of spectral imaging, this is applied to reduce the noise in the material density images to enhance image quality.

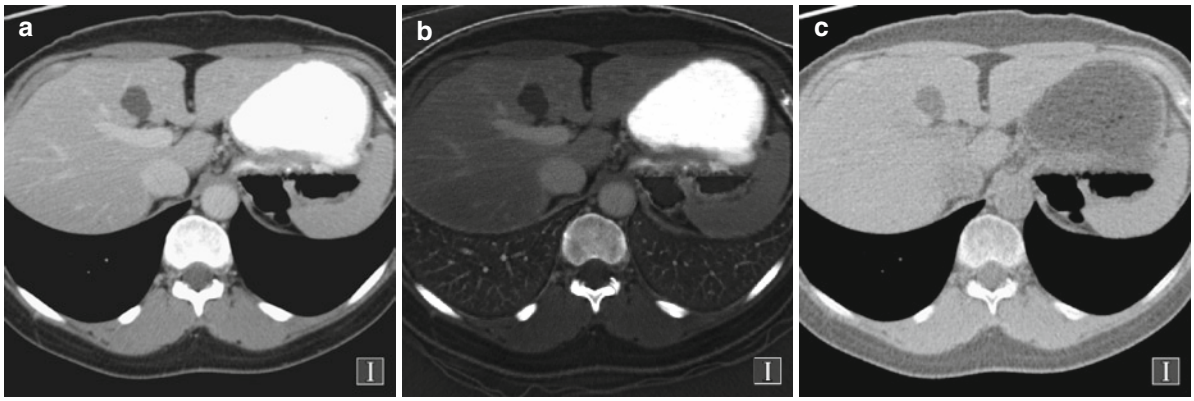

Fig. 2 Example of GSI noise reduced material density images: (**a**) monochromatic; (**b**) iodine density; (**c**) water density; images courtesy of Dr. Sahani, Massachusetts General Hospital, Boston, MA

presently an area of active research. As a consequence, the GSI viewer concurrently enables both applications research and workflow efficiency for routine work. The GSI viewer empowers the researcher with the ability to view and quantitatively analyze the data from multiple perspectives. In this section we overview the GSI viewer's analysis and visualization tools.

GSI data is commonly visualized as a monochromatic image, which resembles a conventional kVp image, but with fewer artifacts. The user may interactively change the keV [40–140 keV] if desired to attain the desired contrast. It is also common to visualize the data as a material basis pair. Material bases may be dynamically changed to meet the user's needs. An example of a monochromatic image and it's corresponding material density images are presented in Fig. 2.

The GSI Viewer also calculates the effective atomic number, Z_{eff}, of dual energy data. This representation describes the data in terms of the periodic elements most closely representing its energy sensitive attenuation behavior. It often provides insight regarding the material's composition. Knowledge of the effective atomic number of critical tissue types or specific contrast agents may be leveraged to define and import custom basis materials thereby allowing for the enhancement of specific anatomical structures.

The attenuation profile of the object vs. keV may also be graphically depicted by a spectral HU curve. In addition, the contrast to noise ratio of multiple selected ROIs as a function of keV can also be shown. An example is presented in Fig. 3a. The user can quickly assess the attenuation differences between the ROIs, as well as identify the monochromatic keV which best balances the user's needs in terms of contrast and noise.

Viewing multiple images concurrently may not be desirable or efficient for some workflows. As a means of integrating the information, the viewer has the capability to provide the material density, or other auxiliary information, as a color overlay on the monochromatic image. An example of this is presented in Fig. 3b.

To further identify trends and support additional learnings from the data, the viewer supports plotting graphic histograms and scatter plots. As a result, there is a variety of ways to visualize the same data to best make use of dual energy.

The GSI viewer utilizes standard and user defined protocols for the automation of routine work, and the support of research investigations.

6 Future Research/Applications

GSI supports full field of view projection based material decomposition. While a discussion of abdominal applications of GSI may be found in (Tkaczyk et al. 2009; Joshi et al. 2010), fast kV switching also provides the speed necessary to explore dual energy CT angiography (Pack et al. 2009). The following is a brief discussion on the potential of using GSI for CT cardiac imaging.

Research into GSI cardiac half scans from 0.35 s per rotation acquisitions is promising, and, prior to the

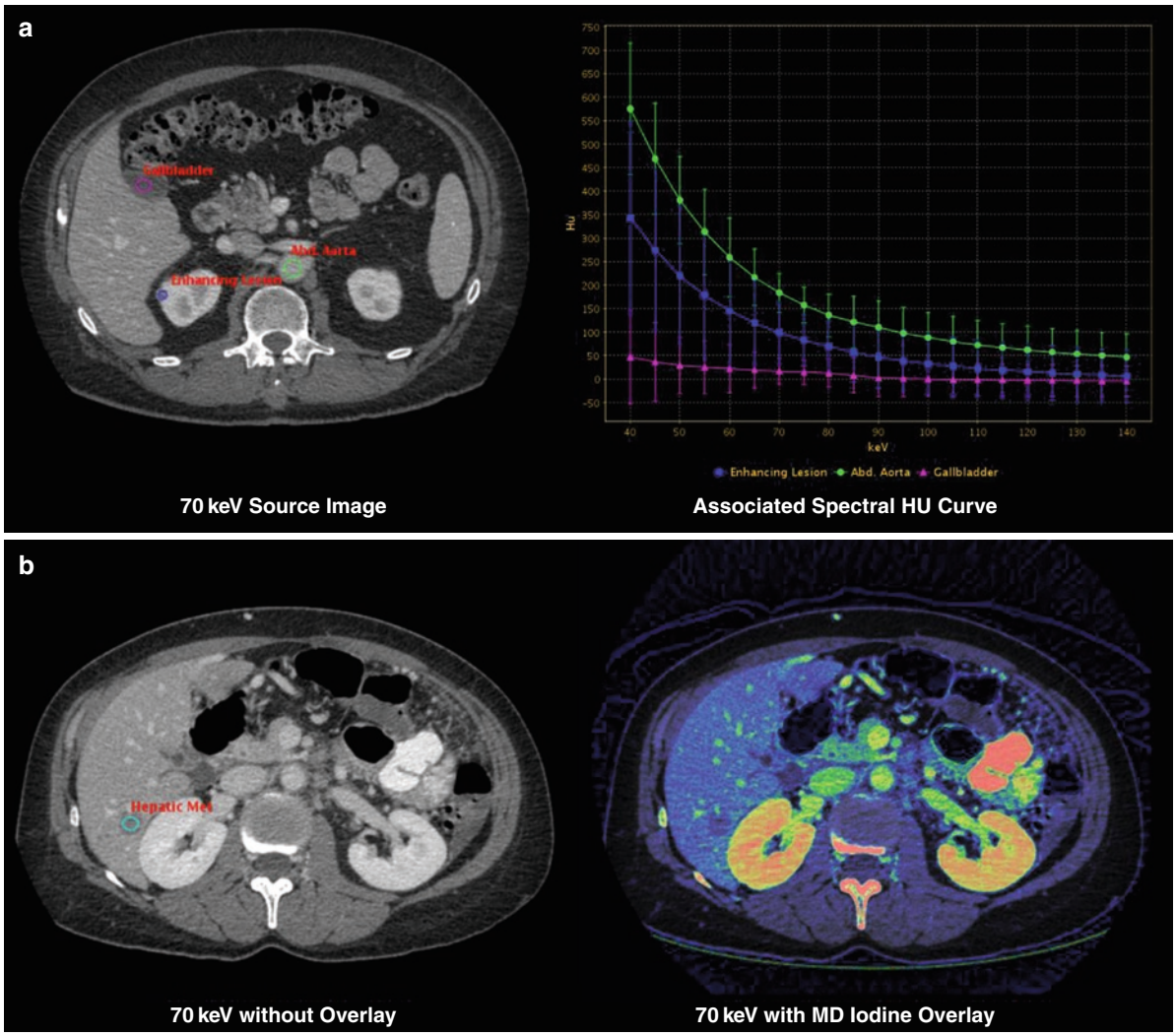

Fig. 3 (**a**) Example of a spectral HU curve. (**b**) Example of an iodine material basis overlay map on a monochromatic image; images courtesy of Dr. Amy Hara, Mayo Clinic, Scottsdale, AZ

publication of this book, is a technology in development. A brief example of a patient image can be seen in Fig. 4. The temporal requirements of CT angiography have made it an excellent application for testing and demonstrating the benefits of a GSI implementation.

The research to date with GSI cardiac angiography has aligned with exploring potential benefits of dual energy relative to conventional single kVp imaging. Promising areas of research, which still require further clinical capability assessments and confirmation, include the potential for increased accuracy in coronary stenosis sizing through improved differentiation of calcified plaque and iodinated contrast lumen, the potential for reduced calcium blooming, the potential to do calcium scoring in a contrast scan, and exploring the use of monochromatic images for its ability to reduce beam hardening in myocardial perfusion studies. Lastly, GSI is additionally enabling research to explore the measurement and risk profiles of lipid (cholesterol) plaques (Pavlicek et al. 2010).

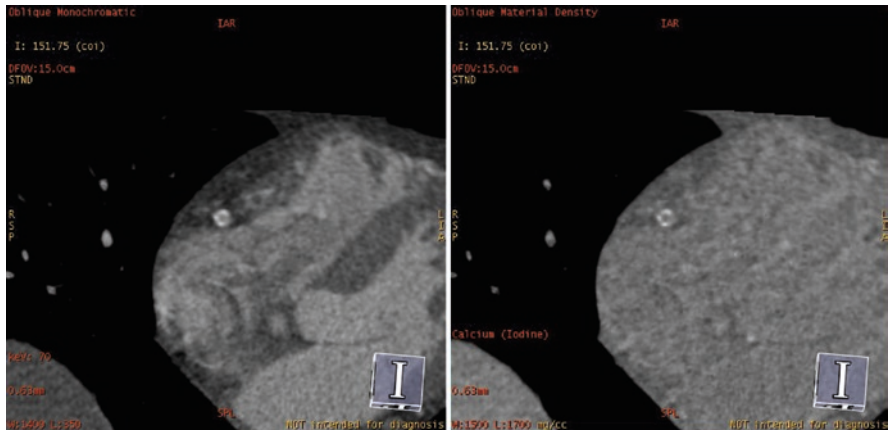

Fig. 4 Example of a monochromatic and calcium MD cardiac fast switching scan. Images courtesy of Dr. Prasad Panse, Mayo Clinic Scottsdale

References

Alvarez R, Macovski A (1976) Energy-selective reconstructions in X-ray CT. Phys Med Biol 21(5):733–744

Kalender WA, Perman WH, Vetter JR, Klotz E (1986) Evaluation of a prototype dual-energy computed tomographic apparatus. I. Phantom studies. Med Phys 13(3):334–339

Alvarez R, Seppi E (1979) A comparison of noise and dose in conventional and energy selective computed tomography. IEEE Trans Nucl Sci NS–26(2):2853–2856

Li B, Yadava G, Hsieh J (2010) Head and body CTDIw of dual energy x-ray CT with fast-kVp switching. Paper 7622–69, SPIE Medical Imaging, San Diego, Feb 2010

Fan J, Hsieh J, Sainath P, Crandall PS (2010) Evaluation of the adaptive statistical iterative reconstruction technique for cardiac computed tomography imaging. Paper 7622–101, SPIE Medical Imaging, San Diego, Feb 2010

Tkaczyk JE, Langan DA, Wu X, Xu D, Hara A, Pavlicek W, Licato P, Leverentz J (2009) Quantization of liver tissue in fast-switched dual kVp computed tomography using linear discriminant analysis. Paper 7258–15, SPIE Medical Imaging, Feb 2009

Joshi MC, Langan DA, Sahani DV, Ramesh AK, Aluri S, Procknow K, Wu X, Rahul Bhotika R, Okerlund DR (2010) Fast kV switching dual energy CT effective atomic number accuracy for kidney stone characterization. Paper 7622–128, SPIE Medical Imaging, Feb 2010

Pack JD, Langan DA, Wu X, Xu D, Benson TM, Schmitz AM, Tkaczyk JE, Pavlicek W, Boltz TF II, Payden R, Licato P, Leverentz J (2009) Fast kVp switching CT imaging of a dynamic cardiac phantom. Paper 7258–150, SPIE Medical Imaging, Feb 2009

Pavlicek W, Panse P, Amy K, Hara AK, Boltz T, Paden R, Licato P, Chandra N, Okerlund DR, Bhotika R, Langan DA (2010) Initial use of fast switched dual energy CT for coronary artery disease. Paper 7622–66, SPIE Medical Imaging, Feb 2010

Dual-Energy Algorithms and Postprocessing Techniques

Cynthia H. McCollough, Bernhard Schmidt, Xin Liu, Lifeng Yu, and Shuai Leng

Contents

Abstract

› Recently, dual energy CT has been routinely used in clinical practice for the applications of bone removal, kidney stone composition differentiation, gout identification, and generating virtual non-contrast images. This is mainly due to the material differentiation capability of dual energy CT in which patients are scanned with two distinguished beam energies. Processing algorithms used to obtain material-specific information were reviewed, including projection-based, image-based and hybrid methods. Pros and cons of each algorithm were compared. Different type of images generated from dual energy data sets (e.g. blended image, material-selective image and energy-selective image) were summarized and appropriate clinical applications were discussed. Finally, dose performance of dual energy CT, in comparison with single energy CT, was analyzed with the consideration of image quality.

C.H. McCollough (✉)
CT Clinical Innovation Center, Department of Radiology, Organization Mayo Clinic, Rochester, MN, USA
e-mail: mccollough.cynthia@mayo.edu

B. Schmidt
Division Siemens Healthcare, Organization Computed Tomography CTE PA, Siemensstrasse 1, Forchheim, Germany

X. Liu
CT Clinical Innovation Center, Department of Radiology, Organization Mayo Clinic, Rochester, MN, USA

L. Yu
CT Clinical Innovation Center, Department of Radiology, Organization Mayo Clinic, Rochester, MN, USA

S. Leng
CT Clinical Innovation Center, Department of Radiology, Organization Mayo Clinic, Rochester, MN, USA

1 Introduction

In CT imaging, materials having different chemical compositions can be represented by the same, or very similar, CT numbers, making the differentiation and classification of different types of tissues extremely challenging. A classical example is the difficulty in differentiating between calcified plaques and iodine-containing

T.R.C. Johnson et al. (eds.), *Dual Energy CT in Clinical Practice*, Medical Radiology,
DOI: 10.1007/174_2010_36

blood. Although these materials differ in atomic number considerably, depending on the respective mass density or iodine concentration, bone and iodinated blood may appear identical. In addition to the difficulty in differentiating and classifying tissue types, the accuracy with which material concentration can be measured is degraded by the presence of multiple tissue types. For example, when measuring the amount of iodine enhancement of a soft tissue lesion, the measured mean CT number over the lesion reflects not only the enhancement due to iodine, but also the CT number of the underlying tissue.

The reason for these difficulties in differentiating and quantifying different tissue types is that the measured CT number of a voxel is related to the linear attenuation coefficient $\mu(E)$, which is not unique for any given material but is a function of the material composition, the photon energies interacting with the material, and the mass density of the material. As can be seen in Fig. 1, the same value of linear attenuation coefficient can be obtained for two different materials (e.g., iodine and bone) at a given energy, depending on the mass densities.

In dual-energy CT, an additional attenuation measurement is obtained at a second energy, allowing the differentiation of the two materials (Fig. 1). Assuming the use of monoenergetic X-rays, at approximately 100 keV the same linear attenuation coefficients are measured for bone and iodine. Data acquired at approximately 40 keV would allow the differentiation of the two materials. Although medical X-ray tubes generate a polyenergetic spectra, the general principle remains valid. Thus, dual-energy CT can be defined as the use of (1) attenuation measurements acquired with different energy spectra and (2) knowledge of the changes in attenuation between the two spectra in order to differentiate and classify tissue composition. Dual-energy CT was initially explored and described by Godfrey Hounsfield, who stated in 1973, "two pictures are taken of the same slice, one at 100 kV and the other at 140 kV… so that areas of high atomic numbers can be enhanced. Tests carried out to date have shown that iodine ($z=53$) can be readily differentiated from calcium ($z=20$)" (Hounsfield 1973).

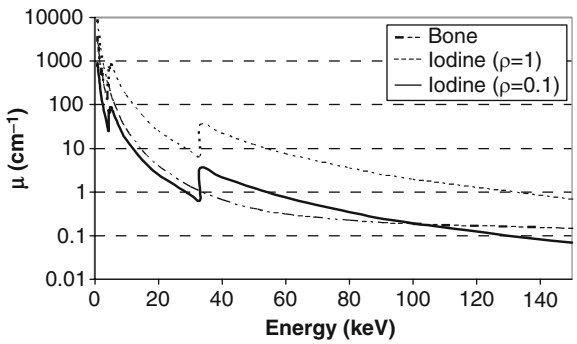

Fig. 1 Linear attenuation coefficient μ as a function of energy for bone (assuming $\rho=1$ g/cm^3), iodine (assuming $\rho=1$ g/cm^3), and iodine with lower density (assuming $\rho=0.1$ g/cm^3). Since the linear attenuation coefficient is determined by the mass attenuation coefficient and the density, the same value for μ(E) can be attained although the materials are different. Reprinted with permission from (Schmidt and McCollough 2007)

2 How to Process

2.1 Projection Space Approach

The first investigations of dual-energy processing methods for CT were made by Alvarez and Macovski in 1976 (Macovski et al. 1976; Alvarez and Macovski 1976). They demonstrated that using a conventional X-ray source having a broad energy spectrum, one can still separate the attenuation coefficient into the contributions from (1) photoelectric effect and (2) Compton scattering, which can be approximately modeled using a material's effective atomic number (Z_{eff}) and effective mass density (ρ_{eff}), and knowledge of the X-ray energy spectra (E). With measurements made at two different X-ray tube potentials, one can characterize any material in its image by its effective atomic number and effective density.

Alternatively, due to the fact that the mechanisms responsible for X-ray attenuation are limited to the photoelectric effect and Compton scattering for X-ray energies in the diagnostic range ($E<140$ keV), the mass attenuation coefficient, μ/ρ, of any material can be expressed with sufficient accuracy as a linear combination of the photoelectric and Compton attenuation coefficients. Consequently, it can also be expressed as a linear combination of the attenuation coefficients of two basis materials (Kalender et al. 1986):

$$\mu(\mathrm{r},E)=\left(\frac{\mu}{\rho}\right)_1(E)\cdot\rho_1(\mathrm{r})+\left(\frac{\mu}{\rho}\right)_2(E)\cdot\rho_2(\mathrm{r}) \quad (1)$$

where the two basis materials differ in their photoelectric and Compton characteristics, $(\mu/\rho)_i(E)$, $i=1,2$ denotes

the mass attenuation coefficients of the two basis materials, and $\rho_i(\mathrm{r})$, $i = 1,2$ denotes the mass densities of the two basis materials at location r . In dual-energy CT, the detected signal intensity can be expressed as

$$I_m = \int S_m(E)\, D(E) E \exp \left\{ -\left(\frac{\mu}{\rho}\right)_1 (E)\cdot L_1 - \left(\frac{\mu}{\rho}\right)_2 (E)\cdot L_2 \right\} dE \qquad (2)$$

where $m = low, high$ denotes the energy index, $S_m(E)$ denotes the X-ray spectra, and $D(E)$ denotes the detector response. $L_1 = \int dl\rho_1(r)$ and $L_2 = \int dl\rho_2(r)$ represent the attenuation density line integrals for the two basis materials. Numerical methods and a calibration step are required to solve L_1 and L_2 , and conventional reconstruction methods are subsequently used to generate an effective density map for each of the two basis materials (Macovski et al. 1976; Alvarez and Macovski 1976). Using the two basis material effective density images, the linear attenuation coefficient of the subject $\mu(r,E)$ can be calculated for any photon energy. In this manner, a pseudo monoenergetic image can be created.

The projection space decomposition approach can be used to generate material-selective images (e.g., water-only and iodine-only images), or energy-selective images (i.e., pseudo monoenergetic images) that are free of beam-hardening effects. Beam-hardening effects are avoided because, already having determined the mass density of each basis material at each point in the image, the linear attenuation coefficient is calculated using only the attenuation coefficients of the two basis materials at the desired photon energy (e.g., 70 keV).

The biggest challenge of projection-data-based methods is data consistency between the low- and high-energy data. Any kind of motion, change in contrast agent concentration, or internal pulsation will lead to severe artifacts in the reconstructed dual-energy data. Several applications were reported utilizing dual-energy CT, focusing primarily on lung, liver, and tissue characterization (Johnson et al. 1983; Cann et al. 1982; Goldberg et al. 1982; Adams et al. 1982; Chiro et al. 1979; Wang et al. 2003). However, due to several technical limitations, dual-energy CT was not adopted into routine clinical practice. The primary limitation was that data for different tube voltages were acquired at two different times. Patient motion that occurred between the two acquisitions severely degraded the quality of the resultant images.

2.2 Image Space Approach

The simplest way to process dual-energy data is to perform a weighted subtraction or addition for the separately reconstructed images at different beam energies (i.e., image blending). The low-voltage images (typically 80 kV) are multiplied by a weighting factor and subtracted from or added to the high-voltage images (140 kV) to obtain material-specific information. As shown in Fig. 2, bone signal can be suppressed to form a "soft tissue only" image or the soft tissue signal can be suppressed to form a "bone signal only" image. This is analogous to basis material decomposition. However, the computation is performed with reconstructed images rather than sinogram data.

As discussed above, the total mass attenuation coefficient of an object containing two constituent elements is the weighted summation of the two element's mass attenuation coefficients. To simplify the mathematical derivation and focus on the error propagation, we assume the dual-energy measurements are made with two monochromatic X-ray beams of high energy E_H and low energy E_L. Thus, we model the effective linear attenuation coefficient at two different X-ray tube potentials (low and high) as

$$\mu_{eff,L} = \rho_{eff}\left[m_1 \left(\frac{\mu}{\rho}\right)_{1,L} + (1-m_1)\left(\frac{\mu}{\rho}\right)_{2,L} \right], \qquad (3)$$

$$\mu_{\mathrm{eff},H} = \rho_{\mathrm{eff}}\left[m_1 \left(\frac{\mu}{\rho}\right)_{1,H} + (1-m_1)\left(\frac{\mu}{\rho}\right)_{2,H} \right], \qquad (4)$$

Or,

$$\mu_{eff,L} = \rho_{eff}\left[\alpha \frac{Z_{eff}^{\ k}}{E_L^{\ n}} + \beta f_{KN}(E_L) \right], \qquad (5)$$

$$\mu_{eff,H} = \rho_{eff}\left[\alpha \frac{Z_{eff}^{\ k}}{E_H^{\ n}} + \beta f_{KN}(E_H) \right], \qquad (6)$$

where Z_{eff} is the effective atomic number, $f_{KN}(E)$ is the Klein-Nishina function, $\kappa \approx 3 \sim 4$ and $n \approx 3 \sim 3.5$, and α, β are constants (Macovski et al. 1976; Alvarez and Macovski 1976). In (3) and (4), the unknowns are the mass fraction m_1 and effective mass density ρ_{eff}. In (5) and (6), the unknowns are Z_{eff} and ρ_{eff}. The effective linear attenuation coefficients μ_{eff} can be obtained from the dual-energy CT image data using the relationship:

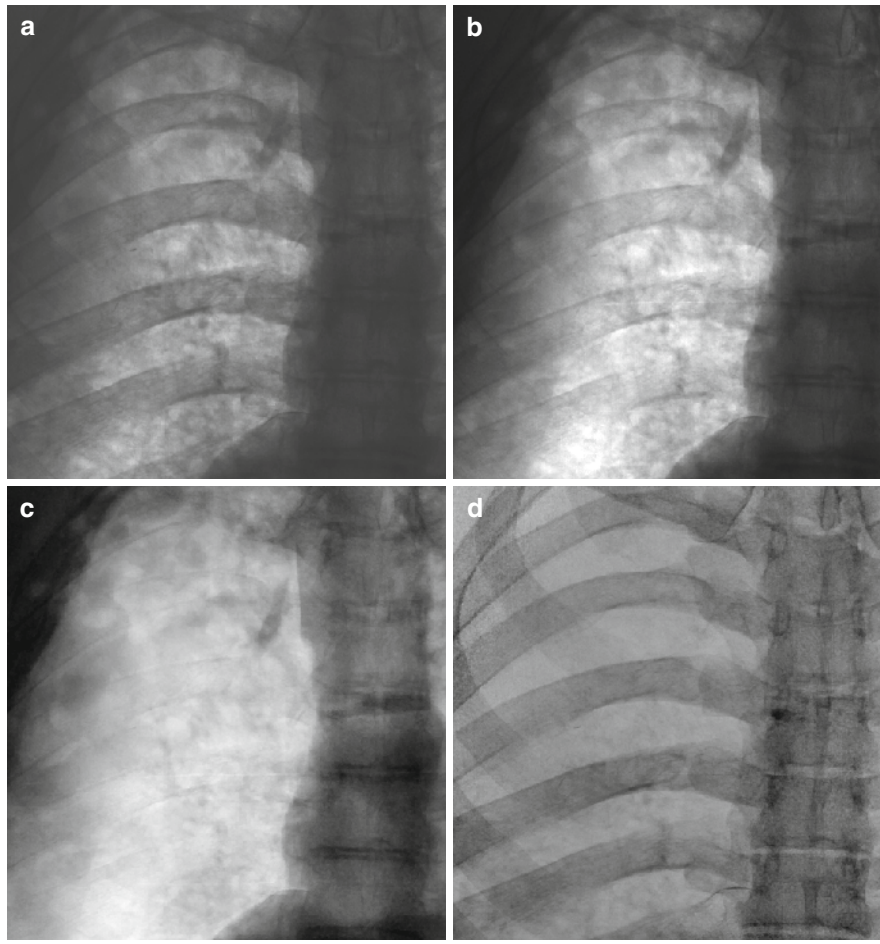

Fig. 2 Chest radiograph acquired using a (**a**) low- and (**b**) high-energy tube potential. With dual-energy techniques, postprocessed (**c**) soft-tissue-only and (**d**) bone-only images can be calculated. Reprinted with permission from (Schmidt and McCollough 2007)

$$\mu_{eff,L\ or\ H} = \left(\frac{CT\#_{L\ or\ H}}{1000} + 1\right) \cdot \mu_{water,L\ or\ H}. \tag{7}$$

Therefore, one can perform chemical identification (i.e., material decomposition) based on equations (3–6) using the reconstructed dual-energy images. It should be pointed out that the image-space-based dual-energy algorithms do not automatically remove beam-hardening effects as do projection-spaced algorithms. Image space approaches rely on accurate beam-hardening corrections being applied prior to image reconstruction. Maass et al. have proposed a hybrid dual-energy material decomposition algorithm that uses a generalized data correction function (in projection space) to preprocess the raw datasets prior to reconstruction of the images used to form the material-selective images (Maass et al. 2009). Simulations and phantom studies have shown that the quality of material decomposition images generated by this hybrid method is better than that of images generated by the traditional image-space-based methods (Maass et al. 2009).

3 Type of DE Image

3.1 Blended Image

In dual-energy CT applications, in addition to the material-specific information, a single set of nonmaterial-specific images can be generated from the dual-energy data to provide images for the purpose of routine diagnostic interpretation. These nonmaterial-specific

images are referred to here as "blended" images, as they combine data from the low- and high-energy images. Clinically, both the blended images and the dual-energy processed images provide value to the examination.

Although either the low-energy or the high-energy images could be used independently for the routine diagnostic interpretation, the image quality would be inferior to that of a single-energy dataset acquired at the same total dose simply because each image set from the dual-energy scan is generated with about one-half of the radiation dose used in the single-energy scan. The low-energy scan (typically 80 kV) provides images with improved iodine contrast enhancement, but often with increased noise level due to the increased absorption coefficients of iodine and tissue at lower photon energies. Conversely, the high-energy scan provides images with lower iodine contrast enhancement, but often with better noise properties. By combining the low- and high-energy images, the mixed images utilize all of the radiation doses delivered by the dual-energy scan, resulting in better image quality than either of the low- and high-energy images alone (Yu et al. 2009).

Generally, there are two types of image blending methods, namely linear and nonlinear image blending. For linear image blending, the blended image is given by

$$I = w_L I_L + w_H I_H, \tag{8}$$

where I_i $(i=L,H)$ denotes the low- and high-energy images, w_i $(i=L,H)$ is the blending ratio for the low- and high-energy images, and $w_L + w_H = 1$. By increasing the blending ratio more toward the 80 kV image, the iodine contrast information will improve, but the noise in the image will increase, since both characteristics are linked. This means that by shifting the blending ratio in the opposite direction, the blended image will contain less noise, but also less iodine contrast information. An optimal blending ratio exists for generating the highest iodine contrast to noise ratio (CNR) for a particular patient size and dose division between low- and high-energy scans (Yu et al. 2009). A second and more sophisticated approach to blend the two images is to combine the images in a nonlinear fashion. This can be accomplished via a variety of different algorithms. Eusemann et al. compared six nonlinear blending algorithms and showed that a blending ratio based on a moidal blending (i.e., modified sigmoidal blending) provided the best image characteristics of any of the blended images (Eusemann C et al. 2008; Holmes et al. 2008). This moidal blending approach (implemented as Siemens syngo(R) DE optimum contrast) utilizes low kV image data for image regions that show iodine enhancement, and uses high kV image information for nonenhanced or only slightly enhanced regions. Figure 3 schematically illustrates the linear and nonlinear image blending algorithms.

3.2 Material-Selective Image

Clinical dual-energy CT applications include bone removal, iodine quantification, and material characterization. A weighted subtraction is the simplest way to differentiate materials. Similar to what has been done for almost two decades in chest radiography, bone can be suppressed or emphasized (Fig. 2). Alternatively, new applications can be explored, such as using dual-energy subtraction to differentiate iron from calcium, which may allow for the differentiation between hemorrhagic and calcified plaques, which both appear bright in single-energy CT images (Langheinrich et al. 2006; McCollough et al. 2006).

Another way to process dual-energy data is to use the material decomposition methods discussed in Sect. 2. Processing data in this way allows the differentiation between different atomic elements and therefore chemical compositions. In current material-selective applications, the algorithm is used to decompose a mixture into its three constituent materials, such as contrast material, soft tissue, and fat.

In principle, dual-energy CT scan quantify an object with not more than two constituent elements because it only provides two independent measurements. For three-material decomposition using only two different spectral measurements, one additional condition must be provided to solve for three unknowns. One solution is to assume that the sum of the volumes of three constituent materials is equivalent to the volume of the mixture (i.e., volume conservation). Explicitly, the volume fractions of three materials can be expressed as

$$f_1 + f_2 + f_3 = 1, \tag{9}$$

where f_1, f_2, and f_3 are the volume fractions of materials 1, 2, and 3. Therefore, the effective density ρ_{eff} of the three-material mixture is

$$\rho_{\text{eff}} = f_1\rho_1 + f_2\rho_2 + (1 - f_1 - f_2)\rho_3. \tag{10}$$

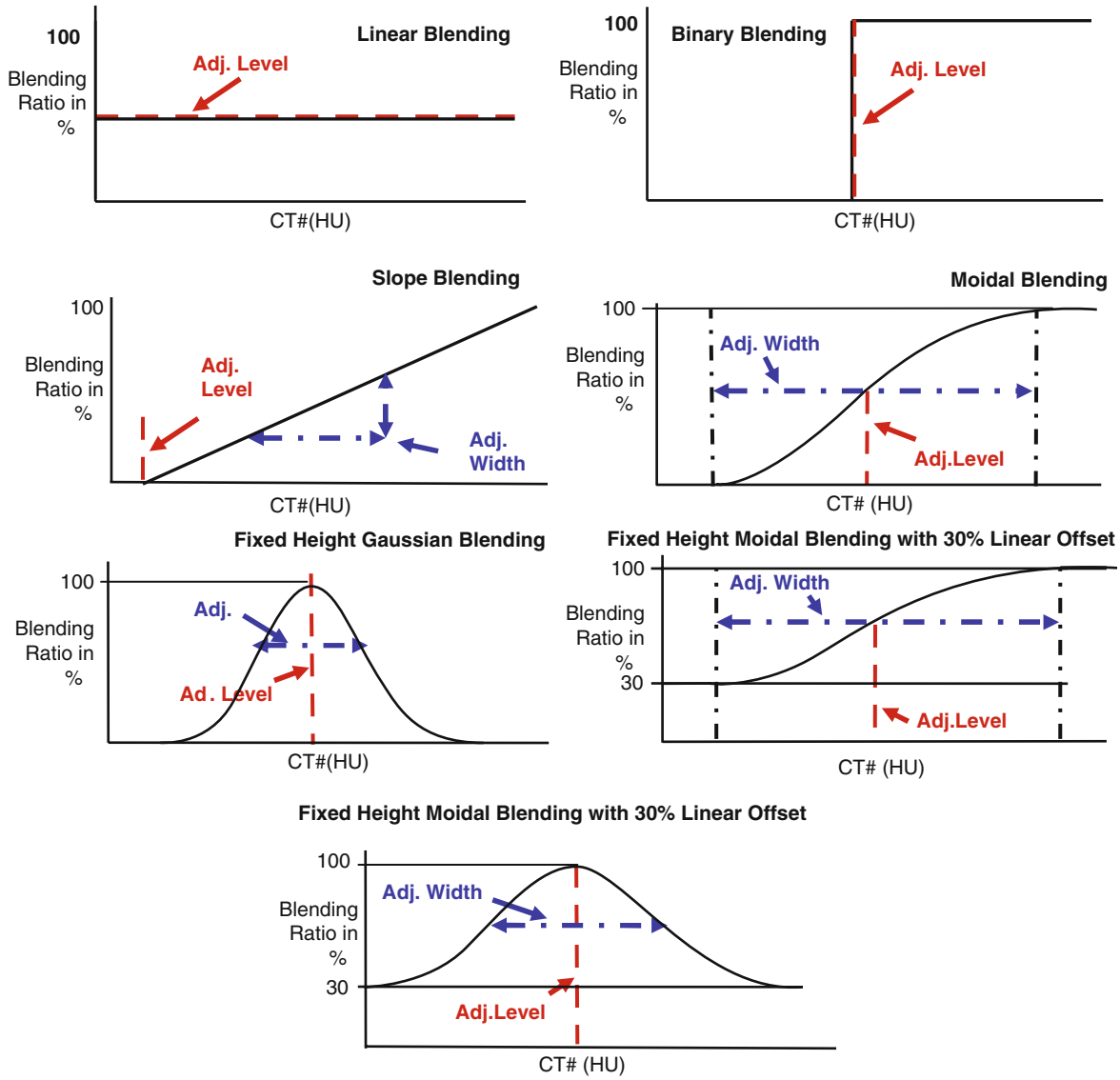

Fig. 3 Graphical illustration of linear and nonlinear blending algorithms. The dotted lines represent user adjustable parameters. Reprinted with permission from (Eusemann et al. 2008)

The mass attenuation μ_m of the mixture can then be expressed as

$$\begin{aligned}\mu_m &= m_1\mu_{m1} + m_2\mu_{m2} + m_3\mu_{m3} \\ &= (\rho_1 f_1\mu_{m1} + \rho_2 f_2\mu_{m2} + \rho_3 f_3\mu_{m3}) / \rho_{eff},\end{aligned} \tag{11}$$

where m_1, m_2, and m_3 are the mass fractions for each material. This yields four unknowns: f_1, f_2, f_3, and ρ_{eff}. Equations (9) and (10) provide two additional criteria to those provided by the dual-energy measurement. This allows three-material decomposition using a dual-energy CT technique.

However, the constant volume assumption is not always true. For example, the volume of a salt–water mixture is not equal to the sum of the individual volumes of salt and water. For a very dilute solution, the effective density is simply the water density. Therefore, a more generalized method uses a semiempirical dual-energy CT method to estimate the effective density in the absence of volume conservation (Liu et al. 2009).

One major challenge for three-material decomposition is the numerical stability of the decomposition process. It has been shown that the numerical stability (i.e., noise level) is dependent upon the difference of the

dual-energy ratios, where we define the dual-energy ratio as the ratio of the CT numbers of a material at two different energies (Kachelriess and Kalender 2005; Kelcz et al. 1979). To separate materials having similar dual-energy ratios, the decomposition process becomes ill-conditioned (i.e., unstable numerical solutions). Special procedures, such as a perturbation method, have to be used to obtain reasonable solutions. A very effective alternative method is to increase the difference of the dual-energy ratios, thereby increasing numerical stability. This can be accomplished by adding additional filtration to the high-energy X-ray beam, thereby minimizing the overlap of the X-ray spectra at the two different tube potentials (Primak et al. 2009). In current clinical applications, three-material decomposition is only applied in situations where a high atomic number contrast agent, such as iodine, is involved, because the dual-energy ratio of iodine is very different from that of tissue or bone. Pure tissue images can be calculated by only displaying the signal contribution from fat and tissue, thereby suppressing the iodine signal and creating a "virtual noncontrast" image (Fig. 4). Alternatively, bone can be suppressed and the iodine-containing vascular structures displayed. This automatic bone removal allows CT angiographic applications in regions where complex bone anatomy previously interfered with the visualization of vascular anatomy.

3.3 Energy-Selective Image

The outcome of the dual-energy material decomposition is a map (i.e., image) of the effective atomic number and effective density of each voxel, or a map (i.e., image) of the fraction of the total mass in the voxel associated with each of the two basis materials. These results can be used to generate the linear-attenuation coefficient map of the object under study at any energy within the diagnostic energy range. Thus, a pseudo monoenergetic image can be created at any desired energy. In principle, the pseudo monoenergetic image created using a projection-based method is free of beam-hardening artifacts. The pseudo monoenergetic image can still be created in image space after image reconstruction, which may provide a flexible way to control image noise and contrast, and to generate a single set of images for diagnosis, just as with the linearly blended low- and high-energy images. However, the monoenergetic image generated in image space still suffers from the beam-hardening artifacts.

A critical question is how the noise in the pseudo monoenergetic image compares to the noise produced by a single-energy CT scan using the same dose. Analytical and experimental studies have shown that there exists an optimal energy at which the pseudo monoenergetic image is comparable to the conventional image with the same noise for a given dose (Alvarez and Macovski 1976; Alvarez and Seppi 1979; Lehmann et al. 1981). The optimal energy can be derived analytically through an analysis of variance, which demonstrates that the optimal energy is near the average of the two effective energies at the two tube potentials.

4 Determinants of IQ/Dose

Currently, several applications, such as bone removal, iodine quantification, and kidney stone characterization have been implemented clinically. One common question is whether dual-energy CT requires more dose than does single-energy CT, acknowledging that a dual-energy scan provides material-specific information in addition to images that mimic a conventional single-energy scan. Either monochromatic images or mixed images blended from the low- and high-tube potential data acquisition can be generated from a dual-energy scan. One phantom study performed on a dual-source scanner demonstrated that as long as the patient is not too large, the images blended from the low- and high-tube potential data yield similar or even better iodine CNR than a typical 120 kV image acquired using the same radiation dose (Yu et al. 2009). Figure 5 compares the iodine CNR in the dual-energy blended images and the single-energy images for the same radiation dose when the 80 kV dose fraction in the dual-energy scans varied from 0.3 to 0.7. The CNR values in the dual-energy blended images were between those of the 80 and 140 kV single-energy images. In comparison with 120 kV, which is typically used in most adult CT practices, the CNR in the dual-energy mixed images was similar or higher. Thus, dual-energy CT can be performed routinely in small to average-sized patients at the same dose level as single-energy CT, yet potentially provides more diagnostic information than conventional single-energy CT. Further, pseudo monochromatic imaging from dual-energy CT

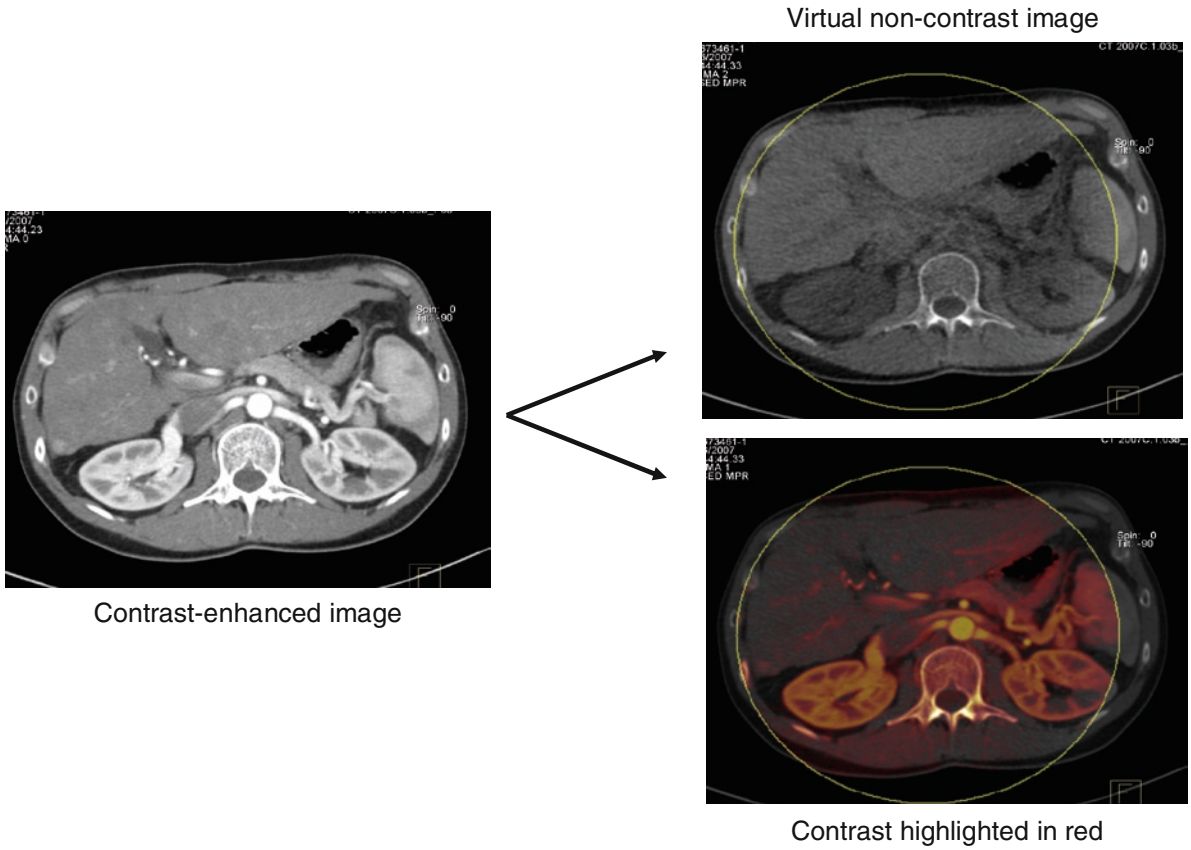

Fig. 4 Three-material decomposition: although data are acquired after iodinated contrast agent has been injected (**a**), the dual-energy information can be used to produce images wherein the contrast agent is removed (**b**) or color coded and shown on top of the noniodine image (**c**). Reprinted with permission from (Schmidt and McCollough 2007)

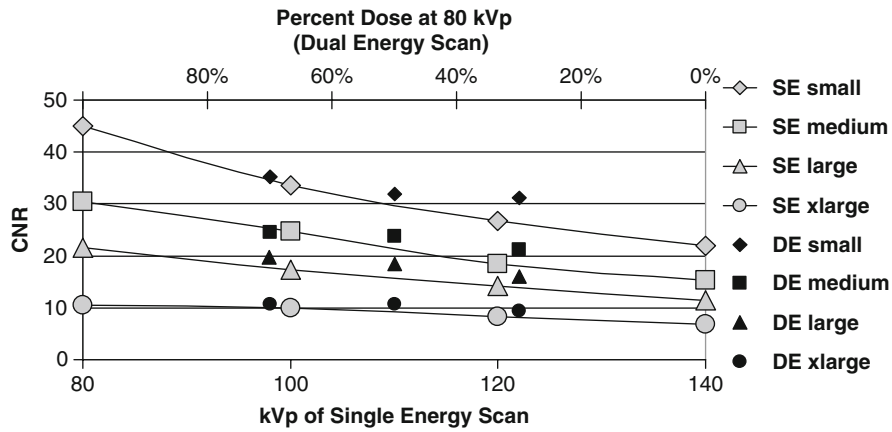

Fig. 5 Iodine contrast to noise ratio (CNR) in the dual-energy mixed images (*black symbols*) and the single-energy images (*grey symbols*) for the same total radiation dose. The CNR in single-energy images is shown as a function of kV for each phantom size. The CNR in dual-energy mixed images is shown when the 80 kV dose fraction varied from 30 to 70% for each phantom size (top horizontal axis). Reprinted with permission from (Yu et al. 2009)

can greatly reduce beam-hardening artifacts (Alvarez and Macovski 1976; Alvarez and Seppi 1979).

Another application of dual-energy CT is virtual noncontrast imaging (Johnson et al. 2007). Many CT exams involve scans both before and after contrast injection. Dual-energy CT allows the creation of "virtual" precontrast images from a postcontrast dual-energy scan, which has the potential to avoid the precontrast scan and thereby to reduce the total radiation dose. However, the amount of dose reduction is highly dependent on the image quality of the virtual noncontrast images created in a dual-energy postcontrast scan. Due to the noise amplification during dual-energy processing (Kelcz et al. 1979), the virtual images often suffer from a high noise level. Greater separation between the low- and high-energy X-ray spectra may improve the image quality in virtual noncontrast images and allow more significant radiation dose reduction (Primak et al. 2009).

References

Hounsfield GN (1973) Computerized transverse axial scanning (tomography): part I. description of system. Br J Radiol 46:1016–1022

Macovski A, Alvarez RE, Chan JL, Stonestrom JP, Zatz LM (1976) Energy dependent reconstruction in X-ray computerized tomography. Comput Biol Med 6:325–336

Alvarez RE, Macovski AA (1976) Energy-selective reconstructions in X-ray computerised tomography. Phys Med Biol 21:733–744

Kalender WA, Perman WH, Vetter JR, Klotz E (1986) Evaluation of a prototype dual-energy computed tomographic apparatus. I. Phantom studies. Med Phys 13:334–339

Johnson RJ, Zhu XP, Isherwood I, Morris AI, McVerry BA, Triger DR, Preston FE, Lucas SB (1983) Computed tomography: qualitative and quantitative recognition of liver disease in haemophilia. J Comput Assist Tomogr 7:1000–1006

Cann CE, Gamsu G, Birnberg FA, Webb WR (1982) Quantification of calcium in solitary pulmonary nodules using single- and dual-energy CT. Radiology 145:493–496

Goldberg HI, Cann CE, Moss AA, Ohto M, Brito A, Federle M (1982) Noninvasive quantitation of liver iron in dogs with hemochromatosis using dual-energy CT scanning. Invest Radiol 17:375–380

Adams JE, Chen SZ, Adams PH, Isherwood I (1982) Measurement of trabecular bone mineral by dual energy computed tomography. J Comput Assist Tomogr 6:601–607

Chiro GD, Brooks RA, Kessler RM, Johnston GS, Jones AE, Herdt JR, Sheridan WT (1979) Tissue signatures with dual-energy computed tomography. Radiology 131:521–523

Wang B, Gao Z, Zou Q, Li L (2003) Quantitative diagnosis of fatty liver with dual-energy CT. An experimental study in rabbits. Acta Radiol 44:92–97

Maass C, Baer M, Kachelriess M (2009) Image-based dual energy CT using optimized precorrection functions: a practical new approach of material decomposition in image domain. Med Phys 36:3818–3829

Yu L, Primak AN, Liu X, McCollough CH (2009) Image quality optimization and evaluation of linearly mixed images in dual-source, dual-energy CT. Med Phys 36:1019–1024

Eusemann C, Holmes DI, Schmidt B, Flohr T, Robb R, McCollough C, Hough D, Huprich J, Wittmer M, Siddiki H and Fletcher J (2008) Dual energy CT – how to best blend both energies in one fused image. Proc. SPIE, Vol. 6918, 691803 (2008); doi:10.1117/12.773095

Holmes DR 3rd, Fletcher JG, Apel A, Huprich JE, Siddiki H, Hough DM, Schmidt B, Flohr TG, Robb R, McCollough C, Wittmer M, Eusemann C (2008) Evaluation of non-linear blending in dual-energy computed tomography. Eur J Radiol 68:409–413

Langheinrich AC, Michniewicz A, Sedding DG, Lai B, Jorgensen SM, Bohle RM, Ritman EL (2006) Quantitative x-ray imaging of intraplaque hemorrhage in aortas of apoE$^{-/-}$/LDL$^{-/-}$ double knockout mice by synchrotron-based micro-CT and X-ray fluorescence microscopy. Invest Radiol 41:645–650

McCollough C, Kantor B, Primak A, Dzyubak O, Krauss B, Schmidt, Flohr T and Ritman E (2006) Fast, dual-energy, multi-slice CT Can discriminate Fe and Ca. Circulation 114(18 suppl) II:724–725

Liu X, Yu L, Primak AN, McCollough CH (2009) Quantitative imaging of element composition and mass fraction using dual-energy CT: three-material decomposition. Med Phys 36:1602–1609

Kachelriess M, Kalender WA (2005) Presampling, algorithm factors, and noise: considerations for CT in particular and for medical imaging in general. Med Phys 32:1321–1334

Kelcz F, Joseph PM, Hilal SK (1979) Noise considerations in dual energy CT scanning. Med Phys 6:418–425

Primak AN, Ramirez Giraldo JC, Liu X, Yu L, McCollough CH (2009) Improved dual-energy material discrimination for dual-source CT by means of additional spectral filtration. Med Phys 36:1359–1369

Alvarez RE, Seppi E (1979) A comparison of noise and dose in conventional and energy selective computed tomography. IEEE Trans Nucl Sci 26:2853–2856

Lehmann LA, Alvarez RE, Macovski A, Brody WR, Pelc NJ, Riederer SJ, Hall AL (1981) Generalized image combinations in dual KVP digital radiography. Med Phys 8:659–667

Johnson TR, Krauss B, Sedlmair M, Grasruck M, Bruder H, Morhard D, Fink C, Weckbach S, Lenhard M, Schmidt B, Flohr T, Reiser MF, Becker CR (2007) Material differentiation by dual energy CT: initial experience. Eur Radiol 17:1510–1517

Schmidt B, McCollough CH (2007) Dual-energy computed tomography. In: Thomas C. Gerber, Birgit Kantor, Eric E. Williamson (eds) Computed tomography of the cardiovascular system. Informa Healthcare, London, pp 451–462

Part II

Vascular System

Head and Neck

Dominik Morhard and Susanne Jochum

Contents

Abstract

› Technical improvements have established CT angiography as a standard noninvasive imaging modality for the evaluation of the vascular system of head and neck. This chapter provides information about dedicated protocols for scanning and postprocessing of DE CTA and DE virtually unenhanced NECT, with special focus on ischemic and hemorrhagic stroke as well as on evaluation of stenosis.

1 Clinical Background

With constant technical improvements over the last decade, CT angiography has been established as a standard noninvasive imaging modality for the evaluation of the vascular system of head and neck. CTA displaced invasive digital subtraction angiography (DSA) and duplex ultrasound in many routine and emergency situations and rendered the evaluation of the supraaortic vessels possible even for smaller hospitals and nonspecialized physicians. Patient comfort, safety, and cost-effectiveness represent other advantages. Major limitations of CTA remain the limited ability to differentiate between calcified plaques and contrast material, rendering precise quantification of calcified stenoses difficult.

Although improvements of spatial resolution and shortened acquisition times in magnetic resonance

D. Morhard
Department of Clinical Radiology, University of Munich, Grosshadern Hospital, Marchioninistrasse 15, 81377 Munich, Germany

S. Jochum (✉)
Institute of Radiology, Westpfalz Clinic, Hellmut-Hartert-Strasse 1, 67655 Kaiserslautern, Germany
e-mail: s.jochum@gmx.de

T.R.C. Johnson et al. (eds.), *Dual Energy CT in Clinical Practice*, Medical Radiology,
DOI: 10.1007/174_2010_45

imaging (MRI) have displaced CTA in some routine indications, CTA remains the imaging modality of choice in imaging of acute stroke, especially in patients with disorientation, in critical condition, or with contraindications for MRI such as cardiac pace makers. The good availability and short examination time of CTA have strengthened its role during off-hours and in smaller hospitals. Limitations of CTA in comparison to MRI are radiation exposure and the lack of robust visualization tools for comprehensible evaluation of the arteries at the base of skull. Even with the introduction of robust semiautomatic bone removal tools like bone subtraction, maximum intensity projections (MIP) of supraaortic CTA datasets without bone which resemble MRI have not established as standard reconstructions in routine (Morhard et al. 2008).

With the introduction of dual energy (DE) CT in modern CT scanners, imaging with more specific information beyond Hounsfield units has become feasible. DE enables material differentiations by analyzing spectral behavior of different materials at different energy levels of X-ray photons; physical details are discussed in Chap. 39. For imaging of the vascular system of head and neck, DE provides two new, major applications: DE bone removal and virtual unenhanced image reconstructions (referred to as "brain hemorrhage" algorithm). DE bone removal is an automatic postprocessing algorithm which uses DE material differentiation to generate exact a bone mask and to subtract it from the DE-CTA dataset. After bone subtraction, multiple display techniques such as thick MIP and volume rendering technique (VRT) can be applied to the new dataset to obtain an MRI-like visualization of the whole dataset, i.e., in one image, without bone. These images make a comprehensible evaluation of all supraaortic vessels possible even in critical areas like the base of skull. In contrast to bone subtraction techniques which use matched bone masks generated on the basis of a first noncontrast scan and a second CTA scan, DE CTA obtains the information for bone masking from the data of one single DE scan. Misregistrations due to patient movement, e.g., swallowing and breathing, between two sequentially acquired scans are no issue in DE CTA bone removal, because both datasets are acquired simultaneously. Only in rare cases with very fast movements during the scan equivalent motion artifacts in both data sets of the 80/100 and 140 kV tube can occur and reduce image quality. Also manual coregistrations of two sequentially acquired datasets become redundant. However, DE CTA is susceptible to other artifacts, which especially affect the proximal part of the supraaortic vessels, the aortic arch, and the subclavian arteries specifically as well as vessels embedded in tight bony canals (Lell et al. 2009b). These artifacts are related to low transmission of low-energy quanta in very dense projections which occur in transversal orientation at the level of the shoulders and to minor extent also in the skull base.

Recent studies of different groups have shown that the use of DE bone removal in head and neck CTA improves image quality and reduces reading time (Morhard et al. 2009; Thomas et al. 2009; Uotani et al. 2009; Watanabe et al. 2009). With the introduction of DE scanners of the second generation, improved scanning techniques and reconstruction algorithms have been implemented. Mainly the use of tin filters for the tube with the higher tube voltage eliminates low-energy quanta and optimizes the spectrum for DE material differentiation, increasing signal-to-noise ratio and decreasing dose at comparable tube currents. In combination with improved reconstruction algorithms, it is now feasible to compensate former low signal-to-noise ratios at the level of the aortic arch to generate bone subtractions of high image quality.

2 Scan Protocol

Like in all DE applications, high contrast attenuation is mandatory for good postprocessing results. Vessel densities of at least 700 HU should be sought for adequate DE bone subtraction. Default reconstruction parameters of the "head bone removal" algorithm usually perform well and "one click reconstructions" without user interaction succeed in about 80–90% of cases. In datasets with suboptimal results of bone subtraction, we propose manual editing of the parameter "maximum" in the standard tool card, i.e., to measure the mean contrast attenuation in the center of the common carotid artery on the 140 kV dataset and add 150 HU.

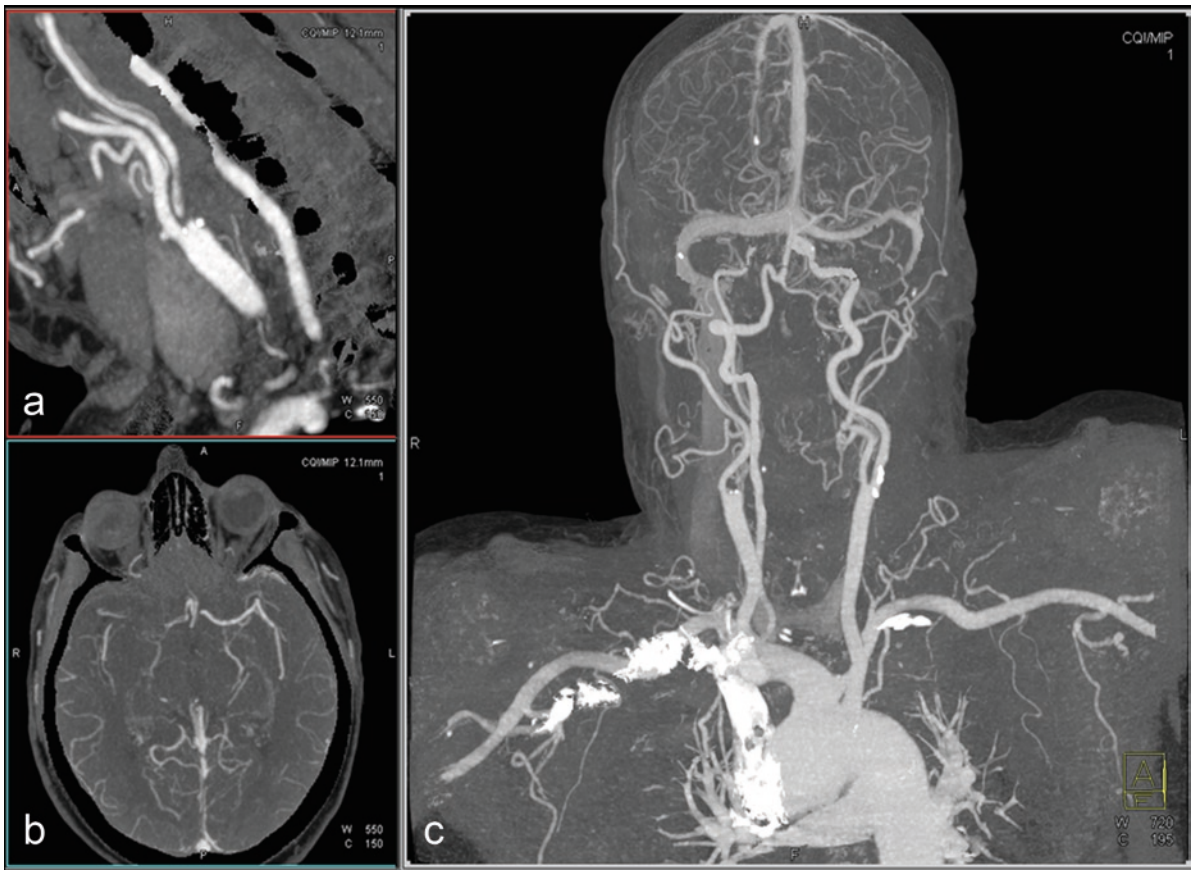

Fig. 1 A 75-year-old female presenting with left-sided hemiparesis and aphasia since 80 min. (**a**) Curved, center-lined MPR visualizing a filiform stenosis of the right proximal internal carotid artery at the level of the carotid bulb due to calcified stenosis. (**b**) Axial 0.75 mm MPR clearly delineates the thrombosis of the right middle cerebral artery (MCA). (**c**) Thick MIP CTA after DE bone subtraction showing the whole supraaortic arteries in one image at excellent image quality. Essential information of collateral blood flow can be assessed in seconds. This image also demonstrates the limitation of large FOV thick MIP reconstruction in the evaluation of small vessel pathologies: a thrombosis of the M1-segment of the right MCA can easily be missed in this image

The scan range should cover the lower edge of the aortic arch to the vertex (Fig. 1). Scan acquisition should be done in craniocaudal scan direction in order to avoid beam-hardening artifacts due to high contrast agent concentrations in the subclavian vein in the early injection phase. The use of automatic dose modulation should be considered individually. Only for obese patients it should be turned on to get proper signal-to-noise ratios at the level of the shoulders. The reason for this recommendation is that automated dose modulation tends to increase tube current at the base of skull and at hypertrophic frontal bones, although unmodulated, lower standard tube currents generally achieve

	Tube A	Tube B
Voltage	140 kV 100 kV	80 kV without tin filter 140 kV with tin filter
Tube current time product	50 mAs 104 mAs	213 mAs without tin filter 104 mAs with tin filter
Pitch	0.9	
Collimation	64–128 × 0.6 mm	
Rotation time	0.28–0.33 s	
Dose modulation	Normal body weight: off obese patients: on	

sufficient image quality even at hypertrophic skull bones at considerably lower dose.

3 Contrast Material Injection

We suggest standardized contrast injection protocols with 50–80 mL of high-concentrated contrast agent (0.35–0.4 mg iodine/mL) at an injection rate of 3.5–5 mL/s followed by a saline chaser of 30–50 mL at the same injection speed. Alternatively, weight-adapted contrast media and saline chaser injection protocols can be used, but normally result in higher absolute contrast agent volumes: 0.4–0.45 g iodine/kg bodyweight at an injection rate of 0.055–0.057 × bodyweight mL/s followed by 30–50 mL saline at identical flow. The scan should start 4 s after bolus tracking in the ascending aorta with a threshold of 100 HU to achieve good midarterial-phase images.

4 Postprocessing

Axial images (MPR, not MIP) at 80/100, 140 kV, and weighted average "120 kV like images" should be reconstructed with a slice thickness of 0.75 mm, an increment of 0.5 mm using the D20 kernel. These images should be used for automated bone subtraction, e.g., using "head bone removal" tool card in the DE application (Siemens Healthcare). Thick MIP reconstructions in radial ranges can be generated from the bone subtracted 0.75 mm axial images. Finally, coronal and sagittal MIP images without bone removal should be reconstructed with 3–5 mm slice thickness and increment. It is recommendable to always correlate findings to thin (1 mm or less) MPR images, especially in the evaluation of small thrombi which can be obscured on MIP or thick MPR images.

For the generation of virtual noncontrast images from a DE CTA dataset, we recommend to reconstruct images at 3 mm slice thickness and increment with a D20 or D30 kernel and apply the "brain hemorrhage" DE postprocessing algorithm (Siemens Healthcare).

5 Diagnostic Evaluation

5.1 Stroke CT and Stenosis Evaluation

As mentioned above, CT is still the modality of choice in stroke imaging. CTA is also commonly applied to evaluate stenoses or correlate findings in duplex sonography or other clinical examinations. With the introduction of DE CT, it is possible to reliably differentiate calcium from contrast media. On the one hand, this makes a visualization of the whole supraaortic vasculature feasible without superimposing bones. On the other hand, it can also provide special visualizations of calcified plaques which are not masked as bone by the bone subtraction algorithm and remain visible after bone removal. With the visualization of calcified plaques, further analysis of lumen narrowing is feasible, e.g., to differentiate soft and hard plaque or to confirm dissections of the intima (Lell et al. 2009a, b; Das et al. 2009; Barreto et al. 2008; Buerke et al. 2009). Considering that routine MRA provides a mere visualization of the vessel lumen, the information on plaque morphology, distribution, and composition is more detailed in DE CT. Although recent developments in postprocessing and the introduction of tin filters have increased quality of bone removal in areas of circular calcified plaques dramatically, truncation artifacts still occur. It remains mandatory to correlate findings, e.g., vessel lumen narrowing, to nonsubtracted multiplanar reconstructions, especially in cases of lumen narrowing in calcified plaques.

5.2 Virtual Unenhanced Images and Brain Hemorrhage

So far, only a few studies report initial results in using DE material differentiation to create virtual nonenhanced images from DE CTA data in order to reduce total dose by replacing the nonenhanced brain scan (NECT). Ferda et al. published data of a study on 25 patients in which virtual unenhanced images were compared to "real" NECT (Ferda et al. 2009). In this study cohort the virtual image quality was found to be sufficient in 96% of cases. The agreement in detection of intracranial bleeding on virtual and NECT reached

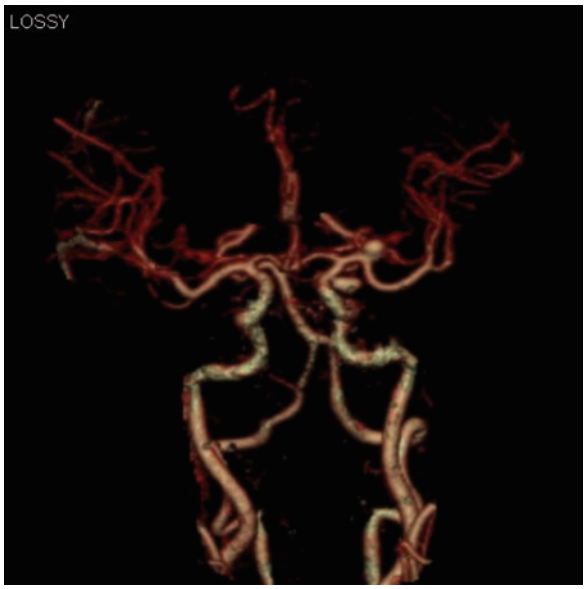

Fig. 2 VRT images of a dual energy CTA with bone removal of a patient with a subarachnoidal hemorrhage showing two aneurysms of the internal carotid artery and the medial cerebral artery

96% in per-lesion analysis and 100% in per-patient analysis. Until studies on larger patient cohorts prove the reliability of the virtual unenhanced images of the brain, this application should only be used in a scientific setting for further research, i.e., in clinical studies with correlation to a real noncontrast scan.

Our own preliminary results concerning the virtual nonenhanced reconstructions revealed some limitations. Especially in patients with subarachnoidal hemorrhage, the image quality of the virtual nonenhanced scan was not satisfactory, i.e., the noise in the generated image was too strong to evaluate subtle hemorrhage in the sulci sufficiently. Improvements in dose modulation and spectral differentiation may make this option viable in the near future, but for now we would not regard the virtual noncontrast reconstruction as sufficient to replace a true noncontrast scan (Fig. 2).

5.3 Intracranial Aneurysm, Angiomas, and Fistulas

The prevalence of intracranial aneurysms is approximately 1–5% (Zhang et al. 2010). The gold standard examination for the detection of these aneurysms was DSA, but recently CT angiography emerged as the primary diagnostic tool to evaluate intracranial aneurysms (Hegde et al. 2009; Lell et al. 2006). Watanabe et. al. found a high sensitivity in the detection of intracerebral aneurysms using CTA (Watanabe et al. 2009) and it has to be shown that DE CT provides equivalent or even better results. Zhang et al. described a possibility to perform arterial phase DE CT angiography without confounding contrast enhancement of the cerebral veins (Zhang et al. 2010).

As scan protocol for the detection of intracranial aneurysms in an early arterial phase, the following parameters are recommendable:

- 50–100 highly concentrated contrast material (370–400 mg iodine/mL) at a flow of 5 mL/s
- For planning of interventional treatment of the aneurysms, a scan range from the aortic arch to the vertex with caudocranial direction
- Otherwise a range from C2 to the vertex, also in caudocranial scan direction
- Bolus tracking with a region of interest in the left atrium or, if the patient is known to have a low cardiac output, in the ascending aorta

The bone removal can serve as a helpful tool to visualize the infraclinoidal parts of the internal carotid artery (Zhang et al. 2010). Bone subtraction algorithms had been available for years, but required the acquisition of a nonenhanced and a subsequent enhanced CTA data set. This can lead to motion artifacts if the patient moves between the scans, which is of course a very common problem in patients with disorientation or acute stroke. There are correction algorithms which can compensate minor changes between the datasets, but the problem remains clinically relevant even with these corrections, because major movements cannot be eliminated. The DE technique which acquires both datasets simultaneously is much less sensitive to patient motion. Therefore, dual-energy-based bone removal may achieve a role in the robust and sensitive detection of intracranial aneurysms (Hegde et al. 2009; Watanabe et al. 2009).

It is important not to read only the VRT and MIP reconstructions, but also the cross-sectional bone-removed images to detect small aneurysms.

Our own results show an increased number of detected aneurysms using DE CTA with bone removal and VRT images compared to multislice CTA without bone removal. Especially aneurysms at the scull base

can be shown very well. The postprocessing tools are especially helpful for colleagues with limited experience in CT interpretation, but even experts benefit from these new methods.

There are not any studies available yet concerning the role of dual energy CT in the detection of intracranial angiomas and fistulas, but the detection of vascular malformations with dual energy is possible and can provide improved visualizations resembling projection angiography. Especially in vascular malformations with high flow and strong dilution of the contrast material in the draining veins, DE CT can provide a visualization of the entire malformation including the venous structures without superimposing bone.

6 Scientific Evidence

Recent studies report surveys on small patient cohorts (15–100 patients) in which DE CT of the vasculature of the head and neck is feasible and provides good to excellent results (Lell et al. 2009a, b; Morhard et al. 2009; Thomas et al. 2009; Uotani et al. 2009; Watanabe et al. 2009). Prospective multicentre studies on large patients cohorts with comparison to DSA, duplex, and/or MRA are not available yet.

References

Barreto M, Schoenhagen P, Nair A et al (2008) Potential of dual-energy computed tomography to characterize atherosclerotic plaque: ex vivo assessment of human coronary arteries in comparison to histology. J Cardiovasc Comput Tomogr 2(4):234–242

Buerke B, Wittkamp G, Seifarth H et al (2009) Dual-energy CTA with bone removal for transcranial arteries: intraindividual comparison with standard CTA without bone removal and TOF-MRA. Acad Radiol 16(11):1348–1355

Das M, Braunschweig T, Mühlenbruch G, Mahnken AH et al (2009) Carotid plaque analysis: comparison of dual-source computed tomography (CT) findings and histopathological correlation. Eur J Vasc Endovasc Surg 38(1):14–19

Ferda J, Novak M, Mirka H et al (2009) The assessment of intracranial bleeding with virtual unenhanced imaging by means of dual-energy CT angiography. Eur Radiol 19(10):2518–2522

Hegde A, Chan LL, Tan L, Illyyas M, Lim WE (2009) Dual Energy CT and its use in neuroangiography. Ann Acad Med Singapore 38:817–820

Lell M, Anders K, Klotz E, Ditt H, Bautz W, Tomandl BF (2006) Clinical evaluation of bone-subtraction CT angiography (BSCTA) in head and neck imaging. Eur Radiol 16:889–897

Lell MM, Hinkmann F, Nkenke E, Schmidt B, Seidensticker P, Kalender WA, Uder M, Achenbach S. (2009) Dual energy CTA of the supraaortic arteries: Technical improvements with a novel dual source CT system. Eur J Radiol, Oct 8

Lell MM, Kramer M, Klotz E, Villablanca P, Ruehm SG (2009b) Carotid computed tomography angiography with automated bone suppression: a comparative study between dual energy and bone subtraction techniques. Invest Radiol 44(6):322–328

Morhard D, Fink C, Becker C, Reiser MF, Nikolaou K (2008) Value of automatic bone subtraction in cranial CT angiography: comparison of bone-subtracted vs. standard CT angiography in 100 patients. Eur Radiol 18(5):974–982

Morhard D, Fink C, Graser A, Reiser MF, Becker C, Johnson TR (2009) Cervical and cranial computed tomographic angiography with automated bone removal: dual energy computed tomography versus standard computed tomography. Invest Radiol 44(5):293–297

Thomas C, Korn A, Krauss B, Ketelsen D, Tsiflikas I, Reimann A, Brodoefel H, Claussen CD, Kopp AF, Ernemann U, Heuschmid M. (2009) Automatic bone and plaque removal using dual energy CT for head and neck angiography: Feasibility and initial performance evaluation. Eur J Radiol, Jun 9

Thomas C, Korn A, Krauss B et al (2009) Automatic bone and plaque removal using dual energy CT for head and neck angiography: feasibility and initial performance evaluation. Eur J Radiol

Uotani K, Watanabe Y, Higashi M et al (2009) Dual-energy CT head bone and hard plaque removal for quantification of calcified carotid stenosis: utility and comparison with digital subtraction angiography. Eur Radiol 19(8):2060–2065

Watanabe Y, Uotani K, Nakazawa T et al (2009) Dual-energy direct bone removal CT angiography for evaluation of intracranial aneurysm or stenosis: comparison with conventional digital subtraction angiography. Eur Radiol 19(4):1019–1024

Zhang LJ, Wu SY, Niu JB et al (2010) Dual-energy CT angiography in the evaluation of intracranial aneurysms: image quality, radiation dose, and comparison with 3D rotational digital subtraction angiography. AJR Am J Roentgenol 194:23–30

Aorta

Wieland H. Sommer

Contents

Abstract

› Most pathologies of the aorta require multiphase MSCT-protocols, which leads to high radiation doses. Especially in patients who routinely have to undergo MSCT, like patients after endovascular aneurysm repair, dose reduction strategies are desirable. Dual Energy CT offers the possibility to create virtual non-contrast images from arterial or venous datasets and therefore decrease radiation exposure. A single phase protocol with a venous-phase CTA and a derived virtual non-contrast enhanced dataset has been evaluated in several studies for patients after endovascular aneurysm repair. Virtual non-contrast images are a reasonable approximation of true non-contrast images and can replace the latter in this patient collective. Future studies should investigate the application of virtual non-contrast images in other aortic pathologies, e.g. intramural hematoma.

1 Clinical Background

Pathologies of the aorta are associated with high morbidity and mortality. Therefore, they require an accurate and efficient diagnostic approach. Multislice technology in computed tomography (MSCT) has extensively improved and expanded the clinical applications for this imaging modality. In many centers MSCT has become the standard of reference in the diagnosis and follow-up of patients with aortic pathologies (Rubin and Kalra 2006; Rubin 2003; Lawler and

W.H. Sommer
Department of Clinical Radiology, University of Munich, Grosshadern Hospital, Marchioninistrasse 15, 81377 Munich, Germany
e-mail: Wieland.Sommer@med.uni-muenchen.de

T.R.C. Johnson et al. (eds.), *Dual Energy CT in Clinical Practice*, Medical Radiology,
DOI: 10.1007/174_2010_46

Fishman 2003; Sommer et al. 2009). The most common clinical pathologies of the aorta include different types of aortic aneurysms and dissections, penetrating aortic ulcers, intramural aortic hematomas, aortitis, and traumatic injuries of the aorta (Theisen et al. 2007). In recent years, MSCT has furthermore become important for the follow-up after endovascular aneurysm repair (EVAR) (Ishida et al. 2007).

Standard CTA protocols of the aorta consist of one to three contrast phases, depending on the suspected diagnosis. Suspected intramural hematoma, aortitis, or EVAR follow-up necessitate nonenhanced CT scanning beside one or two contrast-enhanced phases (Theisen et al. 2007). In follow-up examinations after EVAR, the nonenhanced scan serves to distinguish between calcifications within the thrombosed aneurysm and endoleaks, which are defined as blood flow into the excluded aneurysm through different pathways.

Due to the frequent CT follow-up examinations after EVAR, typically one time per year, strategies for dose reduction are desirable in this patient group. While the standard CTA-protocol for EVAR follow-up is triphasic (nonenhanced, arterial, and venous phase), it could recently be shown that the arterial phase can be omitted without a decrease in diagnostic accuracy (Macari et al. 2006). Using dual energy CTA, virtual-noncontrast (VNC) images can be obtained from contrast-enhanced images by subtracting the iodine information (see Fig. 1). These images have been shown to be a reasonable approximation of true noncontrast (TNC) images and may lead to a further dose reduction of nearly 50% (Sommer et al. 2010; Stolzmann et al. 2008; Chandarana et al. 2008).

2 Physical Background

When both tubes of the Dual Source scanner are operated at different kilovoltages, differences in attenuation can be analyzed and thus materials can be differentiated. This works especially well in materials with large atomic numbers, like iodine and calcium, because their strong photoelectric effect causes a high attenuation at lower photon energies (Johnson et al. 2007).

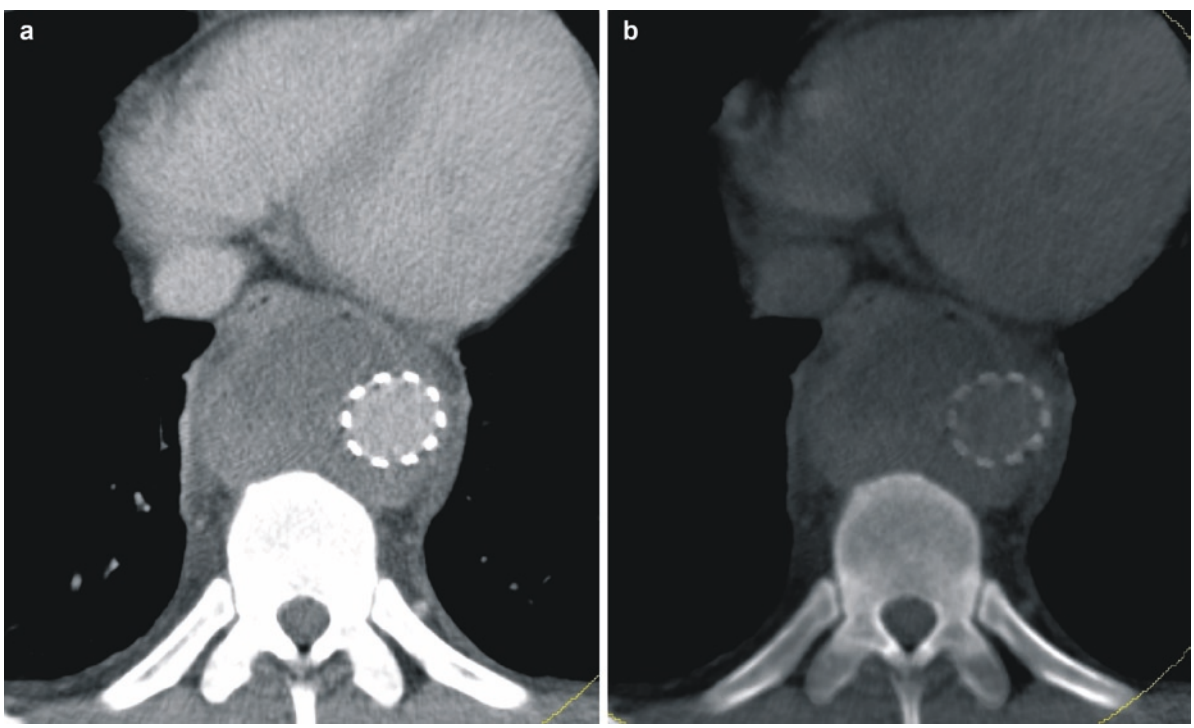

Fig. 1 Direct comparison of a venous-phase dual energy CTA of the thoracic aorta (**a**) and a virtual-noncontrast (VNC) images, which is generated out of it by subtraction of the iodine information (**b**). Compared to true noncontrast images, the aspect of VNC images is smoother and the stentgraft appears less dense

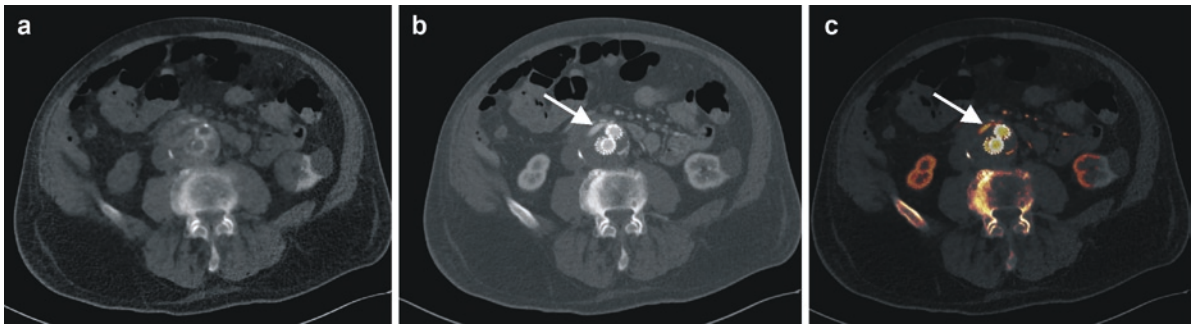

Fig. 2 Beside the VNC image (**a**), which can be generated from the venous-phase dual-energy dataset (**b**), color-coded images may be created to show the iodine distribution (**c**). In this patient, a type III endoleak can be observed in the level of the bifurcation of the Y-shaped abdominal stentgraft

The images acquired by both tubes and detectors of the DSCT system are reconstructed separately and then analyzed by an algorithm referred to as "three material decomposition." These three materials are soft tissue, iodine, and fat. This algorithm uses iodine as a substance with a strong photo effect and two other materials with a linear attenuation at different photon energies, i.e., with a rather weak photo effect, as reference system. Based on these three materials, each voxel of the image with its respective attenuation values, i.e., CT numbers at 140 and 80 kVp, is decomposed into a linear and an iodine-related attenuation, which represent the "unenhanced" density and the enhancement of that voxel. Thus, it is possible to map the iodine distribution, as it is done by color-coded dual-energy CT images (see Fig. 2c) or to create a "virtual" unenhanced image by subtracting the iodine from the average of both acquired CT images (see Figs. 1b and 2a). Since calcium is not among the three materials analyzed in the VNC algorithm, there may be erroneous subtraction of small calcifications by this algorithm.

3 Scan Protocol

Dual Source CT scanners have been shown to achieve good image quality for dual-energy acquisition of the aorta (SOMATOM Definition Dual Source or Definition Flash, Siemens Medical Solutions, Forchheim, Germany). The diameters of the field of view (FOV) of the "B" detector are 26 cm for the Definition Dual Source and 33 cm for the Definition Flash. The central position of the aorta makes dual-energy imaging of aortic pathologies feasible in both scanners.

Most of the published articles describe that the use of the Definition Dual Source (Sommer et al. 2010; Stolzmann et al. 2008; Chandarana et al. 2008) with the "A" tube was set to a voltage of 140 kVp at a reference tube current-time product of 110 mAs, while the corresponding values are 80 kV and reference 467 mAs for the "B" tube (Sommer et al. 2010). This relationship is necessary to achieve a similar output of photons from the "A" and "B" tubes. Dose modulation should be used (CareDose 4D) to achieve a constant image noise and save radiation dose. A pitch of 0.7 and 0.5 s rotation time are reasonable parameters for the dual energy scan (Sommer et al. 2010). Based on previous experience, a collimation of 14×1.2 mm was employed in these publications to achieve a sufficient signal-to-noise ratio in both acquisitions and in order to compensate noise in 80 kVp acquisitions. For the second-generation Dual Source scanners (Definition Flash), the new tin filter and the hardened 140 kVp spectrum make it possible to use 100 kVp as reference spectrum with the side effect of a weaker CNR as reflected in our measurements in iodine and water samples (Schenzle et al. 2010).

4 Contrast Material Injection

A dual energy venous-phase scan is typically acquired about 70 s after initiation of intravenous injection of a nonionic contrast agent (1.3 mL/kg patient body weight at 370 mg/mL iodine concentration; flow 4 mL/s, followed by a saline chaser bolus of 100 mL at equivalent

injection rate) (Stolzmann et al. 2008). For the detection of endoleaks with one single contrast-enhanced phase, other studies report scan delays about 40 s after initiation of the injection (Sommer et al. 2010). This leads to an improved enhancement of endoleaks which directly arise from the aorta (type I, III and IV), while type II endoleaks may be better opacified in later phases. In our experience, this intermediate delay is a good compromise for a single-phase protocol.

5 Postprocessing

DECT images are normally reconstructed using a slice thickness of 3.0 mm and a reconstruction increment of 1.5 mm. From the DE acquisition, three different sets of images are generated automatically: 80 kV images, 140 kV images, and weighted average images, consisting of 70% information from the 140 kV image and 30% of the 80 kV scan. The weighted average images are similar to a single-energy acquisition at 120 kV (see Fig. 1a). With the new spectral combination of Sn140 and 100 kV, an equal contribution of both datasets, i.e., a weighting factor of 0.5, results in 120 kV-like image with quite exactly equivalent Hounsfield-density.

A specific dual-energy postprocessing workstation is used for image analysis (Syngo MMWP Version VA 34, Siemens Medical Solutions, Forchheim, Germany) and for the generation of other image types.

In summary, the following algorithms are helpful for the fast and accurate evaluation of dual-energy datasets of the aorta:

- VNC images (see Figs. 1b and 2a). A DE postprocessing preset called "Liver VNC" is used for the generation of these images.
- Color-coded datasets to map the iodine distribution: i.e., fused images, consisting of VNC or weighted average images with the overlaying iodine information from dual energy venous-phase scans (see Fig. 2c). The same "Liver VNC" algorithm serves to generate the color-coded DECT images.
- A further algorithm called "hard plaque" is used in order to differentiate between iodine and calcium. The former is colored in blue, the latter in red (see Fig. 3).

6 Diagnostic Evaluation

In the available scientific literature on the value of dual-energy technique for CTA of the aorta, there are mainly reports on follow-up examinations after EVAR (Sommer et al. 2010; Stolzmann et al. 2008; Chandarana et al. 2008). To our knowledge, all the current literature is based on the experience with the SOMATOM Dual Source scanner and a 140/80 kVp combination.

Comparison of VNC images, created from venous-phase dual-energy datasets, and TNC images resulted in a slightly inferior image quality of VNC images. Possible sources of error are erroneous subtraction of calcium and the smoothed aspect of the VNC images, which may make it difficult to assess the struts of the stentgraft. According to our recent experience, image quality was significantly improved by the introduction of the Sn140/100 kVp combination on the SOMATOM Definition Flash.

Beside the use of VNC images, color-coded datasets, in which iodine information is superimposed in color, were tested for their diagnostic value. These images give a good overview in one single examination and may lead to a faster interpretation (Sommer et al. 2010). Since the information of noncontrast images is included in these datasets, it is feasible to use this single dataset for the assessment of endoleaks (see Fig. 2c).

The "hard-plaque" algorithm has not been extensively investigated in the literature. It seems to give a good visualization of iodine and calcium distribution in the dataset, but has some weaknesses in the differentiation of smaller calcifications (see Fig. 3).

There is good agreement between TNC and VNC CT numbers measured within the aortic lumen, both adjacent to and within aortic stentgrafts. Due to increased image noise and beam hardening on the low kV CT data, larger standard deviation of average densities measured on VNC images was observed. The accuracy of the VNC density values can be further improved by entering actual measured reference values of soft tissue density on 80 and 140 kVp images into the advanced parameters of the dual-energy software.

Most importantly, diagnostic accuracy for the detection of endoleaks is not impaired by using VNC images. Although image quality is described as inferior in the current literature (based on the combination

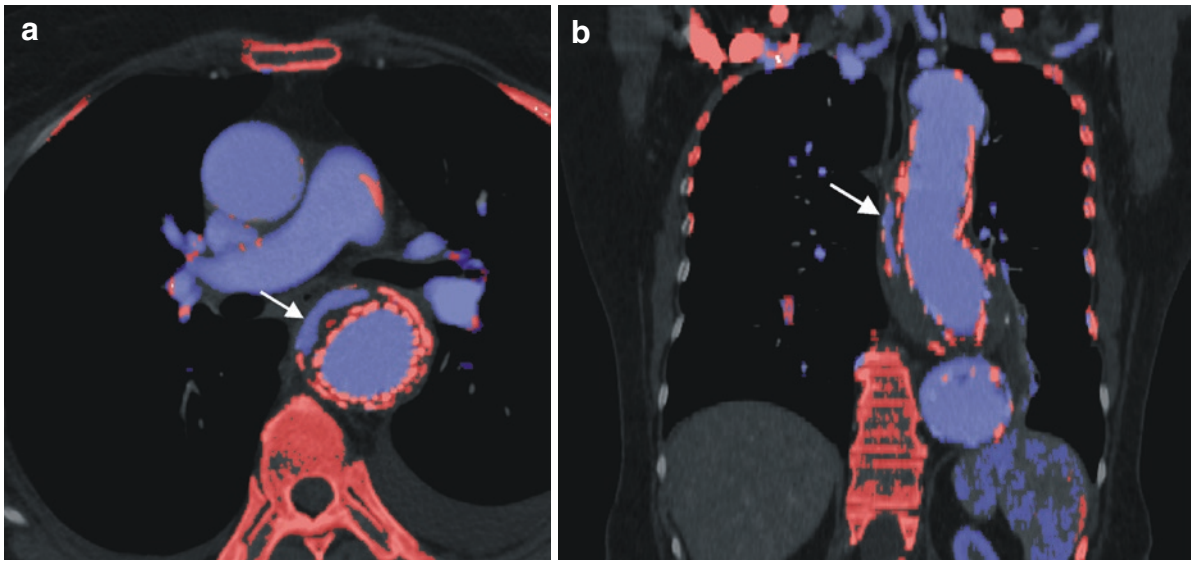

Fig. 3 Application of the "hard plaque" algorithm to a dual-energy dataset. Iodine is colored in *blue*, while calcium and also the stentgraft are colored in *red*. In axial (**a**) and coronal slices (**b**) of this 53-year-old male patient, iodine is detected in the excluded aneurysm sac outside the stentgraft. This corresponds to a type I endoleak, supplied from the distal end of the stentgraft

140/80 kVp), it still displays enough information to classify hyperdense material within the aneurysm sac either as a calcification or as an endoleak.

7 Scientific Evidence

Although there are many aortic pathologies, all studies that were published to date describe the value of Dual Source CTA for follow-up after EVAR. This is most likely due to the special benefit of dose reduction in these patients, since they have to undergo many CT follow-up examinations for the rest of their life. The use of a single-phase protocol (dual energy CT in venous phase) in these patients reduces the radiation dose by 41–44% compared to a dual-phase protocol (TNC phase and venous phase) (Sommer et al. 2010; Stolzmann et al. 2008).

Quantitative and qualitative analyses of VNC and TNC images underline that DECT-based VNC images are a reasonable approximation of true unenhanced single-energy CT images. Although VNC image quality is slightly inferior, overall acceptance for diagnostic reading in patients with EVAR is described as good. The erroneous subtraction of small, focal calcifications can partly affect diagnostic accuracy, although the venous phase alone is mostly sufficient to rule out an endoleak and identify the erroneously subtracted voxels as calcifications in those cases. Overall, the radiologist has to get used to a slightly different aspect of the VNC image especially for the combination of 140/80 kVp, compared to TNC images, i.e., the smoothed aspect and that calcifications appear less dense.

The main application of the dual-energy technique in CTA examinations of the aorta is the possibility to create VNC images. Although there are only publications available for follow-up examinations after EVAR, the diagnostic evaluation of other pathologies such as intramural hematoma and aortitis may also profit from the possibility to create VNC images without additional dose.

References

Chandarana H, Godoy MC, Vlahos I, Graser A, Babb J, Leidecker C et al (2008) Abdominal aorta: evaluation with dual-source dual-energy multidetector CT after endovascular repair of aneurysms–initial observations. Radiology 249(2):692–700

Ishida M, Kato N, Hirano T, Shimono T, Shimpo H, Takeda K (2007) Thoracic CT findings following endovascular stent-graft treatment for thoracic aortic aneurysm. J Endovasc Ther 14(3):333–341

Johnson TR, Krauss B, Sedlmair M, Grasruck M, Bruder H, Morhard D et al (2007) Material differentiation by dual energy CT: initial experience. Eur Radiol 17(6):1510–1517

Lawler LP, Fishman EK (2003) Multidetector row computed tomography of the aorta and peripheral arteries. Cardiol Clin 21(4):607–629

Macari M, Chandarana H, Schmidt B, Lee J, Lamparello P, Babb J (2006) Abdominal aortic aneurysm: can the arterial phase at CT evaluation after endovascular repair be eliminated to reduce radiation dose? Radiology 241(3):908–914

Rubin GD (2003) CT angiography of the thoracic aorta. Semin Roentgenol 38(2):115–134

Rubin GD, Kalra MK (2006) MDCT angiography of the thoracic aorta. In: Saini S, Rubin GS, Kalra MK (eds) MDCT: a practical approach. Springer, Berlin, p 111

Schenzle JC, Sommer WH, Neumaier K, Michalski G, Lechel U, Nikolaou K et al (2010) Dual energy CT of the chest: how about the dose? Invest Radiol 45:347–353

Sommer WH, Theisen D, Wintersperger B, (2009) CT angiography of the aorta. Reiser MF, Becker CR, Nikolaou K, Glazer G. (eds.) 3rd ed., XII, 628 p. 982 illus., 200 in color., Hardcover 292–306

Sommer WH, Graser A, Becker CR, Clevert DA, Reiser MF, Nikolaou K et al (2010) Image quality of virtual non-contrast images derived from dual energy CT angiography after endovascular aneurysm repair. J Vasc Interv Radiol 21:315–321

Stolzmann P, Frauenfelder T, Pfammatter T, Peter N, Scheffel H, Lachat M et al (2008) Endoleaks after endovascular abdominal aortic aneurysm repair: detection with dual-energy dual-source CT. Radiology 249(2):682–691

Theisen D, Tengg-Kobligk H, Michaely H, Nikolaou K, Reiser MF, Wintersperger BJ (2007) CT angiography of the aorta. Radiologe 47(11):982–992

Peripheral Arteries

Wieland H. Sommer and Carolin Brockmann

Contents

Abstract

› Dual Energy bone removal and plaque removal are useful tools for peripheral run-off CT-angiography. Dual Energy bone removal shows significant advantages over software-based bone removal tools with less vessel segmentation errors, especially in the lower leg, where small vessels may run directly adjacent to the bones. It is a "one-click application", works without user interaction, and therefore, shows high practicability for clinical routine. Bone-removed MIPs of peripheral arteries may serve as a useful tool for a fast evaluation of large datasets and provide a good overview for surgical planning in patients suffering from PAD.

1 Clinical Background

In the diagnostic assessment of peripheral arterial occlusive disease noninvasive techniques such as magnetic resonance tomography angiography (MRA) and computed tomography angiography (CTA) have replaced the former gold standard of digital subtraction angiography (DSA). Advances in computer tomography (CT) technologies like increased number of detector rows, thinner collimation, faster rotation speed and larger scanning ranges facilitated and improved the assessment of arterial disease of the extremities by CTA.

Numerous studies on CTA of the peripheral arteries using single source multi detector row CT have already proven its accuracy with sensitivities and specificities above 90% up to 99% (Catalano et al. 2004; Fraioli

W.H. Sommer (✉)
Department of Clinical Radiology, University of Munich,
Grosshadern Hospital, Marchioninistrasse 15,
81377 Munich, Germany
e-mail: Wieland.Sommer@med.uni-muenchen.de

C. Brockmann
Department of Clinical Radiology and Nuclear Medicine,
University Medical Center Mannheim,
Medical Faculty Mannheim of the University of Heidelberg,
Theodor-Kutzer-Ufer 1-3, 68167 Mannheim, Germany

T.R.C. Johnson et al. (eds.), *Dual Energy CT in Clinical Practice*, Medical Radiology,
DOI: 10.1007/174_2010_37

et al. 2006; Heuschmid et al. 2003; Martin et al. 2003; Mesurolle et al. 2004; Ofer et al. 2003; Ota et al. 2004; Portugaller et al. 2004).

Due to its high spatial resolution acquiring submillimeter slices, CT data sets often exceed an amount over 1,000 cross-sectional images. Therefore, appropriate visualization techniques are required both for radiologists and for vascular clinicians in order to obtain a rapid overview and 3-dimensional orientation of the peripheral vessels. The main techniques used for postprocessing of CTA are the volume rendering technique (VRT), multiplanar reconstructions (MPR) and maximum intensity projections (MIPs).

While the VRT results in a good 3D-overview of different anatomical structures with a partially semitransparent visualization of structures with different CT-densities (Tengg-Kobligk et al. 2007), MIPs provide a convenient "DSA-like" visualization of the peripheral vasculature. Since only the voxels with the highest density in the respective projection are displayed in MIPs, bones with a similar density as contrasted vessels need to be removed in order to evaluate larger vascular territories in one image. Vessel wall calcifications and bones adjacent to the vessels are often limiting factors in the segmentation process of bone removal techniques. Although software-based bone removal has improved significantly over recent years, still most current bone removal tools require manual corrections to a certain degree, making this method potentially time-consuming and error-prone.

The introduction of dual source CT systems and with it the possibility of dual energy imaging provoked a further step in the improvement of CTA of the run-off due to its ability of a detailed tissue characterization (Brockmann et al. 2009; Meyer et al. 2008; Sommer et al. 2009). Based on spectral differentiation of density values derived from two synchronous CT scans at different tube voltages characterization of bony structures, vessel wall calcifications and contrast agent became possible (Tran et al. 2009). The dual energy technique in CTA provides a reliable image quality of the peripheral arterial system comparable to the gold standard of DSA (Brockmann et al. 2009).

2 Physical Background

The separation of contrast agent, bony structures and calcified plaque is the key in the visualization of the vascular system of the extremities. Therefore a material selective imaging of iodine is necessary. A further atomic substrate that needs to be characterized is calcium, to detect cortical bone and vessel wall calcifications. The mass attenuation coefficients of calcium hydroxylapatite and cortical bone are relatively high due to their effective atomic numbers of 16.04 and 13.23, respectively. The material-specific X-ray absorption spectra depending on the X-ray energy allow the separation of contrast agent, bony structures and vessel wall calcifications although all three materials exhibit similarly high CT numbers of about 200 Hounsfield units (HU) and above at 140 kV.

Based on material decomposition, dual energy CTA postprocessing algorithms enable the characterization of iodine and calcium and therefore a complete removal of bony structures and vessel wall calcifications is possible, resulting in a pure vascular image.

3 Scan Protocol

Scans of the run-off are acquired in a craniocaudal direction and cover the region from the distal abdominal aorta through the ankles. Patients should be asked to breath gently during the imaging procedure.

For the first generation of dual source CT-scanners (Somatom Definition, Siemens Healthcare, Forchheim, Germany) tube potentials of 140 and 80 kV at exposures of about 90 and 380 mAs per rotation are advisable for an optimal differentiation of iodine and calcium. This relation is necessary to achieve a quantitatively similar output of photons from the "A" and "B" tubes. Since a scan of the peripheral run-off typically starts at the diaphragm and covers the whole abdomen and the lower extremities, a collimation of 14×1.2 mm is chosen to achieve a sufficient signal to noise ratio in both acquisitions. Using second generation dual source CT-scanners (Somatom Definition Flash, Siemens Healthcare), insufficient transmission of thin 80 kVp projections in large or dense objects such as the abdomen can be avoided using a combination of a tin filtered 140 kVp and a 100 kVp spectrum (Primak et al. 2009). This combination also allows the use of a thin 0.6 mm collimation for the entire scan from the diaphragm to the toes.

For dual source CTA of the lower run-off, a rotation time of 0.5 s and a pitch factor of 0.6–0.7 are advisable. A field of view of 380 mm seems to be adequate.

Reported radiation doses in recent literature of dual energy CT-angiographies of the lower run-off range

around 10 mSv (Sommer et al. 2009). This is comparable to standard CT-protocols and seems to be in line with other publications, which do not report a significant increase in radiation dose by dual energy protocols (Johnson et al. 2007).

4 Contrast Material Injection

A volume of 140–160 mL of nonionic iodinated contrast material of at least 300 mg iodine per ml should be administered intravenously with a power injector at an injection rate of 4 mL/s. Alternatively, the bolus can be divided into two thirds with a high flow rate of 5.0–5.5 mL/s, followed by the last third of the bolus at a flow rate of 3 mL/s (Fleischmann 2005). A subsequent saline bolus injection of 40–50 mL at a flow rate ensures good image quality. Bolus triggered acquisition timing is necessary to initiate the CTA. For this purpose a region-of-interest (ROI) is placed in the distal aorta. The scan should be started immediately after the enhancement curve reaches its peak with a minimum of at least 200 HU.

5 Postprocessing

From the primary dataset, overlapping images are typically reconstructed with a slice thickness of 1.5 mm and an increment of 1.0 mm, using a soft dual energy convolution kernel (D20).

From the primary dual energy examination, the scanner may generate three different series of images: 80 kV images, 140 kV images and weighted average images. The latter are based on CT density information from both detectors, using 70% information from the 140 kV and 30% information of the 80 kV scan. These images resemble 120 kV datasets.

A specific Dual Energy software is generally used, typically at a dedicated workstation (Syngo; Version VA20 or higher, Siemens Healthcare). A fully automated bone removal can be performed and 3-dimensional bone-removed MIP datasets are automatically generated. These can be rotated in all directions and are helpful to give an overview of the entire dataset and for demonstration purposes (see Fig. 1b, c). The first software versions still had some difficulties with certain areas of bone removal, typically bone marrow of the pelvis and the removal of the patella. However, this was overcome by later versions (e.g., Version VA20 or higher).

Beside bone-removal, a so-called "plaque removal tool" may be used in order to visualize the remaining lumen in calcified segments (see Fig. 1c). This is helpful in clinical routine; however, one should take into account, that blooming artifacts are not eliminated by dual energy acquisition. Therefore the size of calcified plaques is still overestimated and one should be careful with the estimation of the severity of stenoses.

6 Diagnostic Evaluation

Weighted average images approximately resemble 120 kV images of standard CT scanners and should be used for the assessment of vessel stenoses in axial sections. Eighty kilovolt peak datasets may have additional value due to higher attenuation values of iodine, and one might also consider taking this information into account in case of questionable stenoses.

The strength of dual energy bone removal is to provide a fast overview in patients without significant pathologies, in whom MIPs are sufficient to "screen" the dataset. For clinicians, bone removed MIPs are helpful to provide an overview over a dataset, which often exceeds 1,000 cross-sectional images. However, in areas of dense calcifications or stenoses, it remains necessary to correlate the finding on MIPs to the primary axial image data.

Dual energy plaque removal may further speed up the reading of these datasets, since the remaining lumen can be estimated in MIP datasets. As described above, the overestimation of calcified plaques due to blooming artifacts should always be taken into account.

Even in severely calcified segments, sensitivity, specificity, and accuracy of dual energy bone removed MIPs was above 90%, whereas the conventional bone removal technique showed a substantial decrease of sensitivity, specificity, and accuracy (Brockmann et al. 2009) (see Fig. 2).

7 Scientific Evidence

One of the main benefits of dual energy based bone removal tools is its superior image quality, especially for the lower leg. It could be shown that it is even superior to manually corrected software-based bone-

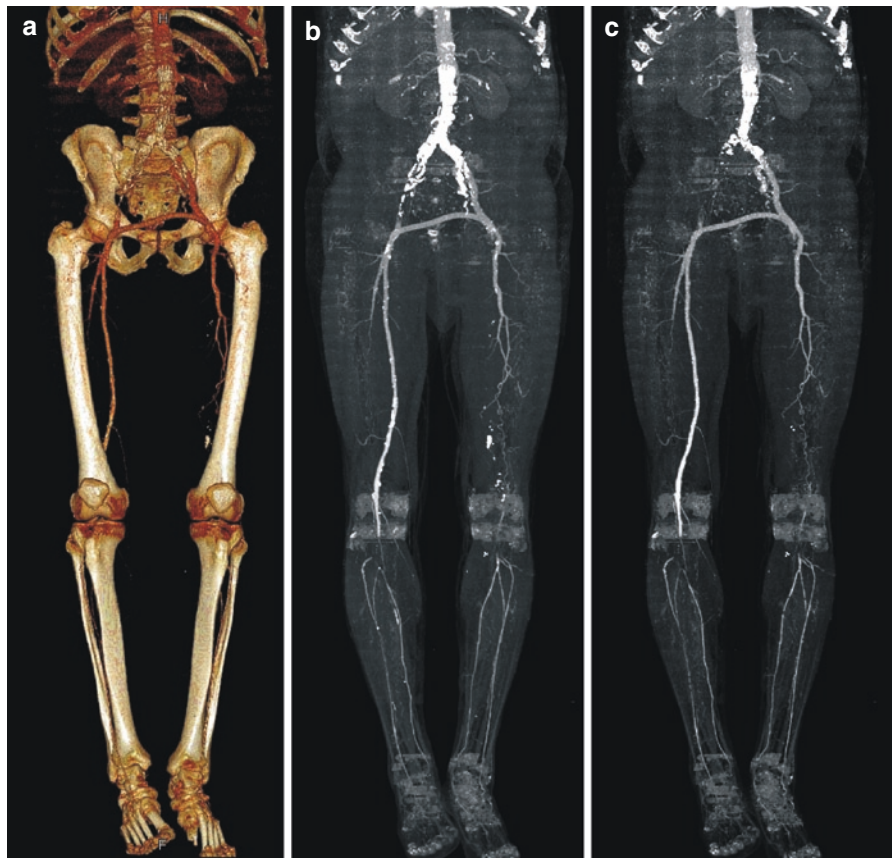

Fig. 1 VRT (**a**) and bone-removed MIP (**b**), as well as bone- and plaque-removed MIP (**c**) of a 69-years-old patient with PAOD stage III. The right iliac artery is occluded and a cross-over bypass supplies the right leg. The right popliteal artery as well as the left superficial femoral artery, are occluded and collateralized. The bone-removed MIP was created without any manual corrections and gives a good overview over the large dataset (**b**). Removal of calcified plaques helps to evaluate the lumen of the contrasted vessels. The stentgraft in the abdominal aorta is not removed by this technique (**c**)

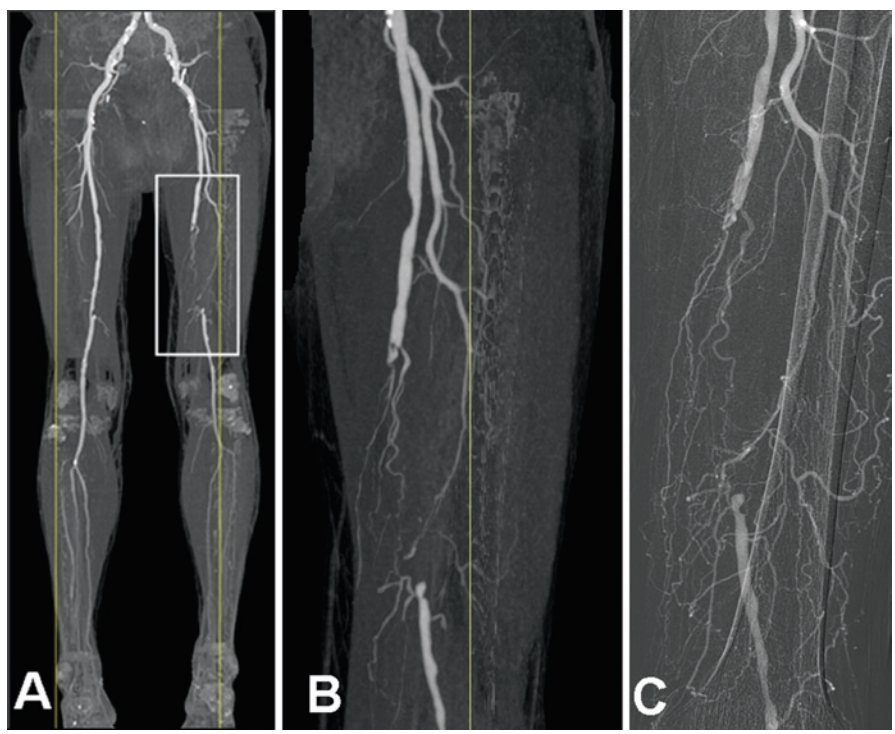

Fig. 2 DE CTA (**a**) in a patient presenting an occlusion of the left superficial femoral artery. Dual energy bone removal (**b**) shows a good correlation with DSA (**c**)

removal tools (Brockmann et al. 2009; Sommer et al. 2009). Recent publications have shown, that more than 90% of dual energy generated bone-removed MIPs are adequate for clinical routine (Brockmann et al. 2009; Meyer et al. 2008; Sommer et al. 2009).

In terms of vessel segmentation errors in MIP images, dual energy based bone-removal is also superior to software-based algorithms, even after manual corrections (Sommer et al. 2009). These vessel segmentation errors tend to occur in infrapopliteal segments due to the close proximity of bones and small vessels. This makes a correct differentiation of purely software-based algorithms almost impossible.

Even after applying dual energy based bone removal, some residual bones may still be present in the datasets (Meyer et al. 2008; Sommer et al. 2009). Recent publications have shown that these are most often the patella, pelvis, the femur and the spine. However, since these articles were published, software algorithms have improved tremendously, so that according to our current clinical experience with this bone removal tool, residual bones do not impair image quality.

Yet, the ability to be completely standardized and automated is the most convincing argument for dual energy bone removal. In clinical routine, it is a "one-click" application. Although manual corrections are still possible after dual energy bone removal, it does not seem to be necessary in clinical routine.

For dual energy bone removal the contrast enhancement seems to play a critical role, since it could be observed that higher attenuation values lead to higher image quality of the bone removal.

A limitation of the current dual energy scan protocol using 140 and 80 kV setting is the rather thick collimation of 1.2 mm which is necessary to achieve a sufficient signal-to-noise ratio (SNR) at 80 kV voltage in the trunk. The inherent reduction in spatial resolution may affect the accuracy of software-based bone-removal tools. This however is solved by second generation dual energy CT-scanners with additional filters to harden the 140 kV spectrum, thus increasing the spectral difference and the SNR of the dual energy information and making it possible to use 0.6 mm collimation at 100 kV instead of 80 kV tube voltage.

Overall, dual energy technique in CTA of the lower extremity runoff provides a robust image quality of the peripheral arterial system comparable to the gold standard of DSA (Brockmann et al. 2009). For radiologists, it represents a valuable tool for an overview technique over large datasets.

References

Brockmann C, Jochum S, Sadick M, Huck K, Ziegler P, Fink C et al (2009) Dual-energy CT angiography in peripheral arterial occlusive disease. Cardiovasc Intervent Radiol 32(4): 630–637

Catalano C, Fraioli F, Laghi A, Napoli A, Bezzi M, Pediconi F et al (2004) Infrarenal aortic and lower-extremity arterial disease: diagnostic performance of multi-detector row CT angiography. Radiology 231(2):555–563

Fleischmann D (2005) How to design injection protocols for multiple detector-row CT angiography (MDCTA). Eur Radiol 15(suppl 5):E60–E65

Fraioli F, Catalano C, Napoli A, Francone M, Venditti F, Danti M et al (2006) Low-dose multidetector-row CT angiography of the infra-renal aorta and lower extremity vessels: image quality and diagnostic accuracy in comparison with standard DSA. Eur Radiol 16(1):137–146

Heuschmid M, Krieger A, Beierlein W, Luz O, Kuettner A, Kopp AF et al (2003) Assessment of peripheral arterial occlusive disease: comparison of multislice-CT angiography (MS-CTA) and intraarterial digital subtraction angiography (IA-DSA). Eur J Med Res 8(9):389–396

Johnson TR, Krauss B, Sedlmair M, Grasruck M, Bruder H, Morhard D et al (2007) Material differentiation by dual energy CT: initial experience. Eur Radiol 17(6):1510–1517

Martin ML, Tay KH, Flak B, Fry PD, Doyle DL, Taylor DC et al (2003) Multidetector CT angiography of the aortoiliac system and lower extremities: a prospective comparison with digital subtraction angiography. AJR Am J Roentgenol 180(4):1085–1091

Mesurolle B, Qanadli SD, El Hajjam M, Goeau-Brissonniere OA, Mignon F, Lacombe P (2004) Occlusive arterial disease of abdominal aorta and lower extremities: comparison of helical CT angiography with transcatheter angiography. Clin Imaging 28(4):252–260

Meyer BC, Werncke T, Hopfenmuller W, Raatschen HJ, Wolf KJ, Albrecht T (2008) Dual energy CT of peripheral arteries: effect of automatic bone and plaque removal on image quality and grading of stenoses. Eur J Radiol 68(3):414–422

Ofer A, Nitecki SS, Linn S, Epelman M, Fischer D, Karram T et al (2003) Multidetector CT angiography of peripheral vascular disease: a prospective comparison with intraarterial digital subtraction angiography. AJR Am J Roentgenol 180(3):719–724

Ota H, Takase K, Igarashi K, Chiba Y, Haga K, Saito H et al (2004) MDCT compared with digital subtraction angiography for assessment of lower extremity arterial occlusive disease: importance of reviewing cross-sectional images. AJR Am J Roentgenol 182(1):201–209

Portugaller HR, Schoellnast H, Hausegger KA, Tiesenhausen K, Amann W, Berghold A (2004) Multislice spiral CT angiography in peripheral arterial occlusive disease: a valuable tool

in detecting significant arterial lumen narrowing? Eur Radiol 14(9):1681–1687

Primak AN, Ramirez Giraldo JC, Liu X, Yu L, McCollough CH (2009) Improved dual-energy material discrimination for dual-source CT by means of additional spectral filtration. Med Phys 36(4):1359–1369

Sommer WH, Johnson TR, Becker CR, Arnoldi E, Kramer H, Reiser MF et al (2009) The value of dual-energy bone removal in maximum intensity projections of lower extremity computed tomography angiography. Invest Radiol 44(5): 285–292

Tengg-Kobligk H, Weber TF, Rengier F, Bockler D, Schumacher H, Kauczor HU (2007) Image postprocessing of aortic CTA and MRA. Radiologe 47(11):1003–1011

Tran DN, Straka M, Roos JE, Napel S, Fleischmann D (2009) Dual-energy CT discrimination of iodine and calcium: experimental results and implications for lower extremity CT angiography. Acad Radiol 16(2):160–171

Plaque Differentiation

Hatem Alkadhi, Paul Stolzmann, Sebastian Leschka, Philippe Cattin, Gabor Székely, and Stefan Saur

Contents

Abstract

› The development of atherosclerotic plaques occurs slowly over decades. This provides an opportunity for diagnostic imaging to identify patients before clinical events occur. Computed tomography (CT) is an important imaging technique that is rountinely used for the noninvasive imaging of the arteries throughout the body. One of the most recent innovations in CT is the use of two tubes with different energy, which is called dual-energy CT. This technique has the potential to improve the abilities to differentiate various body tissues with CT, and to increase the inherently low contrast of single-energy CT. This chapter reviews the current status and potential future role of dual-energy CT to detect, characterize and differentiate atherosclerotic plaques.

H. Alkadhi (✉)
Institute of Diagnostic Radiology, University Hospital Zurich, Zurich, Switzerland and
Cardiac MR PET CT program, Massachusetts General Hospital and Harvard Medical School, Boston, MA, USA
e-mail: hatem.alkadhi@usz.ch

P. Stolzmann and S. Leschka
Institute of Diagnostic Radiology, University Hospital Zurich, Zurich, Switzerland
e-mail: paul.stolzmann@usz.ch and Sebastian.leschka@kssg.ch

P. Cattin
Computer Vision Laboratory, ETH Zurich, Switzerland and Medical Image Analysis Center, University of Basel, Basel, Switzerland
e-mail: cattin@vision.ee.ethz.ch

G. Székely and S. Saur
Computer Vision Laboratory, ETH Zurich, Switzerland
e-mail: szekely@vision.ee.ethz.ch and stefan.saur@mevis.de

1 Introduction

The clinical need of a reliable detection and characterization of atherosclerotic plaques is based on many factors. One of the most important ones is that the detection of plaques points towards the existence of associated stenoses (Alkadhi et al. 2008). Then, plaques themselves are independent predictors of risk for cardiovascular events. For example in coronary arteries, plaques of certain morphology have prognostic value being independent and incremental to the presence or absence of luminal obstruction caused by the plaque (van Werkhoven et al. 2009). In addition, plaque morphology is an important predictor of postoperative outcome

T.R.C. Johnson et al. (eds.), *Dual Energy CT in Clinical Practice*, Medical Radiology,
DOI: 10.1007/174_2010_38

after intervention or surgery, such as e.g. for carotid end-arterectomy (Das et al. 2009). Thus, with regard to each imaging examination, it appears mandatory to not only identify plaques causing a luminal obstruction, but also to describe and characterize the different plaques that usually follow a specific distribution within the arterial vascular system (Saur et al. 2009).

Computed tomography (CT) examinations are well suited for the detection and characterization of calcifications within vessel walls. This holds particularly true for quantifying the amount of calcium in the wall of coronary arteries, where CT can be used for calcium scoring as a noninvasive tool for risk stratification. While the detection and quantification of calcium can be done with good accuracy with CT, the method still falls short in characterizing the different constituents of mixed or purely noncalcified plaques, particularly in small-sized vessels and plaques. CT may be also limited to clearly distinguish the plaques from the surrounding soft tissue, a fact that is particularly true for fatty plaques in the walls of coronary arteries and the adjacent epicardial fat. One of the main reasons for these shortcomings of CT is the modest contrast resolution of the modality and the relatively small attenuation differences that hinder a proper assessment, differentiation, and characterization of these various structures sharing overlapping attenuation values. Although the measured X-ray attenuation coefficient from CT depends both on the material and its density, it is represented by only one attenuation value. Therefore, different materials might show very similar attenuation with overlapping intensity ranges.

As of now, no intensity thresholds for the reliable and accurate separation of lipid tissue from fibrous tissue or other tissues in CT data were reported. This fact hampers an appropriate manual but also automated assessment of the various plaque constituents (Saur et al. 2008). Certainly, it would be desirable to enhance the contrast between the different tissues involved in a preprocessing step to make the subsequent assessment of lipid constituents better feasible.

In recent years, this poor attenuation difference that is common with single-energy CT has been challenged by the introduction of dual-energy CT technology enabling the sampling of voxel attenuation at two different energy spectra. This bi-energetic, measurement of attenuations shows promise for an improved differentiation of the constituents of plaques.

This chapter will briefly recapitulate the rationale of dual-energy CT for plaque imaging, review the most pertinent literature regarding dual-energy CT for imaging the atherosclerotic plaque, and will outline potential future directions of dual-energy CT for characterizing the various constituents of atherosclerotic plaques.

2 Rationale of Dual-Energy CT

A drawback of single-energy CT is that different materials may show similar attenuation behaviour at single radiation energy levels. This shortcoming can be overcome by measuring the attenuation of the material at two different energy levels.

Dual-energy X-ray acquisitions have been evaluated on basic phantoms since more than three decades (Chiro et al. 1979; Genant and Boyd 1977; Lehmann et al. 1981; Millner et al. 1979; Kalender et al. 1986; Vetter et al. 1986). These studies used conventional single-source CT systems for dual-energy acquisitions by scanning twice in a row with different tube voltages. However, limitations in CT hardware and software technology hampered the expansion of dual-energy CT to further clinical applications (Kelcz et al. 1979). Most importantly, motion artefacts from patient or organ movement as well as respiration hindered a proper registration of the two data sets. Finally, the low photon output at low energy levels limited the applicability of the technique for routine use.

This lasted until 2005 when the first generation dual-source CT system was introduced (Flohr et al. 2006). One of the most important features of this system is that two X-ray sources with an angular offset of 90° are mounted onto the rotating gantry. The two tubes can be operated at a single energy level for doubling the temporal resolution for improved coronary imaging at 83 ms (Scheffel et al. 2006) or 75 ms (Leschka et al. 2009). The two tubes can also be operated at two different energy levels, thus acquiring data in the dual-energy mode in a simultaneous fashion (Flohr et al. 2006).

Since then, other approaches also have been developed by the various vendors enabling the acquisition of dual-energy CT data. These include a single-source ultra-fast kV-switching approach where two consecutive data sets at e.g. 80 and 140 kV are acquired. Another approach is characterized by energy discriminating detectors having an upper scintillator which stops and detects the lower-energy X-rays and a bottom scintillator which stops and detects the higher-energy X-ray photons.

In order to benefit from the different attenuation characteristics at different energy levels, two most opposing energy levels, which are still justified in terms of noise and exposure, are selected for a dual-energy acquisition. For the dual-source CT system, a tube voltage of 140 kV is normally selected for the high energy image whereas for the low energy image, a tube voltage of 80 or 100 kV – depending on the application and body constitution of the patient – is selected. The tube current is then adjusted to corresponding low and high values, respectively.

Through a dual-energy acquisition, two different intensity values can be assigned to a voxel, namely the one measured at the low energy level and the one at the high energy level. Different approaches exist that make benefit of this additional information provided for each voxel as opposed to conventional single-source CT. Most apply directly on the *original intensity space* that is spanned by the intensities of the low and high energy image. Others, in contrast, decompose the low and high energy image into other descriptors like characteristic tissues or into the density and atomic number.

2.1 Original Intensity Space

When remaining in the original intensity space, each voxel is represented by a point in the 2D space spanned by the density values of the low and high energy image. Through this additional dimension, materials can be better differentiated as each tissue has a specific attenuation characteristic at the selected energy levels and thus appears at specific locations within the intensity space. Boll et al. (2006) proposed a subtraction of the high and low energy image for a better characterization of tissues. Johnson et al. (2007) and Stolzmann et al. (2008a) used a 2D threshold – a line in the intensity space – for better differentiation. Besides the separation of tissues through 2D thresholds or clustering approaches, three-material decomposition can be applied in the original intensity space (Johnson et al. 2007). For this, three idealized materials (e.g. soft tissue, bone, and iodine) are defined in the intensity space (Petersilka et al. 2008). Hence, two ideal vectors originating from a common start point (e.g. at soft tissue) and ending at two different points (e.g. one vector from soft tissue to iodine, one vector from soft tissue to bone) can be defined.

Based on these two vectors, a coordinate system can be derived. With this new coordinate system, a given voxel can now be described by the proportions of each of the three idealized materials. Furthermore, a material separation and a subsequent segmentation can be performed for every voxel (Petersilka et al. 2008). The usage of the aforementioned two approaches brought about material analysis capabilities with several clinical applications, such as bone removal (Sommer et al. 2009; Yamamoto et al. 2009; Uotani et al. 2009), iodine content computation (Johnson et al. 2007), virtual non-contrast imaging (Scheffel et al. 2007; Stolzmann et al. 2008b; Graser et al. 2009), differentiation between calcium and iodine (Tran et al. 2009) or between blood, blood mixed with pus, bile, and urine (Mahnken et al. 2009), for lung ventilation assessment (Chae et al. 2008), for classification of kidney stones (Stolzmann et al. 2008a, 2009; Primak et al. 2007), as well as for the evaluation of perfusion defects in the lung (Pansini et al. 2009; Pontana et al. 2008; Thieme et al. 2008) and myocardium (Ruzsics et al. 2009).

2.2 Dual-Energy CT Imaging of Plaques

Boll et al. (2006) assessed ex vivo specimens of atherosclerotic coronary arteries with dual-energy CT and correlated the results with histopathology. Using a 16-slice CT scanner and two consecutive scans at 90 and 140 kV, the authors found that the contrast-to-noise ratios of all tissues could be successfully distinguished with CT. Contrast-to-noise ratios with dual-energy CT were significantly higher for the vessel wall and fibromuscular plaque constituents as compared with single-energy CT. Moreover, the coronary lumen could be better delineated with dual-energy CT.

In another study, Boll et al. (2008) evaluated whether dual-energy CT with a double-decker detector with specific image postprocessing techniques would enhance the accuracy of calcified plaque quantification beyond that of conventional single-energy CT. The authors imaged coronary specimens with atherosclerosis in a moving phantom with 64-slice CT in the dual-energy mode and found a higher accuracy for measuring calcified plaque sizes with dual-energy CT along with reduced tissue blooming and beam hardening as compared to single-energy CT.

Barreto et al. (2008) aimed at a noninvasive characterization of coronary atherosclerotic plaques with dual-energy dual-source CT (scanning the specimens consecutively at 80 and 140 kV) and compared the plaque characteristics from CT with that from

histopathology. The authors found that calcified lesions attenuated significantly more at 80 kV in both contrast- and noncontrast- enhanced scans, whereas fibrous plaques attenuated more at 80 kV only in contrast-enhanced scans. No differences could be found for lipid-rich plaques, and using dual-energy index calculations, only densely calcified plaques could be distinguished from other plaque types except of fibrocalcific plaques in contrast-enhanced images.

Our own ex vivo research with dual-energy dual-source 64-slice CT for coronary atherosclerotic plaque differentiation indicates an improved differentiation of noncalcified plaques from contrast in the arterial lumen at 80 kV, and a better differentiation of calcification from contrast within the vessel lumen at a single-energy of 120 kV (Fig. 1). Moreover, we found that – in the presence of an overlap of CT attenuation values of predominantly fibrous and lipid plaques at a single-energy of 120 kV – dual-energy CT provides an improved differentiation of these plaques.

3 Potential Future Directions for Dual-Energy CT Plaque Imaging

With dual-energy CT, it is usual to fuse the low- and high-energy image into a blended data set. This so-called *weighted average image* is reconstructed by mixing linearly the 80 kV and the 140 kV image.

Behrendt et al. (2009) further evaluated this approach by varying the weighting factor. For evaluation, they measured the signal-to-noise ratio as well as the intensity changes for different weighting factors and concluded best results with a weighting factor of 0.5 for the enhancement of the ascending aorta and paraaortal fat.

Holmes et al. (2008) developed and evaluated several nonlinear blending functions including a binary blending function, a slope blending function, a gaussian function, and a modified sigmoid function. The authors found that nonlinear blending of dual-energy CT data can provide an improvement in the contrast-to-noise

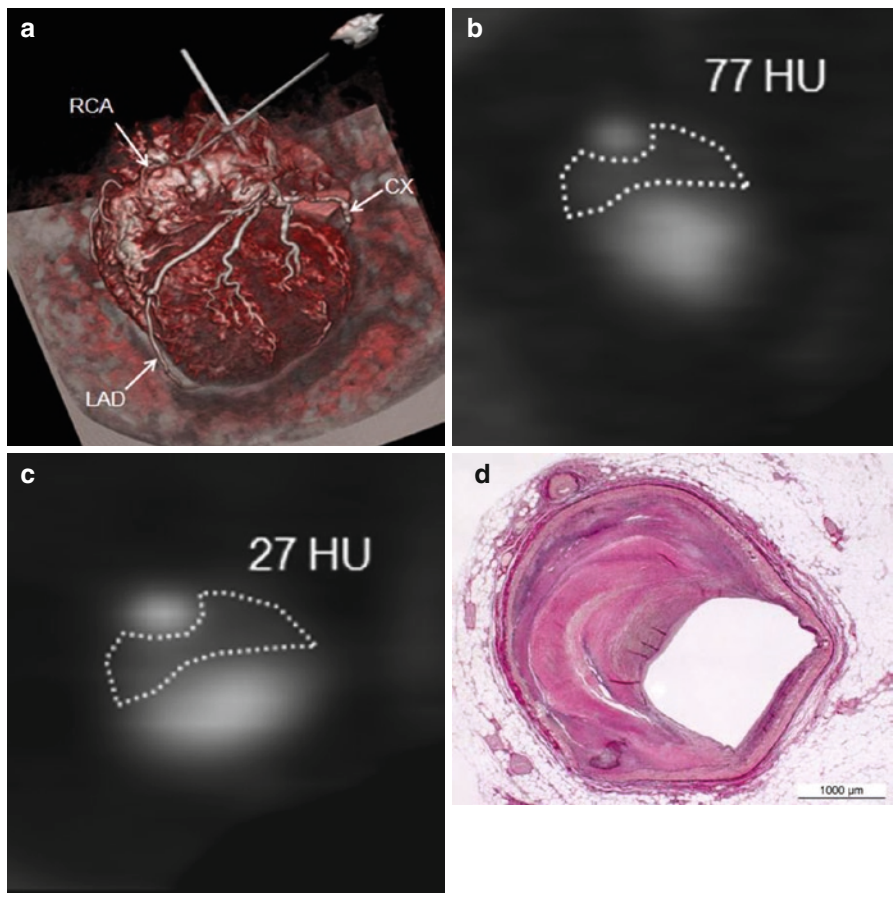

Fig. 1 Volume rendered CT image of a heart specimen (**a**). The right coronary artery (RCA), the left anterior descending artery (LAD), and the circumflex artery (CX) are filled with a mixture of iodinated contrast media and saline solution. Cross-sectional images of one coronary plaque at 80 kVp (**b**) and 140 kVp (**c**) demonstrate a large difference in CT numbers of the noncalcified component between both energies. Plaque was classified as Stary type VIII based on histology stained with hematoxylin and eosin (**d**)

ratio over linear blending and is accompanied by a visual preference for nonlinear blended images.

Lehmann et al. (1981) used a nonlinear transformation on the high and low energy images to generate energy-independent images which are based on two selected basis materials. Thereafter, characteristic linear combinations of these two basis images are used to create a single so-called *cancellation* image. Depending on a single parameter ϕ, this algorithm cancelled the contrast between two materials to enhance a third one, or it improved the contrast between materials – both demonstrated on experimental settings with a stationary X-ray source. We followed this approach and investigated its suitability to improve the assessment of atherosclerosis on clinical dual-energy CT data sets.

The concept of tissue cancellation allows a broad range of applications while being able to cancel or to improve the contrast between tissues. We have applied and tested this method on clinically acquired dual-energy CT data sets to evaluate its ability to improve the assessment of atherosclerosis by improving the tissue contrast (Saur et al. 2009; Saur 2009).

Figure 2 exemplarily depicts a CT slice showing a mixed plaque in the abdominal aorta at 80 and 140 kV, and using the weighted average and cancellation image.

When comparing the contrast improvement for all possible tissue pair combinations among adipose, calcium, lumen, and soft tissue, the cancellation image shows – with a single optimized ϕ – a mean contrast improvement of 25% (±25%) when compared to the 140 kV image. When taking the weighted average image as reference, the mean contrast improvement in the cancellation image is still 7% (±5%) with no significant differences in the signal to noise ratios of the tissues in both images. Figure 3 shows the contrast improvement factor (CIF) – defined as the contrast ratio between cancellation and reference image (Saur et al. 2009) – for various tissue pair combinations with the weighted average image and 140 kV image as reference images.

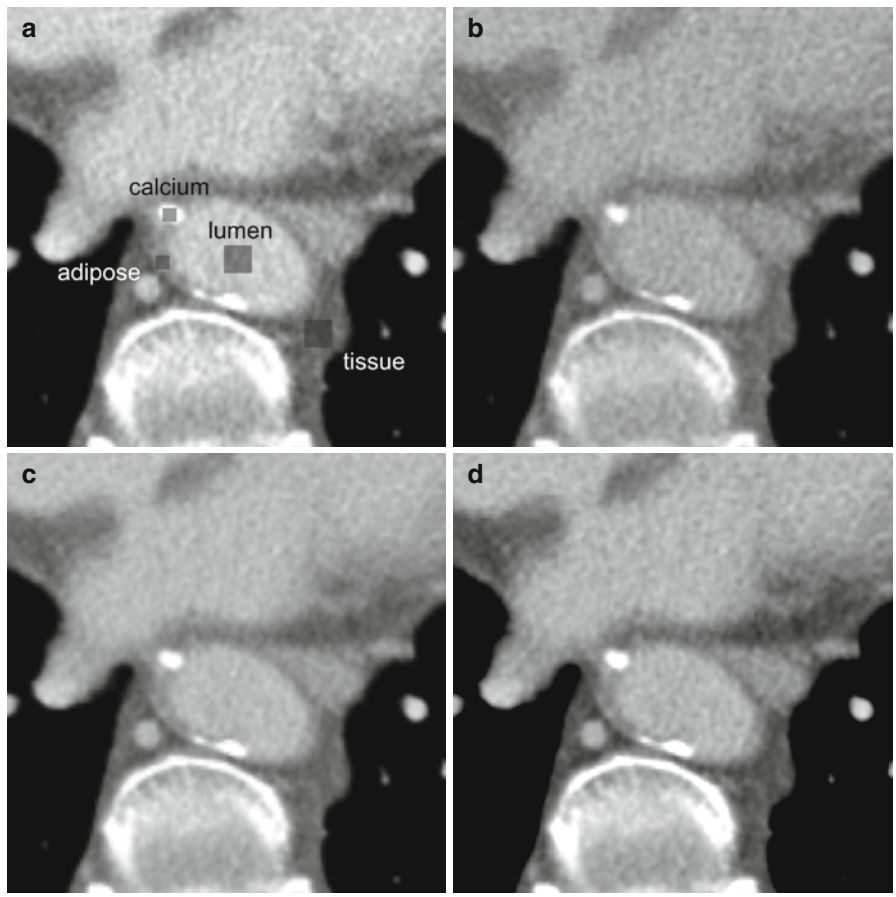

Fig. 2 CT image showing the contrast between selected tissues (adipose, calcium, lumen, soft tissue) in the 80 kV (**a**), 140 kV (**b**), weighted average (**c**) and cancellation (**d**) image, respectively. The cancellation image (**d**) provided the highest contrast between the various plaque components

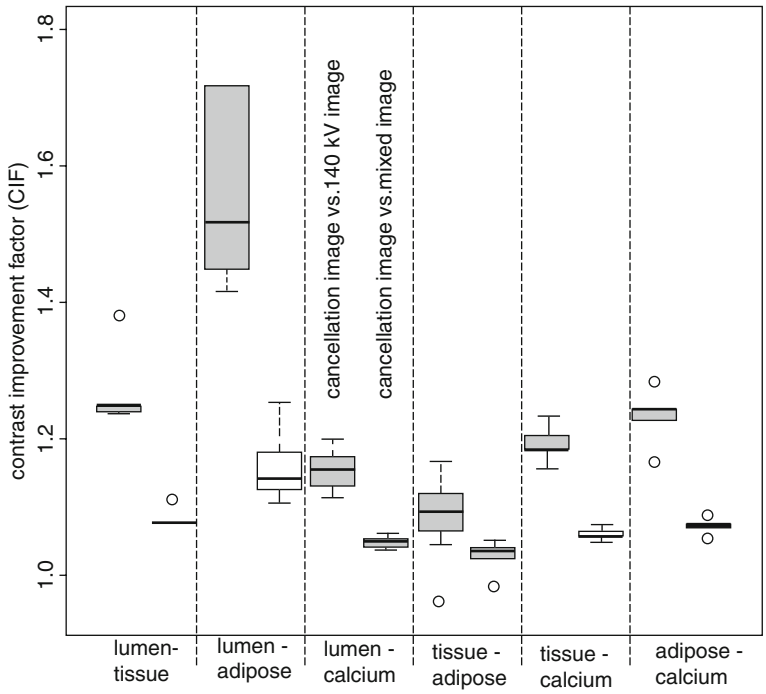

Fig. 3 Box and whisker plots showing the contrast improvement factor for various tissue combinations between the tissue cancellation and the 140 kV image (*grey*) as well as between the tissue cancellation and the weighted average image (*white*)

4 Conclusion

Improving the capabilities of atherosclerotic plaque imaging will be one of the main challenges for cardiovascular imaging in the next decade. Dual-energy CT, which has been reintroduced into clinical practice in 2005 through the introduction of dual-source CT (Flohr et al. 2006), has brought upon a considerable number of clinical applications making use of the improved differentiation of tissue at dual-energy CT. Preliminary ex vivo studies extend these applications to dual-energy imaging of atherosclerotic plaques. Nevertheless, dual-energy CT of plaques still is in its early beginning, and huge efforts with both ex vivo and in vivo studies are necessary before dual-energy CT for plaque imaging can be translated into daily radiological practice.

References

Alkadhi H, Scheffel H, Desbiolles L et al (2008) Dual-source computed tomography coronary angiography: influence of obesity, calcium load, and heart rate on diagnostic accuracy. Eur Heart J 29:766–776

Barreto M, Schoenhagen P, Nair A et al (2008) Potential of dual-energy computed tomography to characterize atherosclerotic plaque: ex vivo assessment of human coronary arteries in comparison to histology. J Cardiovasc Comput Tomogr 2:234–242

Behrendt FF, Schmidt B, Plumhans C et al (2009) Image fusion in dual energy computed tomography: effect on contrast enhancement, signal-to-noise ratio and image quality in computed tomography angiography. Invest Radiol 44:1–6

Boll DT, Hoffmann MH, Huber N, Bossert AS, Aschoff AJ, Fleiter TR (2006) Spectral coronary multidetector computed tomography angiography: dual benefit by facilitating plaque characterization and enhancing lumen depiction. J Comput Assist Tomogr 30:804–811

Boll DT, Merkle EM, Paulson EK, Mirza RA, Fleiter TR (2008) Calcified vascular plaque specimens: assessment with cardiac dual-energy multidetector CT in anthropomorphically moving heart phantom. Radiology 249:119–126

Chae EJ, Seo JB, Goo HW et al (2008) Xenon ventilation CT with a dual-energy technique of dual-source CT: initial experience. Radiology 248:615–624

Chiro GD, Brooks RA, Kessler RM et al (1979) Tissue signatures with dual-energy computed tomography. Radiology 131:521–523

Das M, Braunschweig T, Muhlenbruch G et al (2009) Carotid plaque analysis: comparison of dual-source computed tomography (CT) findings and histopathological correlation. Eur J Vasc Endovasc Surg 38:14–19

Flohr TG, McCollough CH, Bruder H et al (2006) First performance evaluation of a dual-source CT (DSCT) system. Eur Radiol 16:256–268

Genant HK, Boyd D (1977) Quantitative bone mineral analysis using dual energy computed tomography. Invest Radiol 12: 545–551

Graser A, Johnson TR, Hecht EM et al (2009) Dual-energy CT in patients suspected of having renal masses: can virtual

nonenhanced images replace true nonenhanced images? Radiology 252:433–440
Holmes DR III, Fletcher JG, Apel A et al (2008) Evaluation of non-linear blending in dual-energy computed tomography. Eur J Radiol 68:409–413
Johnson TR, Krauss B, Sedlmair M et al (2007) Material differentiation by dual energy CT: initial experience. Eur Radiol 17:1510–1517
Kalender WA, Perman WH, Vetter JR, Klotz E (1986) Evaluation of a prototype dual-energy computed tomographic apparatus. I. Phantom studies. Med Phys 13:334–339
Kelcz F, Joseph PM, Hilal SK (1979) Noise considerations in dual energy CT scanning. Med Phys 6:418–425
Lehmann LA, Alvarez RE, Macovski A et al (1981) Generalized image combinations in dual KVP digital radiography. Med Phys 8:659–667
Leschka S, Stolzmann P, Desbiolles L et al (2009) Diagnostic accuracy of high-pitch dual-source CT for the assessment of coronary stenoses: first experience. Eur Radiol 19:2896–2903
Mahnken AH, Stanzel S, Heismann B (2009) Spectral rhoZ-projection method for characterization of body fluids in computed tomography: ex vivo experiments. Acad Radiol 16:763–769
Millner MR, McDavid WD, Waggener RG, Dennis MJ, Payne WH, Sank VJ (1979) Extraction of information from CT scans at different energies. Med Phys 6:70–71
Pansini V, Remy-Jardin M, Faivre JB et al (2009) Assessment of lobar perfusion in smokers according to the presence and severity of emphysema: preliminary experience with dual-energy CT angiography. Eur Radiol 19: 2834–2843
Petersilka M, Bruder H, Krauss B, Stierstorfer K, Flohr TG (2008) Technical principles of dual source CT. Eur J Radiol 68:362–368
Pontana F, Faivre JB, Remy-Jardin M et al (2008) Lung perfusion with dual-energy multidetector-row CT (MDCT): feasibility for the evaluation of acute pulmonary embolism in 117 consecutive patients. Acad Radiol 15:1494–1504
Primak AN, Fletcher JG, Vrtiska TJ et al (2007) Noninvasive differentiation of uric acid versus non-uric acid kidney stones using dual-energy CT. Acad Radiol 14:1441–1447
Ruzsics B, Schwarz F, Schoepf UJ et al (2009) Comparison of dual-energy computed tomography of the heart with single photon emission computed tomography for assessment of coronary artery stenosis and of the myocardial blood supply. Am J Cardiol 104:318–326
Saur SC (2009) Quantitative assessment of atherosclerosis in coronary arteries. In: Van Gool L, Székely G, Gross M, Schiele B (ed) Selected readings in vision and graphics, pp 1–150, Hartung-Gorre
Saur SC, Alkadhi H, Regazzoni L, Eugster S, Székely G, Cattin PC (2009) Contrast enhancement with dual energy CT for the assessment of atherosclerosis. Bildverarbeitung in der Medizin 13:1–5
Saur SC, Alkadhi H, Desbiolles L, Szekely G, Cattin PC (2008) Automatic detection of calcified coronary plaques in computed tomography data sets. Med Image Comput Comput Assist Interv 11:170–177
Saur SC, Cattin PC, Desbiolles L, Fuchs TJ, Szekely G, Alkadhi H (2009b) Prediction rules for the detection of coronary artery plaques: evidence from cardiac CT. Invest Radiol 44:483–490
Scheffel H, Alkadhi H, Plass A et al (2006) Accuracy of dual-source CT coronary angiography: first experience in a high pre-test probability population without heart rate control. Eur Radiol 16:2739–2747
Scheffel H, Stolzmann P, Frauenfelder T et al (2007) Dual-energy contrast-enhanced computed tomography for the detection of urinary stone disease. Invest Radiol 42:823–829
Sommer WH, Johnson TR, Becker CR et al (2009) The value of dual-energy bone removal in maximum intensity projections of lower extremity computed tomography angiography. Invest Radiol 44:285–292
Stolzmann P, Scheffel H, Rentsch K et al (2008a) Dual-energy computed tomography for the differentiation of uric acid stones: ex vivo performance evaluation. Urol Res 36: 133–138
Stolzmann P, Frauenfelder T, Pfammatter T et al (2008b) Endoleaks after endovascular abdominal aortic aneurysm repair: detection with dual-energy dual-source CT. Radiology 249:682–691
Stolzmann P, Kozomara M, Chuck N et al (2009) In vivo identification of uric acid stones with dual-energy CT: diagnostic performance evaluation in patients. Abdom Imaging
Thieme SF, Becker CR, Hacker M, Nikolaou K, Reiser MF, Johnson TR (2008) Dual energy CT for the assessment of lung perfusion–correlation to scintigraphy. Eur J Radiol 68:369–374
Tran DN, Straka M, Roos JE, Napel S, Fleischmann D (2009) Dual-energy CT discrimination of iodine and calcium: experimental results and implications for lower extremity CT angiography. Acad Radiol 16:160–171
Uotani K, Watanabe Y, Higashi M et al (2009) Dual-energy CT head bone and hard plaque removal for quantification of calcified carotid stenosis: utility and comparison with digital subtraction angiography. Eur Radiol 19:2060–2065
van Werkhoven JM, Schuijf JD, Gaemperli O et al (2009) Prognostic value of multislice computed tomography and gated single-photon emission computed tomography in patients with suspected coronary artery disease. J Am Coll Cardiol 53:623–632
Vetter JR, Perman WH, Kalender WA, Mazess RB, Holden JE (1986) Evaluation of a prototype dual-energy computed tomographic apparatus. II. Determination of vertebral bone mineral content. Med Phys 13:340–343
Yamamoto S, McWilliams J, Arellano C et al (2009) Dual-energy CT angiography of pelvic and lower extremity arteries: dual-energy bone subtraction versus manual bone subtraction. Clin Radiol 64:1088–1096

Part III

Thoracic Imaging

Lung Perfusion

Radko Krissak and Christian Fink

Contents

Abstract

› Pulmonary perfusion imaging is conventionally performed by lung scintigraphy using technetium-labeled albumin spheres that are temporarily trapped in the pulmonary capillaries and thus visualize pulmonary perfusion. Although per definition lung perfusion is a dynamic process of pulmonary blood flow over time, imaging of the pulmonary capillary bed or blood volume is an accepted surrogate for lung perfusion. By visualizing the contrast agent distribution in the lung parenchyma, spiral dual energy CT angiography (CTA) provides the opportunity to assess pulmonary vessels and pulmonary perfusion within one fast examination. There is already substantial evidence that pulmonary CTA and dual energy CT (DECT) lung perfusion visualization have complimentary roles in the diagnosis of pulmonary embolism. A simultaneous detection of a clot in a pulmonary artery in the pulmonary CTA and of a perfusion defect in DECT lung perfusion in the corresponding lung segment indicate an occlusive PE. Future studies have to investigate if DECT of lung perfusion might also play a role in the assessment of lung diseases such as emphysema, cystic fibrosis or interstitial lung disease. Dedicated scan and contrast material injection protocols for DECT of lung perfusion as well as post-processing techniques are provided in this chapter. Possible pitfalls in data interpretation are discussed.

R. Krissak (✉) and C. Fink
Department of Clinical Radiology and Nuclear Medicine,
University Medical Center Mannheim,
Medical Faculty Mannheim of the University of Heidelberg,
Theodor-Kutzer-Ufer 1-3, 68167 Mannheim, Germany
e-mail: radko.krissak@umm.de

T.R.C. Johnson et al. (eds.), *Dual Energy CT in Clinical Practice*, Medical Radiology,
DOI: 10.1007/174_2010_40

1 Clinical Background

Pulmonary embolism (PE) is a very common disease associated with a significant morbidity and potential mortality. The clinical diagnosis of PE is difficult and challenging because common symptoms, such as dyspnea, tachycardia, acute chest pain, and syncope, are unspecific, or may not be present in all patients. Therefore, imaging plays a key role to establish the diagnosis of PE (Goldhaber 2004; Remy-Jardin et al. 2007). The high spatial resolution of CTA ideally allows visualization of the pulmonary arteries down to the sixth-order branches (Schoepf and Costello 2004; Ghaye et al. 2001). As a consequence, multidetector CTA has emerged as the diagnostic standard for the assessment of patients with suspected PE in the past years and has replaced perfusion scintigraphy in most institutions (Remy-Jardin et al. 2007). Although CTA allows the visualization of small peripheral PE in the majority of cases, the relevance of these findings remains somewhat unclear, especially if accidentally found in asymptomatic patients. Moreover, the condition of many patients with large emboli is surprisingly good, especially if the emboli are nonocclusive. Thus, additional functional information, such as lung perfusion imaging, might be clinically useful for patient management, even though the diagnosis of PE has already been made with CTA. So far, pulmonary perfusion imaging is performed by lung scintigraphy using technetium-labeled albumin spheres that are temporarily trapped in the pulmonary capillaries and thus visualize pulmonary perfusion. The major limitations of pulmonary perfusion scintigraphy are the restricted availability especially outside normal working hours, the long acquisition time in emergency situations, and the poor spatial resolution. By visualizing the contrast agent distribution in the lung parenchyma, spiral dual-energy CTA provides the opportunity to assess pulmonary perfusion simultaneously, and thus to assess all the relevant information within one fast (emergency) examination.

2 Physical Background

In the past, various techniques have been evaluated for the assessment of lung perfusion in patients with suspected PE using CT. Dynamic multisection electron beam CT has been evaluated for the evaluation of pulmonary perfusion (Schoepf et al. 2000). Another attempt was to generate perfusion-weighted maps by color-coding the density of lung parenchyma in contrast-enhanced CTA (Wildberger et al. 2001). A subtraction technique of whole-thorax multidetector CT scans acquired before and after intravenous contrast within a single breathhold was also proposed (Wildberger et al. 2005). In all these approaches, color-coded parametric maps of lung perfusion were calculated to visualize PE-related perfusion defects. The evaluation of lung perfusion was limited by the fact that either an additional unenhanced scan had to be performed to assess the iodine distribution in the lung, or only that only maps of density distribution (and not iodine distribution) were available if the unenhanced scan was omitted. The first procedure might be limited by misregistration artifacts if breathhold levels of the unenhanced and contrast-enhanced scan do not match. The latter technique may be limited if the density of lung tissue is elevated by other reasons, such as ground-glass opacities (e.g., in pulmonary edema or pneumonia).

Because iodine compared to other materials, e.g., to soft tissue, shows a proportionally larger increase of CT values with decreasing X-ray tube voltage, dual-energy CT can be used to visualize the distribution of iodinated contrast material in different organs. The selective iodine imaging using dual-energy CT was already proposed by Hounsfield (1973) and further investigated in the late 1970s (Riederer and Mistretta 1977; Zatz 1976). Technical limitations of the CT scanners at that time prevented the development of routine clinical applications. The biggest constraint was that the dose in the low-voltage data was much lower than in the high-voltage data, since the tube voltage was switched without adapting the tube current. Therefore, the noise level in the low-voltage data was significantly higher (Seidensticker and Hofmann 2008). The radiation dose of the patients was not acceptable if the scan was performed at energies around the iodine K edge (33 keV), which would allow good iodine separation at contiguous tube voltages and thus similar noise levels.

Recent generations of high-end MDCTs are able to acquire dual-energy data by applying two X-ray tubes and two corresponding detectors at different kV and mA settings simultaneously in a dual-source CT (Siemens), by ultra-fast kV switching in a single-source CT (GE) or by compartmentalization of detected X-ray photons into energy bins by the detectors of a

single-source CT operating at constant kV and mA settings (Philips). All these approaches eliminate registration problems and allow selective visualization of iodine distribution with high spatial resolution.

Although per definition lung perfusion is a dynamic process of pulmonary blood flow over time, imaging of the pulmonary capillary bed or blood volume is an accepted surrogate for lung perfusion. During the first pass of an intravenously injected contrast agent bolus, the distribution of the contrast agent can be considered as a good estimate of the local perfusion. Thus by visualizing the iodine distribution in the capillary bed of lung parenchyma, dual-energy CTA can be utilized for lung perfusion imaging in patients with suspected PE.

3 Scan Protocol

The scan protocols recommended for dual-energy lung perfusion scans by Siemens are presented in Table 1. Currently there are no published protocols for CT systems of other vendors.

The protocol aims to display both the pulmonary arteries and the pulmonary perfusion from a single scan. The scan direction should be caudocranial to avoid streak artifacts due to highly concentrated contrast material in the subclavian vein or superior vena cava. Furthermore, a large saline flush should be used to wash out the contrast material in the superior vena cava by the time this region is scanned. The provided 14 × 1.2 mm collimation on the Siemens Definition and the slice width of 2 mm on both dual-source scanners are recommended for dual-energy scans and reconstructions to provide an improved signal to noise ratio and has less scatter radiation artifacts for dual-energy postprocessing.

Positioning of the patient in the center of the scanner is required using dual-source systems to ensure that the entire pulmonary parenchyma is covered by the smaller field-of-view of the second tube detector array (26 cm Siemens Definition, 33 cm Siemens Definition Flash). In patients with a large body habitus, peripheral lung may be not covered by the smaller system and, as a result, dual-energy data manipulation can only be performed inside the area covered by both tubes.

Table 1 Scan protocols recommended for a dual-energy lung perfusion scan on the currently available dual-source systems (Siemens)

	Siemens Definition	Siemens Definition Flash
Scan mode	Spiral dual energy	Spiral dual energy
Scan area	Diaphragm to lung apex	Diaphragm to lung apex
Scan direction	Caudocranial	Caudocranial
Scan time (s) (for 300 mm length)	11	9
Tube voltage A/B (kV)	140/80	100/140Sn (tin filter)
Tube current A/B (quality ref. mAs)	47/235	89/76
Dose modulation	CARE dose4D on	CARE dose4D on
$CTDI_{Vol}$ (mGy)	9.2	7.3
Rotation time (s)	0.33	0.28
Pitch	0.55	0.55
Slice collimation (mm)	1.2	0.6
Acquisition	14 × 1.2 mm	64 × 0.6 mm
DE composition factor	0.3	0.6
Slice width (mm)	2	2
Reconstruction increment (mm)	1.4	1.4
Reconstruction kernel	D30f	D 30f

4 Contrast Material Injection

High-concentration iodine-based contrast material is recommended for DECT scan to improve the differentiation of iodine by the dual-energy postprocessing algorithm. As already mentioned in the scan protocol section, thoracic DECT scans should be acquired in the caudocranial direction so that the chaser bolus was being injected by the time the scan reached the upper chest to avoid streak artifacts due to highly concentrated contrast material in the subclavian vein or superior vena cava which may mimic perfusion defects. Pulmonary arteries and lung parenchyma are both evaluable in an optimal scan. The scan delay should be a little longer (e.g., 7 s) to allow the contrast material to pass into the lung parenchyma. Bolus tracking should be used for timing with the trigger region of interest placed in the pulmonary artery. We found no significant difference in pulmonary artery contrast between test bolus and automatic bolus tracking in a study performed in our department, and we recommend automatic bolus tracking because it is operator friendly and independent. The patient should be instructed to hold his breath at mild inspiration to avoid excessive influx of nonenhanced blood from the inferior vena cava (Table 2).

5 Postprocessing

The only currently commercially available software ("syngo DE Lung PBV" by Siemens HealthCare) for DECT lung perfusion image analysis is part of the dual-energy postprocessing software package available for the Siemens syngo MultiModality Workplace. For the calculation of iodine distribution in the lung parenchyma, a modified version of the so-called three-material decomposition is used. First, the base materials have to be defined, which are air and soft tissue, and be entered into a 80–140 kV diagram. Then to consider and later on being able to calculate iodine distribution in the parenchyma, iodine is added as a third material. To calculate the amount of iodine distribution in a certain area, the 80–140 kV values of the region of interest is entered into the diagram and then projected down on the line between air and soft tissue. The length of the vector represents the iodine distribution. Only voxels containing lung parenchyma are considered for the decomposition by using thresholds to minimize the calculation efforts and to optimize viewing. The lung parenchyma is color coded using gray scale 16-bit or hot metal 16-bit color coding (default setting) with different optional color scales available. The computation

Table 2 Injection protocols recommended for a dual-energy lung perfusion scan

	Iodine concentration 370 mg I/mL	Iodine concentration 400 mg I/mL
Injection scheme	Monophasic	Monophasic
Iodine delivery rate	1.48 g/s	1.6 g/s
CM volume	90 mL	80 mL
CM flow rate	4 mL/s	4 mL/s
Body weight adaptation	1.29 mL/kg	1.14 mL/kg
Bolus timing	Bolus tracking	Bolus tracking
Bolus tracking threshold	100 HU	100 HU
ROI position	Pulmonary trunk	Pulmonary trunk
Scan delay	7 s	7 s
Saline flush volume	60 mL	60 mL
Saline injection rate	4 mL/s	4 mL/s
Needle size	18 G	18 G
Injection site	Antecubital vein	Antecubital vein

Tested on dual-source systems (Siemens) for two high-concentration iodine-based contrast materials

time of the perfusion maps by the software is negligible. The software enables a multiplanar view of the color-coded dataset. The software also enables to set a mixing ratio between a non color-coded "virtual 120 kV dataset" as reference and the segmented and color-coded lung parenchyma. This mixing ratio can be fluently set between 0% showing a "normal CT image" and 100% where only the color-coded segmented lung parenchyma is displayed. Windowing functionality for the original and color-coded dataset, basic measurement tools, and a few dual-energy-specific measurements are also available.

6 Diagnostic Evaluation

The main clinical application for DECT lung perfusion image analysis is the detection of PE.

Normal color-coded images show symmetric and homogenous lung iodine distribution, indicating physiologic and equally distributed perfusion. Depending on the used color coding, the color coding should be homogenous without any localized changes, otherwise a regional perfusion defect, e.g., an acute central PE or a chronic recurrent PE, has to be considered. Due to the supine position of the patient during the scan, there is a physiological redistribution of the lung perfusion with relatively lower perfusion in the ventral regions and relatively higher perfusion in the dorsal regions. This redistribution shows a smooth transition in the color-coded images, is symmetrical, and should not be mistaken for a bilateral ventral perfusion defect.

Local perfusion defects are considered to be consistent with PE especially if they are peripherally located, triangular-shaped, and in a segmental distribution (Figs. 1c and d).

Sources of false-positive results should be kept in mind to avoid misdiagnoses. Streak and beam hardening artifact resulting from high-concentration contrast agent in the thoracic veins and right cardiac chambers can commonly cause heterogeneous artifacts and must be considered when an unexpected perfusion anomaly is noted adjacent to an area of high contrast enhancement (Figs. 2).

7 Scientific Evidence

Several approaches to assess the pulmonary perfusion in CT were made in the past decade. Dynamic multisection electron beam CT was performed by Schopf et al. (2000) to assess the pulmonary blood flow. This was possible only in a scanning volume of 7.6 cm, required a long patient breathhold, and was connected with a high additional radiation dose. The evaluation of perfusion-weighted color display of the density of lung parenchyma in contrast-enhanced (single energy) CTA in patients with suspected PE performed by Wildberger et al. (2001) could provide additional information about the perfusion of the lung, especially in patients without other findings influencing the lung density. To selectively visualize iodine content of the lungs (and thus the lung perfusion) a subtraction technique of whole-thorax multidetector CT scans acquired before and after intravenous contrast within a single breathhold was introduced by Wildberger et al. (2005) in a further animal study, which was limited by a longer breathhold time and additional radiation dose.

Shortly after the introduction of the first dual-source system, Johnson et al. (2007) could initially demonstrate sufficient differentiation and depiction of contrast material distribution in dual-energy scans with this device. First clinical applications including DECT lung perfusion imaging were also proposed. In a first feasibility study on lung perfusion, Fink et al. (2008) reported the sensitivity and specificity of DECT for the assessment of PE was 100% on a per patient basis, whereas, on a per segment basis the sensitivity and specificity ranged between 60–66.7% and 99.5–99.8% with pulmonary CTA as standard of reference in 24 patients with suspected PE, in whom four patients actually had PE. In a subsequent comparative study, Thieme et al. (2008) examined a small group of patients with DECT and ventilation/perfusion scintigraphy showing a good agreement between both modalities. The same research group presented the diagnostic results of pulmonary perfusion DECT in 93 patients a year later, attesting this method with a high reliability in the detection of defects in pulmonary parenchymal iodine distribution that correspond to embolic vessel occlusion (Thieme et al. 2009). A group of 117

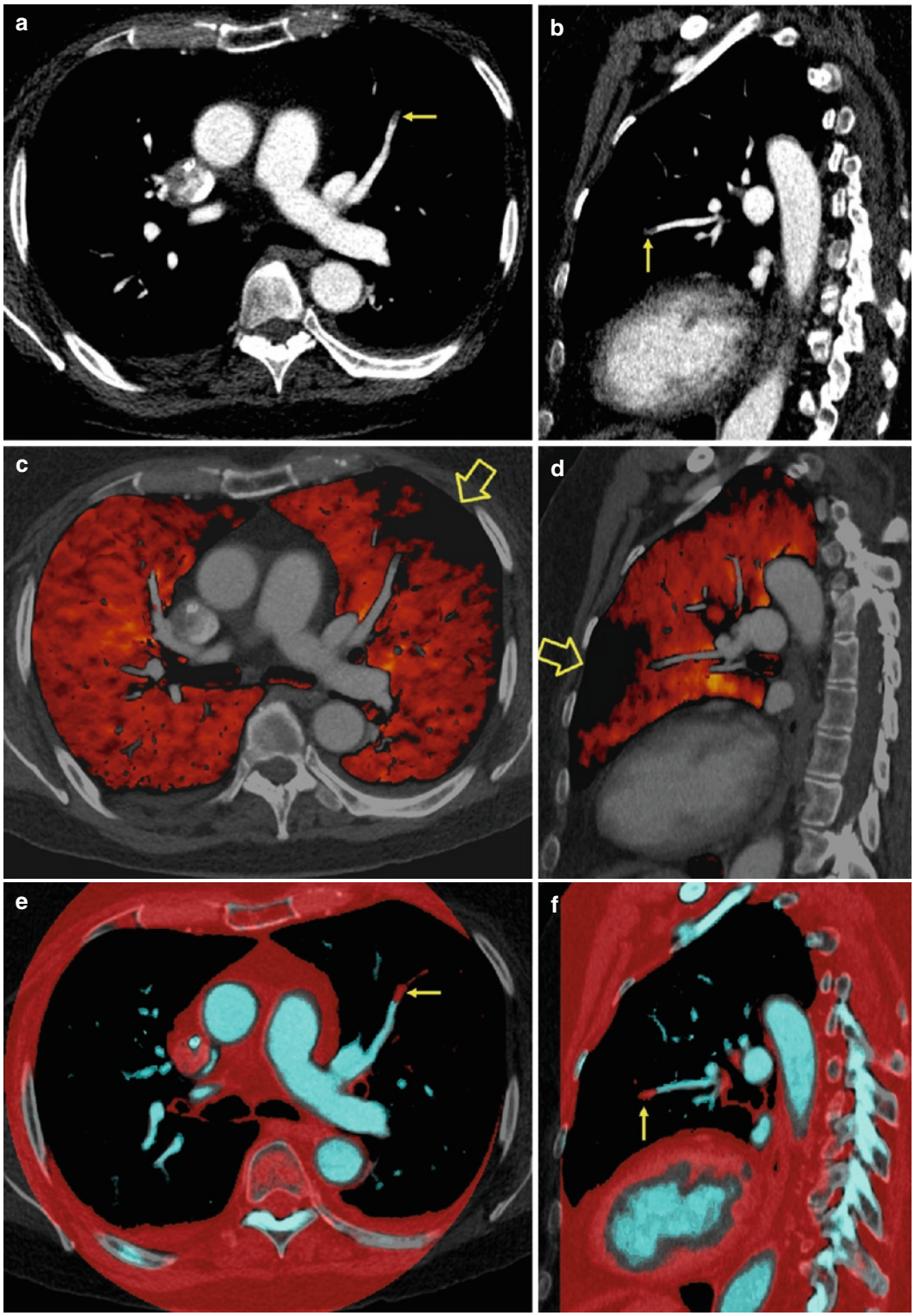

Fig. 1 Dual-energy CTA of a 65-year-old female patient with PE. Virtual 120 kV oblique axial (**a**) and sagittal (**b**) reconstructions showing a segmental embolus in the lingula segment of the left lung (*arrows*). A corresponding wedge-shaped perfusion defect is clearly visualized (*open arrows*) in the oblique axial (**c**) and sagittal (**d**) reconstructions by color coding the contrast agent distribution in the lung parenchyma. By color coding the iodine content in lung vessels, the embolus can be directly identified and visualized – *arrows* in (**e**) and (**f**)

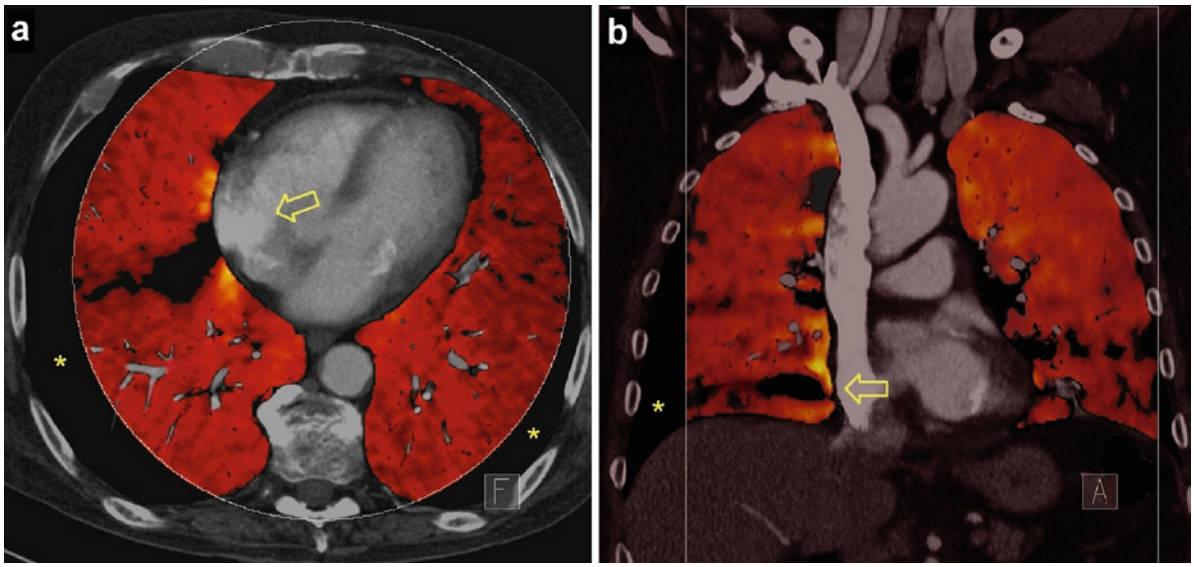

Fig. 2 Dual-energy CTA of a 54-year-old female without PE. Highly concentrated contrast media in the right atrium mimics a perfusion defect in the axial image (**a**). On the coronal reconstruction (**b**), however, the apparent perfusion defect is clearly identified as a horizontally orientated band-like artifact that runs through the right lung (*open arrow*). Due to the limited size of the B-detector system, lung perfusion of the subpleural lung cannot be completely assessed in this patient (*asterisk*)

patients was examined by Pontana et al. (2008) to investigate the accuracy of dual-energy computed tomography in the depiction of perfusion defects in patients with acute PE, concluding that simultaneous information on the presence of endoluminal thrombus and lung perfusion impairment can be obtained with DECT. In an experimental animal (rabbit) study by Zhang et al. (2009a), conventional pulmonary CTA identified pulmonary emboli in only 12 lobes and absence of emboli in 18 pulmonary lobes, corresponding to a sensitivity and specificity of 67% and 100%, respectively. In contrast, DECT with lung perfusion images correctly identified pulmonary emboli in 16 of 18 pulmonary lobes, and the absence of emboli in 11 of 12 lobes, corresponding to sensitivity and specificity of 89% and 92%, respectively, for detecting pulmonary emboli. Zhang et al. (2009b) also compared the ability of DECT and perfusion scintigraphy to detect PE with a pathological standard of reference in a rabbit model. The diagnostic accuracy of detecting PE was higher in DECT lung perfusion (sensitivity and specificity of 100% and 98%) than perfusion scintigraphy (sensitivity and specificity of 68% and 81%) in this study. The extent of perfusion defects in DECT was correlated to the right ventricular/left ventricular ratio and to the CTA obstruction score by Chae et al. (2010), revealing a good correlation between these parameters. Therefore, lung perfusion DECT images may be helpful not only for diagnosis but also for assessing the severity of PE.

Besides the analysis of iodine distribution on a parenchymal level, DECT might also be used for an improved visualization of pulmonary vascular iodine distribution. This might be useful to resolve the ambiguity of low HU-values, which are either caused by intravascular embolus, low contrast enhancement, or by partial volume effects with surrounding air in higher-order vessels. Additional review of the DE-CTA with a dedicated software algorithm color-coding lung vessels with high iodine content blue and soft tissue or vessels with low or no iodine content due to PE red was performed in a study by our group (Krissak et al. 2010). This color-coding algorithm has a high negative predictive value of 94.1% on a segmental base, which is important for reliable exclusion of segmental PE. An additional review of the DE-CTA by this algorithm enables a higher diagnostic security particularly for less experienced readers in an emergency situation (Figs. 1e and f).

Furthermore, DECT lung perfusion images and visualization of vascular iodine distribution may assist in detecting small pulmonary emboli that are not evident at conventional MDCT pulmonary angiography. Thieme et al. (2008) found that corresponding perfusion defects were observed in DECT and scintigraphy in two patients

in whom there was no visible intravascular clots in pulmonary CTA images. They suggested that the observed pulmonary perfusion defects probably corresponded to segments of prior embolism with reperfused segmental vessels and residual peripheral thrombosed vessels that were too small to visualize in pulmonary CTA. This phenomenon was also suggested in the study by Pontana et al. (2008), in which four subsegmental perfusion defects were depicted by DECT lung perfusion images without the visualization of endoluminal thrombi within the corresponding arteries.

In a first feasibility study, Ferda et al. (2009) investigated the relations between iodine and air distribution by comparing the iodine distribution maps and minimum intensity projection images. Similarly to perfusion/ventilation scintigraphy, they were able to differentiate between different patterns of iodine and air distribution, depending on the underlying disease (PE, air trapping, emphysema, interstitial edema, inflammation, and interstitial lung diseases).

In summary, there is already substantial evidence that pulmonary CTA and DECT lung perfusion have complimentary roles in the diagnosis of PE and DECT lung perfusion images increase the sensitivity for detection of PE. It can be presumed that a simultaneous detection of a clot in a pulmonary artery in the pulmonary CTA and of a perfusion defect in DECT lung perfusion in the corresponding lung segment indicate an occlusive PE. It remains unclear whether DECT lung perfusion imaging really can identify even tiny pulmonary emboli that are not evident at conventional pulmonary CTA. Future studies have to investigate if DECT of lung perfusion might also play a role in the assessment of lung diseases such as emphysema, cystic fibrosis, or interstitial lung disease.

References

Chae EJ, Seo JB, Jang YM et al (2010) Dual-energy CT for assessment of the severity of acute pulmonary embolism: pulmonary perfusion defect score compared with CT angiographic obstruction score and right ventricular/left ventricular diameter ratio. AJR Am J Roentgenol 194:604–610

Ferda J, Ferdova E, Mirka H et al (2009) Pulmonary imaging using dual-energy CT, a role of the assessment of iodine and air distribution. Eur J Radiol [Epup ahead of print]

Fink C, Johnson TR, Michaely HJ et al (2008) Dual-energy CT angiography of the lung in patients with suspected pulmonary embolism: initial results. Rofo

Ghaye B, Szapiro D, Mastora I et al (2001) Peripheral pulmonary arteries: how far in the lung does multi-detector row spiral CT allow analysis? Radiology 219:629–636

Goldhaber SZ (2004) Pulmonary embolism. Lancet 363: 1295–1305

Hounsfield GN (1973) Computerized transverse axial scanning (tomography). 1. Description of system. Br J Radiol 46: 1016–1022

Johnson TR, Krauss B, Sedlmair M et al (2007) Material differentiation by dual energy CT: initial experience. Eur Radiol 17:1510–1517

Krissak R, Henzler T, Reichert M, Krauss B, Schoenberg SO, Fink C (2010) Enhanced visualization of lung vessels for diagnosis of pulmonary embolism using dual energy CT angiography. Invest Radiol 45:341–346

Pontana F, Faivre JB, Remy-Jardin M et al (2008) Lung perfusion with dual-energy multidetector-row CT (MDCT): feasibility for the evaluation of acute pulmonary embolism in 117 consecutive patients. Acad Radiol 15:1494–1504

Remy-Jardin M, Pistolesi M, Goodman LR et al (2007) Management of suspected acute pulmonary embolism in the era of CT angiography: a statement from the Fleischner Society. Radiology 245:315–329

Riederer SJ, Mistretta CA (1977) Selective iodine imaging using K-edge energies in computerized x-ray tomography. Med Phys 4:474–481

Schoepf UJ, Costello P (2004) CT angiography for diagnosis of pulmonary embolism: state of the art. Radiology 230: 329–337

Schoepf UJ, Bruening R, Konschitzky H et al (2000) Pulmonary embolism: comprehensive diagnosis by using electron-beam CT for detection of emboli and assessment of pulmonary blood flow. Radiology 217:693–700

Seidensticker PR, Hofmann LK (2008) Dual source CT imaging. Springer, Berlin

Thieme SF, Becker CR, Hacker M, Nikolaou K, Reiser MF, Johnson TR (2008) Dual energy CT for the assessment of lung perfusion–correlation to scintigraphy. Eur J Radiol 68:369–374

Thieme SF, Johnson TR, Lee C et al (2009) Dual-energy CT for the assessment of contrast material distribution in the pulmonary parenchyma. AJR Am J Roentgenol 193:144–149

Wildberger JE, Niethammer MU, Klotz E, Schaller S, Wein BB, Gunther RW (2001) Multi-slice CT for visualization of pulmonary embolism using perfusion weighted color maps. Rofo 173:289–294

Wildberger JE, Klotz E, Ditt H, Spuntrup E, Mahnken AH, Gunther RW (2005) Multislice computed tomography perfusion imaging for visualization of acute pulmonary embolism: animal experience. Eur Radiol 15:1378–1386

Zatz LM (1976) The effect of the kVp level on EMI values. Selective imaging of various materials with different kVp settings. Radiology 119:683–688

Zhang LJ, Zhao YE, Wu SY et al (2009a) Pulmonary embolism detection with dual-energy CT: experimental study of dual-source CT in rabbits. Radiology 252:61–70

Zhang LJ, Chai X, Wu SY et al (2009b) Detection of pulmonary embolism by dual energy CT: correlation with perfusion scintigraphy and histopathological findings in rabbits. Eur Radiol 19:2844–2854

Lung Ventilation

Sven F. Thieme, Sandra Högl, and Thorsten R.C. Johnson

Contents

Abstract

› There have been attempts to use the radiodense noble gas xenon gas (Xe, atomic number Z = 54) as a contrast agent for CT lung ventilation imaging since the end of the 1970s. However, as this approach required repeated chest CT scans, due to an increased patient dose and potential misregistration, this method was not transferred to clinical practice. With the advance of Dual Energy CT (DECT), it has become possible to quantify and map inhaled xenon within the respiratory system in a single Dual Energy (DE) scan. As inhaled xenon has anesthetic properties in higher concentrations, xenon-enhanced DECT has to be performed with caution in patients with respiratory diseases. Although expert knowledge is rather small to date, first results confirm the potential of an increased diagnostic value of xenon-enhanced DECT of the lungs that can bring together high-resolution (HR) morphological and additional functional information. This chapter elucidates the potentials and drawbacks of the method.

S.F. Thieme (✉) and T.R.C. Johnson
Department of Clinical Radiology, University of Munich,
Grosshadern Hospital, Marchioninistrasse 15,
81377 Munich, Germany
e-mail: sven.thieme@med.uni-muenchen.de

S. Högl
Department for Anaesthesiology, University of Munich,
Grosshadern Hospital, Marchioninistrasse 15,
81377 Munich, Germany

T.R.C. Johnson et al. (eds.), *Dual Energy CT in Clinical Practice*, Medical Radiology,
DOI: 10.1007/174_2010_30

Abbreviations

COPD	Chronic obstructive pulmonary disease
CTPA	CT pulmonary angiography
DE	Dual energy
DECT	Dual energy CT
HR	High-resolution
Kr	Krypton
MDCT	Multidetector computed tomography
MRI	Magnetic resonance imaging
NMDA	*N*-methyl-D-aspartic acid
SNR	Signal-to-noise ratio
Xe	Xenon

1 Background: Basic Principles

Respiratory diseases are among the leading causes of morbidity and death in Western civilizations. According to a prognosis of the European Lung Foundation, 11.9 million out of 68 million deaths worldwide will be caused by lung diseases in 2020. Globally, in terms of mortality, incidence, prevalence, and costs, respiratory diseases rank second after cardiovascular diseases, while in some countries they are already the leading cause of death (http://www.european-lung-foundation.org/). Therefore, an early and detailed diagnostic evaluation of the respiratory system is necessary to prevent and treat respiratory diseases. In this diagnostic workup, besides functional assessment by means of pulmonary function tests, imaging techniques play an important role, including morphological and functional lung assessment. While pulmonary function tests allow a global assessment of the extent of lung ventilation changes, a detailed analysis of regional pathologies remains inaccessible. However, some pathologic entities such as chronic obstructive pulmonary disease (COPD), asthma, cystic fibrosis, or bronchiolitis obliterans syndrome following lung transplantation can show distinct heterogeneities of lung ventilation. Therefore, imaging methods displaying the regional distribution of ventilation changes can play an important role in the management of these diseases, e.g., for an early detection of pathological changes in ventilation pattern, in the selection of lung areas with impaired function prior to lung volume reduction surgery, or in the assessment of therapy response. For example, in patients developing smoking-related COPD/pulmonary emphysema, ventilation imaging has shown its potential in the assessment of the severity of the disease and in an early detection of pathologic regional ventilation changes (Woodhouse et al. 2005).

Presently, lung ventilation imaging is mainly realized using planar inhalation scintigraphy or cross-sectional nuclear medicine methods (Harris and Schuster 2007; Petersson et al. 2007; Roach et al. 2008), while magnetic resonance imaging (MRI) with inhalation of polarized noble gases, i.e., ^{3}Helium or ^{129}Xenon (Fain et al. 2007; Hopkins et al. 2007; Kauczor 2003; Kauczor et al. 2002; Matsuoka et al. 2008), or gadolinium chelate aerosoles (Mosbah et al. 2008; Haage et al. 2001), is not generally applied in clinical practice. A drawback is a rather limited morphological information on pulmonary microstructure that is provided by these imaging methods as well as a rather time-consuming examination process.

Whenever high-resolution (HR) morphological information on pathologic changes of the lung parenchyma is required for an optimized treatment of lung diseases, which is the case in a variety of diseases including COPD and pulmonary emphysema, fibrosis, or small airways disease, multidetector computed tomography (MDCT) is the first-line imaging modality. With HR protocols using thin slices and hard convolution kernels, MDCT can provide this important morphological information with high spatial resolution and short acquisition time.

In the field of functional lung imaging, Dual Energy CT (DECT) has proven to be able to map the iodine distribution in the lung parenchyma during the parenchymal phase of contrast material distribution and to detect perfusion changes or defects (DECT iodine mapping or "perfusion imaging," see Chap. 1). Additionally, a fully diagnostic volumetric HR dataset is provided by this technique. Thus, DECT is able to combine morphological and functional lung imaging in a single dual energy (DE) scan (Fink et al. 2008; Pontana et al. 2008; Thieme et al. 2008, 2009; Zhang et al. 2009).

Stable xenon (Xe, atomic number Z=54, K edge: 34.6 keV) is radiopaque and has X-ray absorption characteristics that resemble those of iodine (atomic number Z=53) and other materials with a high atomic number. Those high-Z materials share the characteristic of a relatively increased photon absorption with decreasing photon energies due an increase in photoelectric interactions ("photo effect") (Kruger et al. 1977). It has

been shown that the local xenon concentration is linearly related to the X-ray attenuation in CT and that inhalation of a gas mixture containing 30% xenon and 70% oxygen leads to a significant increase in pulmonary X-ray absorption (Murphy et al. 1989). Based on these properties, xenon can serve as an inhalative CT contrast agent for an evaluation of regional gas transport and lung ventilation.

Being a noble gas, xenon is chemically inert and is exhaled by the lungs without chemical transformation. This property makes xenon safe and applicable even in critically ill patients with hepatic and renal impairment or in patients suffering from contrast agent allergies. Although named after the Greek word ξένον ("stranger"), xenon is not a stranger to the medical society, especially not for anesthesiologists. Knowledge of the analgesic and sedative properties of xenon goes back to 1946, and since 2005, xenon is approved for use in anesthesia in Germany (Latchaw et al. 1987). Being soluble in blood and body tissue, inhaled xenon interacts with a variety of molecular targets in anesthesia-relevant brain regions and can act as an *N*-methyl-D-aspartic acid (NMDA) receptor antagonist. Its favorable pharmacokinetic profile with fast induction and emergence, its high circulatory stability, and its cardio- and neuroprotective properties are close to those of an "ideal anesthetic" and make xenon anesthesia even possible in multimorbid patients (Sanders and Maze 2005). Additionally, the lacking effects on the myocardial contractility, cardiac index, blood pressure, and vascular resistance (Boomsma et al. 1990; Luttropp et al. 1993) make xenon even attractive and applicable for long-term sedation of critically ill patients (Bedi et al. 2002). However, the high cost (approximately 34 €/L) has hindered its wide clinical application. Xenon is a trace gas in the Earth's atmosphere, occurring at approximately 1 part per 11.5 million (Hanne et al. 2001) and is obtained commercially as a byproduct of pure oxygen production. Xenon seems to have no toxic, allergic, mutagenic, fetotoxic, or carcinogenic properties and appears environmentally safe (Harris and Barnes 2008). Xenon neither adds to atmospheric pollution nor contributes to the depletion of ozone layer when emitted because it simply goes back to the atmosphere. There have been attempts to use stable xenon gas as a contrast agent for CT lung ventilation imaging since the end of the 1970s. These previous approaches were based on sequential chest CT scans with registration of xenon-related changes of X-ray attenuation within the pulmonary parenchyma. Using this approach, a static visualization of regional ventilation can be achieved, while a dynamic ventilation assessment including a quantification of wash-in and wash-out characteristics requires more than two scans. The feasibility of mapping the pulmonary ventilation by xenon ventilation CT could be shown in animals (Gur et al. 1979; Tajik et al. 2002; Kreck et al. 2001; Chon et al. 2005; Marcucci et al. 2001; Robertson et al. 2005) and healthy human volunteers (Murphy et al. 1989; Herbert et al. 1982). However, probably because of an increased patient dose caused by the need of repeated chest CT scans and potential misregistrations due to varying levels of inspiration, this method had not been used in clinical care (Gur et al. 1981; Simon 2005). With dual-source scanners that can acquire two spiral CT datasets with different photon spectra simultaneously – similar to DE iodine mapping for the assessment of lung perfusion – DECT now has the potential to map xenon distribution patterns by directly visualizing the inhaled xenon gas at a certain time point without the need of a previous unenhanced scan.

The feasibility of xenon ventilation CT with DE technique was shown by Chae et al. (2008) in eight healthy volunteers and four patients with obstructive lung disease. The subjects inhaled a mixture of 30% xenon and 70% oxygen over a closely fitting face mask for 1 min and 30 s. Static regional ventilation could be displayed with exact match to the thin-section lung-window CT images. Additionally, dynamic measurements were performed. The group also reported the application in a child with bronchial atresia (Goo et al. 2008) in which typical ventilation abnormalities, i.e., collateral ventilation and air trapping, were well demonstrated on xenon ventilation CT.

Despite the sedative properties of xenon, concentrations below 40% may be inhaled without significant side effects (Bedi et al. 2002). One of the major adverse effects is respiratory depression. However, in a study with 1,830 subjects who breathed stable xenon in a concentration of 32% for more than 2 min (4 min 20 s in most instances) for a xenon-enhanced CT brain perfusion study, the reported prevalence of respiratory depression was low (3.6%) and the majority of the cases involved subclinical mild respiratory delay (Latchaw et al. 1987). Other adverse effects include somnolence, headache, nausea, and psychological effects, such as lightheadedness and labile emotion (Latchaw et al. 1987; Yonas et al. 1981). As mentioned above, for xenon-ventilation DECT, only short xenon inhalation times of 2 min or less are required and an

inspired xenon fraction of 30% seems to be adequate in free-breathing subjects. Thus, the rate of adverse effects with this xenon administration scheme should be even smaller than the reported incidence. However, in the xenon DECT study performed by Chae et al. one patient and one volunteer reported discomfort during xenon inhalation. Thus, patients receiving xenon for pulmonary imaging because of an impaired gas exchange must be under continuous medical observation, as a respiratory delay in these patients might have more severe implications than in healthy volunteers. Especially, respiratory rate, oxygen saturation, and blood pressure should be monitored carefully by anesthesia-trained personnel during and after the examination, at least until experience in larger patient number is obtained.

2 Patient Preparation

In principle, xenon-enhanced ventilation DECT can be performed in patients with various pulmonary diseases leading to changes in the regional ventilation, e.g., COPD and asthma. No specific measures are required prior to the examination. In free-breathing patients, a close-fitting face mask delivering a xenon/oxygen mixture to the patients seems to be sufficient for an adequate xenon signal in the pulmonary parenchyma. As Chae et al. (2008) could show, a xenon concentration of 30% is sufficient for an adequate signal in free-breathing patients.

There are no known contraindications to xenon breathing except for a massively increased oxygen demand prohibiting additional xenon ventilation because of an inevitable oxygen reduction. Furthermore, as xenon has been shown to lead to an increase in cerebral blood flow in anesthetic concentrations (Reyle-Hahn and Rossaint 2000), xenon should not be administered to patients with abnormal intracranial pressure.

Despite the strong dependence of regional lung ventilation on body position, predominantly caused by the effects of gravity with a relative increase of the ventilation in the gravity-dependent parenchyma (West and Dollery 1960), an upright patient position that would be the most physiological setting for a ventilation examination is not achievable with current scanners. Thus, patient position should be supine and the interpretation should take a possible influence of this position into account.

3 Scan Protocol

Based on our own experience and on the results previously reported by Chae et al. (2008), xenon ventilation DECT can be successfully performed using the Somatom Definition scanner (Siemens Healthcare, Forchheim, Germany). The successor dual-source CT system (Somatom Definition FLASH, Siemens Healthcare) offers some new features and technical improvements that require some modifications in the image acquisition protocol (Thieme et al. 2010).

Assuming a monoexponential form of the wash-in curve of xenon (Kety 1951) for nondiseased lung tissue, relatively short equilibration times of less than 2 min during the wash-in phase of xenon have been shown (Murphy et al. 1989). This means that an alveolar xenon concentration nearly equal to the inspiratory concentration is reached within this time period. Assuming that equilibration times in areas of restricted lung ventilation are markedly prolonged, the CT data derived from a single DECT lung volume acquisition at the time point of alveolar xenon gas equilibration in nondiseased lung should display areas of impaired ventilation by mapping the local xenon concentration. In areas of hypoventilation, the local xenon concentration is expected to be reduced, leading to a decreased xenon signal in DE ventilation maps. Such static lung ventilation imaging after xenon inhalation for 2 min, which displays local ventilation inhomogeneities and allows the detection of ventilation defects, seems to be the major advantage of DECT and the main improvement in the field of functional pulmonary CT imaging. For dynamic ventilation imaging based on a time-resolved measurement of CT attenuation changes during wash-in or wash-out of xenon and the calculation of flow values, DECT does not seem to offer major advantages over conventional single-source CT but would suffer from the same drawbacks with an increased patient dose and potential image misregistrations.

To keep the patient dose as low as possible, we propose following scan parameters for a DE xenon scanning on the Definition scanner.

The scan range should include the entire lungs from apex to basis. To optimize spectral contrast, tube voltages should be set to 140 kVp for tube A and 80 kVp for tube B with attenuation-based tube current modulation: 30 effective mAs for tube A and 117 effective mAs for tube B; detector collimation should be set to 14×1.2 mm for an optimized signal-to-noise ratio (SNR); rotation time, 0.5 s; pitch, 0.7. No intravenous contrast material should be administered because of the effects caused by

iodine and xenon cannot be distinguished in DE parameter mapping. The scan should be started ~2 min after the start of xenon breathing and should be performed during a deep inspiration breath hold. Optimally, the time of acquisition should be tailored to the alveolar xenon concentration, i.e., the scan should be started as soon as an expiratory concentration of 30% is reached. Thus, an equilibration of xenon concentrations between areas of normal and restricted ventilation should be avoided.

As a result of the technical modifications of the Definition FLASH scanner, harder X-ray spectra can be obtained using a 100 kVp lower-energy spectrum for the first tube and a filtered 140 kVp spectrum with a 0.1 mm tin filter for the second tube. As these harder spectra provide an improved general transmission with less noise, a thinner collimation of 128×0.6 mm can be used without a relevant decrease in SNR. Further parameters in the FLASH scanner should be set to: tube currents, 165 and 140 effective mAs with attenuation-based modulation; rotation time, 0.28 s; and pitch, 0.55.

Our own experience from phantom studies could show that the CT dose index can be kept identical for both protocols with 5.4 mGy to yield equal image noise in the average images (Schenzle et al. 2010). For comprehensive functional DECT imaging including lung perfusion, a second CT scan after intravenous contrast material injection (CTPA) is required. For the assessment of ventilation and perfusion, the scan parameters should be kept identical for this second iodine-enhanced scan.

4 Technical Requirements for Xenon Application

To accomplish xenon ventilation DECT studies in critically ill patients requiring mechanical ventilation, an approved anesthesia machine is necessary for xenon application. To our knowledge, the Tangens 2C (EKU Elektronik, Germany) currently represents the only commercially available anesthesia machine for xenon application in the European Union. It contains an electronically controlled anesthesia delivery system that continuously monitors gas concentrations inside the breathing circuit in a closed-loop feedback control and delivers xenon and oxygen into the system in the amount needed to maintain constant gas concentrations and circulating gas volume. As the inspiratory as well as the expiratory xenon concentration can be measured by this ventilator, a cost-effective and safe xenon application is assured. Moreover, the Tangens 2C provides various ventilation patterns, e.g., manual/spontaneous ventilation, pressure- and volume-controlled ventilation, and synchronized intermittent mandatory ventilation. Furthermore, it allows a maximum positive end-expiratory pressure of 20 mbar. These features make xenon application possible even in critically ill patients with severe pulmonary conditions.

5 Xenon Ventilation CT in Combination with Iodine Mapping in Critically Ill Patients

We used the Tangens 2C in a xenon-DECT imaging study in 13 mechanically ventilated, critically ill patients with severe pulmonary impairment (e.g., Acute Respiratory Distress Syndrome, pulmonary fibrosis, pneumonia) and deterioration of the gas exchange during intensive care treatment. Directly prior to the CT examination, the respiration regimen was modified to inspiratory fractions of 50% oxygen and 50% stable xenon (AirLiquide, Düsseldorf, Germany) in order to obtain a strong xenon enhancement. If necessary for proper controlled mechanical ventilation, sedation of the patient was deepened prior to CT scanning after connection to the ventilator and patients were ventilated with 100% oxygen for at least 5 min for proper denitrogenation, i.e., removal of nitrogen from the airways. Then, the automatic xenon dosing was activated and the wash-in phase was started. The expiratory xenon concentration was continuously monitored, and CT scanning was started at an expiratory xenon concentration of 30%. After the ventilation scan, respiration parameters were switched to 100% oxygen. In 10 patients, an additional DE lung perfusion examination was additionally performed. Intravenous contrast material injection (Iopromide, Ultravist 370, Bayer Schering Pharma) was initiated as soon as a threshold value of less than 5% expiratory xenon concentration was reached (3–5 min after switching to 100% oxygen). Eighty milliliters of contrast material were injected at 4.0 mL/s, followed by 100 mL saline. An additional perfusion DECT scan was acquired. Mechanical ventilation was not paused during the scans.

Using this regimen, xenon inhalation did not lead to any relevant side effects or ventilation impairment in this patient population with compromised pulmonary function (Thieme et al. 2010).

6 Postprocessing

Based on the acquired data from both detectors, HR lung-window images can be reconstructed, as well as soft-tissue images, with standard convolution kernels. These reconstructions are fully diagnostic for morphological assessment.

For the generation of ventilation maps, separate sets of images are reconstructed from both simultaneous spiral acquisitions using specific soft kernels that do not alter object edges (D20). For satisfactory xenon SNR, slice thickness should be 3 mm with 1 mm increment. The resulting high energy (140 or Sn140 kVp) and low energy (80 or 100 kVp) image datasets can be postprocessed on a specific workstation (Syngo Multi Modality Workplace, Siemens Healthcare). Color-coded distribution maps of xenon are generated with specific DE postprocessing software approved by the U.S. Food and Drug Administration. This software analyzes the density values in the corresponding high and low energy CT datasets using a three material decomposition algorithm for air, soft tissue, and xenon to quantify and visualize the photo effect caused by xenon. Ventilation images, i.e., xenon distribution maps, are reconstructed with a slab thickness of 3 mm.

7 Diagnostic Evaluation

In our feasibility study in 13 patients from the intensive care unit who were under continuous artificial respiration, we found a good correlation of the xenon ventilation maps with the patients' underlying lung diseases and with pathological morphological findings observed in the lung-window images of the CT scans. For example, in three patients with pulmonary fibrosis, ventilation was compromised with several defects in the xenon maps. In a patient with bullae in emphysematous lung tissue, a xenon signal within the bullae indicated connection to the airways and ventilation.

In one patient with pneumothorax treated with a chest tube, a xenon enhancement in the basal parts of the pneumothorax revealed the site of an airway-to-pneumothorax fistula. One patient showed parenchymal changes in the right lower lobe that were indicative for bronchiolitis, i.e., micronodular opacities, tree-in-bud pattern, and lobular hypoattenuation. This patient showed a ventilation deficit in the respective lung areas, presumably indicating focal air trapping due to bronchiolitic small airway obstruction (Fig. 1a). In the respective lung area, no perfusion defect could be detected in the additionally acquired iodine distribution map (Fig. 1b).

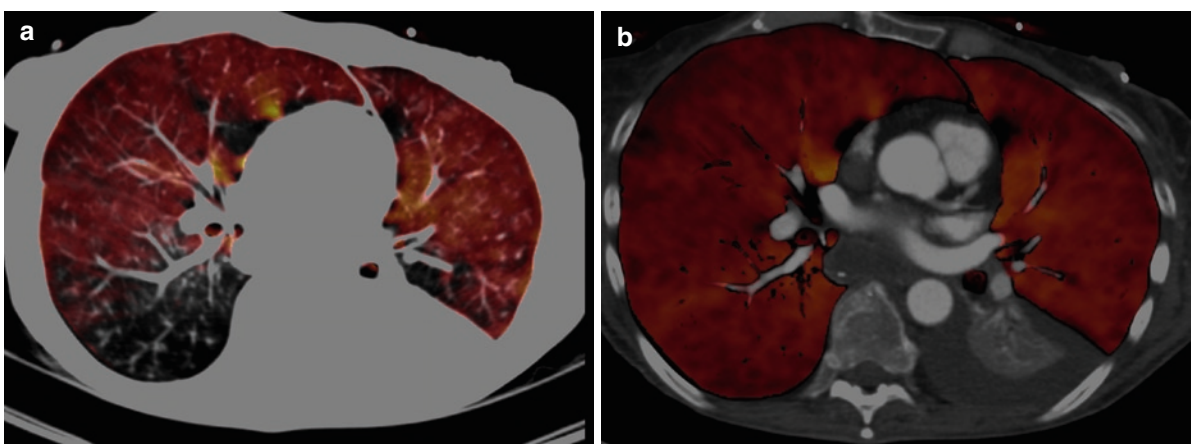

Fig. 1 Forty-nine year-old female patient with postinfectious bronchilitis. Transversal CT image in lung window with superimposed color-coded xenon distribution map (**a**) shows slightly hypoattenuating lobules in the right lower lobe as well as small nodular opacities and branching tubular subpleural structures consistent with bronchiolitis. A ventilation defect in the right lower lobe corresponding to the area of bronchiolitis is visualized, indicating focal air trapping. CT image in angiographic window with super-imposed color-coded DE iodine distribution map (**b**) shows no perfusion restriction in the area of hypoventilation. The left lower lobe is partially atelectatic due to pleural effusion (courtesy of Thieme et al. 2010)

8 Limitations of the Method

A certain drawback in the diagnostic evaluation of xenon ventilation maps in CT may be caused by the inherent physical and mechanical properties of xenon with a significantly increased density and viscosity when compared to normal air. Thus, the distribution of xenon in the airways may well differ from the distribution of inhaled air. Moreover, airway resistance depends on *viscosity* of the inhaled gas mixture whenever laminar flow is present and is *density*-dependent in the presence of turbulent flow. Studies have shown an increase in peak airway pressure in mechanically ventilated patients when a mixture of 33% xenon and 67% oxygen was inhaled,

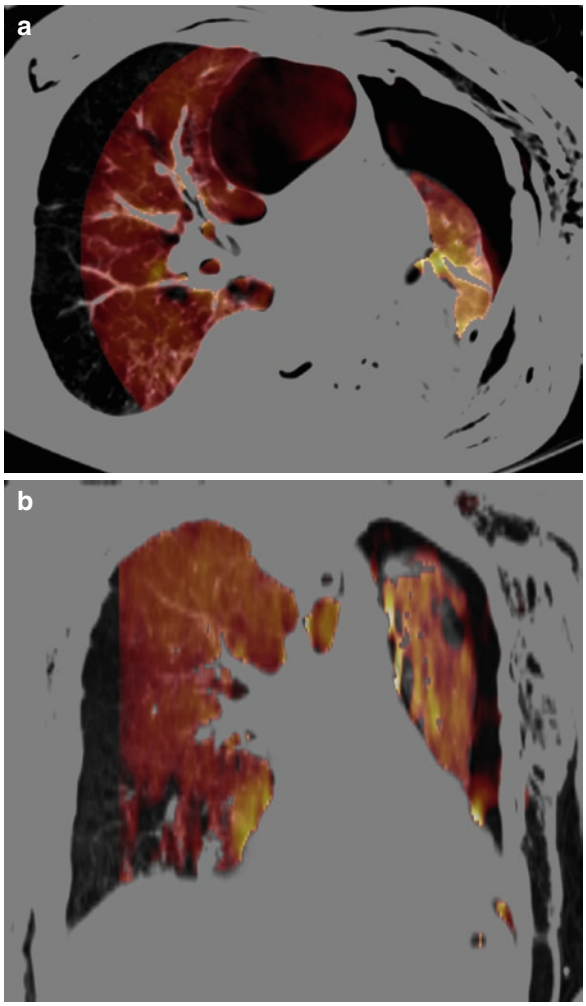

Fig. 2 Sixty-five year-old male patient with left lung transplantation. Fused image of lung window and xenon enhancement map at a suprahilar level (**a**) shows decreased ventilation of the emphysematous right lung with relative hyperventilation of the left-sided graft. An anteriorly located bulla in the right upper lobe shows little xenon enhancement indicating moderate ventilation. Left pneumothorax and soft tissue emphysema are shown. Coronal reformation at the level of the trachea (**b**) shows xenon enhancement within the pneumothorax indicating a fistula of the visceral pleura. This finding was in accordance with a persistent partial collapse of the left lung in spite of chest tube therapy (courtesy of Thieme et al. 2010)

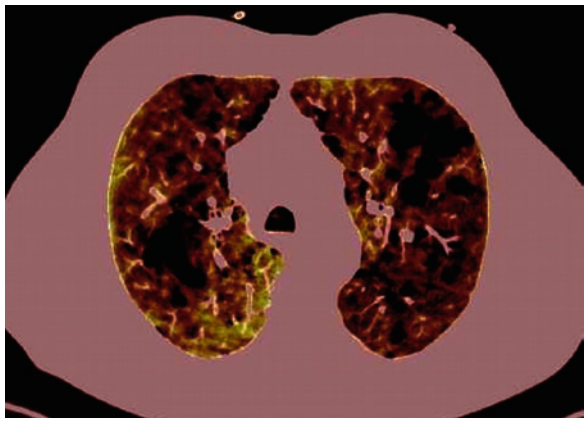

Fig. 3 Sixty-nine year-old male patient with idiopathic pulmonary fibrosis. Transversal CT image in lung window with superimposed color-coded xenon distribution map shows inhomogeneous lung ventilation with multiple defects corresponding to areas of cystic parenchymal destruction and fibrotic changes

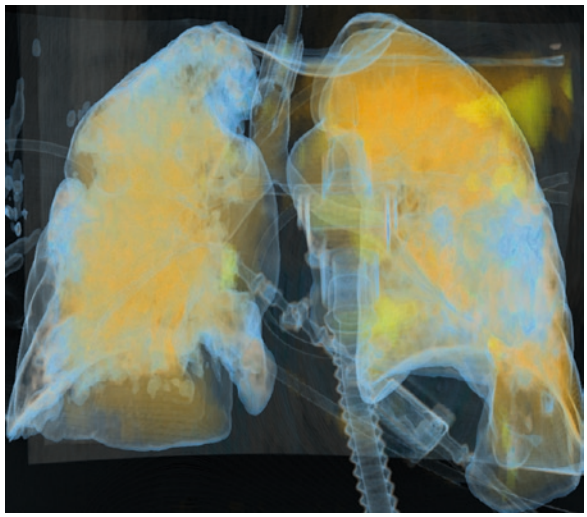

Fig. 4 Volume-rendering technique image of the parenchymal xenon distribution in a 40 year-old female patient with adult respiratory distress syndrome (ARDS) shows rather homogeneous lung ventilation

confirming that the airway resistance increased significantly. The authors assumed that the reason for this increase in airway resistance was a more peripherally located zone of transition from turbulent to laminar gas flow than with air or oxygen ventilation (Rueckoldt et al. 1999). Ventilation maps may additionally be hampered by the fact that xenon partially diffuses into blood and tissue, and it remains unclear to which extent the absorption decreases the alveolar concentration. The potential impact on local xenon concentration caused by these characteristics of xenon gas has not yet been investigated, and therefore, the interpretation of xenon distribution maps as "ventilation maps" remains an assumption.

As the number of xenon-enhanced DECT examinations is still rather limited, further studies including larger patient groups are required for a systematic evaluation of the actual clinical value of this promising imaging technique and its potential drawbacks.

Theoretically, some of the drawbacks of xenon ventilation imaging could be overcome when xenon is replaced by krypton (Kr, Z=36). This radiodense noble gas has shown its potential as CT ventilation contrast agent (Winkler et al. 1977), has no documented side effects in humans, and is less soluble than xenon. However, as krypton is much less radiopaque than xenon, Chon et al. could show that the CT enhancement related to Kr was about threefold lower than the xenon-related enhancement both at lower (80 kV) and higher (120 kV) tube voltages, so that the CT contrast that is achievable with Kr alone seems to be insufficient for an expedient DE imaging approach. However, in an animal model, a mixture of 30% Xe/30% Kr could be shown to lead to a CT enhancement similar to the effect of 40% Xe (Chon et al. 2007). Thus, a potential further reduction of the inspiratory xenon concentration might be reached by adding krypton gas to the inspiratory gas mixture.

9 Conclusion

In summary, xenon-enhanced DECT ventilation imaging is a novel technique that is able to display pulmonary ventilation defects in CT without additional radiation exposure. Xenon inhalation in concentrations below 40% has little side effects and seems to be a relatively safe and expedient method to supplement a standard pulmonary CT scan with qualitative and quantitative information on regional lung ventilation. Potentially, these additional findings can help to identify lung areas with restricted ventilation and help to adjust and improve patients' therapies. In principle and in spite of inherent drawbacks of the method that are caused by the physical properties of xenon and the necessity of a supine patient position in CT, xenon-enhanced DECT can be considered an alternative ventilation imaging method, especially as a substitute for inhalation scintigraphy, whenever additional HR information on lung morphology is required. Further investigations will be needed to define the role of xenon-enhanced DECT and comprehensive imaging protocols including xenon-enhanced ventilation and iodine-enhanced perfusion DECT imaging in a clinical diagnostic workup of the lung.

References

Bedi A, McCarroll C, Murray JM, Stevenson MA, Fee JP (2002) The effects of subanaesthetic concentrations of xenon in volunteers. Anaesthesia 57:233–241

Boomsma F, Rupreht J, Veld AJ Man in 't, de Jong FH, Dzoljic M, Lachmann B (1990) Haemodynamic and neurohumoral effects of xenon anaesthesia. A comparison with nitrous oxide. Anaesthesia 45:273–278

Chae EJ, Seo JB, Goo HW et al (2008) Xenon ventilation CT with a dual-energy technique of dual-source CT: initial experience. Radiology 248:615–624

Chon D, Simon BA, Beck KC et al (2005) Differences in regional wash-in and wash-out time constants for xenon-CT ventilation studies. Respir Physiol Neurobiol 148:65–83

Chon D, Beck KC, Simon BA, Shikata H, Saba OI, Hoffman EA (2007) Effect of low-xenon and krypton supplementation on signal/noise of regional CT-based ventilation measurements. J Appl Physiol 102:1535–1544

Fain SB, Korosec FR, Holmes JH, O'Halloran R, Sorkness RL, Grist TM (2007) Functional lung imaging using hyperpolarized gas MRI. J Magn Reson Imaging 25:910–923

Fink C, Johnson TR, Michaely HJ et al (2008) Dual-energy CT angiography of the lung in patients with suspected pulmonary embolism: initial results. Rofo 180(10):879–83

Goo HW, Chae EJ, Seo JB, Hong SJ (2008) Xenon ventilation CT using a dual-source dual-energy technique: dynamic ventilation abnormality in a child with bronchial atresia. Pediatr Radiol 38:1113–1116

Gur D, Drayer BP, Borovetz HS, Griffith BP, Hardesty RL, Wolfson SK (1979) Dynamic computed tomography of the lung: regional ventilation measurements. J Comput Assist Tomogr 3:749–753

Gur D, Shabason L, Borovetz HS et al (1981) Regional pulmonary ventilation measurements by xenon enhanced dynamic computed tomography: an update. J Comput Assist Tomogr 5:678–683

Haage P, Adam G, Karaagac S et al (2001) Mechanical delivery of aerosolized gadolinium-DTPA for pulmonary ventilation assessment in MR imaging. Invest Radiol 36:240–243

Hanne P, Marx T, Musati S, Santo M, Suwa K, Morita S (2001) Xenon: uptake and costs. Int Anesthesiol Clin 39:43–61

Harris PD, Barnes R (2008) The uses of helium and xenon in current clinical practice. Anaesthesia 63:284–293

Harris RS, Schuster DP (2007) Visualizing lung function with positron emission tomography. J Appl Physiol 102: 448–458

Herbert DL, Gur D, Shabason L et al (1982) Mapping of human local pulmonary ventilation by xenon enhanced computed tomography. J Comput Assist Tomogr 6:1088–1093

Hopkins SR, Levin DL, Emami K et al (2007) Advances in magnetic resonance imaging of lung physiology. J Appl Physiol 102:1244–1254

Kauczor HU (2003) Hyperpolarized helium-3 gas magnetic resonance imaging of the lung. Top Magn Reson Imaging 14:223–230

Kauczor HU, Hanke A, Van Beek EJ (2002) Assessment of lung ventilation by MR imaging: current status and future perspectives. Eur Radiol 12:1962–1970

Kety SS (1951) The theory and applications of the exchange of inert gas at the lungs and tissues. Pharmacol Rev 3:1–41

Kreck TC, Krueger MA, Altemeier WA et al (2001) Determination of regional ventilation and perfusion in the lung using xenon and computed tomography. J Appl Physiol 91:1741–1749

Kruger RA, Riederer SJ, Mistretta CA (1977) Relative properties of tomography, K-edge imaging, and K-edge tomography. Med Phys 4:244–249

Latchaw RE, Yonas H, Pentheny SL, Gur D (1987) Adverse reactions to xenon-enhanced CT cerebral blood flow determination. Radiology 163:251–254

Luttropp HH, Romner B, Perhag L, Eskilsson J, Fredriksen S, Werner O (1993) Left ventricular performance and cerebral haemodynamics during xenon anaesthesia. A transoesophageal echocardiography and transcranial Doppler sonography study. Anaesthesia 48:1045–1049

Marcucci C, Nyhan D, Simon BA (2001) Distribution of pulmonary ventilation using Xe-enhanced computed tomography in prone and supine dogs. J Appl Physiol 90: 421–430

Matsuoka S, Hunsaker AR, Gill RR et al (2008) Functional MR imaging of the lung. Magn Reson Imaging Clin N Am 16:275–289, ix

Mosbah K, Ruiz-Cabello J, Berthezene Y, Cremillieux Y (2008) Aerosols and gaseous contrast agents for magnetic resonance imaging of the lung. Contrast Media Mol Imaging 3:173–190

Murphy DM, Nicewicz JT, Zabbatino SM, Moore RA (1989) Local pulmonary ventilation using nonradioactive xenon-enhanced ultrafast computed tomography. Chest 96:799–804

Petersson J, Sanchez-Crespo A, Larsson SA, Mure M (2007) Physiological imaging of the lung: single-photon-emission computed tomography (SPECT). J Appl Physiol 102: 468–476

Pontana F, Faivre JB, Remy-Jardin M et al (2008) Lung perfusion with dual-energy multidetector-row CT (MDCT): feasibility for the evaluation of acute pulmonary embolism in 117 consecutive patients. Acad Radiol 15: 1494–1504

Reyle-Hahn M, Rossaint R (2000) Xenon – a new anesthetic. Anaesthesist 49:869–874

Roach PJ, Bailey DL, Harris BE (2008) Enhancing lung scintigraphy with single-photon emission computed tomography. Semin Nucl Med 38:441–449

Robertson HT, Kreck TC, Krueger MA (2005) The spatial and temporal heterogeneity of regional ventilation: comparison of measurements by two high-resolution methods. Respir Physiol Neurobiol 148:85–95

Rueckoldt H, Vangerow B, Marx G et al (1999) Xenon inhalation increases airway pressure in ventilated patients. Acta Anaesthesiol Scand 43:1060–1064

Sanders RD, Maze M (2005) Xenon: from stranger to guardian. Curr Opin Anaesthesiol 18:405–411

Schenzle JC, Sommer WH, Neumaier K, Michalski G, Lechel U, Nikolaou K et al (2010) Invest Radiol 45(6):347–353

Simon BA (2005) Regional ventilation and lung mechanics using X-ray CT. Acad Radiol 12:1414–1422

Tajik JK, Chon D, Won C, Tran BQ, Hoffman EA (2002) Subsecond multisection CT of regional pulmonary ventilation. Acad Radiol 9:130–146

Thieme SF, Becker CR, Hacker M, Nikolaou K, Reiser MF, Johnson TR (2008) Dual energy CT for the assessment of lung perfusion – correlation to scintigraphy. Eur J Radiol 68:369–374

Thieme SF, Hoegl S, Nikolaou K, Fisahn J, Irlbeck M, Maxien D et al (2010) Eur Radiol. [Epub ahead of print]

Thieme SF, Johnson TR, Lee C et al (2009) Dual-energy CT for the assessment of contrast material distribution in the pulmonary parenchyma. AJR Am J Roentgenol 193: 144–149

West JB, Dollery CT (1960) Distribution of blood flow and ventilation-perfusion ratio in the lung, measured with radioactive carbon dioxide. J Appl Physiol 15:405–410

Winkler SS, Holden JE, Sackett JF, Flemming DC, Alexander SC (1977) Xenon and krypton as radiographic inhalation contrast media with computerized tomography: preliminary note. Invest Radiol 12:19–20

Woodhouse N, Wild JM, Paley MN et al (2005) Combined helium-3/proton magnetic resonance imaging measurement of ventilated lung volumes in smokers compared to never-smokers. J Magn Reson Imaging 21:365–369

Yonas H, Grundy B, Gur D, Shabason L, Wolfson SK Jr, Cook EE (1981) Side effects of xenon inhalation. J Comput Assist Tomogr 5:591–592

Zhang LJ, Zhao YE, Wu SY et al (2009) Pulmonary embolism detection with dual-energy CT: experimental study of dual-source CT in rabbits. Radiology 252:61–70

Pulmonary Nodules and Lung Cancer

Thomas Henzler, Gerald Schmid-Bindert, and Christian Fink

Contents

Abstract

› Worldwide, lung cancer is the leading cause of cancer mortality in men and women. The therapeutic options for lung cancer have been substantially improved. Sophisticated surgical techniques have increased the number of patients considered as being technically resectable. On the other hand, multimodal treatment strategies using induction chemotherapy or radiotherapy have increased the number of patients finally undergoing surgical resection. But even in inoperable patients, new chemotherapeutic agents or targeted therapies have improved the survival of patients with lung cancer. As a consequence, the demands for diagnostic radiology in patients with lung cancer have changed. The differentiation of iodinated contrast media by DECT is a potential surrogate marker for regional blood volume and thus angiogenesis, which has already been used for non-invasive characterization of pulmonary nodules. Future studies have to evaluate further potential applications of DECT in lung cancer staging and response evaluation.

T. Henzler (✉) and C. Fink
Department of Clinical Radiology and Nuclear Medicine,
University Medical Center Mannheim,
Medical Faculty Mannheim of the University of Heidelberg,
Theodor-Kutzer-Ufer 1-3, 68167 Mannheim, Germany
e-mail: thomas.henzler@umm.de

G. Schmid-Bindert
Interdisciplinary Thoracic Oncology,
University Medical Center Mannheim,
Medical Faculty Mannheim of the University of Heidelberg,
Theodor-Kutzer-Ufer 1-3, 68167 Mannheim, Germany

1 Introduction

1.1 Clinical Background

Worldwide, lung cancer is the leading cause of cancer mortality in men and women. The most common incident form of cancer in Europe in 2008 was lung cancer followed by colorectal cancer and breast cancer in women.

T.R.C. Johnson et al. (eds.), *Dual Energy CT in Clinical Practice*, Medical Radiology,
DOI: 10.1007/174_2010_53 © Springer-Verlag Berlin Heidelberg 2011

Prognosis of lung cancer is poor; only 7% of patients will survive for 5 years, and most patients may only be treated by palliation. However, around 20% of patients present early enough to be treated with curative intent and will have a relatively good prognosis. The therapeutic options for this group of patients with lung cancer have been substantially improved. Sophisticated surgical techniques have increased the number of patients considered as being technically resectable. In addition, multimodal treatment strategies using induction chemotherapy or radiotherapy have increased the number of patients finally undergoing surgical resection. But even in inoperable patients, new chemotherapeutic agents or targeted therapies have improved the survival of patients with NSCLC.

Contrast-enhanced CT of the chest remains the standard imaging test in patients with suspected pulmonary nodules or lung cancer. The broad clinical use of thin-section multi–detector CT inevitably leads to the detection of a large number of pulmonary nodules. Previous lung cancer screening trials have shown that the majority of individuals with a certain risk profile will have at least one non-calcified pulmonary nodule. At surgical biopsy, approximately 50% of these indeterminate pulmonary nodules will turn out to be benign (Swensen 2000). Therefore, non-invasive characterization of pulmonary nodules by imaging is of major importance in the clinical work-up of incidentally detected pulmonary nodules. Using standard contrast enhanced CT, the characterization of pulmonary nodules is based on simple morphological criteria e.g., irregular or spiculated margins as a sign for malignancy or calcifications as a sign of benignity. Non-invasive functional imaging techniques such as 18-F-FDG PET-CT and dynamic contrast enhanced CT and MRI provide valuable information about tissue-specific parameters such as metabolism or microcirculation which can be used to differentiate between benign and malignant pulmonary nodules. Neoangiogenesis promotes tumor growth by supplying neoplastic cells with required nutrients. Furthermore, it plays a major role in tumor cell metastasis by limiting the integrity of the vessel wall. It has been shown that there is a difference in vascularity between benign and malignant nodules, which can be used for tumor characterization. Differences in vascularity can be demonstrated by many different modalities, including histology (Zielinski & Kulig 1984), conventional angiography (Viamonte 1965), dynamic contrast enhanced CT (Littleton et al. 1990; Swensen et al. 2000), and MRI (Kono et al. 1993; Guckel et al. 1996). Several studies have further demonstrated that 18-F-FDG uptake at PET-CT positively correlates with tumor aggressiveness and the degree of angiogenesis of pulmonary nodules (Dewan et al. 1995; Orlacchio et al. 2007; Gupta et al. 1992; Kubota et al. 1988; Patz et al. 1993). However, PET-CT is still not widely available, Moreover, integration of dynamic contrast enhanced CT and MRI into a routine morphologic imaging protocol is challenging, as several acquisitions and contrast injections are required.

Dual energy CT (DECT) allows a selective visualization of iodinated contrast media in a single scan, and thus may be used as a surrogate for local blood volume (Johnson et al. 2007). In addition to the functional component of DECT a standard CT scan with imaging properties equivalent to a standard single energy CT scan can be processed. The following chapter will review the potential of DECT for pulmonary nodule characterization. Furthermore potential applications of DECT in lung cancer staging and response evaluation will be discussed.

2 Characterization of Pulmonary Nodules Using Dynamic Contrast-Enhanced CT

Due to tumor angiogenesis, regional blood flow and blood volume and consecutively contrast enhancement is increased in malignant pulmonary nodules. Changes in perfusion and vascular permeability can be assessed by means of dynamic contrast-enhanced CT, which is based on analysis of time-density curves acquired with consecutive scans after injection of a bolus of iodinated contrast material (Swensen 2000; Swensen et al. 2000; Li et al. 2008; Swensen et al. 1995b, 1992; Yamashita et al. 1995; Zhang & Kono 1997). The feasibility of dynamic contrast-enhanced CT for the characterization of pulmonary nodules has been demonstrated by a large number of studies using different scanning protocols. A common finding in all studies was that malignant nodules tend to show a higher contrast-enhancement than benign ones. This was also confirmed by a prospective, multicenter trial evaluating dynamic contrast-enhanced CT for the differentiation of benign and malignant pulmonary nodules (Swensen et al. 2000).

Several studies have correlated the results of dynamic contrast-enhanced CT to histological parameters of tumor angiogenesis such as microvessel density (MVD) or expression of vascular endothelial growth factor (VEGF) expression. In a study by Yi et al. performed in 54 indeterminate pulmonary nodules, a moderate positive correlation between MVD

and VEGF expression with the peak enhancement of dynamic contrast-enhanced CT was found. However, no significant difference in the MVD of benign and malignant pulmonary nodules was observed. In contrast, malignant pulmonary nodules showed a significantly higher VEGF expression (Yi et al. 2004).

In another study, Tateishi et al. evaluated the correlation of tumor enhancement with MVD and VEGF expression in 130 patients with histological proven lung cancer (Tateishi et al. 2002). They found a significantly higher peak enhancement of VEGF-positive tumors than in VEGF-negative tumors. There was also a significant positive correlation ($r = 0.65$) between the peak enhancement of VEGF-positive lung tumors with the MVD. Neither the tumor enhancement and VEGF-status, nor MVD showed a meaningful correlation with the tumor size. In contrast, lymph node positive lung cancers showed a higher peak enhancement, VEGF-expression and MVD than lymph node negative cancers.

The correlation of angiogenesis and contrast-enhancement also may be used for the assessment of tumor response to antiangiogenic or radiation therapy. It has been reported (Garcia-Barros et al. 2003) that microvascular damage is a key mechanism in tumor response to radiation. Therefore, reduced volume of the vascular bed following radiation therapy would be reflected by reduced blood flow, blood volume, and permeability–surface area product. Ng et al. (Ng et al. 2007) found that hypofractionated radiotherapy increased tumor vascular blood volume and permeability of NSCLC. In a recently published study by Wang et al., it has been demonstrated that NSCLC with higher perfusion is more sensitive to radiochemo therapy than that with lower perfusion. Moreover, the study suggests that after radiochemo therapy, findings at perfusion CT are a significant predictor of early tumor response and overall survival among patients with NSCLC.

Although dynamic contrast-enhanced CT is valuable for the differentiation of malignant from benign nodules, the technique has several limitations which have to be considered.

First, with standard CT equipment as been used in the majority of studies, the sample volume of dynamic contrast-enhanced CT is restricted to a single or couple of transverse slices, which might be problematic for a quantitative assessment of angiogenesis in patients with multiple pulmonary nodules or large tumors. Although, the capability to cover larger tissue volume (Ng et al. 2007) and whole tumors (Li et al. 2008) became feasible with the most recent multidetector CT scanner systems with broad detector arrays up to 16 cm or shuffle mode acquisitions, other limitations of dynamic contrast-enhanced CT become more relevant such as a considerable radiation dose for the patient. Moreover, post-processing and evaluation of tumor perfusion data is neither standardized nor generally available which limits the integration of this technique into clinical routine.

3 Dual-Energy CT for Characterization of Pulmonary Nodules

Similar as for other body regions, DECT can be used to process a virtual non-enhanced CT data set from a contrast-enhanced DECT data set that has similar imaging characteristics than a true non-enhanced CT data set (Fig. 1). Furthermore, the iodine content can be selectively visualized by DECT and visualized by color-coding which can be fused onto the standard density-based gray scale CT image (Johnson et al. 2007).

It has been proposed that the processing of virtual unenhanced CT images from a contrast-enhanced DECT data set might be useful for the characterization

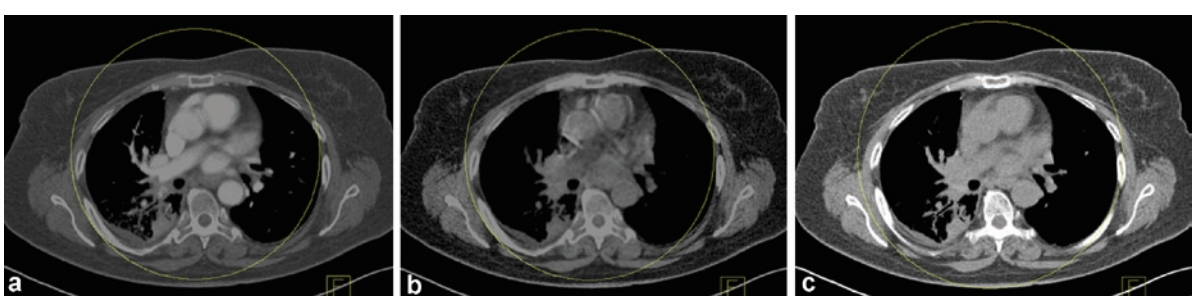

Fig. 1 Contrast enhanced (**a**), virtual non-enhanced (**b**) and true non-enhanced (**c**) DECT of a 75-year-old woman with NSCLC of the right lower lobe. The virtual non-enhanced image processed from the contrast enhanced DECT data set shows similar density characteristics of the tumor of the right lower lobe than the true non-enhanced CT data set. For example no calcifications are observed within the tumor

of pulmonary nodules by allowing a clear visualization of small calcifications as an indication for benign nodules. Due to this DECT can obviate the routine need for true unenhanced acquisitions (Chae et al. 2008) and thus reduce the radiation exposure to patients.

By analyzing the degree of enhancement of a pulmonary nodule following injection of iodinated contrast media malignant pulmonary nodules can be differentiated from benign nodules (Swensen et al. 1995b, 1992; Yamashita et al. 1995; Zhang & Kono 1997; Jeong et al. 2005).

Due to the selective visualization of iodine by DECT, the degree of enhancement can be analyzed by DECT without the need of a separate unenhanced scan. It may be assumed that if the scan delay is chosen in an appropriate way the iodine map of DECT may be used as a surrogate for the regional blood volume. Future studies will have to show, if a DECT scan can be used for the estimation of dynamic contrast-enhanced CT parameters. The main clinical benefit of a single acquisition DECT scan compared to a dynamic contrast enhanced CT would be that the whole tumor is covered within a single scan and that the method is not as susceptible for respiratory motion as the data is acquired within a single scan during a single breathhold. Moreover, radiation dose and patient room time could be significantly reduced.

Besides the differentiation of pulmonary nodules (Figs. 2 and 3) another potential application of DECT could be the evaluation of therapy response by analyzing changes in the tumor iodine distribution, especially in patients undergoing novel targeted therapy, e.g., vascular endothelial growth factor (VEGF) inhibitors (Fig. 4).

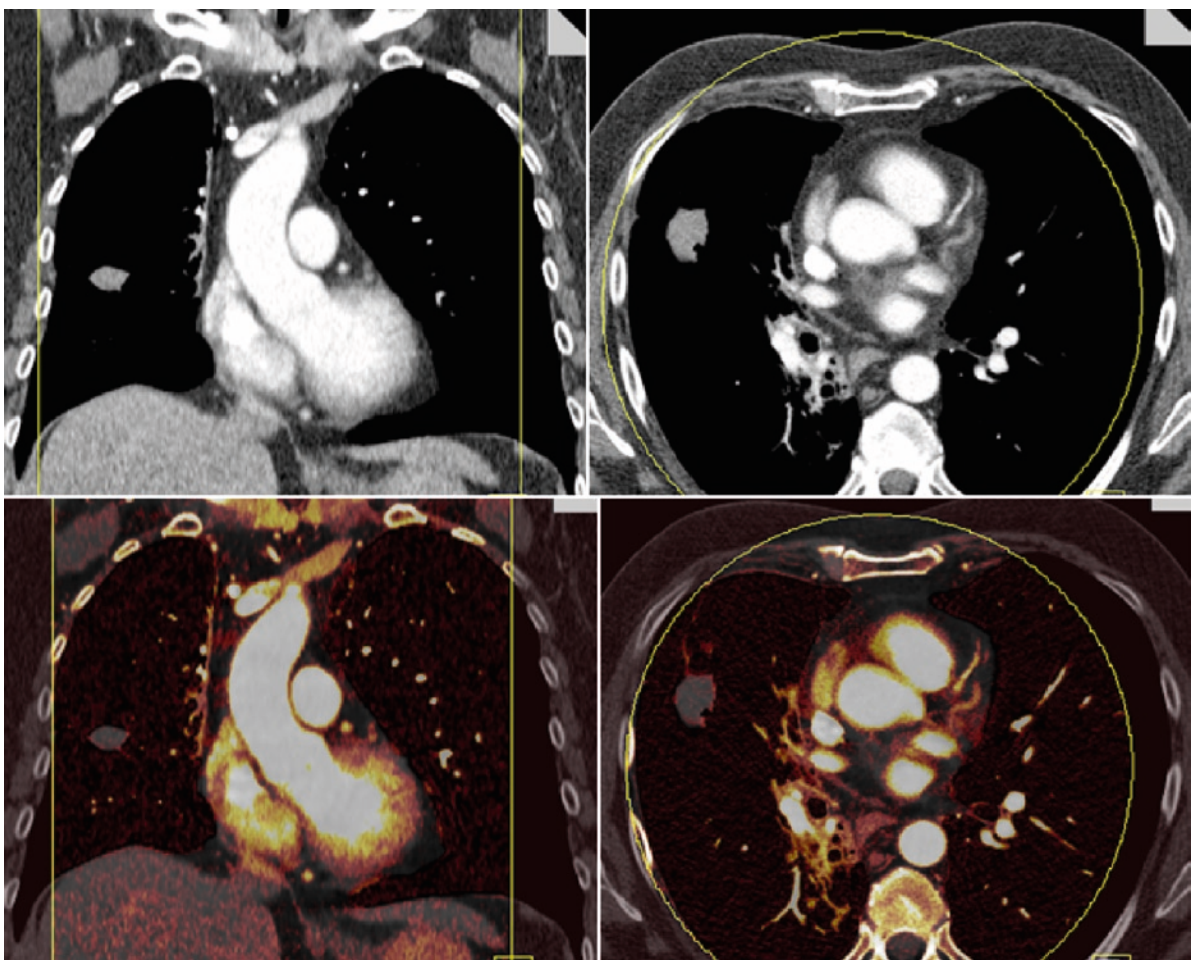

Fig. 2 DECT of a 63-year-old patient with an incidentally detected pulmonary nodule of soft tissue density and unclear dignity. DECT iodine maps (lower row) show only minor iodine uptake of the nodule indicating a benign lesion. CT guided biopsy revealed a hamartoma

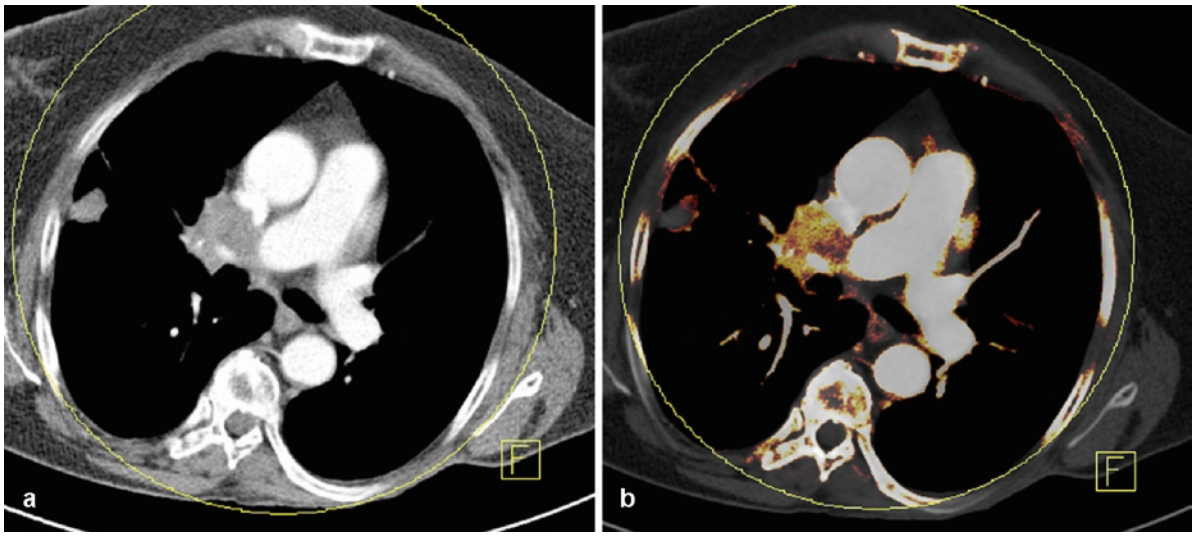

Fig. 3 Seventy-four-year-old patient with a central NSCLC and an additional peripheral pulmonary nodule of soft tissue density and unclear dignity within the right upper lobe (**a**). DECT iodine map (**b**) shows high iodine uptake of the central NSCLC but only minor iodine uptake within the peripheral pulmonary nodule as an indicator of benignity. Follow up CT scans revealed an inflammatory pseudotumor

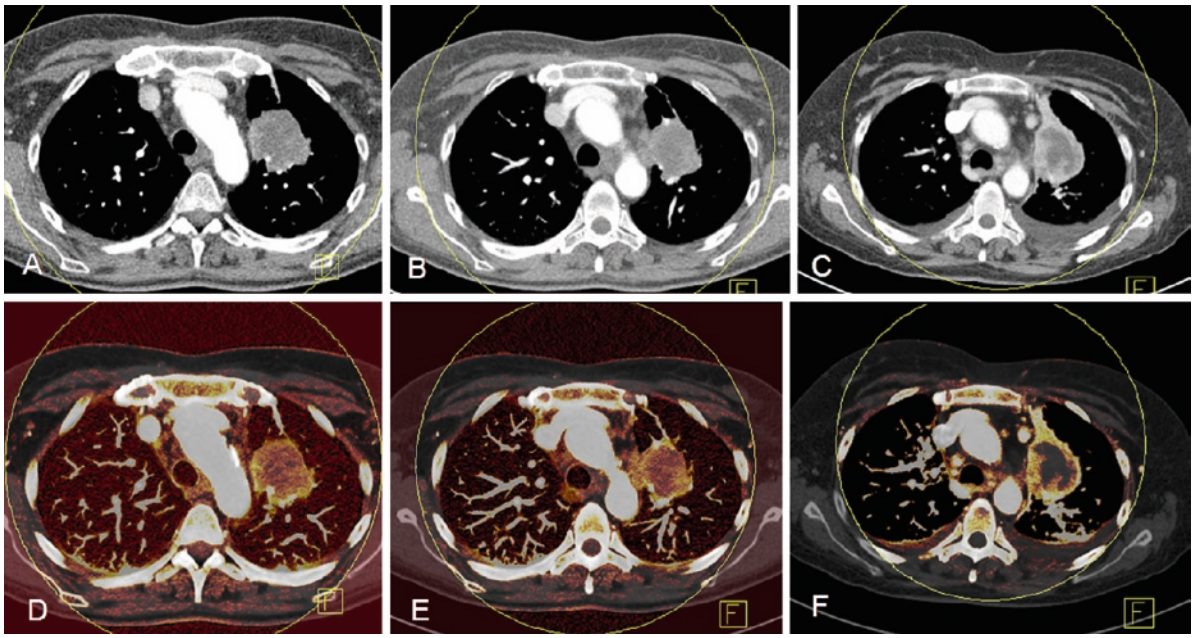

Fig. 4 Sixty-seven-year-old patient with NSCLC of the left upper lobe before (**a**, **d**) as well as two (**b**, **e**) and four (**c**, **f**) months after targeted therapy with a vascular endothelial growth factor (VEGF) receptor antibody. DECT iodine maps demonstrate decreasing tumor iodine uptake as a sign of therapy response. In contrast the "virtual" 120 kV DECT images show only minor density changes and stable tumor size according to RECIST criteria

Although Response Evaluation Criteria in Solid Tumors (RECIST) are the standard criteria for response evaluation of lung cancer in clinical trials, estimation of tumor response based on lesion size has several disadvantages which have to be considered (Fig. 5). First, response evaluation with morphologic imaging

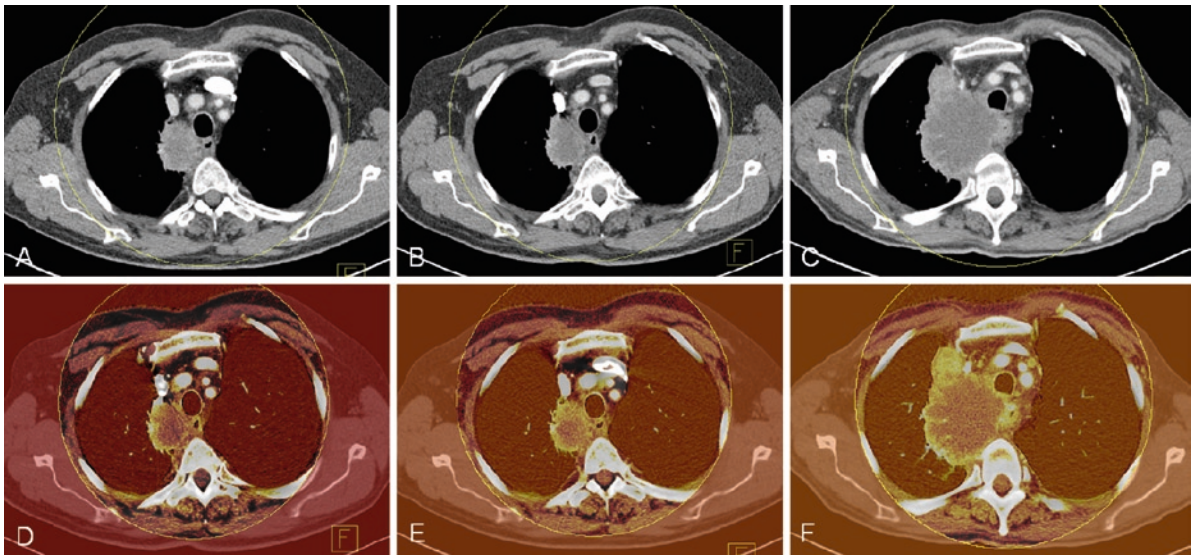

Fig. 5 DECT examinations of a 54-year-old patient with NSCLC of the right upper lobe at diagnosis (**a**, **d**) as well as three (**b**, **e**) and six (**c**, **f**) months after begin of chemotherapy. "Virtual" 120 kV CT images (*upper row*) show stable tumor size between the first and second CT scan and a massive tumor progression at the third CT scan. DECT iodine maps show a consistently high, or even increasing, iodine uptake of the tumor between the first and second CT scan indicating a non-responder. At the third CT scan there is a clear increase of iodine uptake as a sign of progression. Future studies have to evaluate whether tumor iodine uptake could be used as a surrogate parameter for response evaluation

has limitations in reliable differentiation of necrotic tumor or fibrotic scar from residual viable tumor tissue. Second, the objective response rates for various platinum-based regimens are in the range of 20–40% for advanced NSCLC (Guckel et al. 1996; Dewan et al. 1995). Because of the relatively slow tumor shrinkage a substantial percentage of patients may undergo several weeks of toxic therapy without clinical benefit. Thus, early prediction of tumor response is of particular importance to patients with advanced NSCLC. Furthermore, some of the new targeted therapies are cytostatic rather than cytoreductive, in which case successful treatment does not actually reduce tumor size, posing new demands on imaging techniques (de Geus-Oei et al. 2008; de Geus-Oei et al. 2007).

4 Scientific Evidence

Until now there is only one published study on DECT for the evaluation of pulmonary nodules. In this study, Chae et al. (Chae et al. 2008) investigated 49 consecutive patients who were scheduled for percutaneous needle aspiration of a pulmonary nodule with both, a standard non-enhanced single energy scan and a dedicated DECT performed on a first-generation dual source CT (SOMATOM Definition, Siemens).

In all patients, a dataset from the 80 kV tube, a dataset from the 140 kV tube, and a set of weighted average images were acquired from both a non-enhanced and a contrast-enhanced scan with a 3 minute scan delay. DECT was performed with 1.2 mm collimation, 50 mAs (effective) at 140 kV and 210 mAs (effective) at 80 kV, pitch of 0.7, and rotation time of 0.5 s. Tube currents of two x-ray tubes of 80 and 140 kV were fixed at a ratio of approximately 4:1. Image data were reconstructed with a section thickness of 2.0 mm using a D30 kernel and an increment of 2.0 mm. DECT image data were analyzed in this study by using the application "syngo Liver VNC" (Siemens), which is designed to process non-enhanced liver scans from contrast-enhanced DECT scans.

On virtual non-enhanced images, the number and size of calcifications within pulmonary nodules and lymph nodes were compared with those of a true non-enhanced average weighted CT image. On contrast, enhanced average weighted images, the number of detected calcifications was also recorded to determine how many calcifications are obscured on the average

weighted CT images. Attenuation was measured in two regions of interests in each pulmonary nodule. To assess whether differentiation of iodine was successful, the CT numbers of pulmonary nodules on virtual non-enhanced and true non-enhanced weighted average images, as well as CT numbers of the pulmonary nodules on iodine-enhanced image and the degree of enhancement were compared. The sum of CT numbers of pulmonary nodules on iodine-enhanced image and virtual non-enhanced image was compared with the CT number on contrast-enhanced weighted average image. The CT numbers of pulmonary nodules on iodine-enhanced image and the degree of enhancement were compared in terms of their diagnostic accuracy for distinguishing malignant and benign nodules with a 20-HU threshold, which was selected as a cutoff value based on previous studies on dynamic contrast enhanced CT (Swensen et al. 2000, 1995b, 1992; Yamashita et al. 1995; Swensen et al. 1995a).

In this study, 20 calcifications were present in pulmonary nodules of four patients and 45 calcifications were present in the lymph nodes of 11 patients on non-enhanced weighted average images. On virtual non-enhanced images, 85.0% (17 of 20) of calcifications in the nodules and 97.8% (44 of 45) of calcifications in the lymph nodes were detected. On virtual non-enhanced images, the sizes of the calcifications were smaller than those on non-enhanced weighted average images. The margin characteristics between virtual non-enhanced image and non-enhanced weighted average image showed a strong agreement. Virtual non-enhanced images had more noise in the majority of patients but had the same diagnostic quality than true non-enhanced images. Comparison of the CT number on non-enhanced weighted average and virtual non-enhanced images showed good agreement in this study. The CT numbers of pulmonary nodules on iodine-enhanced image and the degree of enhancement as determined by the difference of CT numbers of the contrast-enhanced and non-enhanced weighted average CT images also showed good agreement. The sum of the CT numbers of pulmonary nodules on iodine-enhanced image and virtual non-enhanced image showed a strong agreement with that on enhanced weighted average image. A total of 45 of 49 nodules were confirmed as benign or malignant on the basis of percutaneous needle aspiration, whereas four nodules could not confirmatively diagnosed. This was equivalent to a rate of malignancy of 55.6% (25 of 45 nodules). The results of both the CT number on iodine-enhanced images and the degree of enhancement showed that malignant nodules showed a significantly higher enhancement than benign nodules ($p = 0.001$). By comparing the diagnostic accuracy with a cutoff value of 20 HU for malignant nodules, iodine-enhanced images had a higher sensitivity and accuracy than the degree of enhancement.

Chae et al. used a contrast injection protocol with a fixed 3-min delay after injection of 100 mL iomeprol-300 (flow rate 3 mL/s). The rationale for this protocol was that most malignant pulmonary nodules will show the peak enhancement at approximately 3 min (Swensen et al. 1992; Jeong et al. 2005). For tumor staging an additional chest CT scan with a delay of 1 min was performed.

As the proposed scan protocol might not be practical in clinical routine we currently evaluate the feasibility of performing DECT with a fixed delay of 35 s using 80 mL iomeprol-400 with a flow rate of 2.5 mL/s. The advantage of this protocol is that no additional CT scan for tumor staging is required which reduces the radiation dose.

As in pulmonary embolism imaging, the scan direction with our contrast injection protocol should be caudo-cranial, because high-density contrast material in the superior vena cava and the right heart can affect the quality of the color coded iodine maps. Positioning of the patient in the center of the scanner is required using first generation dual-source CT to ensure that as much of the pulmonary parenchyma is covered by the smaller field-of-view of the second tube detector array. But even then in some patients the peripheral lung may be not covered obviating to characterize the iodine distribution in peripheral subpleural pulmonary nodules (Fig. 6). However, with the recently introduced second generation of DSCT scanners this might be improved as the field of view of the smaller detector was increased from 26 to 33 cm.

5 Conclusion

The differentiation of iodinated contrast media by DECT may be a potential surrogate marker for regional blood volume and thus angiogenesis. In pulmonary imaging, this is of potential value for non-invasive characterization of pulmonary nodules and response assessment in lung cancer.

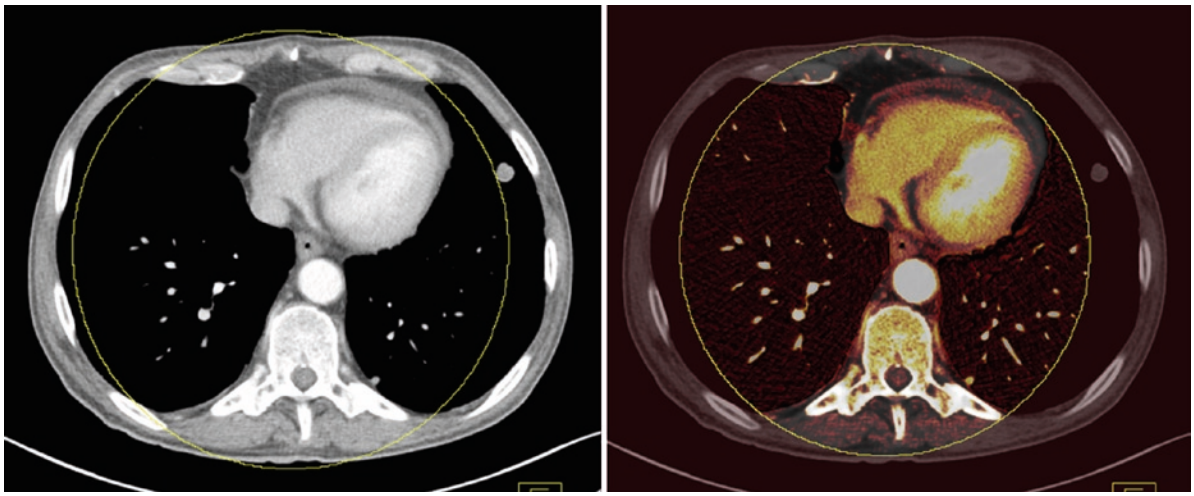

Fig. 6 Forty-eight-year-old patient with an incidentally detected pulmonary nodule of soft tissue density and unclear dignity. The field of view of the smaller B detector of the first generation dual source CT scanner is indicated by the yellow circle. In this patient, assessment of iodine uptake by DECT was not feasible as the pulmonary nodule was located outside the field of view of the B detector

Future studies have to evaluate whether the assessment of iodine as a surrogate for angiogenesis can be used for response assessment especially in patients undergoing targeted therapy. Furthermore, the technique might be used to differentiate viable tumor tissue from postobstructive atelectasis or fibrotic scar.

References

Chae EJ, Song JW, Seo JB, Krauss B, Jang YM, Song KS (2008) Clinical utility of dual-energy CT in the evaluation of solitary pulmonary nodules: initial experience. Radiology 249(2):671–681

Dewan NA, Reeb SD, Gupta NC, Gobar LS, Scott WJ (1995) PET-FDG imaging and transthoracic needle lung aspiration biopsy in evaluation of pulmonary lesions. A comparative risk-benefit analysis. Chest 108(2):441–446

Garcia-Barros M, Paris F, Cordon-Cardo C, Lyden D, Rafii S, Haimovitz-Friedman A, Fuks Z, Kolesnick R (2003) Tumor response to radiotherapy regulated by endothelial cell apoptosis. Science 300(5622):1155–1159

de Geus-Oei LF, van der Heijden HF, Visser EP, Hermsen R, van Hoorn BA, Timmer-Bonte JN, Willemsen AT, Pruim J, Corstens FH, Krabbe PF, Oyen WJ (2007) Chemotherapy response evaluation with 18F-FDG PET in patients with non-small cell lung cancer. J Nucl Med 48(10):1592–1598

de Geus-Oei LF, van Laarhoven HW, Visser EP, Hermsen R, van Hoorn BA, Kamm YJ, Krabbe PF, Corstens FH, Punt CJ, Oyen WJ (2008) Chemotherapy response evaluation with FDG-PET in patients with colorectal cancer. Ann Oncol 19(2):348–352

Guckel C, Schnabel K, Deimling M, Steinbrich W (1996) Solitary pulmonary nodules: MR evaluation of enhancement patterns with contrast-enhanced dynamic snapshot gradient-echo imaging. Radiology 200(3):681–686

Gupta NC, Frank AR, Dewan NA, Redepenning LS, Rothberg ML, Mailliard JA, Phalen JJ, Sunderland JJ, Frick MP (1992) Solitary pulmonary nodules: detection of malignancy with PET with 2-[F-18]-fluoro-2-deoxy-D-glucose. Radiology 184(2):441–444

Jeong YJ, Lee KS, Jeong SY, Chung MJ, Shim SS, Kim H, Kwon OJ, Kim S (2005) Solitary pulmonary nodule: characterization with combined wash-in and washout features at dynamic multi-detector row CT. Radiology 237(2):675–683

Johnson TR, Krauss B, Sedlmair M, Grasruck M, Bruder H, Morhard D, Fink C, Weckbach S, Lenhard M, Schmidt B, Flohr T, Reiser MF, Becker CR (2007) Material differentiation by dual energy CT: initial experience. Eur Radiol 17(6):1510–1517

Kono M, Adachi S, Kusumoto M, Sakai E (1993) Clinical utility of Gd-DTPA-enhanced magnetic resonance imaging in lung cancer. J Thorac Imaging 8(1):18–26, Winter

Kubota K, Matsuzawa T, Fujiwara T, Abe Y, Ito M, Hatazawa J, Ido T, Ishiwata K, Watanuki S (1988) Differential diagnosis of solitary pulmonary nodules with positron emission tomography using [11C]L-methionine. J Comput Assist Tomogr 12(5):794–796

Li Y, Yang ZG, Chen TW, Deng YP, Yu JQ, Li ZL (2008) Whole tumour perfusion of peripheral lung carcinoma: evaluation with first-pass CT perfusion imaging at 64-detector row CT. Clin Radiol 63(6):629–635

Littleton JT, Durizch ML, Moeller G, Herbert DE (1990) Pulmonary masses: contrast enhancement. Radiology 177(3): 861–871

Ng QS, Goh V, Milner J, Padhani AR, Saunders MI, Hoskin PJ (2007) Acute tumor vascular effects following fractionated radiotherapy in human lung cancer: In vivo whole tumor assessment using volumetric perfusion computed tomography. Int J Radiat Oncol Biol Phys 67(2):417–424

Orlacchio A, Schillaci O, Antonelli L, D'Urso S, Sergiacomi G, Nicoli P, Simonetti G (2007) Solitary pulmonary nodules: morphological and metabolic characterisation by FDG-PET-MDCT. Radiol Med 112(2):157–173

Patz EF Jr, Lowe VJ, Hoffman JM, Paine SS, Burrowes P, Coleman RE, Goodman PC (1993) Focal pulmonary abnormalities: evaluation with F-18 fluorodeoxyglucose PET scanning. Radiology 188(2):487–490

Swensen SJ (2000) Functional CT: lung nodule evaluation. Radiographics 20(4):1178–1181

Swensen SJ, Morin RL, Schueler BA, Brown LR, Cortese DA, Pairolero PC, Brutinel WM (1992) Solitary pulmonary nodule: CT evaluation of enhancement with iodinated contrast material – a preliminary report. Radiology 182(2)): 343–347

Swensen SJ, Brown LR, Colby TV, Weaver A (1995a) Pulmonary nodules: CT evaluation of enhancement with iodinated contrast material. Radiology 194(2):393–398

Swensen SJ, Morin RL, Aughenbaugh GL, Leimer DW (1995b) CT reconstruction algorithm selection in the evaluation of solitary pulmonary nodules. J Comput Assist Tomogr 19(6): 932–935

Swensen SJ, Viggiano RW, Midthun DE, Muller NL, Sherrick A, Yamashita K, Naidich DP, Patz EF, Hartman TE, Muhm JR, Weaver AL (2000) Lung nodule enhancement at CT: multicenter study. Radiology 214(1):73–80

Tateishi U, Kusumoto M, Nishihara H, Nagashima K, Morikawa T, Moriyama N (2002) Contrast-enhanced dynamic computed tomography for the evaluation of tumor angiogenesis in patients with lung carcinoma. Cancer 95(4):835–842

Viamonte M Jr (1965) Angiographic evaluation of lung neoplasms. Radiol Clin North Am 3(3):529–542

Yamashita K, Matsunobe S, Tsuda T, Nemoto T, Matsumoto K, Miki H, Konishi J (1995) Solitary pulmonary nodule: preliminary study of evaluation with incremental dynamic CT. Radiology 194(2):399–405

Yi CA, Lee KS, Kim EA, Han J, Kim H, Kwon OJ, Jeong YJ, Kim S (2004) Solitary pulmonary nodules: dynamic enhanced multi-detector row CT study and comparison with vascular endothelial growth factor and microvessel density. Radiology 233(1):191–199

Zhang M, Kono M (1997) Solitary pulmonary nodules: evaluation of blood flow patterns with dynamic CT. Radiology 205(2):471–478

Zielinski KW, Kulig A (1984) Morphology of the microvascular bed in primary human carcinomas of lung. Part I: Three-dimensional pattern of microvascular network. Pathol Res Pract 178(3):243–250

Myocardial Perfusion

Markus Weininger, U. Joseph Schoepf, Doo Kyoung Kang, Thomas Henzler, and Balasz Ruzsics

Contents

M. Weininger (✉) and B. Ruzsics
Department of Radiology and Radiological Science,
Medical University of South Carolina,
Ashley River Tower, 25 Courtenay Drive,
Charleston, SC 29401, USA
e-mail: weininge@musc.edu

U.J. Schoepf
Department of Radiology and Radiological Science,
Medical University of South Carolina,
Ashley River Tower, 25 Courtenay Drive,
Charleston, SC 29401, USA and
Department of Medicine, Division of Cardiology,
Medical University of South Carolina,
Charleston, SC, USA,
e-mail: schoepf@musc.edu

D.K. Kang
Department of Radiology, Ajou University Hospital,
Suwon, South Korea

T. Henzler,
Department of Radiology and Radiological Science,
Medical University of South Carolina,
Ashley River Tower, 25 Courtenay Drive,
Charleston, SC 29401, USA and
Department of Clinical Radiology and Nuclear Medicine,
University Medical Center Mannheim,
Medical Faculty Mannheim of the University of Heidelberg,
Theodor-Kutzer-Ufer 1-3, 68167 Mannheim, Germany

Abstract

› Myocardial perfusion is an important prognostic marker in the management of patients with suspected coronary artery disease as it demonstrates the hemodynamic consequences of coronary artery stenosis. The traditional diagnostic algorithm is based on a combination of physiological and anatomical testing using different modalities. Physiological testing, such as nuclear imaging, has been extensively validated for determining the effect of stenoses on the myocardial perfusion but provides only limited anatomical information. Conversely, anatomical testing, such as invasive coronary angiography, can directly visualize and grade coronary artery stenosis but has limitations for gauging their hemodynamic effect on the myocardial perfusion.

T.R.C. Johnson et al. (eds.), *Dual Energy CT in Clinical Practice*, Medical Radiology,
DOI: 10.1007/174_2010_31

- Accordingly, a single test allowing the comprehensive evaluation of all aspects of coronary artery disease is clinically desirable. There is early evidence that cardiac computed tomography (CT) performed in single- or dual-energy mode has the potential for an integrative evaluation of both, coronary artery anatomy as well as changes in the myocardial blood supply. Cardiac dual-energy CT is based on the more recent technology of dual-source CT, and exploits the fact that iodine-based contrast medium has unique spectral characteristics when penetrated with different X-ray energy levels, enabling mapping of the iodine (and thus blood) distribution within the myocardium.
- This chapter provides an overview about the role and current state of dual-energy CT in the evaluation of the myocardial perfusion.

1 Introduction

With an overall death rate of 262.5 per 100,000 in 2006, cardiovascular disease remains a most prevalent health issue in the United States and Western societies (Lloyd-Jones et al. 2009; Murray and Lopez 1997a, b). This has led to steady advancements in the development of both invasive and noninvasive techniques for the diagnosis and treatment of coronary artery disease (CAD). Myocardial perfusion imaging (MPI) has proven to be a valuable and reliable methodology in both, the diagnosis and prognosis of patients with CAD (Bastarrika et al. 2009; George et al. 2006). Pharmacologic-induced coronary vasodilation with dipyridamole or adenosine during the infusion of radionuclide tracers (Tl-201 or Tc-99m-sestamibi) has been shown to be as accurate as exercise stress testing with single photon emission tomography in diagnosing coronary disease (George et al. 2006). In addition, MPI can assess the physiologic significance of a stenosis and appropriately risk-stratify patients with intermediate stenosis (Gupta et al. 1992; Miller and Verani 1994; Nguyen et al. 1990).

Advances in computed tomography (CT) with growing applications in the noninvasive diagnosis of CAD have the potential of making cardiac CT an essential cornerstone in cardiovascular imaging (Bastarrika et al. 2009). The usefulness of multidetector row CT (MDCT) for ruling out significant coronary artery stenosis and for providing prognostic information in patients with suspected CAD has repeatedly been demonstrated (George et al. 2006, 2009; Lell et al. 2009; Leschka et al. 2009; Meijboom et al. 2008a, b; Ruzsics et al. 2009a). However, in its current form the diagnostic value of cardiac CT in further evaluating the functional significance of coronary stenosis remains uncertain as only limited data are available on this specific issue (Gaemperli et al. 2007; Hacker et al. 2005; Namdar et al. 2005). The strict morphological evaluation of coronary arteries using CT coronary angiography and the limited ability for dynamic evaluations of the passage of contrast medium through the myocardium on MDCT have been proven to be insufficient for a comprehensive evaluation and management of individuals with suspected CAD as it proved to be surprisingly difficult to predict the hemodynamic relevance of stenosis strictly based on anatomical data (Hacker et al. 2005; Rispler et al. 2007; Schuijf et al. 2006).

In clinical practice the physiological significance of coronary artery stenosis is typically assessed with MPI modalities during pharmacologically induced hyperemia. Single photon emission computed tomography (SPECT) is the most widely used modality, although magnetic resonance imaging (MRI) has demonstrated its superiority for detecting nontransmural perfusion defects mainly due to its higher spatial resolution (Hendel et al. 2006, 2009; Klocke et al. 2003; Schwitter et al. 2008).

However, according to current literature, the most recent advances in CT, including greater detector coverage and the availability of two generations of dual-source CT (DSCT), suggest the feasibility of CT as a stand-alone technology for an integrative evaluation of coronary heart disease allowing both, detailed assessment of coronary arteries and hemodynamic evaluation of detected coronary artery stenoses performing dynamic myocardial volume perfusion imaging of the heart (Ruzsics et al. 2008a, b, 2009a, b; Choi et al. 2009; Schwarz et al. 2008; Thilo et al. 2009).

2 Clinical Background

Myocardial perfusion is one of the most important prognostic indicators to determine patient outcome in the management of CAD (Marcassa et al. 2008). The underlying rationale of perfusion imaging is to demonstrate the hemodynamic consequence of an existing coronary artery stenosis on myocardial perfusion and function, which can be accentuated using ergometric exertion or by the administration of pharmacological agents simulating vasodilation (adenosine or dipyridamole) or exercise (dobutamine) (Schwarz et al. 2008).

Current guidelines recommend the use of clinically established noninvasive imaging tests, such as stress echocardiography and stress single photon emission CT, and MRI (Gibbons et al. 2003).

Stress echocardiography is based on the concept that ischemia induced by cardiovascular stress manifests as regional wall motion abnormality distal to an obstructive coronary lesion (Armstrong and Zoghbi 2005). A recent study by Heijenbrok-Kal comparing stress echocardiography with invasive coronary angiography reported a sensitivity of 79.1% and a specificity of 87.1% for the detection of coronary artery stenosis larger than 50% (Heijenbrok-Kal et al. 2007).

Nuclear perfusion studies using SPECT are based on the detection of perfusion-dependent emission rates of radiopharmaceuticals, which have been distributed throughout the blood flow and integrated into the myocardium (Maddahi et al. 1994). In the last decade several meta-analyses have been performed summarizing published data for each test, including a comparison of SPECT to invasive coronary angiography, reporting a sensitivity of 90.5% and a specificity of 81% for the detection of stenoses larger than 50% (Heijenbrok-Kal et al. 2007).

Similar to echocardiography, the detection of CAD using MRI is based on the detection of regional wall motion abnormalities during pharmacological stress using dobutamine or on the detection of perfusion defects with first-pass contrast enhancement of the myocardium after the administration of adenosine or dipyridamole using peak signal intensity and the slope of the signal intensity time curve as perfusion parameters (Eichenberger et al. 1994; Manning et al. 1991; Nagel et al. 1999; Schwitter et al. 2001; Wilke et al. 1997). Utilizing the detection of wall motion abnormalities, sensitivities of 86.2% and specificities of 87.5% have been reported for the diagnosis of coronary artery stenosis of more than 50% in comparison to invasive catheterization (Nagel et al. 1999). Comparable results have been reported for the identification of first-pass perfusion deficits (Merkle et al. 2007). Recently, the combination of a negative myocardial MR perfusion and dobutamine stress study has been reported to provide the highest negative predictive value in regard to the 3-year-cumulative event rate of patients with known or suspected CAD (Jahnke et al. 2007).

3 Dual-Energy CT for the Evaluation of Myocardial Perfusion

Dual-energy imaging as a subtraction technique based on the different tissue attenuation characteristics of soft tissue and bone has been recognized for a long time (Brody et al. 1981a, b; Genant and Boyd 1977). First attempts to apply the concept of dual-energy to CT date back more than two decades (Chiro et al. 1979; Kalender et al. 1986; Vetter et al. 1986). These early experimental prototypes ordinarily required the acquisition of two separate CT scans at different kilovolts levels with subsequent image coregistration, which limited the clinical application and precluded examination of the beating heart. However, with the introduction of the DSCT, the usefulness of this technique to perform contrast-enhanced, retrospectively ECG-gated DSCT angiography for noninvasive coronary artery stenosis detection has recently been demonstrated (Heuschmid et al. 2007; Johnson et al. 2007a; Leber et al. 2007).

The implementation of the dual-tube/dual-detector concept also for the first time enables a clinical acquisition of dual-energy CT (DECT) studies with a single CT examination (Flohr et al. 2006; Johnson et al. 2007b). When operated in dual-energy mode, the two tubes emit X-ray spectra of different energy levels that can be simultaneously registered in the corresponding detector array. At any given point in time, this provides synchronous dual-energy image information for the entire anatomy within the volume examined. There is early evidence that dual-energy techniques can be successfully applied to contrast-enhanced, retrospectively ECG-gated coronary CT angiography to evaluate the iodine signature within the myocardial blood pool (Ruzsics et al. 2008a).

4 Technical Background: Concept of Dual-Source CT and Dual-Energy Imaging

4.1 First-Generation Dual-Source CT

The first-generation DSCT system (SOMATOM Definition, Siemens Healthcare, Erlangen, Germany) comprises two X-ray tubes and two corresponding detectors, which are mounted onto the rotating gantry with an angular offset of 90°. One of the detectors covers the entire scan field of view (50 cm in diameter), whereas the other detector is restricted to a smaller, central field of view (26 cm in diameter) (Flohr et al. 2006; Petersilka et al. 2008). Using a dual-energy mode, the two acquisition systems can be operated independently with respect to tube voltage and current settings, allowing a simultaneous acquisition of high and low X-ray energy spectra during a single scan and facilitating a more detailed characterization of tissues (Flohr et al. 2006; Petersilka et al. 2008). The application of this principle has been proposed to the imaging of high-molecular weight contrast material and for the visualization of dynamic myocardial contrast enhancement corresponding to myocardial perfusion (Ruzsics et al. 2008a, b, 2009b).

4.2 Second Generation Dual-Source CT

Besides an increased scan field of the detector and high-pitch modes for fast spiral scanning, the most important improvement of second generation DSCT (SOMATOM Definition Flash, Siemens Healthcare, Erlangen, Germany) with respect to dual-energy perfusion imaging is prepatient filtration (Petersilka et al. 2008). For dual-energy scanning, the quality of the tube spectra is essential. The delineation of tissue is directly influenced by the differences of Hounsfield values that different tissues exhibit during examination at different tube voltages. As a consequence, a further increase in the voltage of tube A and a further decrease in the voltage of tube B improve dual-energy contrast. However, higher voltages than 140 kV only lead to minimal changes in iodine enhancement, and lower voltages than 80 kV worsen noise and thus soft tissue differentiation (Petersilka et al. 2008). The only possibility for improvement is the implementation of an additional prepatient filtration. The filter should consist of iodine itself or metals like indium, tin, antimony, and tellurium with similar absorption characteristics. With prefiltration of 0.5 mm tin (Sn) on tube A operated at 140 kV and tube B operated at 80 kV, DSCT has demonstrated an 80% improvement of the dual-energy contrast of bone and iodine, leading to increased material separation capabilities (Petersilka et al. 2008).

5 Scan Protocols

5.1 Single-Phase Contrast-Enhanced Dual-Energy Acquisition with First-Generation Dual-Source CT

Contrast-enhanced dual-energy images are acquired using a DSCT system (SOMATOM Definition) in dual-energy mode. A single CT acquisition can be obtained using the following parameters: 330 ms gantry rotation time, pitch of 0.2, 32×0.6 mm collimation with z-flying focal spot technique, and 165 ms temporal resolution (Ohnesorge et al. 2000). In dual-energy mode one tube of the DSCT system is operated with 150 mAs/rotation at 140 kV, the second tube with 165 mAs/rotation at 80 kV for slim (≤140 lbs) individuals, and 165 mAs/rotation at 100 kV for average-sized (≤200 lbs) and larger patients (Ruzsics et al. 2008b). ECG-dependent tube current modulation can be used with wider full dose pulsing windows (e.g., 35–75%) for faster and irregular heart rates and narrow full dose windows (e.g., 60–70%) for slower, more regular heart rates. During the remaining part of the cardiac cycle the tube output is reduced to approximately 20% by a corresponding decrease of the tube currents (Schwarz et al. 2008). Data acquisition should be in a craniocaudal direction with simultaneous recording of the patient's ECG signal to allow for retrospective registration of image reconstruction to the desired cardiac phase. The anatomical range typically extends from the level of the carina to just below the dome of the diaphragm.

Contrast enhancement can be achieved using the following tri-phasic injection protocol (Ruzsics et al.

2008b): the delay time before acquiring data after the start of the contrast injection can be determined by injecting a 20 mL test bolus of a nonionic contrast medium (Ultravist, 370 mgI/mL iopromide, Bayer-Schering, Wayne, NJ, USA) at a flow rate of 6 mL/s through an 18-gauge intravenous antecubital catheter, followed by 30 mL of saline using a dual-syringe injector (Stellant D, Medrad, Indianola, PA, USA). The peak time of test bolus enhancement, as measured by repetitive scanning at the level of the aortic root, should be used as the delay time. Actual contrast enhancement can be achieved by injecting an initial bolus of undiluted contrast medium, which is followed by a constant volume of 50 mL of a 70%/30% saline/contrast medium mixture and 30 mL of pure saline, all injected at 6 mL/s (Meijboom et al. 2008b). The volume of the initial iodine bolus can be individually calculated using the following formula: volume (milliliters) = duration of CT data acquisition (seconds) × 6. If the duration of CT data acquisition is <10 s, a minimum of 60 mL of contrast medium can be used.

5.2 Single-Phase Contrast-Enhanced Dual-Energy Acquisition with Second Generation Dual-Source CT

Using a second generation DSCT (SOMATOM Definition Flash), dual-energy studies can be acquired with retrospective ECG-gating, ECG-dependent tube current modulation, and the following scan parameters: 2 × 64 × 0.6 mm detector collimation with z-flying focal spot technique, 280 ms gantry rotation time, and heart rate adaptive pitch of 0.17–0.2 (Flohr et al. 2006). The tube associated with the larger detector array (B-tube) is operated with 140 mAs/rotation at 140 kV, and the second tube (A-tube) with 165 mAs/rotation at 100 kV. To maximize spatial resolution, the smallest possible field of view that encompasses the entire anatomy of the heart can be chosen for image reconstruction.

For contrast enhancement, a similar protocol as detailed above can be selected.

5.3 Three-Phase Contrast-Enhanced Dual-Energy Acquisition with First-Generation Dual-Source CT

Three-phase DECT studies are a combination of acquisitions during peak adenosine stress, at rest, and 6 min after the last contrast injection (Fig. 1). Similar to single-phase examinations, three-phase dual-energy studies are acquired with retrospective ECG-gating, ECG-dependent tube current modulation, and the following scan parameters: 330 ms gantry rotation time, heart rate-dependent pitch of 0.2–0.43, and 1.5 mm (stress, delayed) or 0.6 mm (rest) collimation. One tube of the DSCT system was operated with 150 mAs/rotation at 140 kV, and the second tube with 165 mAs/rotation at 80 kV.

Similar to stress perfusion MRI, stress testing using DECT is performed administering adenosine with a rate of 140 µg/min/kg under physician supervision.

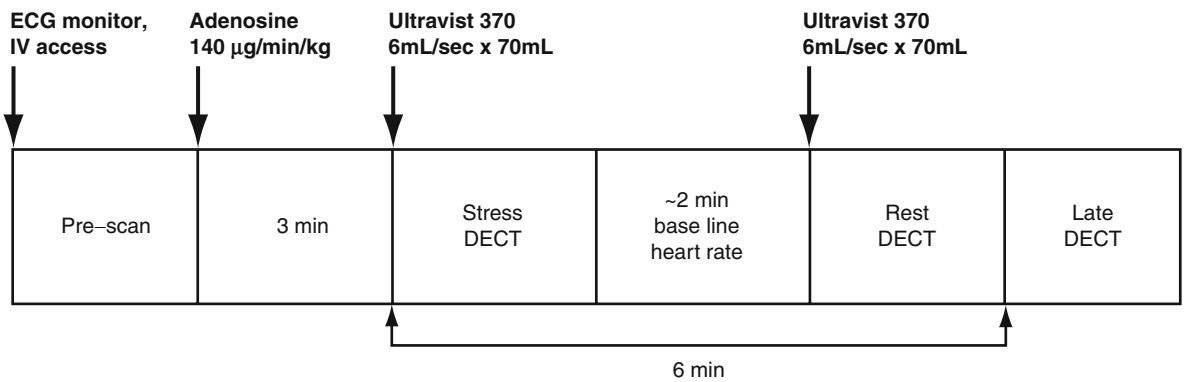

Fig. 1 Flow chart of a study protocol of three-phase DECT using first-generation DSCT

Stress and rest examinations should be contrast-enhanced with 70 mL of iopromide (370 mgI/mL Ultravist, Bayer) for each study, using a dual-syringe injector (Stellant D) and automated bolus triggering.

5.4 Three-Phase Contrast-Enhanced Dual-Energy Acquisition with Second Generation Dual-Source CT

Three-phase DECT studies, comprising peak adenosine-stress acquisitions, and acquisitions at rest and 6 min after the last contrast injection in dual-energy mode, can be accomplished applying the following scan parameters: 2×64×0.6 mm (stress, delayed) or 0.6 mm (rest) detector collimation, 280 ms gantry rotation time, and heart rate adaptive pitch of 0.17–0.2. The tube associated with the larger detector array (B-tube) is operated with 140 mAs/rotation at 140 kV, and the second tube (A-tube) with 165 mAs/rotation at 100 kV.

Contrast enhancement can be achieved by applying a contrast protocol comparable to three-phase acquisitions with first-generation DSCT.

6 Radiation Dose Considerations

Recent reports quantify the average dose equivalent that patients receive during a single-phase dual-energy acquisition using first-generation DSCT of 14±5 and 15.23±2.7 mSv, respectively (Ruzsics et al. 2008b, 2009b). This is in ranges well comparable to average effective radiation dose equivalents applied during single-energy 64-slice CT cardiac studies and less than the combination of morphological and functional tests (i.e., cardiac catheterization plus nuclear MPI), which would otherwise be required to derive a comparably comprehensive diagnosis (Coles et al. 2006; Hausleiter et al. 2006; Mettler et al. 2008). Applying a three-phase scan protocol, the effective radiation dose for first-generation DSCT is reported to be 20.1±2.6 mSv at stress, 15.3±2.0 mSv at rest, and 16.7±5.5 mSv for delayed enhancement. However, using second generation DSCT, radiation dose seems to markedly decrease to 12.8±2.4 mSv for stress, 9.1±3.1 mSv for rest, and 8.2±2.6 mSv for delayed-enhancement phases.

7 Postprocessing and Analysis of Myocardial Perfusion

Based on a single DECT data acquisition using the routine heart perfusion blood volume (PBV) application (*syngo* DualEnergy, Siemens Healthcare, Erlangen, Germany) of the DECT reconstruction algorithm, different image reconstructions can be performed with 0.75 mm reconstructed section width and 0.4 mm reconstruction increment (Ruzsics et al. 2008b, 2009b): (1) only using the high (140 kV) X-ray spectrum; (2) only using the low (80 kV/100 kV) energy X-ray spectrum; (3) merging data (30% low 100 kV energy spectrum and 70% high 140 kV energy spectrum); (4) DECT-based overlay of iodine distribution on "virtual non-contrast" (VNC) reconstructions in short- and long-axis views (Fig. 2) (Ruzsics et al. 2008a; Johnson et al. 2007b).

The specific absorption characteristics of iodine for X-rays of different kilovolt levels enable the computation of the iodine distribution within the myocardium, allowing to analyze the myocardial blood pool (Riederer and Mistretta 1977). The iodine maps are then superimposed onto grayscale multiplanar reformats (MPR) of the myocardium in short- and long-axis views, from which the iodine content in the voxels had been digitally subtracted using the "VNC" application of the dual-energy reconstruction algorithm (Ruzsics et al. 2008a; Johnson et al. 2007b). The resulting final images, which provide combined information on cardiac morphology and myocardial blood pool, can then be used to analyze myocardial perfusion and for the detection of myocardial ischemia based on DECT (Ruzsics et al. 2008b, 2009b).

Data sets are reconstructed using a dedicated dual-energy convolution kernel (D30f) with 1.5 mm thickness and 0.5 mm increment to optimize the signal-to-noise ratio. The generation of the "iodine maps" is a fully automated step. Thick MPR of 5 mm is the most useful for visualizing perfusion defects of the heart (Schwarz et al. 2008). Best results can be achieved when parameters for this calculation are individually adjusted: Determination of the attenuation of corresponding regions of interest (ROI) in the epicardial fat in high-voltage and low-voltage data sets and utilization of results for fat calibration of the heart PBV algorithm. Since the dataset contains a very broad

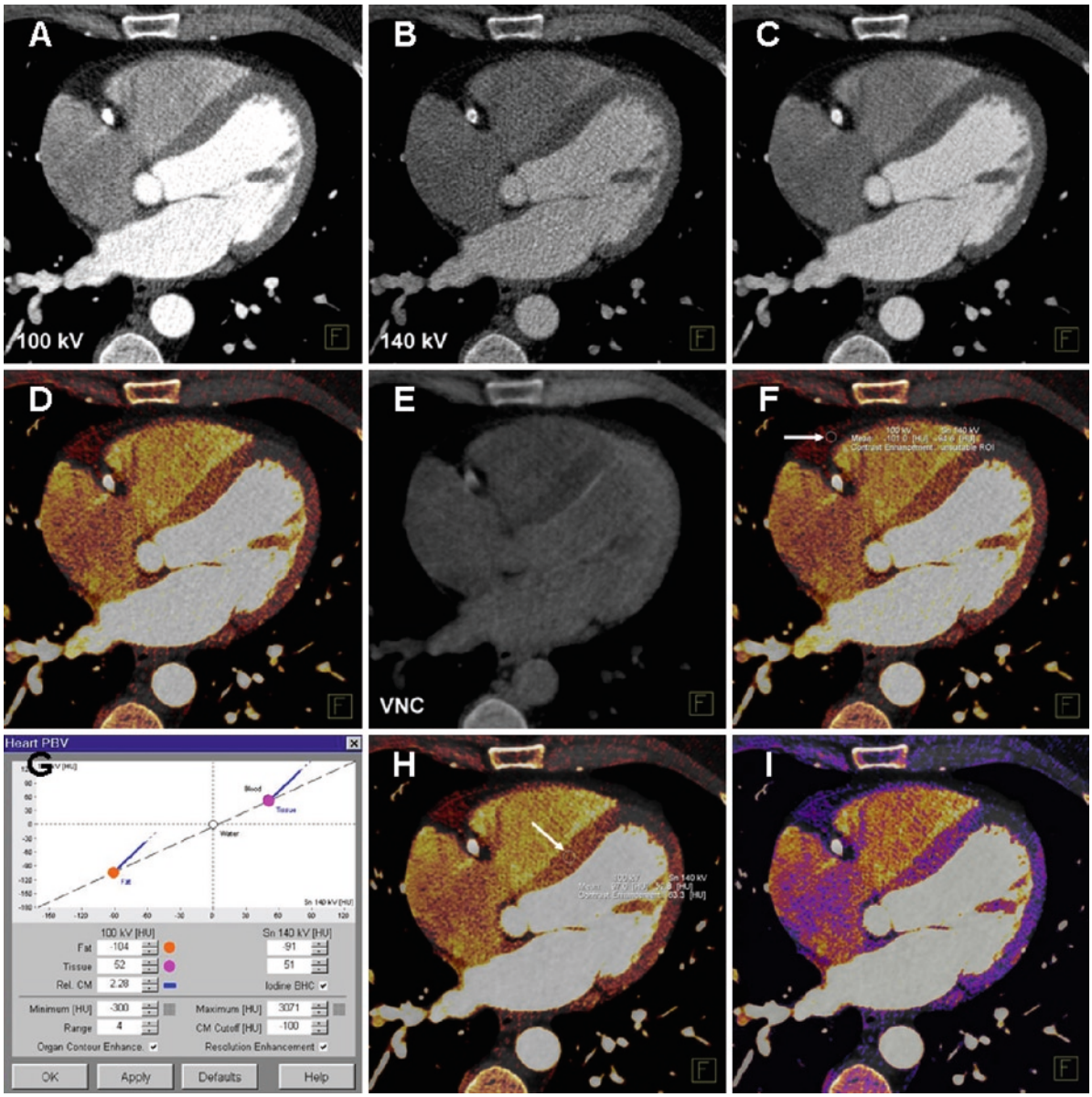

Fig. 2 Myocardial perfusion analysis based on iodine maps using DECT. Transverse 1.5 mm sections simultaneously acquired with low voltage (**a**) and high voltage (**b**), reconstructed with 330 ms temporal resolution and D30f kernel. Calculated merged image (**c**) is created by combining low image noise and high contrast resolution. Color-coded "iodine maps" (**d**) are superimposed onto "virtual non-contrast (VNC)" reconstructions (**e**). The attenuation of region of interest (*arrow*) in the epicardial fat (**f**) on the merged reconstruction is used for calibrating the Heart PBV algorithm (**g**). An area (*arrow*) with the highest iodine content (**h**) in the myocardium is chosen to normalize the iodine map to areas of normal myocardial perfusion. Fifty percent overlay (**i**) of the iodine map and the mixed reconstruction as 5 mm multiplanar reformation show a perfusion defect at cardiac apex. The "Micro-Delta-Hot-Metal" color-coding (**i**) is selected as it most closely resembles the image impression of SPECT myocardial perfusion studies

range of iodine concentrations, it is advisable to normalize the iodine map to areas of normal myocardial perfusion (Schwarz et al. 2008). This seems to be most reliable if areas with the highest iodine content in the myocardial wall are chosen for normalization (Schwarz et al. 2008). Alternatively, the right ventricle or right atrium can be used. The normalization only requires placing one ROI into any position on any slice of any MPR image of the whole data set.

There are several options for color-coding the iodine map. "Micro-Delta-Hot-Metal" color-coding seems to be preferential as it most closely resembles the image impression of SPECT myocardial perfusion studies. Another option to analyze iodine maps is the "General Viewing" reconstruction algorithm (Fig. 3). Using the fusion definition application, different color-codes for low or high kilovolts can be registered. Creating merged images from 70% of low tube voltage and 30% of high tube voltage with "Micro-Delta-Hot-Metal" color-coding seems to be preferential.

Ultimately, the myocardial blood volume is analyzed by determining the iodine content within the myocardium. Because iodinated contrast material is carried through the myocardium with the blood, myocardial perfusion deficits will result in decreased or absent iodine content within the affected myocardial segments, causing a "contrast defect" on CT. Contrast defects on DECT iodine maps can be defined as contiguous and circumscribed areas of decreased or absent iodine content within the left ventricular wall, relative to the remainder of the myocardium (Ruzsics et al. 2009b). Reporting of the perfusion analysis can be done according to the 17-segment model of the AHA/ACC (Cerqueira et al. 2002).

8 Clinical Application

Initial experiences suggest that dual-energy-based spectral CT imaging to evaluate myocardial perfusion is feasible and rest-DECT perfusion analysis correlates very well (90–96%) with fixed perfusion defects at 99m-Tc-Sestamibi-SPECT. In comparison to SPECT, DECT reported 91–92% sensitivity and 91–93% specificity with 91–93% accuracy for detecting myocardial perfusion deficits (Ruzsics et al. 2008b, 2009b). Additionally, coronary CTA had a 90–98% sensitivity, 88–94% specificity, and 92–93% accuracy for the detection of stenoses larger than 50% (Ruzsics et al. 2008b, 2009b). Without the administration of any pharmacological stressors, rest-DECT seems to be capable of identifying most (88%) of the reversible perfusion defects that are otherwise only seen during ergometrically or pharmacologically induced hyperemia at 99m-Tc-Sestamibi-SPECT (Ruzsics et al. 2008b, 2009b). This detection of reversible defects might be due to different myocardial distribution kinetics of iodine-based contrast media compared to radiopharmaceutic tracers of SPECT (Glover et al. 1995; Heymann et al. 1977). The intrinsically higher spatial and contrast resolution of CT in comparison to SPECT might also contribute to explain this phenomenon. This suggests that the quantification of perfusion based on CT has sufficient resolution to show small perfusion abnormalities without the need to administer pharmacological stress. Furthermore, it has been reported that CT myocardial imaging at rest demonstrates a characteristic enhancement pattern due to diminished capacitance of microvessels in the subendocardium during systole in ischemia (Nagao et al. 2008, 2009).

Early research supports the notion that DECT as stand-alone modality has the potential to reliably assess the luminal integrity of the coronary artery system, myocardial function, and myocardial perfusion based on one single contrast-enhanced CT scan within a few seconds and with reasonable radiation dose. The combination of examinations at rest and stress and the addition of delayed-enhancement imaging might allow for an integrative evaluation of coronary heart disease (Figs. 4–6). However, it is too early to predict the defined role of DECT imaging within the clinical pathways and the impact on the management of patients with suspected CAD.

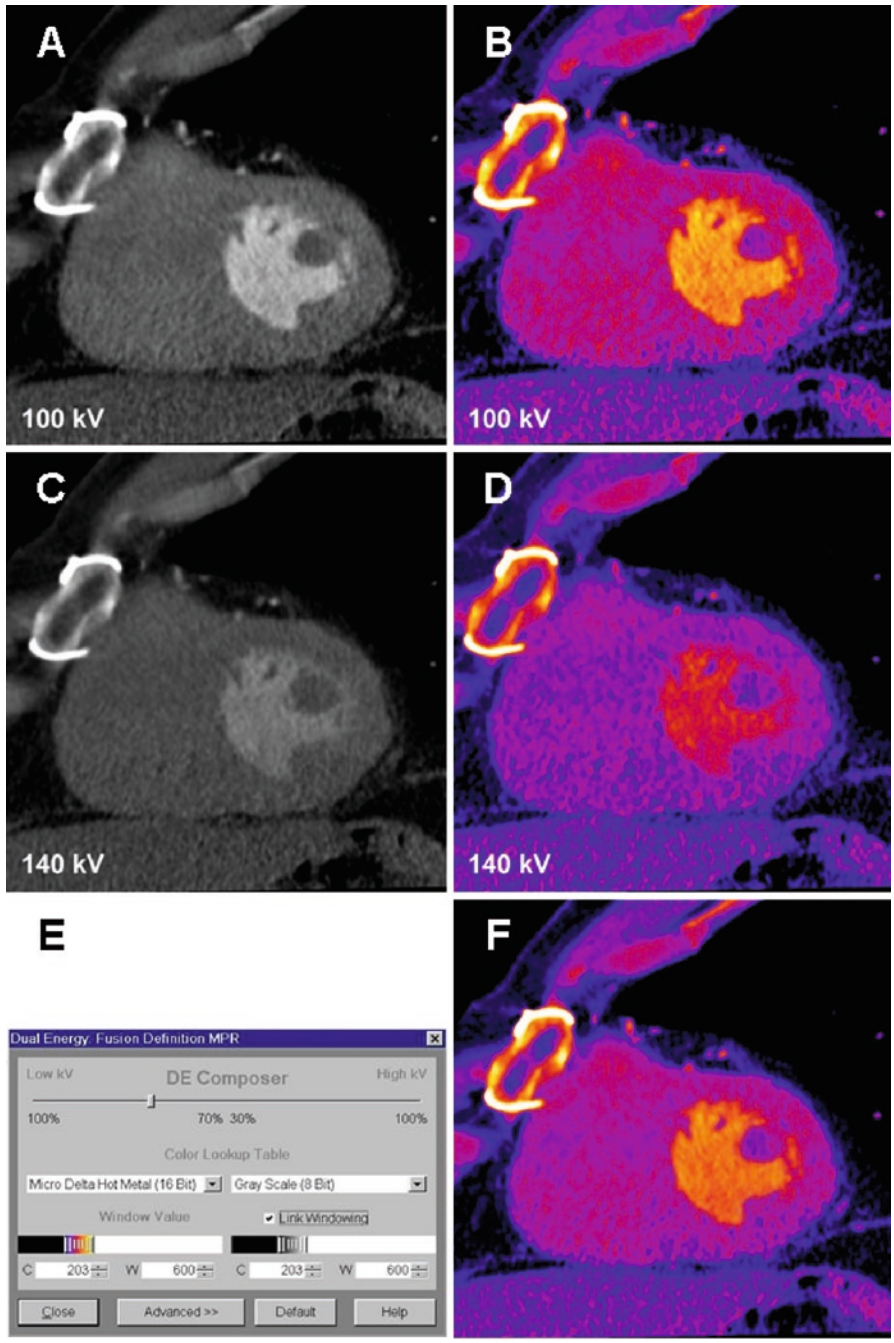

Fig. 3 Myocardial perfusion analysis based on iodine map using fusion definition of "General Viewing" tool. Short-axis view acquired with the low voltage (**a**) is converted to iodine map (**b**) using the color-coding option (Micro-Delta-Hot-Metal) of fusion definition application. Short-axis view acquired with high-voltage (**c**) is also converted to iodine map (**d**) by same application. Data acquired with low kilovolts show higher contrast grayscale image (**a**) and better differentiation of iodine concentration (**b**). Fusion definition (**e**) can simply merge images from low (70%) and high (30%) tube voltage with variable color-coding option. No myocardial iodine defect can be depicted on merged image (**f**) of iodine map acquired with high and low voltages

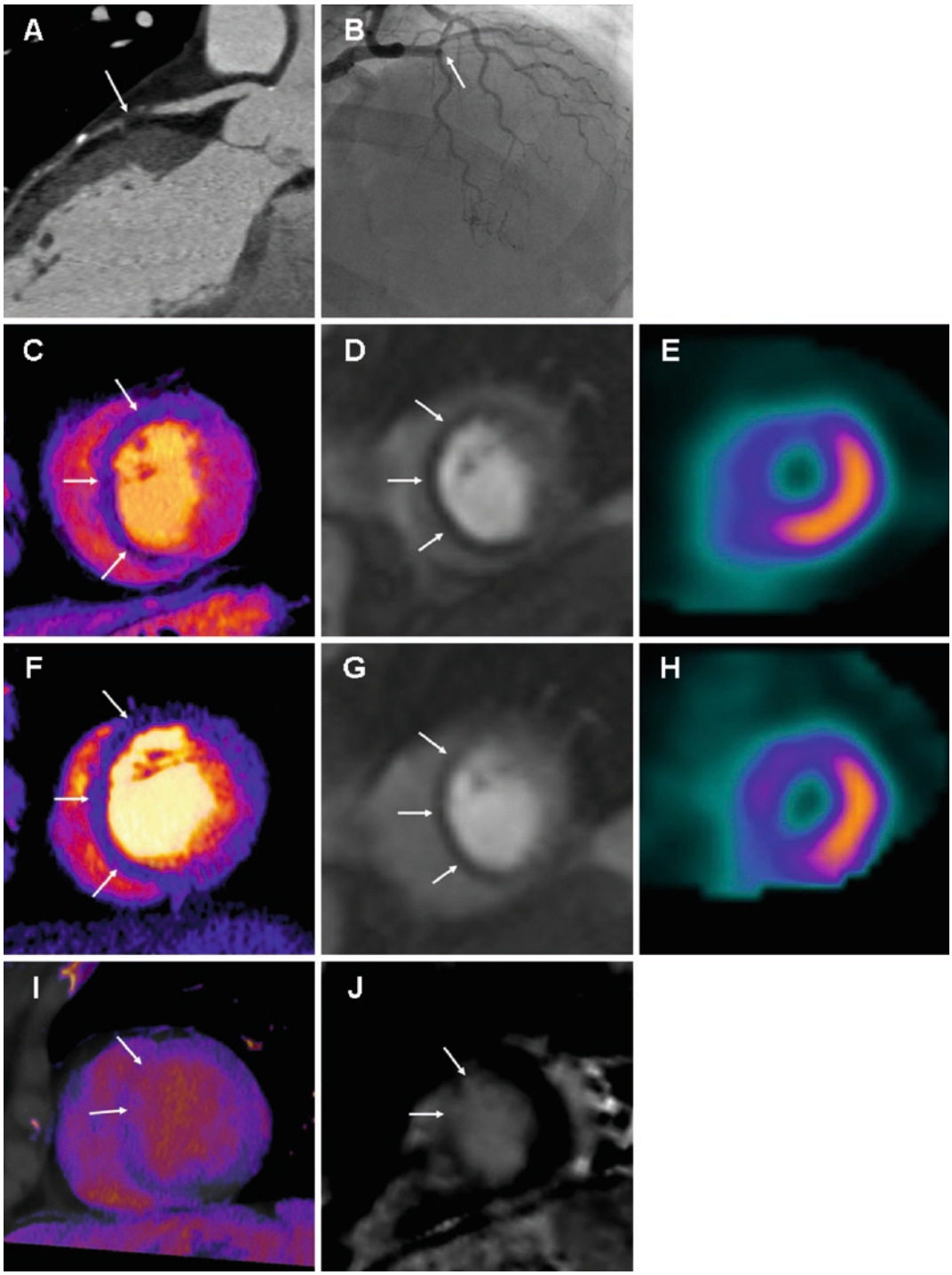

Fig. 4 Fifty-eight-year-old woman with abnormal SPECT examination. Coronary CT angiography (**a**) shows complete occlusion (*arrow*) of proximal left anterior descending artery (LAD). Invasive coronary angiography (**b**) confirms obstruction (*arrow*) of proximal LAD. Short-axis view of adenosine-induced stress (**c**) and rest (**f**) first-generation dual-energy CT at midventricular portion reveals fixed iodine defect of ventricular septum and anteroseptal myocardium of left ventricle (*arrows*) of corresponding LAD territory. Stress (**d**) and rest (**g**) MRI depicts fixed perfusion defect of corresponding ventricular septum (*arrows*). Stress-induced (**e**) and rest (**h**) SPECT reveals fixed perfusion defect of corresponding LAD territory. A transmural iodine uptake representing anteroseptal myocardial infarction (*arrows*) is visible on delayed DECT (**i**). Late-phase MRI (**j**) shows corresponding delayed myocardial hyperenhancement (*arrows*)

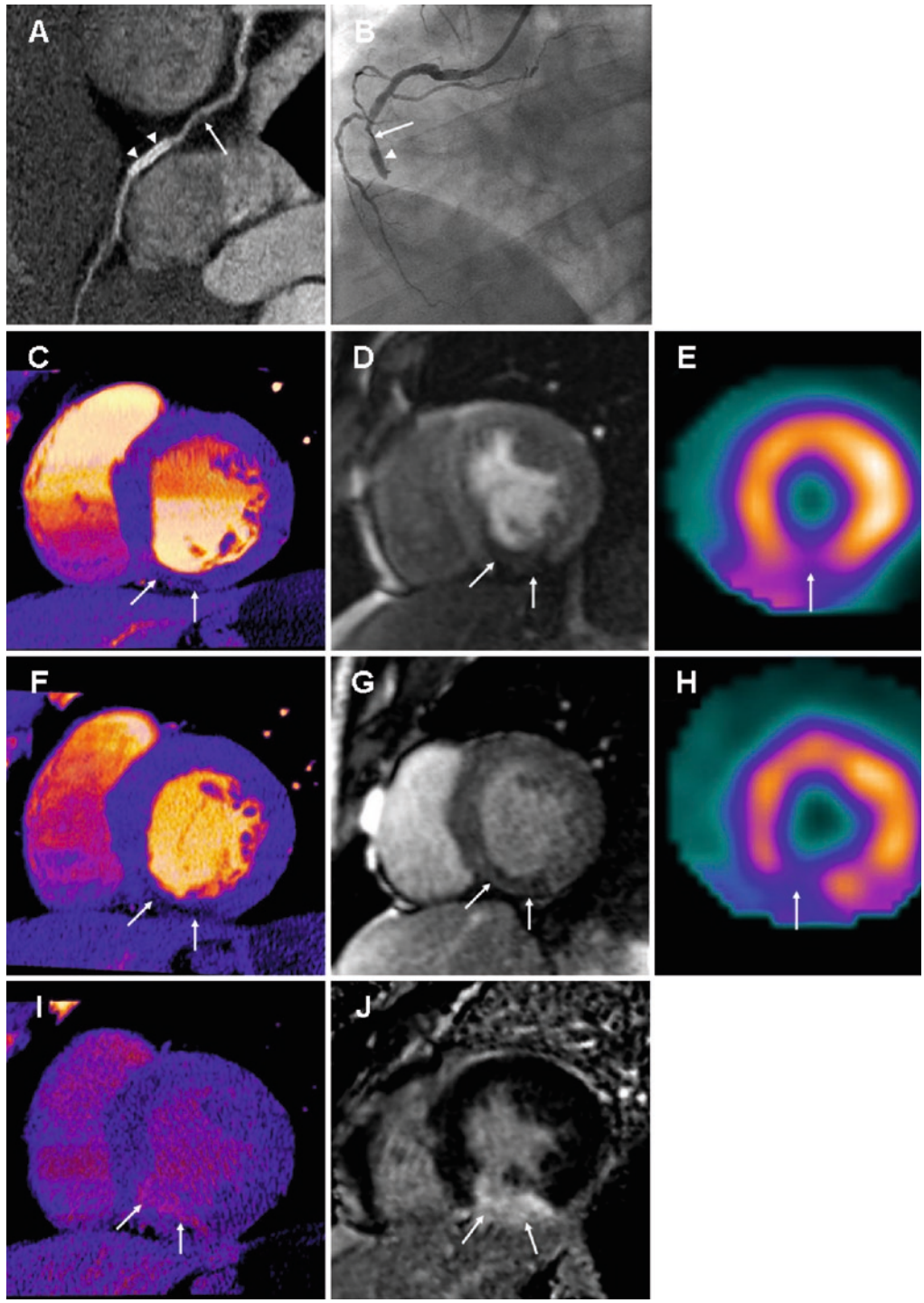

Fig. 5 Forty-six-year-old man with history of coronary artery disease and atypical chest pain. Coronary CTA (**a**) shows significant stenosis (*arrow*) proximal to stent (*arrow heads*) of right coronary artery (RCA) due to noncalcified plaque. Invasive catheterization (**b**) confirms significant mid-RCA stenosis (*arrow*) and patent stent (*arrowhead*), while RCA seems distally occluded with the presence of an antegrade collateral vessel. Short-axis view of adenosine-induced stress (**c**) and rest (**f**) second generation DECT at midventricular portion reveals fixed iodine defect of inferior wall of left ventricle (*arrows*) at RCA territory. Stress (**d**) and rest (**g**) MRI reveals fixed perfusion defect at corresponding inferior wall (*arrows*). Stress-induced (**e**) and rest (**h**) SPECT depicts fixed perfusion defect (*arrows*) at corresponding RCA territory. Delayed myocardial hyperenhancement (*arrows*) representing myocardial infarction is visible on both, late-phase DECT (**i**) and late-phase MRI (**j**)

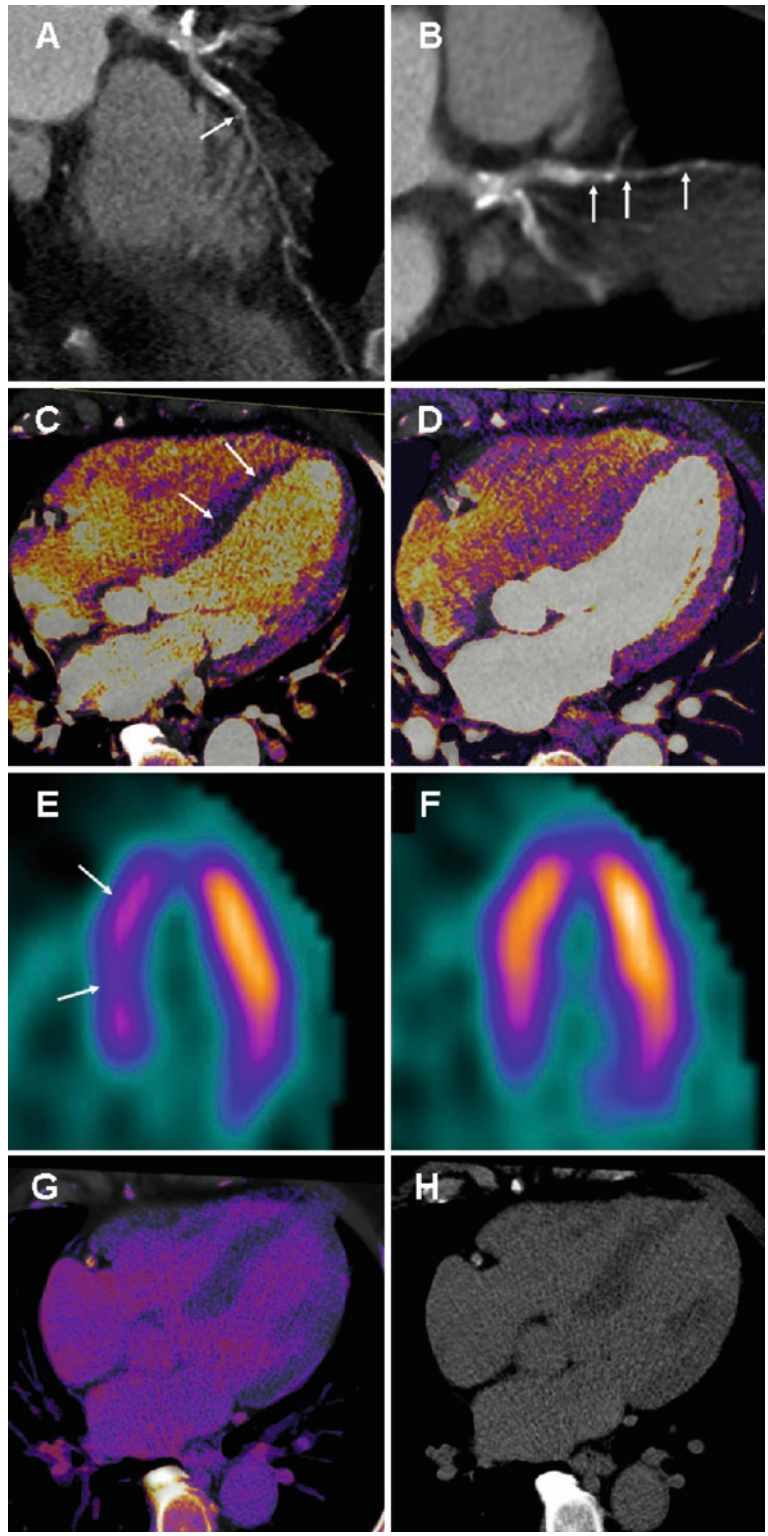

Fig. 6 Seventy-five-year-old woman with elevated troponin and increasing chest pain. Multiple mixed calcified and noncalcified plaques (*arrows*) resulting in higher grade stenoses are visualized at coronary CTA (**a**, **b**) within proximal portion of LAD. Four-chamber views of adenosine-induced stress (**c**) and rest (**d**) first-generation dual-energy CT reveal reversible iodine defect (*arrows*) of ventricular septum at LAD artery territory. Stress-induced (**e**) and rest (**f**) SPECT shows corresponding reversible perfusion defect (*arrows*) at LAD territory. No iodine uptake on delayed DECT (**g**) and no hyperenhancement on grayscale merged image (**h**) can be seen, consistent with myocardial ischemia

References

Armstrong WF, Zoghbi WA (2005) Stress echocardiography: current methodology and clinical applications. J Am Coll Cardiol 45(11):1739–1747

Bastarrika G et al (2009) CT of coronary artery disease. Radiology 253(2):317–338

Brody WR et al (1981a) A method for selective tissue and bone visualization using dual energy scanned projection radiography. Med Phys 8(3):353–357

Brody WR et al (1981b) Dual-energy projection radiography: initial clinical experience. AJR Am J Roentgenol 137(2): 201–205

Cerqueira MD et al (2002) Standardized myocardial segmentation and nomenclature for tomographic imaging of the heart: a statement for healthcare professionals from the Cardiac Imaging Committee of the Council on Clinical Cardiology of the American Heart Association. Circulation 105(4):539–542

Chiro GD et al (1979) Tissue signatures with dual-energy computed tomography. Radiology 131(2):521–523

Choi SI et al (2009) Recent developments in wide-detector cardiac computed tomography. Int J Cardiovasc Imaging 25(suppl 1):23–29

Coles DR et al (2006) Comparison of radiation doses from multislice computed tomography coronary angiography and conventional diagnostic angiography. J Am Coll Cardiol 47(9):1840–1845

Eichenberger AC et al (1994) Ischemic heart disease: assessment with gadolinium-enhanced ultrafast MR imaging and dipyridamole stress. J Magn Reson Imaging 4(3):425–431

Flohr TG et al (2006) First performance evaluation of a dual-source CT (DSCT) system. Eur Radiol 16(2):256–268

Gaemperli O et al (2007) Accuracy of 64-slice CT angiography for the detection of functionally relevant coronary stenoses as assessed with myocardial perfusion SPECT. Eur J Nucl Med Mol Imaging 34(8):1162–1171

Genant HK, Boyd D (1977) Quantitative bone mineral analysis using dual energy computed tomography. Invest Radiol 12(6):545–551

George RT et al (2006) Multidetector computed tomography myocardial perfusion imaging during adenosine stress. J Am Coll Cardiol 48(1):153–160

George RT et al (2009) Adenosine stress 64- and 256-row detector computed tomography angiography and perfusion imaging: a pilot study evaluating the transmural extent of perfusion abnormalities to predict atherosclerosis causing myocardial ischemia. Circ Cardiovasc Imaging 2(3):174–182

Gibbons RJ et al (2003) ACC/AHA 2002 guideline update for the management of patients with chronic stable angina–summary article: a report of the American College of Cardiology/American Heart Association Task Force on Practice Guidelines (Committee on the Management of Patients With Chronic Stable Angina). Circulation 107(1):149–158

Glover DK et al (1995) Comparison between 201Tl and 99mTc sestamibi uptake during adenosine-induced vasodilation as a function of coronary stenosis severity. Circulation 91(3): 813–820

Gupta NC et al (1992) Comparison of adenosine and exercise thallium-201 single-photon emission computed tomography (SPECT) myocardial perfusion imaging. The GE SPECT Multicenter Adenosine Study Group. J Am Coll Cardiol 19(2):248–257

Hacker M et al (2005) Comparison of spiral multidetector CT angiography and myocardial perfusion imaging in the noninvasive detection of functionally relevant coronary artery lesions: first clinical experiences. J Nucl Med 46(8): 1294–1300

Hausleiter J et al (2006) Radiation dose estimates from cardiac multislice computed tomography in daily practice: impact of different scanning protocols on effective dose estimates. Circulation 113(10):1305–1310

Heijenbrok-Kal MH, Fleischmann KE, Hunink MG (2007) Stress echocardiography, stress single-photon-emission computed tomography and electron beam computed tomography for the assessment of coronary artery disease: a meta-analysis of diagnostic performance. Am Heart J 154(3):415–423

Hendel RC et al (2006) ACCF/ACR/SCCT/SCMR/ASNC/NASCI/SCAI/SIR 2006 appropriateness criteria for cardiac computed tomography and cardiac magnetic resonance imaging: a report of the American College of Cardiology Foundation Quality Strategic Directions Committee Appropriateness Criteria Working Group, American College of Radiology, Society of Cardiovascular Computed Tomography, Society for Cardiovascular Magnetic Resonance, American Society of Nuclear Cardiology, North American Society for Cardiac Imaging, Society for Cardiovascular Angiography and Interventions, and Society of Interventional Radiology. J Am Coll Cardiol 48(7):1475–1497

Hendel RC et al (2009) ACCF/ASNC/ACR/AHA/ASE/SCCT/SCMR/SNM 2009 appropriate use criteria for cardiac radionuclide imaging: a report of the American College of Cardiology Foundation Appropriate Use Criteria Task Force, the American Society of Nuclear Cardiology, the American College of Radiology, the American Heart Association, the American Society of Echocardiography, the Society of Cardiovascular Computed Tomography, the Society for Cardiovascular Magnetic Resonance, and the Society of Nuclear Medicine: endorsed by the American College of Emergency Physicians. Circulation 119(22):e561–e587

Heuschmid M et al (2007) Usefulness of noninvasive cardiac imaging using dual-source computed tomography in an unselected population with high prevalence of coronary artery disease. Am J Cardiol 100(4):587–592

Heymann MA et al (1977) Blood flow measurements with radionuclide-labeled particles. Prog Cardiovasc Dis 20(1): 55–79

Jahnke C et al (2007) Prognostic value of cardiac magnetic resonance stress tests: adenosine stress perfusion and dobutamine stress wall motion imaging. Circulation 115(13):1769–1776

Johnson TR et al (2007a) Diagnostic accuracy of dual-source computed tomography in the diagnosis of coronary artery disease. Invest Radiol 42(10):684–691

Johnson TR et al (2007b) Material differentiation by dual energy CT: initial experience. Eur Radiol 17(6):1510–1517

Kalender WA et al (1986) Evaluation of a prototype dual-energy computed tomographic apparatus. I. Phantom studies. Med Phys 13(3):334–339

Klocke FJ et al (2003) ACC/AHA/ASNC guidelines for the clinical use of cardiac radionuclide imaging–executive summary: a report of the American College of Cardiology/American Heart Association Task Force on Practice Guidelines

(ACC/AHA/ASNC Committee to Revise the 1995 Guidelines for the Clinical Use of Cardiac Radionuclide Imaging). J Am Coll Cardiol 42(7):1318–1333

Leber AW et al (2007) Diagnostic accuracy of dual-source multi-slice CT-coronary angiography in patients with an intermediate pretest likelihood for coronary artery disease. Eur Heart J 28(19):2354–2360

Lell M et al (2009) Prospectively ECG-triggered high-pitch spiral acquisition for coronary CT angiography using dual source CT: technique and initial experience. Eur Radiol 19(11):2576–2583

Leschka S et al (2009) Diagnostic accuracy of high-pitch dual-source CT for the assessment of coronary stenoses: first experience. Eur Radiol 19(12):2896–2903

Lloyd-Jones D et al (2009) Heart disease and stroke statistics – 2010 update. A report from the American Heart Association. Circulation 121(7):e46–e215

Maddahi J et al (1994) State-of-the-art myocardial perfusion imaging. Cardiol Clin 12(2):199–222

Manning WJ et al (1991) First-pass nuclear magnetic resonance imaging studies using gadolinium-DTPA in patients with coronary artery disease. J Am Coll Cardiol 18(4):959–965

Marcassa C et al (2008) Clinical value, cost-effectiveness, and safety of myocardial perfusion scintigraphy: a position statement. Eur Heart J 29(4):557–563

Meijboom WB et al (2008a) Diagnostic accuracy of 64-slice computed tomography coronary angiography: a prospective, multicenter, multivendor study. J Am Coll Cardiol 52(25): 2135–2144

Meijboom WB et al (2008b) Comprehensive assessment of coronary artery stenoses: computed tomography coronary angiography versus conventional coronary angiography and correlation with fractional flow reserve in patients with stable angina. J Am Coll Cardiol 52(8):636–643

Merkle N et al (2007) Assessment of myocardial perfusion for detection of coronary artery stenoses by steady-state, free-precession magnetic resonance first-pass imaging. Heart 93(11):1381–1385

Mettler FA Jr et al (2008) Effective doses in radiology and diagnostic nuclear medicine: a catalog. Radiology 248(1): 254–263

Miller DD, Verani MS (1994) Current status of myocardial perfusion imaging after percutaneous transluminal coronary angioplasty. J Am Coll Cardiol 24(1):260–266

Murray CJ, Lopez AD (1997a) Global mortality, disability, and the contribution of risk factors: Global Burden of Disease Study. Lancet 349(9063):1436–1442

Murray CJ, Lopez AD (1997b) Mortality by cause for eight regions of the world: Global Burden of Disease Study. Lancet 349(9061):1269–1276

Nagao M et al (2008) Quantification of myocardial perfusion by contrast-enhanced 64-MDCT: characterization of ischemic myocardium. AJR Am J Roentgenol 191(1):19–25

Nagao M et al (2009) Detection of myocardial ischemia using 64-slice MDCT. Circ J 73(5):905–911

Nagel E et al (1999) Noninvasive diagnosis of ischemia-induced wall motion abnormalities with the use of high-dose dobutamine stress MRI: comparison with dobutamine stress echocardiography. Circulation 99(6):763–770

Namdar M et al (2005) Integrated PET/CT for the assessment of coronary artery disease: a feasibility study. J Nucl Med 46(6):930–935

Nguyen T et al (1990) Single photon emission computed tomography with thallium-201 during adenosine-induced coronary hyperemia: correlation with coronary arteriography, exercise thallium imaging and two-dimensional echocardiography. J Am Coll Cardiol 16(6):1375–1383

Ohnesorge B et al (2000) Cardiac imaging by means of electrocardiographically gated multisection spiral CT: initial experience. Radiology 217(2):564–571

Petersilka M et al (2008) Technical principles of dual source CT. Eur J Radiol 68(3):362–368

Riederer SJ, Mistretta CA (1977) Selective iodine imaging using K-edge energies in computerized X-ray tomography. Med Phys 4(6):474–481

Rispler S et al (2007) Integrated single-photon emission computed tomography and computed tomography coronary angiography for the assessment of hemodynamically significant coronary artery lesions. J Am Coll Cardiol 49(10):1059–1067

Ruzsics B et al (2008a) Images in cardiovascular medicine. Myocardial ischemia diagnosed by dual-energy computed tomography: correlation with single-photon emission computed tomography. Circulation 117(9):1244–1245

Ruzsics B et al (2008b) Dual-energy CT of the heart for diagnosing coronary artery stenosis and myocardial ischemia-initial experience. Eur Radiol 18(11):2414–2424

Ruzsics B, Chiaramida SA, Schoepf UJ (2009a) Images in cardiology: dual-energy computed tomography imaging of myocardial infarction. Heart 95(3):180

Ruzsics B et al (2009b) Comparison of dual-energy computed tomography of the heart with single photon emission computed tomography for assessment of coronary artery stenosis and of the myocardial blood supply. Am J Cardiol 104(3):318–326

Schuijf JD et al (2006) Relationship between noninvasive coronary angiography with multi-slice computed tomography and myocardial perfusion imaging. J Am Coll Cardiol 48(12):2508–2514

Schwarz F et al (2008) Dual-energy CT of the heart–principles and protocols. Eur J Radiol 68(3):423–433

Schwitter J et al (2001) Assessment of myocardial perfusion in coronary artery disease by magnetic resonance: a comparison with positron emission tomography and coronary angiography. Circulation 103(18):2230–2235

Schwitter J et al (2008) MR-IMPACT: comparison of perfusion-cardiac magnetic resonance with single-photon emission computed tomography for the detection of coronary artery disease in a multicentre, multivendor, randomized trial. Eur Heart J 29(4):480–489

Thilo C et al (2009) Integrated assessment of coronary anatomy and myocardial perfusion using a retractable SPECT camera combined with 64-slice CT: initial experience. Eur Radiol 19(4):845–856

Vetter JR et al (1986) Evaluation of a prototype dual-energy computed tomographic apparatus. II. Determination of vertebral bone mineral content. Med Phys 13(3):340–343

Wilke N et al (1997) Myocardial perfusion reserve: assessment with multisection, quantitative, first-pass MR imaging. Radiology 204(2):373–384

Part IV

Neuroradiological Imaging

Neurological Applications

Otto Rapalino, Shervin Kamalian, Rajiv Gupta, Catherine Phan, Stuart Pomerantz, Javier Romero, Mukta C. Joshi, and Michael Lev

Contents

Abstract

› Dual energy computed tomography (CT) methods are revolutionizing neurological imaging by refining material characterization using CT, improving the detection of contrast enhancement, and reducing scatter-related artifacts. These techniques improve our accuracy for differentiation of hemorrhage from calcification and contrast staining. They also allow the selection of lower energy X-ray beams that increase the conspicuity of intravascular enhancement, potentially useful in CT angiograms using low contrast doses. A new type of dual-energy CT technology called Gemstone Spectral Imaging (GE healthcare) also allows the selection of X-ray beams at specific energy levels to optimize parenchymal visualization. These applications offer a glimpse of the significant potential of dual-energy technology to expand the role of computed tomography in neuroimaging and cerebrovascular imaging.

Abbreviations

CDTIvol	Volume CT dose index
CIN	Contrast-induced nephropathy
CNR	Contrast-to-noise ratio
CT	Computed tomography
CTA	Computed tomography angiography
DE	Dual energy
DFOV	Display field of view
FOV	Field of view
GRE	Gradient-recalled echo
GSI	Gemstone spectral imaging

O. Rapalino (✉), S. Kamalian, R. Gupta, C. Phan, S. Pomerantz, J. Romero, and M. Lev
Neuroradiology Division, Department of Radiology, Massachusetts General Hospital, Boston, MA, USA
e-mail: orapalino@partners.org

M.C. Joshi
CT Engineering, GE Healthcare, Arlington, MA, USA

T.R.C. Johnson et al. (eds.), *Dual Energy CT in Clinical Practice*, Medical Radiology,
DOI: 10.1007/174_2010_32

HU	Hounsfield units
keV	Kiloelectron volt
kVp	Peak kilovoltage
ROI	Region of interest
SFOV	Scan field of view
SWI	Susceptibility-weighted imaging
VNC	Virtual noncontrast

1 Clinical Background

The use of conventional CT technology for central nervous system and cerebrovascular imaging has traditionally been limited by scatter-related artifacts and by the limited ability to differentiate among tissues and materials based on a limited range of attenuation values. Dual-energy CT is a revolutionary method for material characterization that improves visualization of vascular structures and identification of contrast enhancement and minimizes scatter-related artifacts.

For example, a common diagnostic dilemma faced by the neuroradiologist is the presence of a focal hyperdensity with intermediate attenuation values (between 70 and 80 HU) within the brain parenchyma on the initial CT scan in a patient with headache or a focal neurological deficit (Fig. 1). Is it a calcification or hemorrhage? MR imaging in this scenario is often difficult to interpret because both hemorrhage and calcification can produce local loss of signal on SWI or GRE sequences. A similar focal hyperdensity also appears in infarcted brain parenchyma after intra-arterial thrombolysis for acute stroke (Fig. 3). In this case, the interpreting radiologist wonders if this hyperdensity is a hemorrhage or contrast blush. The correct identification of the material responsible for this hyperdensity has very important clinical consequences in terms of diagnosis and treatment. Through analysis of the attenuation properties of these materials using X-rays of different energy levels, dual-energy CT imaging offers additional tools for tissue characterization, not only based on attenuation values, but also based on effective *Z*-values, making material composition analysis easier and more accurate.

Similarly, dual-energy imaging, particularly spectral imaging, is useful to improve the visualization of certain anatomic regions, such as the oral cavity, posterior fossa, lower cervical spinal canal, and inferior aspects of the temporal and frontal lobes, which are well known to suffer from significant degradation by scatter- and beam hardening-related artifacts (Papin and Rielly 1988; Barnea and Dick 1986; Dick et al. 1978).

Another potential application of dual-energy imaging is in patients with renal failure. A clinical problem often faced in cerebrovascular imaging in these patients is the necessity of using smaller amounts of intravenous contrast material during the acquisition of CT angiograms, often resulting in suboptimal arterial opacification. Dual-energy CT imaging can be used to perform CT angiograms with lower kiloelectron volt X-ray beams increasing the conspicuity of intravascular enhancement.

Dual-energy technology is also helpful to decrease radiation exposure of patients previously requiring pre and postcontrast scans. The generation of "virtual" noncontrast scans avoids the acquisition of an additional precontrast scan and decreases the overall radiation dose. It is also possible to create iodine maps demonstrating

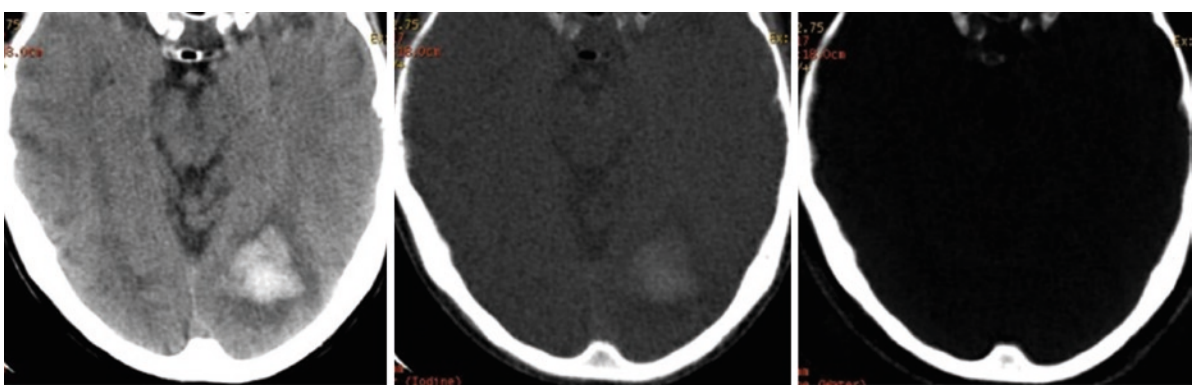

Fig. 1 Intraparenchymal hemorrhage in the left occipital lobe. (**a**) monochromatic image at 65 keV demonstrates a left occipital parenchymal hyperdensity. The hyperdensity persists in the water(calcium) image (**b**) and it disappears in calcium(water) image (**c**) confirming that this hyperdensity represents hemorrhage

the distribution of true parenchymal enhancement, overcoming the limitations produced by the presence of hemorrhagic products (e.g., immediate postoperative period), proteinaceous material, or calcification.

These potential clinical applications clearly demonstrate the great potential of dual-energy technology for neurological and cerebrovascular imaging. Future applications will likely include the use of gadolinium-based probes, gold nanoparticles, and new contrast agents taking advantage of this technology.

2 Physics Background

The materials most commonly used in the dual-energy evaluation of neurological pathologies include blood, iodinated contrast, and calcium. These materials have variable concentrations in the neural tissue and variable clinical importance depending on the specific pathology being evaluated (e.g., blood in cases of parenchymal hemorrhage; calcium and iodinated contrast for cerebrovascular imaging). These materials are qualitatively evaluated in combinations called material pairs. The material pairs typically assessed are water (iodine), water (calcium), iodine (calcium), and their reverse counterparts (Table 1). The images using these material pairs can be interpreted as reflecting the concentration of the first material (in terms of mg/cc) needed to produce the detected attenuation in that pixel, with the second material typically removed from the images.

3 Sample Scan Protocols

Several clinical protocols are available for the acquisition of dual-energy CT images using SOMATOM® definition (Siemens Medical Solutions) and Discovery™ CT750 HD (GE Healthcare) scanners (Tables 2 and 3).

Table 1 Table summarizing the appearance of the most common materials used in dual-energy CT imaging

Material pair	Water (iodine)	Iodine (water)	Water (calcium)	Calcium (water)
Acute blood	Hyperdense	Isodense	Hyperdense	Isodense
Iodinated contrast	Isodense	Hyperdense	Isodense	Mildly hyperdense
Calcification	Iso- to mildly hyperdense	Hyperdense	Iso- to mildly hypodense	Hyperdense

Table 2 Scanning CT parameters for different neuroimaging protocols using the Discovery™ CT750 HD (GE Healthcare) scanner

Protocol	Brain routine	Head CTA	Head and neck CTA
Scan mode	Spiral dual energy with fast kilovolt switching		
Scan area	Head	All intracranial vessels	All supraaortic vessels
Scan direction	Caudocranial		
Exposure time	2.87–4.61		
Tube voltage	80 kV/140 kV		
Tube current	~610		
CTDI vol	88.43	59.82	48.5
Rotation speed	0.6	0.8	0.6
Pitch	0.531:1	0.969:1	0.969:1
Acquisition	0.625 mm thickness/0.625 mm interval		
Reconstruction thickness (mm)	5	1.25	1.25
Reconstruction interval (mm)	5	0.625	0.625
FOV	DFOV = 25 cm	SFOV: head	

Table 3 Scanning CT parameters for the head and neck CTA protocol using the SOMATOM® definition (Siemens Medical Solutions) scanner

Scan mode	Spiral dual energy with dual source	
Scan area	All supraaortic vessels or intracranial	
Scan direction	Caudocranial	
Scan time	14.96 s	
Tube voltage A/B (kV)	140	80
Current tube (mA)	118	499
CTDI vol	66.58 mGy	
Rotation time	1.0 s	
Pitch	0.55	
Slice collimation	14 × 1.2 mm	
Reconstruction thickness	1.5 mm	
Reconstruction interval	0.7	
Reconstruction kernel	D30s	

Table 4 Contrast injection protocol

Iodine concentration	370 mg I/mL	
Protocol	Head CTA	Head and neck CTA
Total contrast volume based on patient's weight	65 mL<180 lbs 80 mL>180 lbs	85 mL<180 lbs 100 mL>180 lbs
Injection scheme	Monophasic	
Injection rate (cc/s)	5	3.5
Bolus timing	bolus tracking	
Bolus tracking threshold	75 HU	
ROI position	Ascending aorta	
Monitoring delay	10 s	
Saline flush volume	40 cc	
Saline injection rate (cc/s)	5	3.5
Needle size	18 G	
Injection site	Antecubital vein	

4 Contrast Material Injection

The type, amount, and rate of injection of contrast material are the same as non-dual-energy scans (Pomerantz et al. 2006). Nonionic iodinated contrast material (typically Isovue 300®) is used routinely. The typical amount of contrast injected for a head CTA is 65 cc for patients weighing less than 180 lbs at 5 cc/s. The contrast dose for patients >180 lbs is 80 cc at the same rate. For neck CTA studies (subacute stroke protocol), the contrast dose is 80 cc injected at 3.5 cc/s. The timing of the injection is determined using bolus triggering or test bolus techniques aiming to a target intra-arterial attenuation values >300 (Pomerantz et al. 2006; Schuknecht 2004). Dual-head power injection with a saline chaser is also routinely used. If delayed images are considered, the amount of contrast is increased to 100 cc and a delayed scan is typically obtained 60 s after the initial injection. A contrast dose of 2 cc/kg is used in the pediatric population and injection rates are individualized depending on the patient's age and type of available vascular access (Table 4).

5 Postprocessing

The dual-energy data obtained with these neuroimaging CT protocols can be postprocessed at the scanner or using dedicated workstations equipped with appropriate postprocessing software (e.g., GSI viewer or Syngo™ DE Brain Hemorrhage software packages). The GSI viewer software (GE Healthcare) allows the user to obtain scatter plots, histogram analysis, or attenuation curves based on the attenuation values, equivalent concentration (mg/cc), and apparent *Z*-values. Images can also be displayed with color overlays based on attenuation or effective *Z*-values. Monochromatic images can be obtained at any desired kiloelectron volt values within the energy spectrum from 40 to 140 keV (101 user selectable energy levels).

Dual-energy data acquired with the SOMATOM® definition (Siemens Medical Solutions) scanner are postprocessed using the Syngo™ DE Brain Hemorrhage module. A three-material decomposition algorithm (brain parenchyma, hemorrhage, and iodine) is used. From the original dual-energy data, a virtual noncontrast (VNC) image and an iodine overlay image are obtained.

6 Potential Diagnostic Utility

6.1 Intracranial Hemorrhage, Contrast Staining, and Calcification

Dual-energy CT techniques, particularly GSI, are very helpful in differentiating intracranial hemorrhage from calcification (Hawkes et al. 1986; Primak et al. 2009; Tran et al. 2009; Ferda et al. 2009) (Figs. 1 and 2) or contrast staining (Fig. 3). Tran et al. (2009) demonstrated that dual-energy CT is very accurate in differentiating between calcification and iodinated contrast staining (accuracy >90%) in the presence of high concentrations of hydroxyapatite and iodine. Calcium removal was also better in regions with high

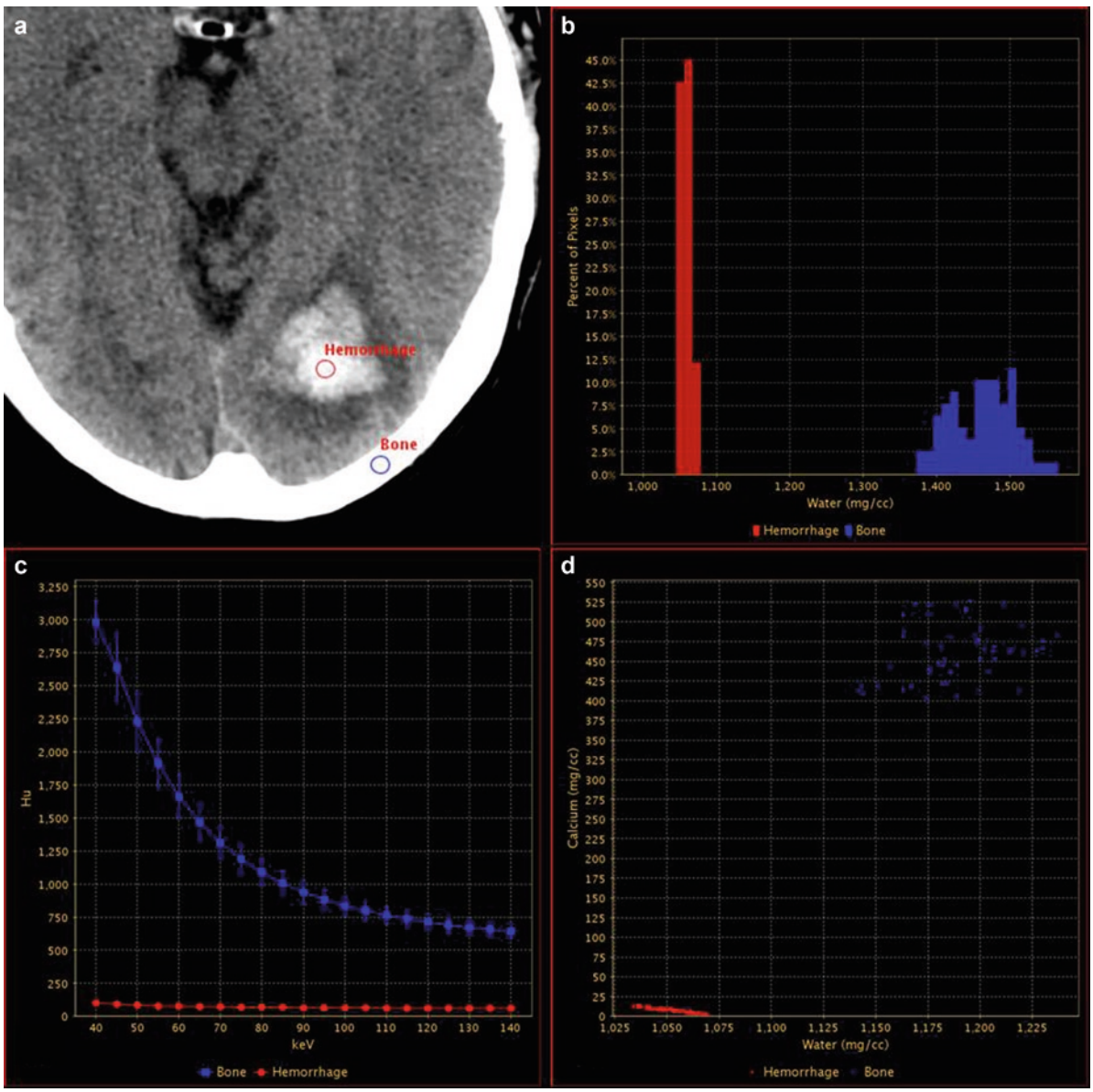

Fig. 2 Differentiation of intraparenchymal hemorrhage and calcification. Axial monochromatic image at 70 keV (**a**) shows the same left occipital parenchymal hemorrhage as in Fig. 1. Regions of interest (ROIs) are present within the hemorrhage and in the diploic space of the adjacent bone. Material composition analysis can be displayed as histograms (**b**), attenuation curves (**c**), or scatter plots (**d**)

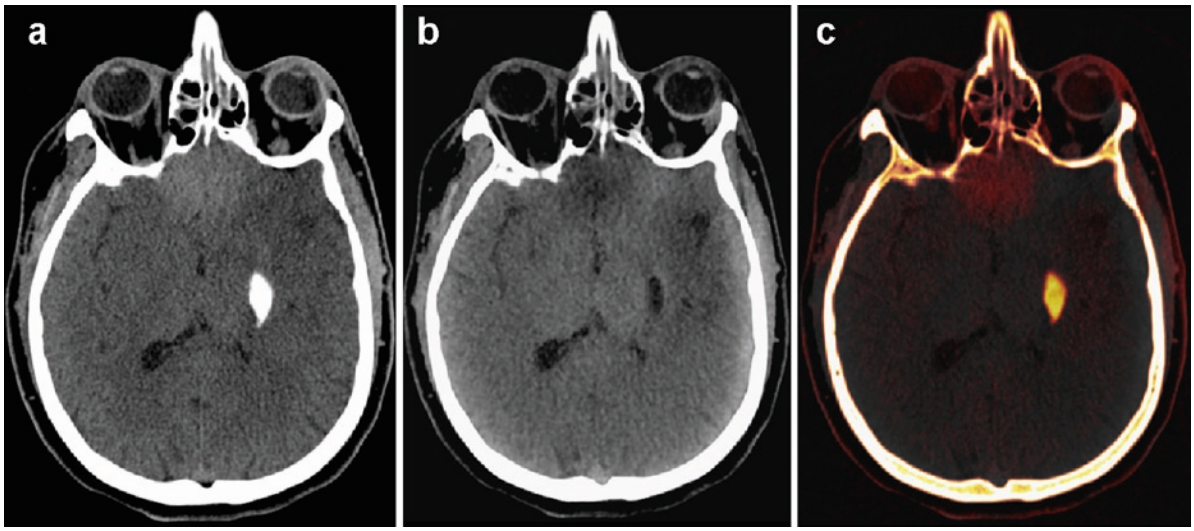

Fig. 3 (**a**) Focal intraparenchymal hyperdensity in the left lenticular nucleus in a patient with a left middle cerebral artery (MCA) infarct after intra-arterial thrombolysis. The hyperdensity disappears in the virtual noncontrast (VNC) image (**b**) and it is replaced by a focal hypodensity related to the infarct. Iodine overlay image (**c**) confirms that this hyperdensity represents contrast staining after intra-arterial thrombolysis. These images were acquired using a SOMATOM® definition (Siemens Medical Solutions) scanner

concentration of hydroxyapatite and contrast material. However, the accuracy values decreased with lower and more clinically relevant concentrations of these materials, with accuracy values of about 81.3 and 78.9%, respectively, for identification of iodinated contrast and calcium hydroxyapatite.

The ability to separate iodine from other materials can be used to generate VNC CT images, avoiding additional radiation exposure of the patient to obtain precontrast images (Graser et al. 2009) (Figs. 3 and 4). Pure iodine maps can also be useful in the characterization of CNS pathologies (e.g., brain tumors) and separating areas of enhancement from areas with increased cell density, intratumoral hemorrhage, increased protein content, or calcification/mineralization (Tran et al. 2009; Balvay et al. 2009).

6.2 Carotid Plaque Characterization

Dual-energy techniques can be used to characterize the different materials present in atheromatous plaques (Das et al. 2009; Barreto et al. 2008) and to suppress calcium deposits within them to improve visualization of intraluminal and plaque enhancement (Lell et al. 2009a, b; Buerke et al. 2009; Chen et al. 2009; Uotani et al. 2009) (Figs. 5 and 6).

Characterization of plaque morphology and composition is increasingly recognized as an important stroke risk factor. Imaging features of the atheromatous plaque that are often considered important in the risk assessment for stroke include the presence of severe luminal stenosis, endothelial ulceration, and vasa vasorum enhancement (Kerwin et al. 2008; Granada and Feinstein 2008; Langheinrich et al. 2007; Romero et al. 2009). Das et al. (2009) demonstrated high sensitivity for detection of atheromatous calcifications, mixed plaques, and fatty changes in plaques using dual-source CT angiography. Barreto et al. 2008 published data showing that dual-energy CT is able to differentiate densely calcified and fibrocalcific plaques from other types of atheromatous plaques (e.g., fibrous or lipid-rich).

6.3 CT Angiography and Perfusion with Low Contrast Volumes

The ability of Gemstone Spectral Imaging (GSI) to provide a wide range of monochromatic kiloelectron volt representations allows the performance of contrast-enhanced CT studies using low concentrations of contrast. The use of low doses of contrast is particularly important in patients with renal dysfunction. The combination of low monochromatic kiloelectron volt

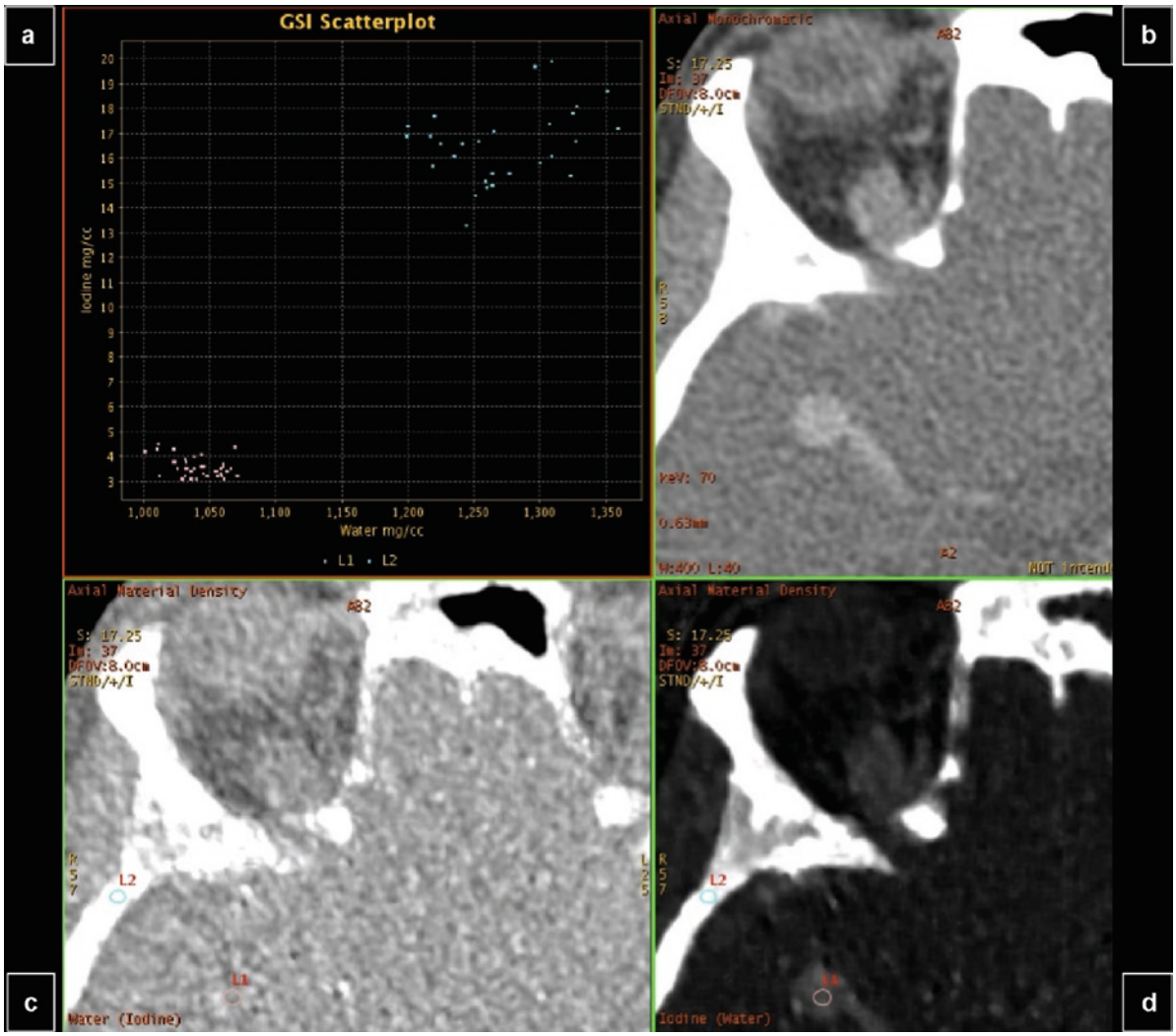

Fig. 4 Differentiation of calcium vs. iodinated contrast using GSI. ROIs were placed in an aneurysm near the right MCA bifurcation and in the right lesser wing of the sphenoid bone. (**a**) Scatter plot analysis of iodine content demonstrates accurate differentiation between contrast material within the aneurysm and calcium present in bone. (**b**) Axial monochromatic image at 70 keV. (**c**) Water (iodine) image demonstrating suppression of iodinated contrast material resulting in a virtual noncontrast image. (**d**) Iodine (water) image demonstrating intraluminal enhancement within the aneurysm

images with the high spatial resolution provided by the Gemstone HD detector results in diagnostic CT angiograms, despite low intravascular concentrations of iodinated contrast (Figs. 7–9). Iodine maps can accurately detect small concentrations of iodinated contrast (Fig. 10).

Contrast-induced nephropathy (CIN) is the third most frequent etiology of acute renal failure in the inpatient setting (Massicotte 2008). The pathogenesis of this condition is poorly understood, but appears to be the result of decreased medullary renal blood flow and a direct tubular cytotoxic/apoptotic effect produced by the contrast material (Thomsen et al. 2008a; Romano et al. 2008; Liss et al. 2009; Kwak et al. 2005). There is also apparent direct correlation between the amount of intravenous contrast administered during a contrast-enhanced CT examination and the risk of developing CIN (Morcos 2009; Marenzi et al. 2009; Holmquist et al. 2009; Thomsen and Morcos 2009; Nyman et al. 2005, 2008; Mekan et al. 2004; Lang et al. 1981; Kane et al. 2008). Kane et al. (2008) demonstrated a direct correlation between the amount of

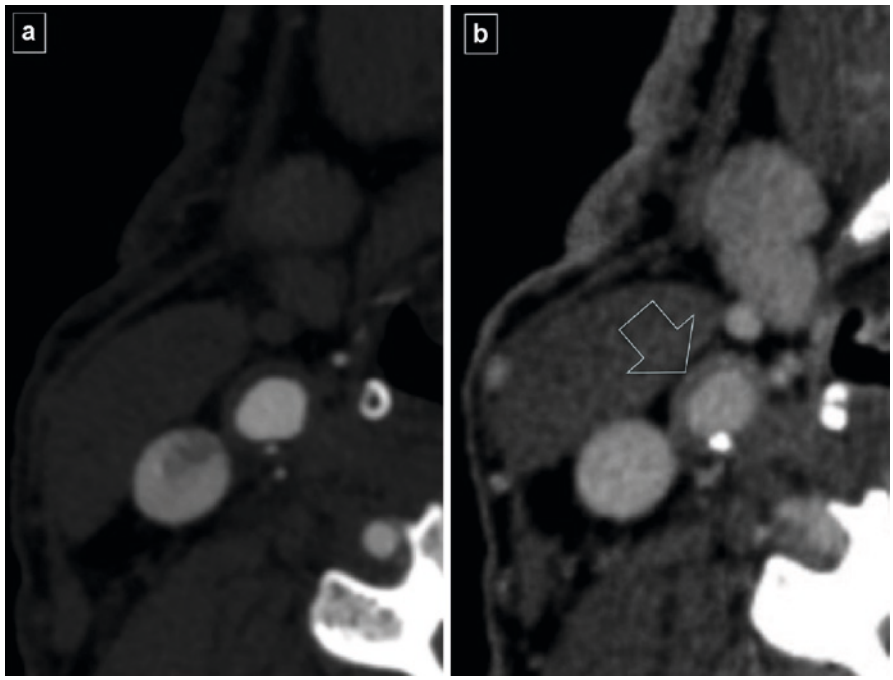

Fig. 5 Axial images at the level of the right internal carotid artery from a conventional CTA (**a**) and from CTA scan using GSI (**b**) (monochromatic image at 40 keV). Wall enhancement representing vasa vasorum enhancement is better identified on the monochromatic GSI image

iodinated contrast used for coronary angiography and the risk of developing CIN in patients with moderate to severe chronic renal dysfunction (Kane et al. 2008). The effect of the concentration and osmolality of iodinated contrast on the development of CIN is controversial (Morcos 2009; Kuhn et al. 2008; Thomsen et al. 2008b; Feldkamp et al. 2006; Barrett et al. 2006; Rosovsky et al. 1996; Solomon 2005), but there are multiple studies supporting the use of nonionic hypoosmolar contrast material to decrease the incidence of CIN (Rosovsky et al. 1996; Hasebroock and Serkova 2009; Dittrich et al. 2007; Rudnick et al. 1995). With the increasing use of computed tomography, there is also growing concern for a parallel increase in the incidence of CIN. The known association of nephrogenic systemic fibrosis (NSF) and gadolinium-based MR agents precludes their use as alternative contrast agents for CT angiography in patients with severe renal dysfunction (Abujudeh et al. 2009; Perazella 2009).

Holmquist et al. (2009), and Holmquist and Nyman (2006) demonstrated that it is feasible to perform pulmonary CT angiograms at 80 kVp using lower doses of iodinated contrast material (200 mg I/kg) in patients with renal failure (eGFR <50 mL/min) for the evaluation of pulmonary embolism. The control group in their study was scanned using 120 kVp and a regular dose of contrast (320 mg I/kg) (Holmquist et al. 2009). Ninety-five percent of these CTA studies were considered technically adequate with similar attenuation values within the pulmonary artery (359 vs. 345 Hu) as well as contrast-to-noise ratios (CNR). The average contrast media dose was 13 and 23 g of iodine, respectively (Holmquist et al. 2009). Similar results were published by Szucs-Farkas et al. (2008a, b) (except for the observation of better image quality in the 120 kVp group). Using an 80 kVp protocol, these authors demonstrated a radiation exposure reduction of about 40% and contrast volume reduction of 25%. The 80 kVp protocol for pulmonary CT angiography can be affected by the additional attenuation of soft tissues in patients weighing >100 kg. This limitation is likely less important in head and neck imaging, considering the smaller cross-sectional size of these structures.

Nakayama et al. (2006) demonstrated that multidetector CT aortography using 40 mL of contrast (300 mg I/mL) and reduced tube voltage of 90 kVp resulted in similar attenuation values in the aorta and visualization of main aortic branches as well as subjective graininess and streak artifacts in comparison with standard tube voltage and 100 mL of contrast. Kalva et al. (2006) showed an increase in up to 90.8% of

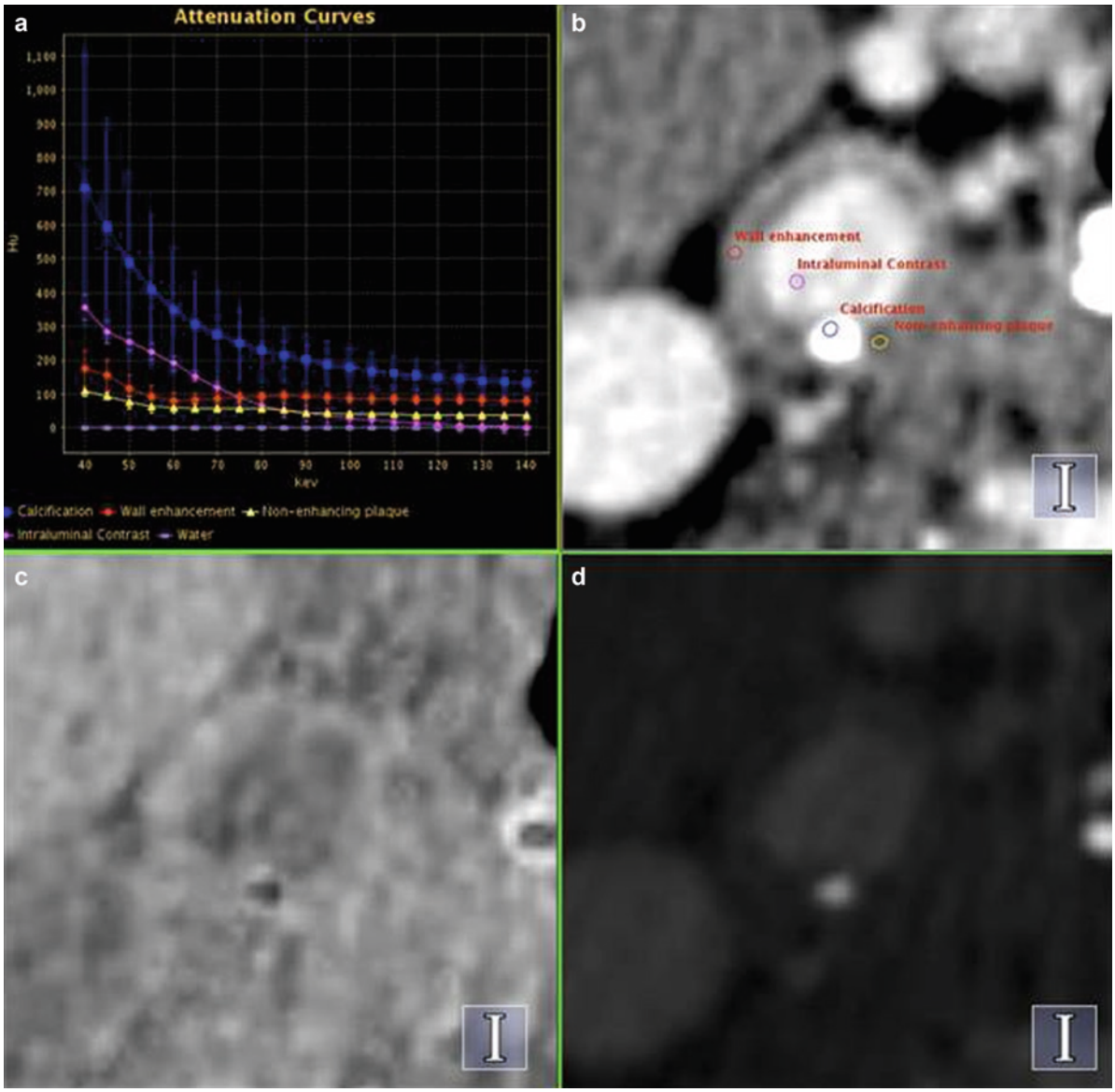

Fig. 6 Images from a GSI CTA at the level of the proximal right internal carotid artery showing different components of an atheromatous plaque. (**a**) Attenuation curves for the different components. (**b**) Monochromatic image at 50 keV (**c**) Water (calcium) image showing suppression of the calcifications in the plaque. (**d**) Calcium (water) image demonstrating the calcified component

attenuation values at 80 kVp in a water phantom containing syringes with iodinated contrast. These authors also performed low peak kilovoltage human studies demonstrating higher intravascular attenuation at 100 kVp (associated with higher image noise) for abdominal CT angiograms. Bahner et al. (2005) performed a similar study using two different kilovoltage levels (80 and 120 kVp) in head CT angiograms without modifying the amount of contrast material. The lower peak kilovoltage scan resulted in approximately 40% reduction in the calculated effective dose, higher intravascular attenuation values, and increased CNR (despite an increase of noise level) (Bahner et al. 2005). Additional studies have been performed confirming the value of lower peak kilovoltage levels to improve contrast opacification in CT angiography and

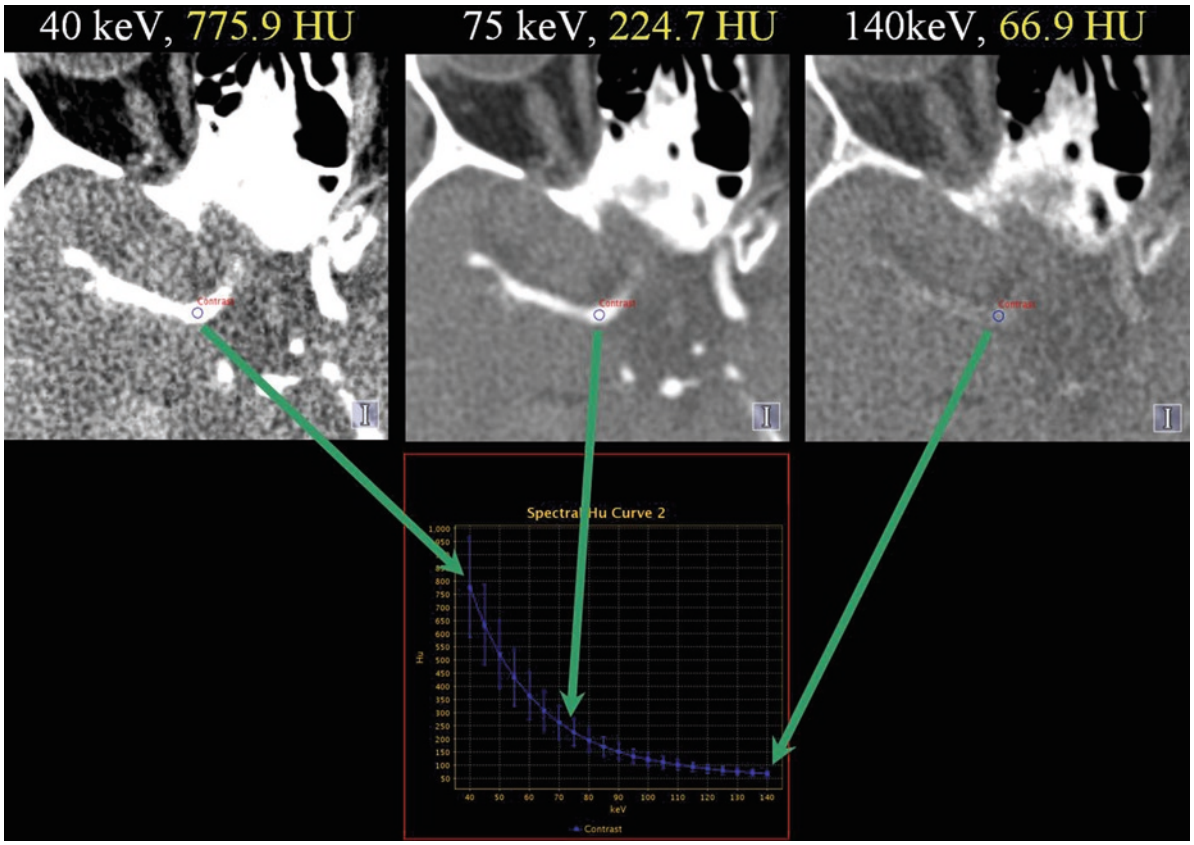

Fig. 7 Three different monochromatic images obtained at progressively higher kiloelectron volt values (40, 75, and 140 keV). A region of interest (ROI) was placed within the right MCA. The attenuation curve analysis demonstrates that the highest intravascular opacification is obtained at low kiloelectron volt values with progressive decrease of the intravascular attenuation with higher kiloelectron volts

other CT applications (Wintersperger et al. 2005; Yanaga et al. 2009).

6.4 Improved Visualization of Anatomic Structures near Osseous or Metallic Surfaces

Dual-Energy CT techniques, particularly GSI, allow the selection of specific monochromatic kiloelectron volt images that are particularly useful to enhance the visualization of important anatomic structures adjacent to osseous or metallic interfaces. At low kiloelectron volt values, images typically experience significant beam hardening and scatter effects. With increasing energy levels, these artifacts are significantly reduced (Fig. 11).

CT evaluation of certain anatomic regions is often degraded by scatter-related and beam hardening artifacts, particularly in the anterior, middle, and posterior fossa, as well as in the oral cavity region (Duerinckx and Macovski 1979). There have been several techniques suggested to minimize these artifacts including changes in gantry angulation (Rozeik et al. 1991; Yeoman et al. 1992; Kinnunen et al. 1990), using multidetector scanning techniques (in comparison with single detector systems) (Jones et al. 2001), iterative reconstruction techniques, helical scanning with a 3D denoising filter (Sasaki et al. 2007), selection of specific energy levels (Mostrom and Ytterbergh 1986; Schmidt 2009), and the use of monochromatic X-rays (Tsunoo et al. 2008; Hemmingsson et al. 1986; Dalstra et al. 2006; Jin et al. 2002; Duerinckx and Macovski 1978).

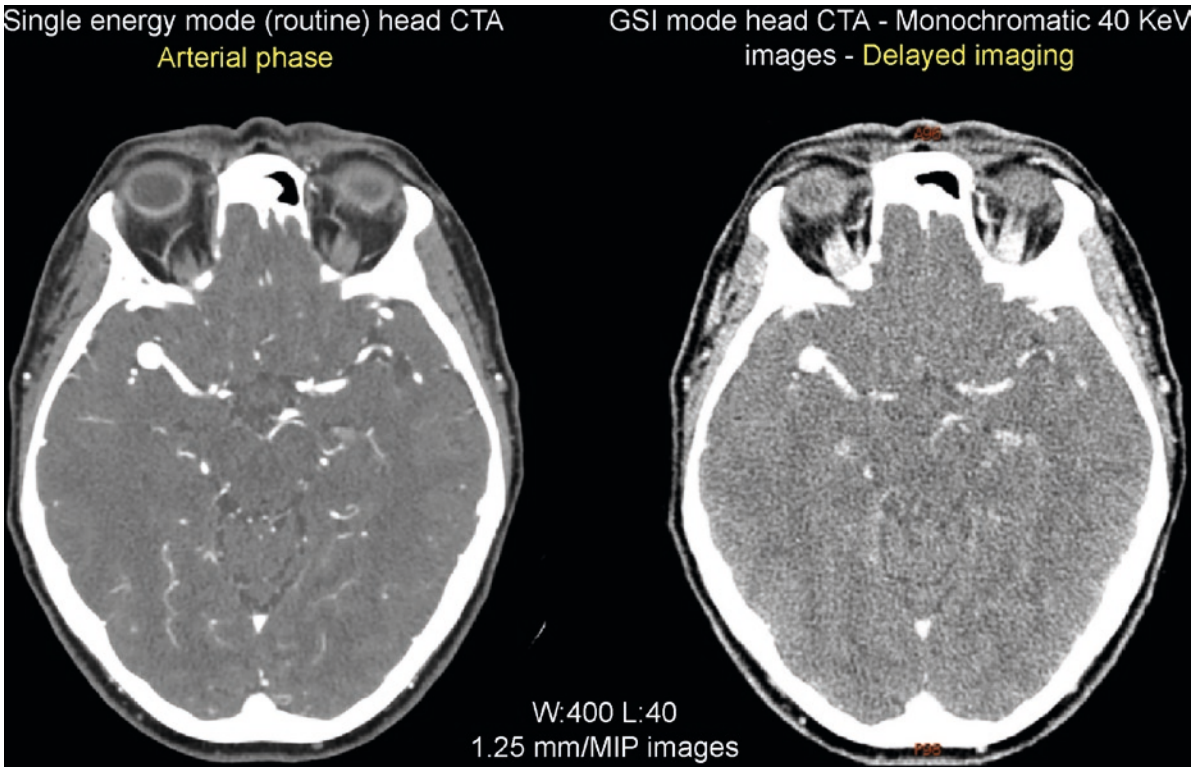

Fig. 8 Examples of an axial MIP image from a conventional CTA and a monochromatic image at 40 keV from a CTA using GSI. The GSI scan was obtained as a delayed acquisition. With the use of low kiloelectron volt monochromatic images, the intravascular opacification is very similar to the conventional CTA. Both images demonstrate a right MCA aneurysm

7 Bone Removal for Intracranial CT Angiograms

Dual-energy CT technology has been used to improve the quality of bone removal in CT angiograms, particularly at the skull (Lell et al. 2009a; Uotani et al. 2009; Deng et al. 2009; Thomas et al. 2009). Lell et al. (2009b) published data suggesting that bone subtraction based on image registration techniques is superior to dual-energy CTA for bone removal and vascular visualization at the skull base.

8 Molecular Imaging

There is promising preliminary research using gold nanoparticles for vascular imaging at low (~40 kVp) and high peak kilovoltage (~140 kVp) values (Jackson et al. 2009). The enhanced detection of gold nanoparticles using dual-energy CT techniques can potentially revolutionize neuro-oncological imaging as well as neurovascular imaging (Popovtzer et al. 2008; Cai et al. 2007; Kim et al. 2007, 2009; Rabin et al. 2006; Hainfeld et al. 2006).

9 Conclusion

Dual-energy CT techniques already have a wide variety of clinical and preclinical applications in neuroimaging and cerebrovascular imaging. These applications include material composition and carotid plaque analysis, CT angiograms with low contrast doses, and reduction of scatter-related artifacts in certain anatomic regions. With the development of new contrast agents and increasing sophistication of our imaging methods, this CT technology will likely solidify its presence among routine diagnostic protocols and new applications will emerge to fully develop its potential.

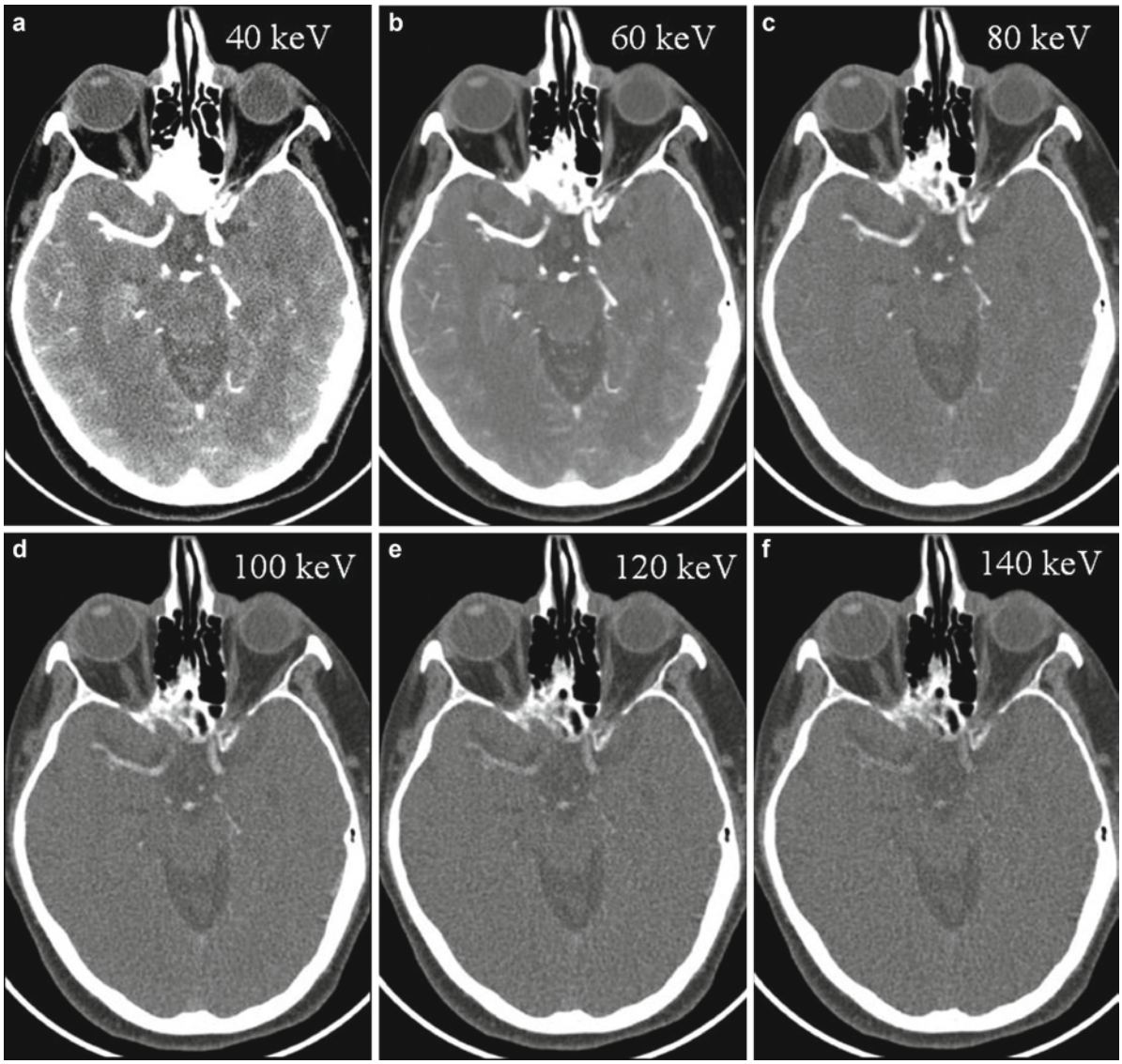

Fig. 9 Effect of different kiloelectron volt levels on the attenuation properties of intravascular contrast (W: 400, L: 40, 1.25 mm with 0.625 intervals). Images (**a**–**f**) demonstrate increasing kiloelectron volt levels (40–140). The maximal intravascular attenuation is achieved at 40 keV associated with increased noise for visualization of the adjacent brain parenchyma. At 60 keV, the degree of intravascular attenuation decreases, but the parenchymal visualization is less noisy. Higher kiloelectron volt values result in decreased intravascular attenuation and increased noise for parenchymal assessment

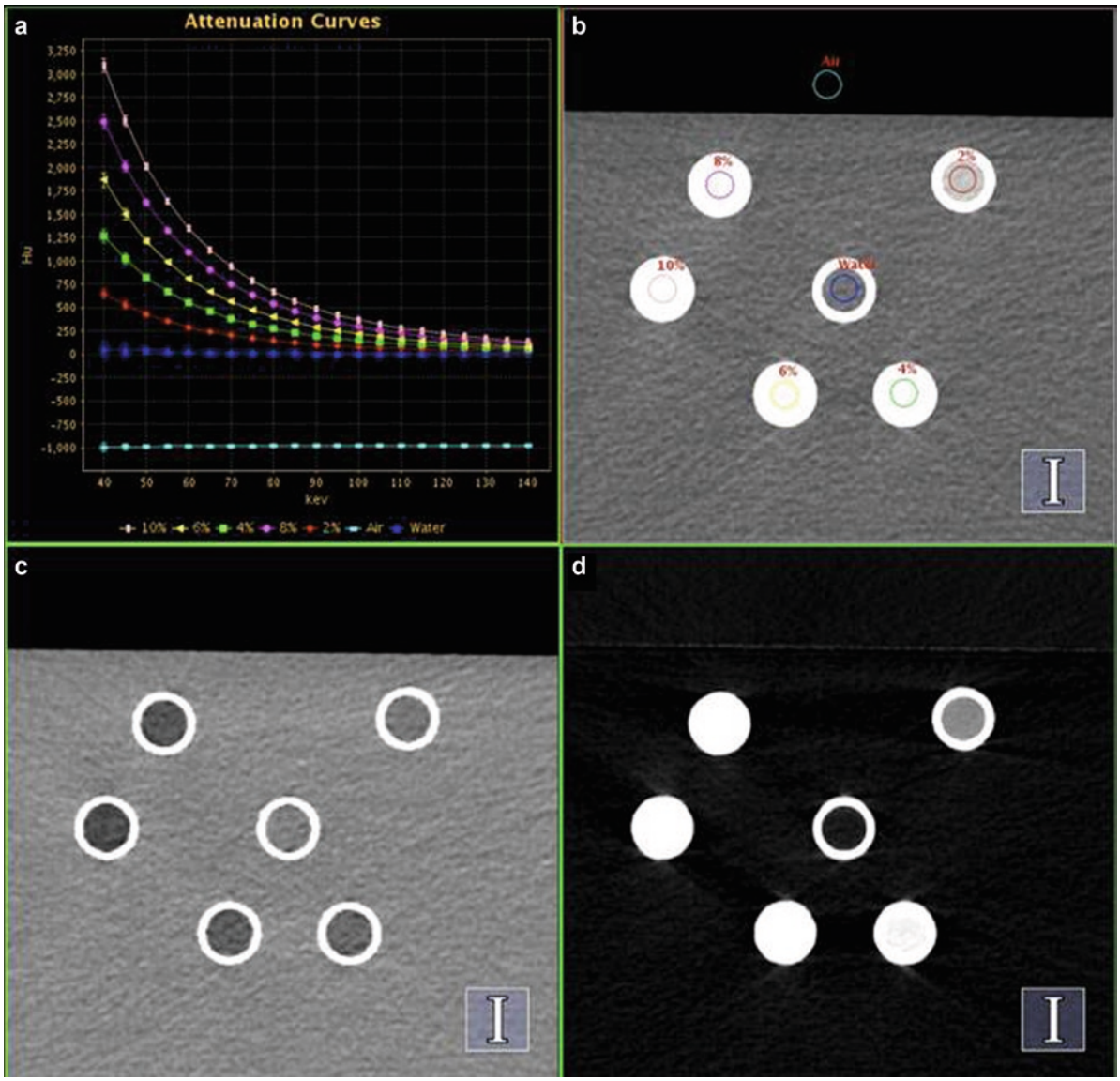

Fig. 10 Phantom study using small tubes containing different concentrations of diluted iodinated contrast (from 2 to 10%) embedded in a matrix of water. Attenuation analysis demonstrates that the use of low energy monochromatic images increases the attenuation values of contrast material within the tubes even at low concentrations of iodine. (**a**) Attenuation analysis. (**b**) Monochromatic 70 keV image. (**c**) Water (iodine) image showing virtual subtraction of iodine. (**d**) Iodine (water) image demonstrating the presence of iodine, even at low concentrations

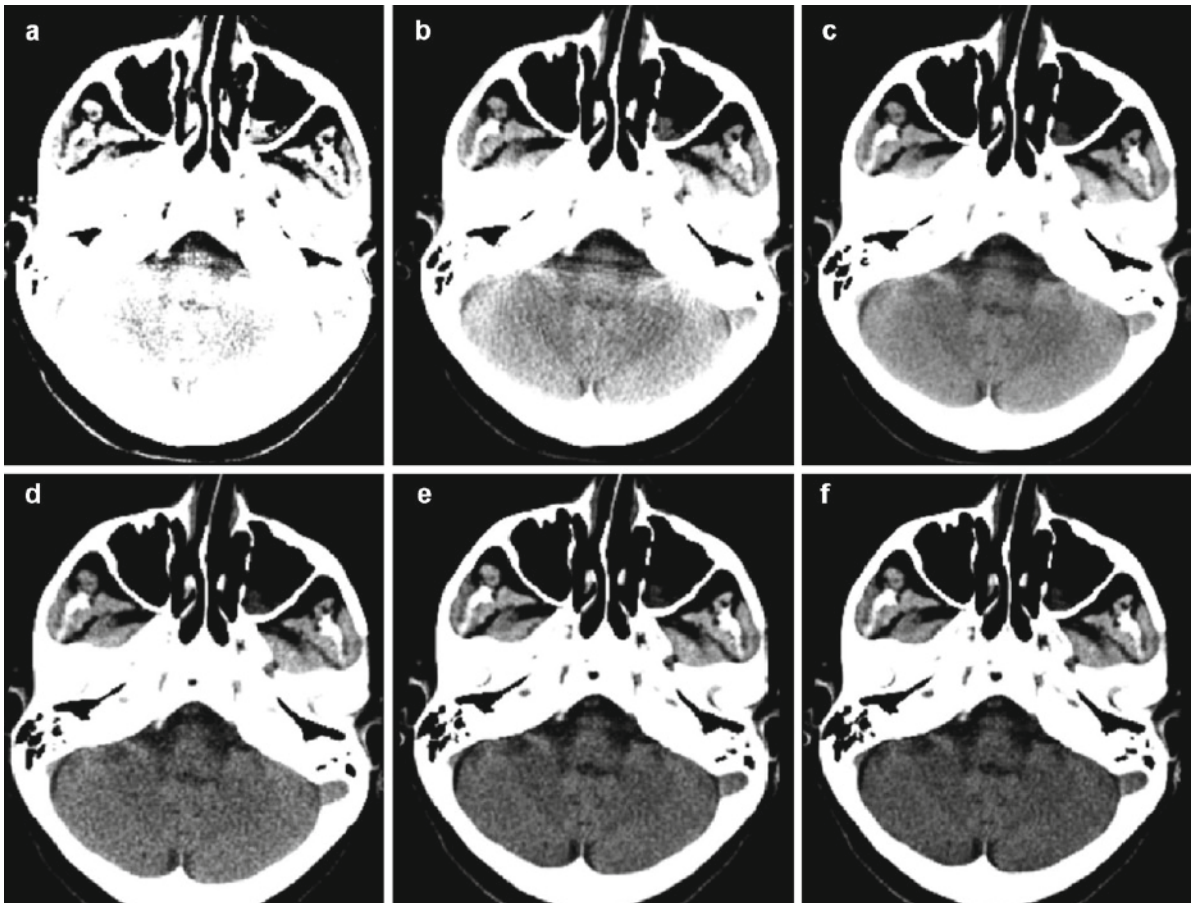

Fig. 11 Monochromatic images acquired at progressively higher kiloelectron volt levels (**a** keV 40, **b** 60, **c** 70, **d** 80, **e** 90, and **f** 100). Beam hardening artifacts produced by the temporal bones obscure the brainstem. These artifacts are more pronounced at low kiloelectron volt values (40–60 keV) and are markedly reduced with energy levels around 80 keV. Higher energy monochromatic images also reduce beam hardening artifacts, but show lower gray–white matter differentiation

References

Abujudeh HH et al (2009) Nephrogenic systemic fibrosis after gadopentetate dimeglumine exposure: case series of 36 patients. Radiology 253(1):81–89

Bahner ML et al (2005) Improved vascular opacification in cerebral computed tomography angiography with 80 kVp. Invest Radiol 40(4):229–234

Balvay D et al (2009) Mapping the zonal organization of tumor perfusion and permeability in a rat glioma model by using dynamic contrast-enhanced synchrotron radiation CT. Radiology 250(3):692–702

Barnea G, Dick CE (1986) Monte Carlo studies of X-ray scattering in transmission diagnostic radiology. Med Phys 13(4): 490–495

Barreto M et al (2008) Potential of dual-energy computed tomography to characterize atherosclerotic plaque: ex vivo assessment of human coronary arteries in comparison to histology. J Cardiovasc Comput Tomogr 2(4):234–242

Barrett BJ et al (2006) Contrast-induced nephropathy in patients with chronic kidney disease undergoing computed tomography: a double-blind comparison of iodixanol and iopamidol. Invest Radiol 41(11):815–821

Buerke B et al (2009) Dual-energy CTA with bone removal for transcranial arteries: intraindividual comparison with standard CTA without bone removal and TOF-MRA. Acad Radiol 16(11):1348–1355

Cai QY et al (2007) Colloidal gold nanoparticles as a blood-pool contrast agent for X-ray computed tomography in mice. Invest Radiol 42(12):797–806

Chen Y et al (2009) Dual-energy CT angiography for evaluation of internal carotid artery stenosis and occlusion. Zhongguo Yi Xue Ke Xue Yuan Xue Bao 31(2):215–220

Dalstra M, Cattaneo PM, Beckmann F (2006) Synchrotron radiation-based microtomography of alveolar support tissues. Orthod Craniofac Res 9(4):199–205

Das M et al (2009) Carotid plaque analysis: comparison of dual-source computed tomography (CT) findings and histopathological correlation. Eur J Vasc Endovasc Surg 38(1):14–19

Deng K et al (2009) Clinical evaluation of dual-energy bone removal in CT angiography of the head and neck: comparison with conventional bone-subtraction CT angiography. Clin Radiol 64(5):534–541

Dick CE, Soares CG, Motz JW (1978) X-ray scatter data for diagnostic radiology. Phys Med Biol 23(6):1076–1085

Dittrich R et al (2007) Low rate of contrast-induced nephropathy after CT perfusion and CT angiography in acute stroke patients. J Neurol 254(11):1491–1497

Duerinckx AJ, Macovski A (1978) Polychromatic streak artifacts in computed tomography images. J Comput Assist Tomogr 2(4):481–487

Duerinckx AJ, Macovski A (1979) Nonlinear polychromatic and noise artifacts in X-ray computed tomography images. J Comput Assist Tomogr 3(4):519–526

Feldkamp T et al (2006) Nephrotoxicity of iso-osmolar versus low-osmolar contrast media is equal in low risk patients. Clin Nephrol 66(5):322–330

Ferda J et al (2009) The assessment of intracranial bleeding with virtual unenhanced imaging by means of dual-energy CT angiography. Eur Radiol 19(10):2518–2522

Granada JF, Feinstein SB (2008) Imaging of the vasa vasorum. Nat Clin Pract Cardiovasc Med 5(suppl 2):S18–S25

Graser A et al (2009) Dual-energy CT in patients suspected of having renal masses: can virtual nonenhanced images replace true nonenhanced images? Radiology 252(2):433–440

Hainfeld JF et al (2006) Gold nanoparticles: a new X-ray contrast agent. Br J Radiol 79(939):248–253

Hasebroock KM, Serkova NJ (2009) Toxicity of MRI and CT contrast agents. Expert Opin Drug Metab Toxicol 5(4): 403–416

Hawkes DJ, Jackson DF, Parker RP (1986) Tissue analysis by dual-energy computed tomography. Br J Radiol 59(702): 537–542

Hemmingsson A, Jung B, Ytterbergh C (1986) Dual energy computed tomography: simulated monoenergetic and material-selective imaging. J Comput Assist Tomogr 10(3):490–499

Holmquist F, Nyman U (2006) Eighty-peak kilovoltage 16-channel multidetector computed tomography and reduced contrast-medium doses tailored to body weight to diagnose pulmonary embolism in azotaemic patients. Eur Radiol 16(5):1165–1176

Holmquist F et al (2009) Minimizing contrast medium doses to diagnose pulmonary embolism with 80-kVp multidetector computed tomography in azotemic patients. Acta Radiol 50(2):181–193

Jackson PA et al (2009) Potential dependent superiority of gold nanoparticles in comparison to iodinated contrast agents. Eur J Radiol 2009 Apr 28. [Epub ahead of print]

Jin H et al (2002) High resolution three-dimensional visualization and characterization of coronary atherosclerosis in vitro by synchrotron radiation X-ray microtomography and highly localized X-ray diffraction. Phys Med Biol 47(24):4345–4356

Jones TR et al (2001) Single- versus multi-detector row CT of the brain: quality assessment. Radiology 219(3):750–755

Kalva SP et al (2006) Using the K-edge to improve contrast conspicuity and to lower radiation dose with a 16-MDCT: a phantom and human study. J Comput Assist Tomogr 30(3): 391–397

Kane GC et al (2008) Ultra-low contrast volumes reduce rates of contrast-induced nephropathy in patients with chronic kidney disease undergoing coronary angiography. J Am Coll Cardiol 51(1):89–90

Kerwin WS et al (2008) MR imaging of adventitial vasa vasorum in carotid atherosclerosis. Magn Reson Med 59(3): 507–514

Kim D et al (2007) Antibiofouling polymer-coated gold nanoparticles as a contrast agent for in vivo X-ray computed tomography imaging. J Am Chem Soc 129(24):7661–7665

Kim JH et al (2009) Intravenously administered gold nanoparticles pass through the blood-retinal barrier depending on the particle size, and induce no retinal toxicity. Nanotechnology 20(50):505101

Kinnunen J et al (1990) Improved visualization of posterior fossa with clivoaxial CT scanning plane. Rontgenblatter 43(12):539–542

Kuhn MJ et al (2008) The PREDICT study: a randomized double-blind comparison of contrast-induced nephropathy after low- or isoosmolar contrast agent exposure. AJR Am J Roentgenol 191(1):151–157

Kwak HS et al (2005) Comparison of renal damage by iodinated contrast or gadolinium in an acute renal failure rat model based on serum creatinine levels and apoptosis degree. J Korean Med Sci 20(5):841–847

Lang EK et al (1981) The incidence of contrast medium induced acute tubular necrosis following arteriography. Radiology 138(1):203–206

Langheinrich AC et al (2007) Vasa vasorum and atherosclerosis – Quid novi? Thromb Haemost 97(6):873–879

Lell MM et al (2009) Dual energy CTA of the supraaortic arteries: technical improvements with a novel dual source CT system. Eur J Radiol. 2009 Oct 8. [Epub ahead of print]

Lell MM et al (2009b) Carotid computed tomography angiography with automated bone suppression: a comparative study between dual energy and bone subtraction techniques. Invest Radiol 44(6):322–328

Liss P et al (2009) Iodinated contrast media decrease renomedullary blood flow. A possible cause of contrast media-induced nephropathy. Adv Exp Med Biol 645:213–218

Marenzi G et al (2009) Contrast volume during primary percutaneous coronary intervention and subsequent contrast-induced nephropathy and mortality. Ann Intern Med 150(3):170–177

Massicotte A (2008) Contrast medium-induced nephropathy: strategies for prevention. Pharmacotherapy 28(9):1140–1150

Mekan SF et al (2004) Radiocontrast nephropathy: is it dose related or not? J Pak Med Assoc 54(7):372–374

Morcos SK (2009) Contrast-induced nephropathy: are there differences between low osmolar and iso-osmolar iodinated contrast media? Clin Radiol 64(5):468–472

Mostrom U, Ytterbergh C (1986) Artifacts in computed tomography of the posterior fossa: a comparative phantom study. J Comput Assist Tomogr 10(4):560–566

Nakayama Y et al (2006) Lower tube voltage reduces contrast material and radiation doses on 16-MDCT aortography. AJR Am J Roentgenol 187(5):W490–W497

Nyman U et al (2005) Contrast-medium-Induced nephropathy correlated to the ratio between dose in gram iodine and estimated GFR in ml/min. Acta Radiol 46(8):830–842

Nyman U et al (2008) Contrast medium dose-to-GFR ratio: a measure of systemic exposure to predict contrast-induced nephropathy after percutaneous coronary intervention. Acta Radiol 49(6):658–667

Papin PJ, Rielly PS (1988) Monte Carlo simulation of diagnostic X-ray scatter. Med Phys 15(6):909–914
Perazella MA (2009) Current status of gadolinium toxicity in patients with kidney disease. Clin J Am Soc Nephrol 4(2): 461–469
Pomerantz SR et al (2006) Computed tomography angiography and computed tomography perfusion in ischemic stroke: a step-by-step approach to image acquisition and three-dimensional postprocessing. Semin Ultrasound CT MR 27(3): 243–270
Popovtzer R et al (2008) Targeted gold nanoparticles enable molecular CT imaging of cancer. Nano Lett 8(12):4593–4596
Primak AN et al (2009) Improved dual-energy material discrimination for dual-source CT by means of additional spectral filtration. Med Phys 36(4):1359–1369
Rabin O et al (2006) An X-ray computed tomography imaging agent based on long-circulating bismuth sulphide nanoparticles. Nat Mater 5(2):118–122
Romano G et al (2008) Contrast agents and renal cell apoptosis. Eur Heart J 29(20):2569–2576
Romero JM et al (2009) Arterial wall enhancement overlying carotid plaque on CT angiography correlates with symptoms in patients with high grade stenosis. Stroke 40(5):1894–1896
Rosovsky MA et al (1996) High-dose administration of nonionic contrast media: a retrospective review. Radiology 200(1): 119–122
Rozeik C et al (1991) Cranial CT artifacts and gantry angulation. J Comput Assist Tomogr 15(3):381–386
Rudnick MR et al (1995) Nephrotoxicity of ionic and nonionic contrast media in 1196 patients: a randomized trial. The Iohexol cooperative study. Kidney Int 47(1):254–261
Sasaki T et al (2007) Improvement in image quality of noncontrast head images in multidetector-row CT by volume helical scanning with a three-dimensional denoising filter. Radiat Med 25(7):368–372
Schmidt TG (2009) Optimal "image-based" weighting for energy-resolved CT. Med Phys 36(7):3018–3027
Schuknecht B (2004) Latest techniques in head and neck CT angiography. Neuroradiology 46(suppl 2):s208–s213
Solomon R (2005) The role of osmolality in the incidence of contrast-induced nephropathy: a systematic review of angiographic contrast media in high risk patients. Kidney Int 68(5):2256–2263
Szucs-Farkas Z et al (2008a) Patient exposure and image quality of low-dose pulmonary computed tomography angiography: comparison of 100- and 80-kVp protocols. Invest Radiol 43(12):871–876
Szucs-Farkas Z et al (2008b) Effect of X-ray tube parameters, iodine concentration, and patient size on image quality in pulmonary computed tomography angiography: a chest-phantom-study. Invest Radiol 43(6):374–381
Szucs-Farkas Z et al (2009) Detection of pulmonary emboli with CT angiography at reduced radiation exposure and contrast material volume: comparison of 80 and 120 kVp protocols in a matched cohort. Invest Radiol 44(12):793–799
Thomas C et al (2009) Automatic bone and plaque removal using dual energy CT for head and neck angiography: feasibility and initial performance evaluation. Eur J Radiol 2009 Jun 9 [Epub ahead of print]
Thomsen HS, Morcos SK (2009) Risk of contrast-medium-induced nephropathy in high-risk patients undergoing MDCT – a pooled analysis of two randomized trials. Eur Radiol 19(4):891–897
Thomsen HS, Morcos SK, Barrett BJ (2008a) Contrast-induced nephropathy: the wheel has turned 360 degrees. Acta Radiol 49(6):646–657
Thomsen HS et al (2008b) The ACTIVE trial: comparison of the effects on renal function of iomeprol-400 and iodixanol-320 in patients with chronic kidney disease undergoing abdominal computed tomography. Invest Radiol 43(3):170–178
Tran DN et al (2009) Dual-energy CT discrimination of iodine and calcium: experimental results and implications for lower extremity CT angiography. Acad Radiol 16(2):160–171
Tsunoo T et al (2008) Measurement of electron density in dual-energy X-ray CT with monochromatic x rays and evaluation of its accuracy. Med Phys 35(11):4924–4932
Uotani K et al (2009) Dual-energy CT head bone and hard plaque removal for quantification of calcified carotid stenosis: utility and comparison with digital subtraction angiography. Eur Radiol 19(8):2060–2065
Wintersperger B et al (2005) Aorto-iliac multidetector-row CT angiography with low kV settings: improved vessel enhancement and simultaneous reduction of radiation dose. Eur Radiol 15(2):334–341
Yanaga Y et al (2009) Low-dose MDCT urography: feasibility study of low-tube-voltage technique and adaptive noise reduction filter. AJR Am J Roentgenol 193(3):W220–W229
Yeoman LJ et al (1992) Gantry angulation in brain CT: dosage implications, effect on posterior fossa artifacts, and current international practice. Radiology 184(1):113–116

Part V

Abdominal Imaging

Liver Imaging

Christian Fink

Contents

Abstract

› Dual energy CT (DECT) has been evaluated for the assessment of focal and diffuse liver disease. By using the spectral information of DECT iodinated contrast media can be selectively visualized to improve the conspicuity of enhancing focal liver lesions, or to suppress the iodine signal to create a virtual non-enhanced CT data set. Furthermore, already in the eighties of the last century, DECT has been evaluated for the assessment of diffuse liver disease such as fatty liver and iron overload. The following chapter reviews the basic principles, clinical protocols, and scientific evidence of hepatic imaging using DECT.

1 Clinical Background

The detection and characterization of focal liver lesions is still one of the most important indications for abdominal CT (Kopp et al. 2002; Boll & Merkle 2009). Although MRI due to its superior soft tissue contrast and multiple contrast options (e.g., diffusion-weighted imaging, liver-specific contrast media, MRCP) is considered superior for the characterization of focal liver lesions, in clinical practice CT often will be the first and only image test performed for this purpose. Regardless, whether CT or MRI is used, the characterization of a focal liver lesion is based on contrast-enhanced multiphasic imaging of its vascularity. While normal liver parenchyma mainly receives blood from the portal vein, liver tumors, whether benign, malignant, primary,

C. Fink
Department of Clinical Radiology and Nuclear Medicine,
University Medical Center Mannheim,
Medical Faculty Mannheim of the University of Heidelberg,
Theodor-Kutzer-Ufer 1-3, 68167 Mannheim, Germany
e-mail: christian.fink@umm.de

T.R.C. Johnson et al. (eds.), *Dual Energy CT in Clinical Practice*, Medical Radiology,
DOI: 10.1007/174_2010_55

or metastases, receive most if not all of their blood from the hepatic artery (Kopp et al. 2002). While some hypervascular tumors may be invisible on portal venous CT, less vascularized tumors will enhance minimally during the hepatic arterial phase and will be hypodense on the subsequent portal venous phase. This is by far the most common enhancement pattern for metastases. Various contrast-enhanced multiphasic CT protocols have been proposed for imaging of focal liver lesions ranging from single-phase to triple phase CT (Kopp et al. 2002; Kitamura et al. 2008; Paulson et al. 1998).

Besides focal liver disease, there are a variety of diffuse diseases of the hepatic parenchyma which usually represent a failure in a hepatic metabolic pathway and can be categorized as storage, vascular, and inflammatory diseases (Boll & Merkle 2009). Important examples include non-alcoholic and alcoholic fatty liver, hemochromatosis, and Wilson's disease. Fatty liver is defined as excessive accumulation of triglycerides within the cytoplasm of hepatocytes caused by different underlying clinical condition such as obesity, diabetes, hyperlipidemia, anorexia nervosa, or alcohol abuse (Hamer et al. 2006). Non-alcoholic and alcoholic steatohepatitis (NASH and ASH) are defined as a combination of steatosis and inflammation eventually progressing to excessive cell injury, fibrosis, and cirrhosis. Sometimes fat distribution in the liver may cause diagnostic confusion by mimicking neoplastic masses (Kawamoto et al. 1998). In hemochromatosis, excessive storage of iron in hepatocytes results in progressive liver damage and subsequent cirrhosis.

Dual energy CT (DECT) has so far been investigated for hepatic imaging for the characterization of three different materials. The selective visualization of iodinated contrast media by DECT has been proposed to improve the conspicuity of enhancing focal liver lesions, or to suppress the iodine signal to create a virtual non-enhanced CT data set. Furthermore, already in the eighties of the last century, DECT has been evaluated for the assessment of diffuse liver disease as in fatty liver and iron overload.

2 Physical Background

Iodine, which is used as an intravenous contrast agent in clinical CT imaging, is an ideal target for DECT as the characteristic x-ray spectrum at 80 kV is very close to the k-edge of iodine, and thus shows a substantially higher attenuation at 80 kV than at higher energy levels. This effect makes it beneficial to use the spectral information to differentiate iodine from other materials that do not show this behavior (Johnson et al. 2007). Using dedicated DECT postprocessing the iodine distribution in the tissue can be selectively visualized using color-coding which can be fused onto the standard density-based gray scale CT image. For imaging of focal liver lesions, the improved sensitivity for iodinated contrast media will potentially increase the conspicuity of hypervascular lesions such as small hepatocellular carcinomas or hypervascular liver metastases (Fig. 1). In addition, the conspicuity of hypovascular lesions (e.g., hypovascular metastasis) during the portal venous phase may be increased as they will appear hypodense relative to the normal hepatic parenchyma which will show maximal iodine enhancement during this phase. Furthermore, the high- and low-kV data sets can be post-processed to isolate iodine from the soft tissue in order to create a virtual non-enhanced CT data set that can potentially be used to replace the a true non-enhanced CT data set of a multiphasic CT protocol (Johnson et al. 2007; Zhang et al. 2010; Graser et al. 2009a) (Figs. 2 and 3). Similar to iodine, other elements with a high atomic number, such as iron, are well suited for DECT imaging. Therefore, DECT has been proposed for non-invasive assessment of iron storage disease.

3 Scan Protocol and Contrast Injection

Other than very early studies that used two separate CT scans performed on a single source CT, most recently published studies on hepatic DECT have been performed on a dual-source CT system. Thus, the scan protocols provided in the following paragraph will be for DECT of the liver using first- or second-generation dual source CT.

Oral contrast media (either positive or negative) is not mandatory for hepatic CT but may be indicated if the scan range of the CT is to be extended to the entire abdomen. The patient is usually positioned supine in the center of the CT couch; in order to compensate for the small FOV of the B-detector, however, the patient may be positioned a little bit to the left. Depending on the indication the scan range covers the upper abdomen (liver dome to iliac crests) or the entire abdomen. The tube voltage is set to 140 and 80 kV on system A and B. To reduce image noise and scatter radiation, a thick detector collimation of 14 × 1.2 mm is recommended for first-generation dual

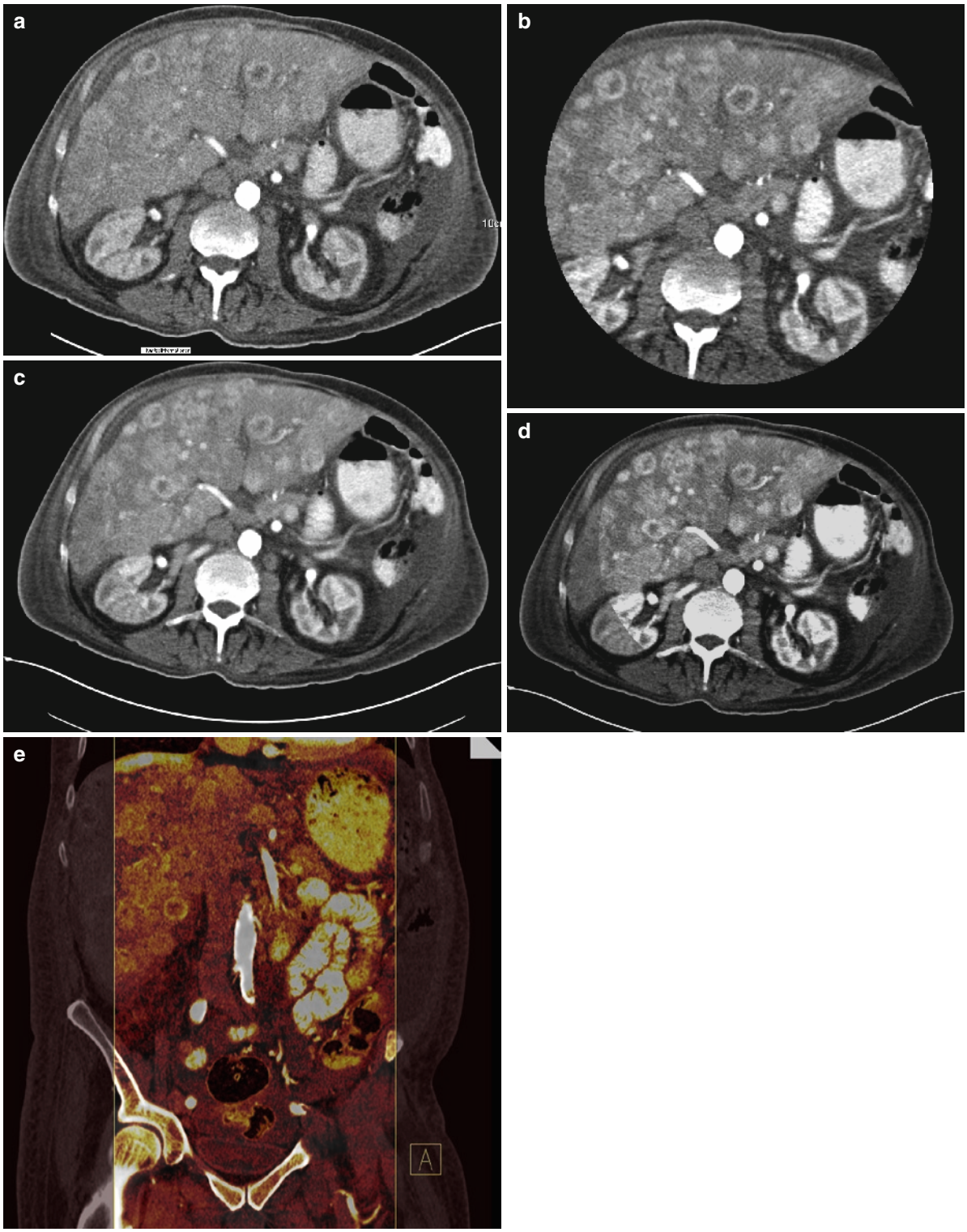

Fig. 1 Contrast-enhanced hepatic DECT of a 63 year old male with hypervascular metastasis of a neuroendocrine cancer. (**a**) 140 kV data set, (**b**) 80 kV data set, (**c**) linear blended virtual 120 kV data set, (**d**) non-linear blended virtual 120 kV data set, (**e**) fused color-coded iodine and virtual 120 kV data set. Due to the higher attenuation of iodine at low kV the hypervascular metastasis show a higher contrast to noise ratio at low kV and in the non-linear blended virtual kV data set (**b** and **d**) Due to the smaller field of view of the B-detector system not the entire field of view contains dual energy information (**e**)

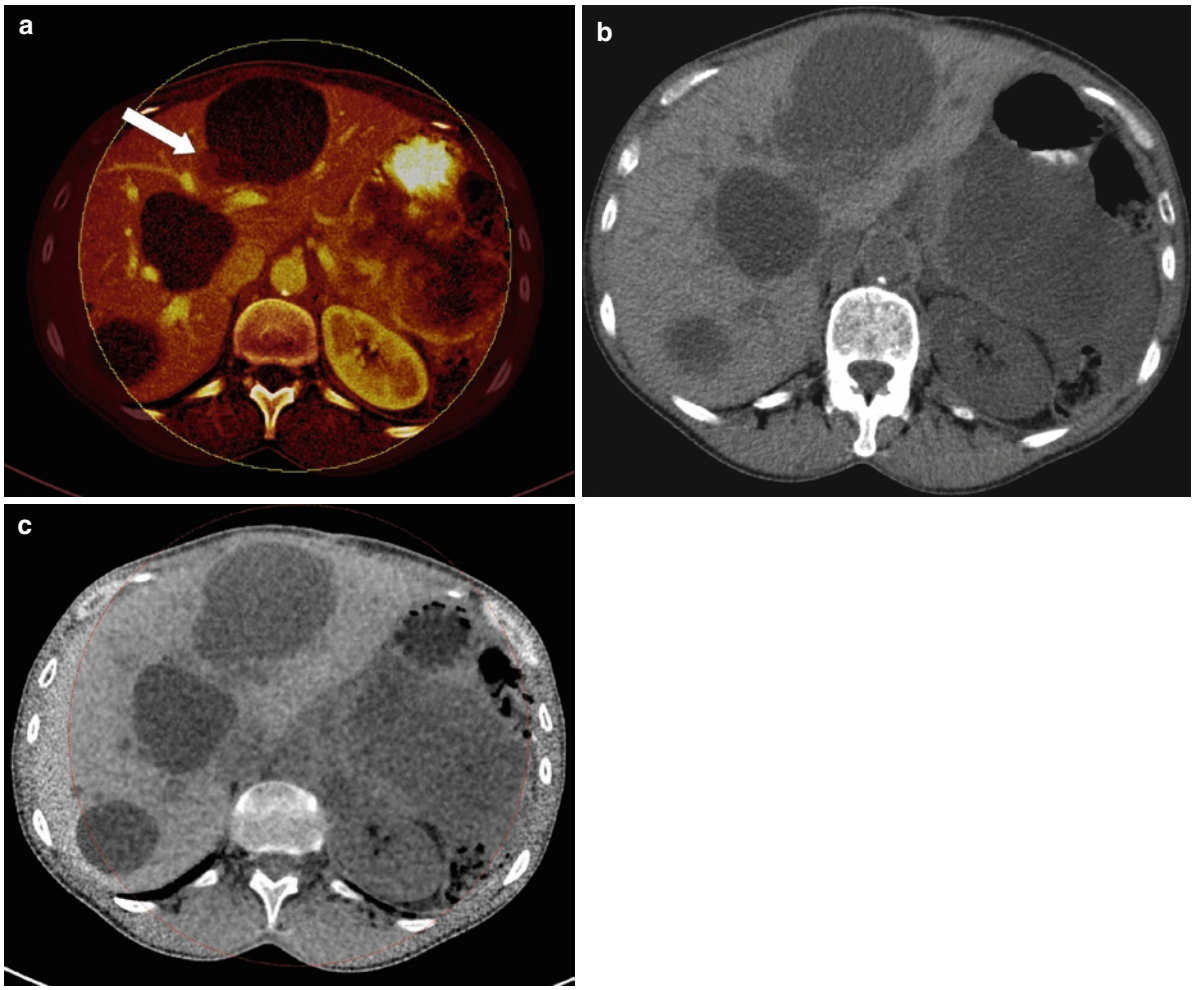

Fig. 2 Contrast-enhanced hepatic DECT of a 49 year old female with metastatic GIST. (**a**) fused color-coded iodine and virtual 120 kV data set, (**b**) virtual non-enhanced data set, (**c**) true non-enhanced single energy CT. By adequate postprocessing iodine, as in the enhancing tumor nodule of one cystic metastasis (**a**, *arrow*) can be entirely suppressed yielding in a virtual non-enhanced data set (**b**) which has similar imaging characteristics as the true non-enhanced single energy CT (**c**)

source CT. Automated tube current modulation (CARE Dose 4D, Siemens) is desirable for DECT to obtain sufficient quanta from the 80 kV tube (Johnson 2009). Quality reference mAs are set to 85 mAs on the 140 kV and 468 mAs on the 80 kV tube. With the second generation of dual source CT, DECT imaging has been improved. First, there is not anymore a major restriction of the field of view, since the size of the smaller detector system was increased from 26 to 32 cm. By improving the spectrum of the 140 kV tube with a tin filtering (140 SN), the tube potential on the second tube can be increased to 100 kV, thus generating a more penetrable x-ray spectrum and higher signal to noise ratio. With the improved signal-to-noise ratio a thinner detector collimation of 32 × 0.6 mm with advantage of improved spatial resolution can routinely be used. A detailed overview of the DECT scan protocols for first- and second-generation dual source CT is given in Table 1.

It was recently shown that using the described tube current settings (i.e., higher tube current on 80 kV system and lower tube current on 140 kV system) the effective radiation dose is equal to a standard 120 kV single energy CT scan (Christner et al. 2010; Thomas et al. 2010).

The contrast injection protocol for DECT of the liver does not differ from standard hepatic single-energy CT protocols. Contrast agent and saline flush should be

injected by means of a mechanical power injector through 16–20-gauge indwelling venous catheters with a flow rate of 2.5–5 mL/s. Approximately 30–40 g of iodine yields sufficient hepatic enhancement, which depending on the used iodine concentration is equivalent to a volume of 75–130 mL. Similarly, the scan delay will be chosen as it would be in standard single energy CT, e.g., 10–20 s after aortic threshold–based scanning initiation for an early or late arterial phase scan and approximately 70 s after begin of the contrast injection for portal venous phase imaging (Boll & Merkle 2009).

4 Post-processing

There are several ways for image processing of DECT data sets. For general viewing, a linear blended CT dataset that resembles image properties similar to a standard 120 kV dataset can be processed. It has been shown that a blending image with a ratio of 70% of the 140 kV data and 30% of the 80 kV data yields an image with similar image characteristics as a standard 120 kV single energy scan (Johnson et al. 2007). Recently, also non-linear blending, e.g., using a modal function has been proposed.

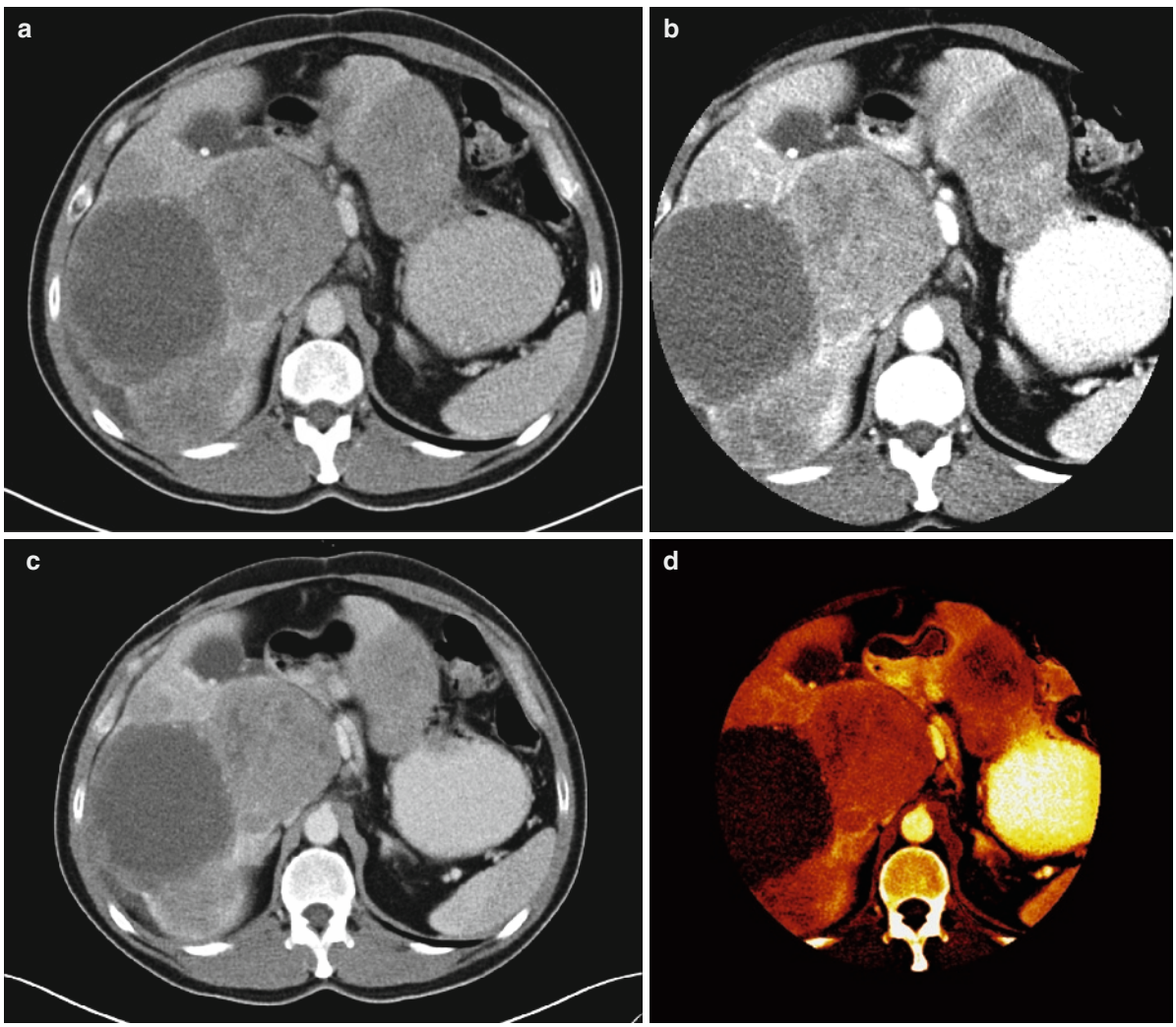

Fig. 3 Contrast-enhanced hepatic DECT of a 59 year old male with metastatic GIST showing cystic and non-cystic hepatic metastasis. (**a**) 140 kV data set, (**b**) 80 kV data set, (**c**) linear blended virtual 120 kV data set, (**d**) color-coded iodine data set, (**e**) fused color-coded iodine and virtual 120 kV data set, (**f**) virtual non-enhanced data set, (**g**) true non-enhanced single-energy CT. The color-coded iodine data set and fused data set (**d**, **e**) nicely demonstrate the increased enhancement of the solid metastasis. The virtual non-enhanced data set (**f**) basically provides the same information as the true non-enhanced single energy CT (**g**)

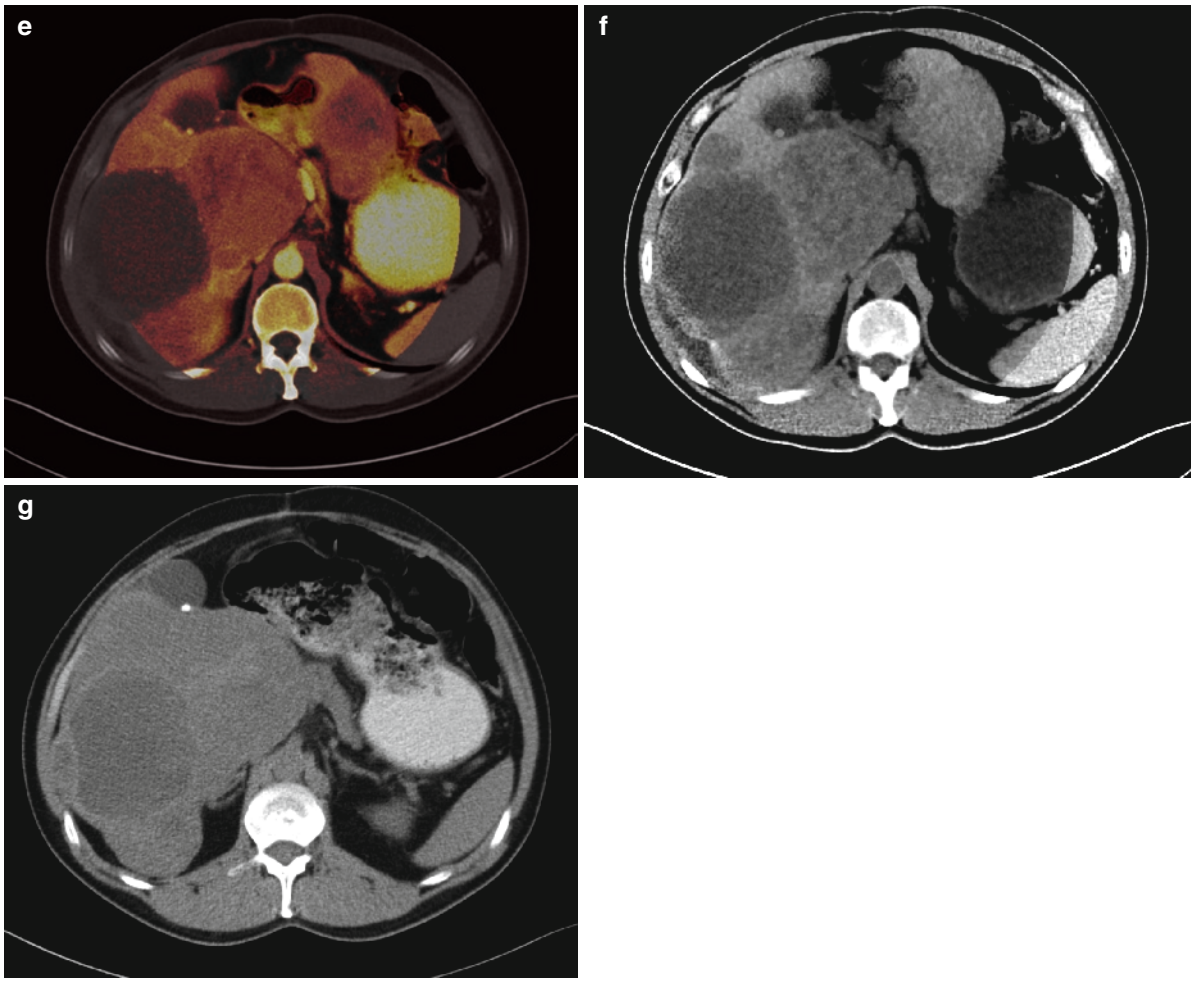

Fig. 3 (continued)

The goal of a non-linear blending postprocessing algorithm is to maintain the contrast of the low-energy scan while achieving the noise characteristics of the high-energy scan. In a liver phantom, it was shown that simulated hypervascular liver lesions yielded a higher CNR using the non-linear blending algorithm, whereas iso- or hypodense liver lesions showed similar CNR in linear and non-linear blended CT data sets (Holmes et al. 2008).

Using dual energy post-processing software based on the dual energy index of materials, a blended gray scale CT data set, a virtual non-enhanced CT data, an iodine data set, and a color-coded data set that shows iodine distribution over the virtual non-enhanced data can be generated (Fig. 3). These images are based on a three-material decomposition of iodine, soft tissue, and fat (Johnson et al. 2007).

5 Diagnostic Evaluation and Scientific Evidence

DECT of the liver has so far been evaluated for the visualization and detection of three different materials, i.e., the detection of iodinated contrast media as well as the assessment hepatic fat infiltration and iron overload.

As described above a virtual non-enhanced CT data set can be calculated from a contrast-enhanced DECT data set (Johnson et al. 2007; Zhang et al. 2010; Graser et al. 2009b). Non-enhanced CT of the liver may provide relevant diagnostic information in various clinical scenarios (Boll & Merkle 2009). These include the search for calcifications e.g., as in calcified metastases of mucinous adenocarcinoma or postinflammatory calcifications such as in echinococcal disease. Also the

Table 1 Recommended scan protocols for hepatic imaging using Siemens definition and Siemens definition flash

	Siemens definition	Siemens definition flash
Scan mode	Spiral dual energy	Spiral dual energy
Scan area	Diaphragm to ilac crest	Diaphragm to iliac crest
Scan direction	cranio-caudal	cranio-caudal
Tube voltage A/B (kV)	140/80	100/140 Sn (tin filter)
Tube current A/B (quality ref. mAs)	85/468	230/177.7
Dose modulation	CARE Dose 4D on	CARE Dose 4D on
$CTDI_{Vol}$ (mGy)	17.5	18.2
Rotation time (s)	0.50	0.50
Pitch	0.55	0.60
Slice collimation (mm)	1.2	0.6
Acquisition	14 × 1.2 mm	32 × 0.6 mm
Reconstruction kernel	D30f	D30f

detection of intrahepatic bile duct concretions is a valid indication for non-enhanced liver CT, as is the search for subcapsular or parenchymal hemorrhage or the post-procedural visualization of Lipiodol after embolization therapy of liver tumors. Following previous studies on DECT of renal masses (Graser et al. 2009a; Brown et al. 2009) recently Zhang et al. evaluated the image characteristics of virtual non-enhanced hepatic DECT (Zhang et al. 2010). In detail CT numbers, signal to noise ratio (SNR), image quality, and contrast to noise (CNR) of virtual non-enhanced hepatic DECT and true non-enhanced hepatic single energy CT of 102 patients were compared. Moreover, the detectability of focal liver lesions and radiation dose of a DECT protocol with and without true non-enhanced CT and were evaluated. Virtual non-enhanced CT images were processed from arterial and portal venous DECT data. It was shown, that there was no significant difference in mean CT numbers of liver, spleen, pancreas and muscle between virtual non-enhanced and true non-enhanced CT images. SNR of virtual non-enhanced hepatic CT was higher than that of the true non-enhanced CT data, a finding that has been previously reported for virtual non-enhanced CT of the kidneys and aorta (Graser et al. 2009a; Stolzmann et al. 2008), and has been explained by the post-processing algorithm which uses a smoothing kernel. The virtual non-enhanced CT images did not visualize 8 (arterial phase DECT) or 16 (portal venous phase DECT) of the 86 focal hepatic lesions visualized on the non-enhanced single energy CT scan. Although this appears to be a high number, the majority of these lesions were either small (<1 cm) or located outside the field of view of the smaller detector system, which is a well-known limitation of first generation dual source CT (Fig. 1). Considering those focal hepatic lesions detectable on virtual non-enhanced and true non-enhanced CT there was no difference in the size, attenuation and CNR, while the SNR of the lesions was higher on the virtual non-enhanced CT images. As shown in a previous study on DECT of renal masses, the replacement of a true non-enhanced CT by a virtual non-enhanced CT, i.e., biphasic hepatic DECT versus triphasic hepatic CT, could significantly lower the radiation dose (Zhang et al. 2010).

Currently we are investigating the potential of DECT to improve the response evaluation of patients with metastatic gastrointestinal stroma tumors (GIST). It has previously been shown, that standard criteria for response, such as a change of tumor size are less reliable in GIST (Benjamin et al. 2007). Instead, Choi et al. have shown that changes of the tumor density in contrast enhanced CT is an accurate surrogate marker for response of GIST following targeted therapy (Choi et al. 2007), as the density correlates well with tumor angiogenesis (Choi 2008). It may be assumed that the selective visualization of iodinated contrast media may even be a more precise surrogate marker as tumor necrosis and intratumoral hemorrhage may also result in pronounced density changes but do not necessarily correlate with the extent of tumor angiogenesis. Based on our initial results, however, we do not see an additional benefit for response assessment of GIST using DECT.

Recently several studies used DECT to evaluate the conspicuity and signal characteristics of focal liver lesions at different kV settings. None of these studies specifically investigated the potential of DECT to create virtual non-enhanced CT data sets or iodine maps. In a study by Robinson et al. DECT performed on a first-generation dual source CT was used to compare the conspicuity and CNR of 44 hypovascular liver metastasis on 80 kV and weighted average 120 kV CT (Robinson et al. 2010). They found, that the attenuation difference between metastases and the normal liver was

significantly higher at 80 kV (78 vs. 57 HU). Also the CNR was significantly higher at 80 kV. This resulted in a significantly higher conspicuity score in the qualitative image evaluation. Similarly, a 64-section dual energy CT scanner with rapid kV switching was recently used for a comparison of 80 and 140 kV CT protocol regarding the diagnostic evaluation of hypervascular liver tumors. The first study performed an intraindividual comparison of 80 kV/675 mA and 140 kV/385 mA late arterial phase CT scanning in 60 malignant hypervascular liver tumors in 48 patients (Marin et al. 2009). Despite a significantly increased image noise and lower overall image quality score the 80 kV protocol yielded significantly higher contrast-to-noise ratio and lesion conspicuity scores when compared to the 140 kV scan protocol. In addition a significantly lower radiation dose was observed with the low kV protocol (5.1 vs. 17.5 mSv). In a subsequent study by the same authors an iterative reconstruction algorithm was successfully used to improve the image quality and decrease the image noise of the 80 kV scan protocol, indicating that the radiation dose might be further decreased using a low kV protocol (Marin et al. 2010).

In a recently published study by Kim et al. different linear and non-linear image fusion algorithms were compared regarding the visualization of hypervascular liver lesions (Kim et al. 2010). They examined a liver phantom containing eight tubes with various concentrations of contrast material and 20 patients with hepatocellular carcinomas on a first generation dual source CT in dual energy mode. CT data of the 80 and 140 kV tube were fused using the linear blending method and nonlinear method with different weighting factors (0.1, 0.3, 0.5, 0.7, and 0.9) and different parameters sets (A–λ: 20, ω: 430; B–λ: 20, ω: 70; C–λ: 250, ω: 430; D–λ: 250, ω: 70). For quantitative analyses of the phantom and patient study, the contrast-to-noise ratio (CNR) of the lesion to liver on arterial phase images, was measured. Furthermore, a qualitative analysis of the clinical CT images was performed by five radiologists regarding lesion conspicuity and overall image quality. It was shown that linear blended images with a higher weighting factor than 0.5 and nonlinear blended images with a wide width provided improved lesion-to-liver CNR over the standard linear blending method (with a weighting factor of 0.3). Similarly, the nonlinear blending method with a low level and a high width provided the most preferred image set for hypervascular hepatocellular carcinoma detection.

In addition to the detection of iodine by DECT several studies have evaluated the ability of DECT to characterize focal or diffuse fat deposition of the liver (Kamel et al. 2001; Mendler et al. 1998; Raptopoulos et al. 1991; Wang et al. 2003). The clinical background for this is the high prevalence of fatty liver infiltration and the potential to progress to liver cirrhosis. Focal fatty infiltration of the liver may further simulate neoplastic masses of the liver, thus DECT could be used for differentiation of liver masses and focal fat deposition.

In a pilot study Raptopoulos et al. performed DECT (140 and 80 kV) of the liver in 21 patients, of which 14 underwent liver biopsy and 7 with normal liver (Raptopoulos et al. 1991). Attenuation differences ($\Delta H = H_{140kV} - H_{80kV}$) were 3.5 HU for normal liver ($n = 7$), 2.5 HU for hypodense liver masses ($n = 6$), 13 HU for fatty liver ($n = 5$), and 0.3 HU for fatty liver combined with hemochromatosis or hemosiderosis ($n = 3$). There was a statistically significant difference between fatty liver and the other groups. A difference greater than 10 HU was unique to fatty infiltration. It was concluded that DECT may help to differentiate focal fatty infiltration of the liver from low-density neoplastic or other lesions, but only if the iron content of the liver is not increased, as elements with high atomic number (e.g., iron) show a higher attenuation at lower x-ray energies.

The results of this pilot study were confirmed in an animal study by Wang et al. (2003). They examined the correlation of attenuation differences (ΔH) at DECT with the volume ratio of liver fat content (VP) as determined by histology. It was shown, that there were significant liver attenuation differences between 90 and 140 kV in the animals with dietary induced fatty liver disease ($\Delta H = 2.5–14$ HU), while there were no differences in the control group ($\Delta H = -0.4$ to 1.4 HU). Furthermore, there was a significant linear correlation between VP values and attenuation differences (ΔH).

However, more recently, another clinical study did not find any relevant benefit of DECT for the assessment of fatty liver disease when compared to single engery CT or ultrasound (Mendler et al. 1998). In detail Mendler et al. examined 27 patients which have been classified by ultrasound of having fatty liver ($n = 16$) or normal liver ($n = 11$). All patients with fatty liver finally underwent liver biopsy. The scan protocol included a non-enhanced single engery CT scan at 140 kV as well as an additional 80 kV

scan. Attenuation measurements were performed in each CT series in the liver as well as in the spleen, muscle, aorta and subcutaneous fat. It was shown that the attenuation difference between 80 and 140 kV (ΔH) of subcutaneous fat was highly significant, confirming the hypothesis of the study that DE might be valuable for the quantification of fatty liver disease. ΔH was also significant in patients with fatty liver and without iron overload. However, if iron overload was present there was no significant difference in the attenuation of fatty liver between 80 and 140 kV. In correlation to histology DECT did not show any significant correlation to the degree of fatty infiltration. Using a threshold of $\Delta H = 9$ HU, as determined from a linear regression analysis, DECT failed to diagnose fatty liver disease in only 1 of the 16 cases, which was inferior to single energy CT (4 out of 16 cases) and ultrasound (all 16 cases). It was concluded that ultrasound was superior to single energy CT and DECT in the diagnosis of fatty liver, especially as iron overload did not reduce the sensitivity for the detection of fatty liver disease. In comparison to ultrasound and single energy CT, DECT appeared to be of no additional value in the diagnosis and quantification of fatty liver. In another study by the group of Raptopoulos published 10 years after their initial pilot study, DECT was used for the diagnosis of fatty liver infiltration as part of the work-up of potential liver donors (Kamel et al. 2001). Of 40 donors examined, 4 had evidence of fatty infiltration at DECT and were excluded from surgery. However, there was no confirmation of these findings.

Already in the eighties of the last century several studies have evaluated the potential of DECT for the quantification of iron deposition in the liver. The determination of liver iron concentration is an important diagnostic criterion for the diagnosis and staging of iron overload diseases, such as hereditary hemochromatosis or hemosiderosis. Until now, liver biopsy with histologic examination of the iron distribution and chemical determination of the iron concentration are still the reference methods in determining liver iron overload. Therefore, non-invasive imaging tests for the quantification of liver iron overload, such MRI or CT, are very promising alternatives to invasive liver biopsy and are especially interesting for therapy monitoring (Roudot-Thoraval et al. 1983; Queiroz-Andrade et al. 2009). Attempts using single energy CT have been disappointing due to the low sensitivity of single energy CT in the diagnosis of patients with mild iron overload and the inability to differentiate between normal iron storage and moderate liver iron overload (Guyader et al. 1989; Bonkovsky et al. 1990; Nielsen et al. 1992). In two pilot studies in a small number of patients and dogs with hemochromatosis an excellent correlation was seen between biopsy and DECT determination of liver iron (Goldberg et al. 1982; Chapman et al. 1980). However, subsequent studies did not entirely achieve positive results. In a study by Nielsen et al. the correlation of single energy CT and DECT attenuation values with liver iron concentration in rats with iron overload was evaluated. Whereas over the entire range of iron concentrations a good correlation between CT attenuation and liver-iron concentration was found, both single energy CT and DECT were insensitive to low concentrations of iron. Disappointingly, DECT was even less accurate than single energy CT in the low iron concentration range (Nielsen et al. 1992). In a study by Klöppel et al. 31 patients with verified hemochromatosis were examined by DECT. They found a high correlation of DECT and several reference methods of iron metabolism (iron determination by absorption spectrometry and histologic examination, serum-iron-level, serum-ferritin-level, relative transferrin saturation, desferal test). With a specificity of nearly 100%, DECT showed a minor or medium iron overload only with low sensitivity (Kloppel et al. 1989). Based on these studies it seems that DECT until now may be too insensitive for the quantification of low iron overload.

6 Conclusion

Based on the few but steadily increasing number of published studies it can be concluded that the differentiation of iodine is the most, but probably also only, valuable application of DECT for hepatic imaging. DECT can be used to improve the conspicuity of hypervascular liver lesions by utilizing the higher attenuation of iodine at low kV levels. In contrast to single energy low kV scanning, however, DECT maintains the noise characteristics of a high-energy scan. In this regard, non linear blending algorithms are a promising alternative to standard lineal blending algorithms. The potential to process a virtual non-enhanced scan, DECT might be used to lower the radiation dose in comparison to a standard multiphasic imaging protocol.

References

Benjamin RS, Choi H, Macapinlac HA et al (2007) We should desist using RECIST, at least in GIST. J Clin Oncol 25:1760–1764

Boll DT, Merkle EM (2009) Diffuse liver disease: strategies for hepatic CT and MR imaging. Radiographics 29:1591–1614

Bonkovsky HL, Slaker DP, Bills EB, Wolf DC (1990) Usefulness and limitations of laboratory and hepatic imaging studies in iron-storage disease. Gastroenterology 99:1079–1091

Brown CL, Hartman RP, Dzyubak OP et al (2009) Dual-energy CT iodine overlay technique for characterization of renal masses as cyst or solid: a phantom feasibility study. Eur Radiol 19:1289–1295

Chapman RW, Williams G, Bydder G, Dick R, Sherlock S, Kreel L (1980) Computed tomography for determining liver iron content in primary haemochromatosis. BMJ 280:440–442

Choi H (2008) Response evaluation of gastrointestinal stromal tumors. Oncologist 13(Suppl 2):4–7

Choi H, Charnsangavej C, Faria SC et al (2007) Correlation of computed tomography and positron emission tomography in patients with metastatic gastrointestinal stromal tumor treated at a single institution with imatinib mesylate: proposal of new computed tomography response criteria. J Clin Oncol 25:1753–1759

Christner JA, Kofler JM, McCollough CH (2010) Estimating effective dose for CT using dose-length product compared with using organ doses: consequences of adopting International Commission on Radiological Protection publication 103 or dual-energy scanning. AJR Am J Roentgenol 194:881–889

Goldberg HI, Cann CE, Moss AA, Ohto M, Brito A, Federle M (1982) Noninvasive quantitation of liver iron in dogs with hemochromatosis using dual-energy CT scanning. Invest Radiol 17:375–380

Graser A, Johnson TR, Hecht EM et al (2009a) Dual-energy CT in patients suspected of having renal masses: can virtual nonenhanced images replace true nonenhanced images? Radiology 252:433–440

Graser A, Johnson TR, Chandarana H, Macari M (2009b) Dual energy CT: preliminary observations and potential clinical applications in the abdomen. Eur Radiol 19:13–23

Guyader D, Gandon Y, Deugnier Y et al (1989) Evaluation of computed tomography in the assessment of liver iron overload. A study of 46 cases of idiopathic hemochromatosis. Gastroenterology 97:737–743

Hamer OW, Aguirre DA, Casola G, Lavine JE, Woenckhaus M, Sirlin CB (2006) Fatty liver: imaging patterns and pitfalls. Radiographics 26:1637–1653

Holmes DR 3rd, Fletcher JG, Apel A et al (2008) Evaluation of non-linear blending in dual-energy computed tomography. Eur J Radiol 68:409–413

Johnson TR (2009) Dual energy CT-technical background. In: Reiser MF, Becker CR, Nikolaou K, Glazer G (eds) Multislice CT. Springer, Berlin, pp 65–73

Johnson TR, Krauss B, Sedlmair M et al (2007) Material differentiation by dual energy CT: initial experience. Eur Radiol 17:1510–1517

Kamel IR, Kruskal JB, Pomfret EA, Keogan MT, Warmbrand G, Raptopoulos V (2001) Impact of multidetector CT on donor selection and surgical planning before living adult right lobe liver transplantation. AJR Am J Roentgenol 176:193–200

Kawamoto S, Soyer PA, Fishman EK, Bluemke DA (1998) Nonneoplastic liver disease: evaluation with CT and MR imaging. Radiographics 18:827–848

Kim KS, Lee JM, Kim SH et al (2010) Image fusion in dual energy computed tomography for detection of hypervascular liver hepatocellular carcinoma: phantom and preliminary studies. Invest Radiol 45:149–157

Kitamura T, Ichikawa T, Erturk SM et al (2008) Detection of hypervascular hepatocellular carcinoma with multidetector-row CT: single arterial-phase imaging with computer-assisted automatic bolus-tracking technique compared with double arterial-phase imaging. J Comput Assist Tomogr 32:724–729

Kloppel R, Reinhardt M, Lieberenz S, Fuchs M, Winnefeld K, Machnik G (1989) The diagnostic value of CT in siderophilia (primary idiopathic hemochromatosis). Gastroenterol J 49:122–125

Kopp AF, Heuschmid M, Claussen CD (2002) Multidetector helical CT of the liver for tumor detection and characterization. Eur Radiol 12:745–752

Marin D, Nelson RC, Samei E et al (2009) Hypervascular liver tumors: low tube voltage, high tube current multidetector CT during late hepatic arterial phase for detection–initial clinical experience. Radiology 251:771–779

Marin D, Nelson RC, Schindera ST et al (2010) Low-tube-voltage, high-tube-current multidetector abdominal CT: improved image quality and decreased radiation dose with adaptive statistical iterative reconstruction algorithm–initial clinical experience. Radiology 254:145–153

Mendler MH, Bouillet P, Le Sidaner A et al (1998) Dual-energy CT in the diagnosis and quantification of fatty liver: limited clinical value in comparison to ultrasound scan and single-energy CT, with special reference to iron overload. J Hepatol 28:785–794

Nielsen P, Engelhardt R, Fischer R, Heinrich HC, Langkowski JH, Bucheler E (1992) Noninvasive liver-iron quantification by computed tomography in iron-overloaded rats. Invest Radiol 27:312–317

Paulson EK, McDermott VG, Keogan MT, DeLong DM, Frederick MG, Nelson RC (1998) Carcinoid metastases to the liver: role of triple-phase helical CT. Radiology 206: 143–150

Queiroz-Andrade M, Blasbalg R, Ortega CD et al (2009) MR imaging findings of iron overload. Radiographics 29: 1575–1589

Raptopoulos V, Karellas A, Bernstein J, Reale FR, Constantinou C, Zawacki JK (1991) Value of dual-energy CT in differentiating focal fatty infiltration of the liver from low-density masses. AJR Am J Roentgenol 157:721–725

Robinson E, Babb J, Chandarana H, Macari M (2010) Dual source dual energy MDCT: comparison of 80 kVp and weighted average 120 kVp data for conspicuity of hypovascular liver metastases. Invest Radiol 47(7):413–418

Roudot-Thoraval F, Halphen M, Larde D et al (1983) Evaluation of liver iron content by computed tomography: its value in the follow-up of treatment in patients with idiopathic hemochromatosis. Hepatology 3:974–979

Stolzmann P, Frauenfelder T, Pfammatter T et al (2008) Endoleaks after endovascular abdominal aortic aneurysm

repair: detection with dual-energy dual-source CT. Radiology 249:682–691

Thomas C, Ketelsen D, Tsiflikas I et al (2010) Dual-energy computed tomography: is there a penalty in image quality and radiation dose compared with single-energy computed tomography? J Comput Assist Tomogr 34:309–315

Wang B, Gao Z, Zou Q, Li L (2003) Quantitative diagnosis of fatty liver with dual-energy CT. An experimental study in rabbits. Acta Radiol 44:92–97

Zhang LJ, Peng J, Wu SY, et al (2010) Liver virtual non-enhanced CT with dual-source, dual-energy CT: a preliminary study. Eur Radiol

Kidney Imaging

Anno Graser

Contents

Abstract

› MDCT is the most important imaging method in patients with suspicious renal masses. Traditionally, multiphasic examinations have to be performed as detection and characterization of malignancy relies on enhancement of masses, and unenhanced images are used for detection of intralesional fat and calcification. Dual energy CT (DECT) has the potential to simplify and improve renal mass characterization by direct visualization of enhancement in a color coded fashion. Based on three-material decomposition principles, DECT enables iodine quantification within every voxel of a CT dataset without the need to acquire unenhanced images. Based on our research we propose a single phase renal mass imaging protocol for MDCT, thereby significantly decreasing radiation exposure to the patient. In summary, renal DECT allows fast and reliable renal mass characterization, and significantly reduces radiation dose by omission of true nonenhanced scans.

1 Clinical Background

Multidetector row computed tomography (MDCT) is the most widely used imaging modality in the diagnostic workup of patients with suspicious renal masses. A standard imaging protocol includes an unenhanced as well as a contrast-enhanced nephrographic phase (delay >70 s) acquisition (Birnbaum et al. 1996; Israel

A. Graser
Department of Clinical Radiology, University of Munich, Grosshadern Hospital, Marchioninistrasse 15, 81377 Munich, Germany
e-mail: anno.graser@med.lmu.de

T.R.C. Johnson et al. (eds.), *Dual Energy CT in Clinical Practice*, Medical Radiology,
DOI: 10.1007/174_2010_41

and Bosniak 2008). Precontrast images are used for baseline density measurements of renal masses, but also provide information about the presence of fat and calcium within a lesion. A mass will be considered benign if it increases in attenuation by no more than 10 Hounsfield units (HU) after the injection of contrast agent (Bosniak and Rofsky 1996); it will be called malignant based on CT imaging features if it enhances by more than 20 HU (Israel and Bosniak 2005; Birnbaum et al. 2007), or if it shows enhancement in the simultaneous presence of calcification and macroscopic fat. By means of MDCT, renal masses can be reliably detected, characterized, and staged; furthermore, a discrimination of clear cell renal cell carcinoma from other histological subtypes, like papillary RCC, is often possible based on characteristic enhancement patterns and the absence or presence of necrosis within a mass (Vikram et al. 2009).

Traditionally, detection of enhancement within a renal mass relies on comparison of measured CT numbers on unenhanced images with those that are measured on contrast-enhanced nephrographic phase images. As a consequence, in a patient with a suspected renal mass, at least two scans of the abdomen will be acquired – an approach that delivers a substantial amount of ionizing radiation. Subtle enhancement often cannot be visually detected, but will be revealed by means of measured CT numbers before and after intravenous contrast injection. Interpretation of renal CT requires extensive experience and knowledge about enhancement characteristics and patterns of different types of malignancy as well as imaging features of benign masses that do not require surgical resection. The ultimate goal of renal CT is reliable and reproducible identification of any patient with malignancy; at the same time, there should be a high level of confidence when calling a mass "benign" in order to avoid unnecessary surgery. Dual-energy CT (DECT) might potentially help to achieve these two goals in one fast acquisition.

2 Technical Background

DECT relies on simultaneous acquisition of CT data at different tube kilovoltages. Since the introduction of the first dual source CT scanner in 2006, it has been shown that DECT can be used to differentiate materials in the scan field (Johnson et al. 2007). On the basis of a principle called three-material decomposition, different postprocessing algorithms are available that enable the identification of iodine, calcium, or uric acid in the image. When each voxel in the image is analyzed for the presence of soft tissue, fat, and iodine, so-called virtual nonenhanced (VNE) images that approximate the image quality and CT number stability of true nonenhanced (TNE) images can be calculated (Graser et al. 2009a, b). Potential abdominal applications of this approach include automated bone subtraction for direct angio CT, imaging of patients post endovascular AAA repair (Chandarana et al. 2008), characterization of urinary calculi (Graser et al. 2008), and imaging of patients with pancreatic, adrenal, and renal masses (Graser et al. 2008). Furthermore, differences in attenuation of data acquired at 80 and 140 kVp may be beneficial in the diagnosis of inflammatory and ischemic bowel disease or poorly vascularized tumors such as pancreatic cancer (Macari et al. 2010). Finally, the attenuation of vessels is substantially greater when acquired at 80 kVp as opposed to 140 kVp. This may improve vessel detection and evaluation at CT angiography and at the same time allow less iodinated contrast material to be administered.

In patients with suspicious renal masses, DECT could possibly obviate the need for non-contrast scanning as VNE images could be used for baseline density measurements of lesions. Thus, a single-phase nephrographic phase CT protocol could be established which has the potential to substantially decrease radiation exposure. Furthermore, color-coded display of the iodine distribution in the scan field could potentially allow the radiologist to determine the presence of enhancement within a renal mass without the need for CT number measurements on both non-contrast and contrast-enhanced images. Additionally, the simultaneous acquisition of high- and low-energy data excludes misregistration or differences in partial volume averaging which represent relevant limitations in multiphase protocols.

2.1 Technical Considerations

In general, DECT can be done using three different technical principles: by means of (1) a dual-source scanner that operates two tubes at different kilovoltages; (2)

a scanner that enables rapid switching of the tube kilovoltage during every rotation; (3) a scanner equipped with a dual-layer detector. At our institution, a dual-source CT (DSCT) scanner (Siemens Somatom Definition Dual Source) was installed in April 2006, and it was replaced by a second generation scanner (Siemens Somatom Definition Flash) in April 2009. Recent advances in DECT technology have lead to increased image quality of low kVp data and better separation of spectra by means of tin filtering. Increased size of the second detector (first generation: 26 cm; second generation: 33 cm) allows for coverage of larger anatomical areas. In renal imaging, both kidneys can now be imaged without exclusion of relevant anatomy. These advances are important for the use of DECT in clinical practice, as on first generation DSCT scanners, the location of suspected renal pathology had to be known in order to correctly position the patient off-center to the contralateral side (Graser et al. 2009a, b). The tin filtering system which is available on the high kVp tube leads to significant beam hardening, thereby enabling much better separation of low- and high-energy spectra. The low-energy tube can now be operated at 100 rather than 80 kVp; this markedly improves the penetration of low kVp photons, decreases cross scatter and image noise, and makes DECT feasible in larger patients. Other DECT applications, like CTA of the carotid arteries and perfusion CT of the lungs, were not affected by quantum noise as much as DECT of the abdomen, which is why this development is of great importance for renal DECT. Even when 100 and Sn140 kVp are used, a dual-energy examination of the abdomen delivers about the same effective radiation dose to the patient as a 120-kVp single-energy acquisition. In comparison to first generation scanners, second generation DECT allows acquisition of up to 128 slices, and collimation can be set to 32×0.6 rather than 14×1.2 mm for the DE acquisition. On both scanners, outer detector rows will be used for scatter correction. For scan parameters of first and second generation renal DECT, see Table 1. Further technical details are provided in Chap. 44.

In renal DECT, we reconstruct 2 mm overlapping axial images from the raw data using 1.5 mm interslice gap to allow for exact three-material decomposition at limited image noise. A slice thickness of 2 mm provides sufficient spatial resolution to load the dataset into the dual-energy postprocessing software (Siemens Syngo MMWP 2009), whereby coronal and sagittal multiplanar reformations (MPRs) are automatically generated. These MPRs are very useful for staging of renal masses and determination of the extension of a mass into the perirenal fat, renal vein, and collecting system. From the dual-energy data set, the scanner generates three different series of images: 80 or 100 kVp images, depending on the scanner type; 140 kVp images; and weighted average images which are based upon data from both detectors, using 70% information from the high kV and 30% from the low kV scan. These images approximate the image quality of a standard 120 kVp scan of the abdomen and are used to determine contrast agent uptake. The postprocessing software can be used to generate both VNE images and color-coded iodine maps; furthermore,

Table 1 Scan parameters for the two dual-source scanners

	Definition DS (tubes A/B)	Definition flash (tubes A/B)
Slices	2×64	2×128
Angular offset (°)	90	95
FoV (cm)	50/26	50/33
Spectra (kVp)	140/80	100/Sn140
Filter (mm)	3 Al, 0.9 Ti	3 Al, 0.9 Ti, 0.4 Sn (B tube only)
Current time product (mAs)	96/404	300/232
Modulation	CareDose4D (*x*, *y*, *z*-axis)	CareDose4D (*x*, *y*, *z*-axis)
Collimation (mm)	14×1.2	32×0.6
Pitch	0.55	0.6
Rotation time (s)	0.5	0.5

Definition DS first generation dual-source CT; *Definition FLASH* second generation dual-source CT

enhancement of a lesion can be directly measured without the need to compare pre- and postcontrast images. This significantly shortens the interpretation times of renal CT (see Sect 2.3).

For renal DECT, we use a standard contrast agent injection of 1.35 mL/kg body weight at a concentration of 370 mg/mL (Ultravist 370, BayerSchering Diagnostics, Berlin, Germany); contrast media is injected at a flow rate of 2 mL/s. The scan range of both the non-contrast and contrast-enhanced nephrographic phases cover the abdomen from the dome of the liver to the iliac crest, while a delayed phase is performed from the dome of the liver to the pubic symphysis in order to cover the entire urinary tract when urothelial malignancy is suspected.

2.2 Comparison of True and Virtual Nonenhanced Images in Renal DECT

The use of DECT in imaging of patients with suspicious renal masses is based upon its unique capability to directly visualize the distribution of iodine in the scan field, and its ability to generate VNE images. These can be used for baseline density measurements within renal masses and normal renal parenchyma. DECT may therefore be used for the differentiation of high-density cysts from solid renal masses.

In order to show that TNE and VNE images are comparable in image quality and noise, a study was conducted at our institution (Graser et al. 2009a, b). In brief, 110 patients underwent renal DECT on a first generation dual-source multidetector row CT scanner. First, a TNE scan of the abdomen was acquired in an inspiratory breath hold using a detector configuration of 64×0.6 mm, a tube potential of 120 kVp, 240 quality reference mAs, and online dose modulation (Graser et al. 2006). Eighty seconds after intravenous injection of a nonionic contrast agent (1.35 mL/kg patient body weight; Ultravist 370, BayerSchering Diagnostics, Berlin, Germany), a dual-energy nephrographic phase scan was acquired from the dome of the liver to the iliac crest operating the "A" tube at 140 kVp and a reference mAs value of 96, and the "B" tube at 80 kVp and 404 reference mAs. On both tubes, online dose modulation was used. For the dual-energy scan, collimation was set to 14×1.2 mm on both detectors. Finally, a single-energy low-dose (120 kVp, 50 reference mAs) delayed phase acquisition was performed from the dome of the liver to the pubic symphysis 220 s after the DECT acquisition.

Dose-length products (DLPs) were recorded from the patient protocol. These values were used for the calculation of individual effective radiation doses, and the effective dose of a triple phase protocol (TNE, DE nephrographic, and delayed phases) was compared to a dual-phase protocol (DE nephrographic and delayed phases only). For comparison of DECT image quality and noise, CT numbers were determined in different anatomical regions throughout the abdomen; these measurements were also used to test CT number stability of DECT-derived VNE images. In addition, two experienced abdominal radiologists rated image quality and noise on a five-point scale. Radiologists finally had to decide whether they would accept VNE images as a replacement for a TNE acquisition on the basis of the overall impression.

Results of the study showed effective radiation exposure for a triple-phase protocol including a true non-contrast scan ranging from 7.49 to 22.59 mSv, with an average of 14.09±3.54 mSv, while a dual-phase protocol consisting of nephrographic dual-energy and delayed phases only was calculated to deliver an effective dose of 9.17±2.51 mSv (range, 4.47–15.53 mSv). The dose reduction achieved by omitting the true non-contrast acquisition was 35.05±4.95%. The average density of the renal parenchyma was 31.6±7.1 HU on VNE and 30.8±4.0 HU on TNE images, respectively, $p=0.29$. Both simple and complex cysts showed comparable CT numbers on true and VNE images. Figure 1 shows a side-by-side comparison of TNE and VNE images acquired at the level of the kidneys.

DECT-based VNE images were well accepted by abdominal staff radiologists: Readers rated 85% of VNE studies as fully acceptable; 13% were rated as "acceptable with restrictions," and only 2% were not accepted, respectively.

In conclusion, this study shows that dual-energy-based VNE images approach the image quality of TNE images and that renal mass DECT has the potential to substantially reduce radiation exposure.

On the basis of results of this study, we concluded that DECT can achieve high image quality in the abdomen, which, due to its larger anteroposterior and lateral diameter, is a more problematic area to image than the neck, the thorax, or extremities. On first generation

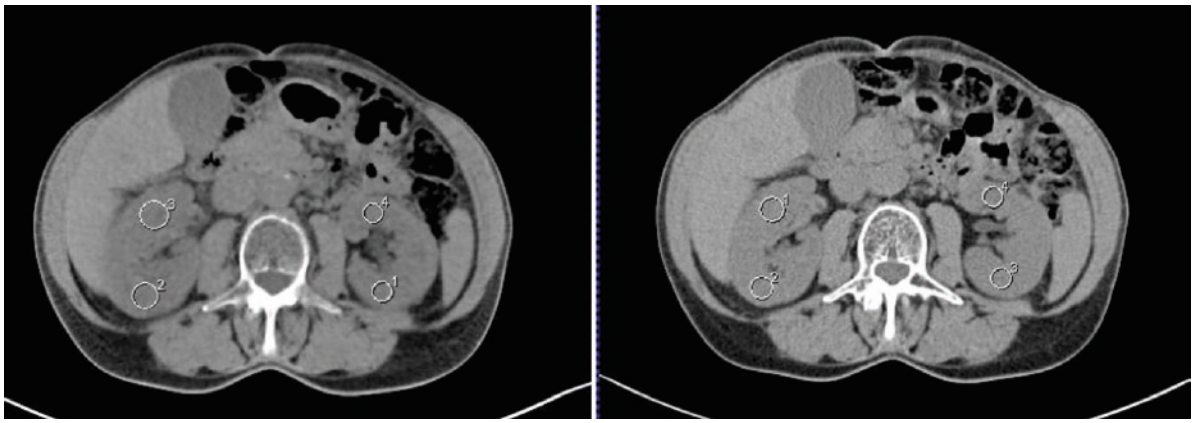

Fig. 1 Virtual (*left*) and true (*right*) nonenhanced axial 3 mm thick images at the level of the renal hilum show comparable image quality. Circular regions of interest were placed on both kidneys in order to confirm Hounsfield unit stability; measured values range from 29 to 31 HU and do not differ significantly

DSCT scanners, it is therefore recommended to use a 14×1.2 mm collimation in order to keep image noise to an acceptable level. As shown in Table 1, the pitch has to be fairly low (0.55) for sufficient photon flux on the low kVp tube. These limitations have been widely overcome on second generation DSCT.

2.3 Characterization of Renal Masses Using Single-Phase DECT

On the basis of our research, VNE images can be used to replace the true non-contrast acquisition. This implies that baseline density measurement of masses as well as identification of calcifications or fat can all be performed on VNE images, thereby obviating the need to acquire a TNE scan. Characterization of renal masses could potentially be done on a single nephrographic phase contrast-enhanced acquisition.

DECT data can be displayed in a color-coded fashion that enables direct visualization of iodine distribution in the image. Potentially, hyperdense renal cysts should therefore be distinguishable from enhancing solid masses. In order to assess the ability of DECT to characterize renal masses as cyst or solid, we performed a clinical trial comparing DECT findings to histopathology or imaging follow-up in 202 patients with suspicious renal masses detected on ultrasound. Of these patients, 174 were scanned on a first generation dual-source scanner (Somatom Definition Dual Souce, Siemens Healthcare), and 28 on the second generation Definition Flash scanner (Siemens Healthcare). After a non-contrast acquisition, a nephrographic phase contrast-enhanced scan was performed using the parameters displayed in Table 1. Again, online dose modulation was used on both tubes, and DLP values were recorded for both non-contrast and dual-energy acquisitions. Enhancement was defined as measured CT number within a certain region of interest on TNE or VNE images subtracted from the density of the same region on a postcontrast image.

From the dual-energy data set, an iodine distribution map was generated by the software which can subsequently be used to subtract iodine from the image, or to generate a color-coded "iodine only" image. This iodine image can be superimposed onto VNE images for immediate visualization of iodine distribution and anatomical information at the same time (Petersilka et al. 2008).

Two abdominal radiologists interpreted all DECT scans in consensus in two separate reading sessions: in the first session, only images derived from the DECT acquisition were used, i. e. color-coded iodine images, weighted average, and virtual unenhanced images; see Fig. 2. If a suspicious renal mass was detected, it had to be characterized as benign or malignant based on the visualization of iodine within the mass on color-coded images derived from the DECT scan. Readers measured enhancement of suspicious masses on DECT images; if a measurement is performed on a color-coded DECT image, the system will display mean±standard deviation

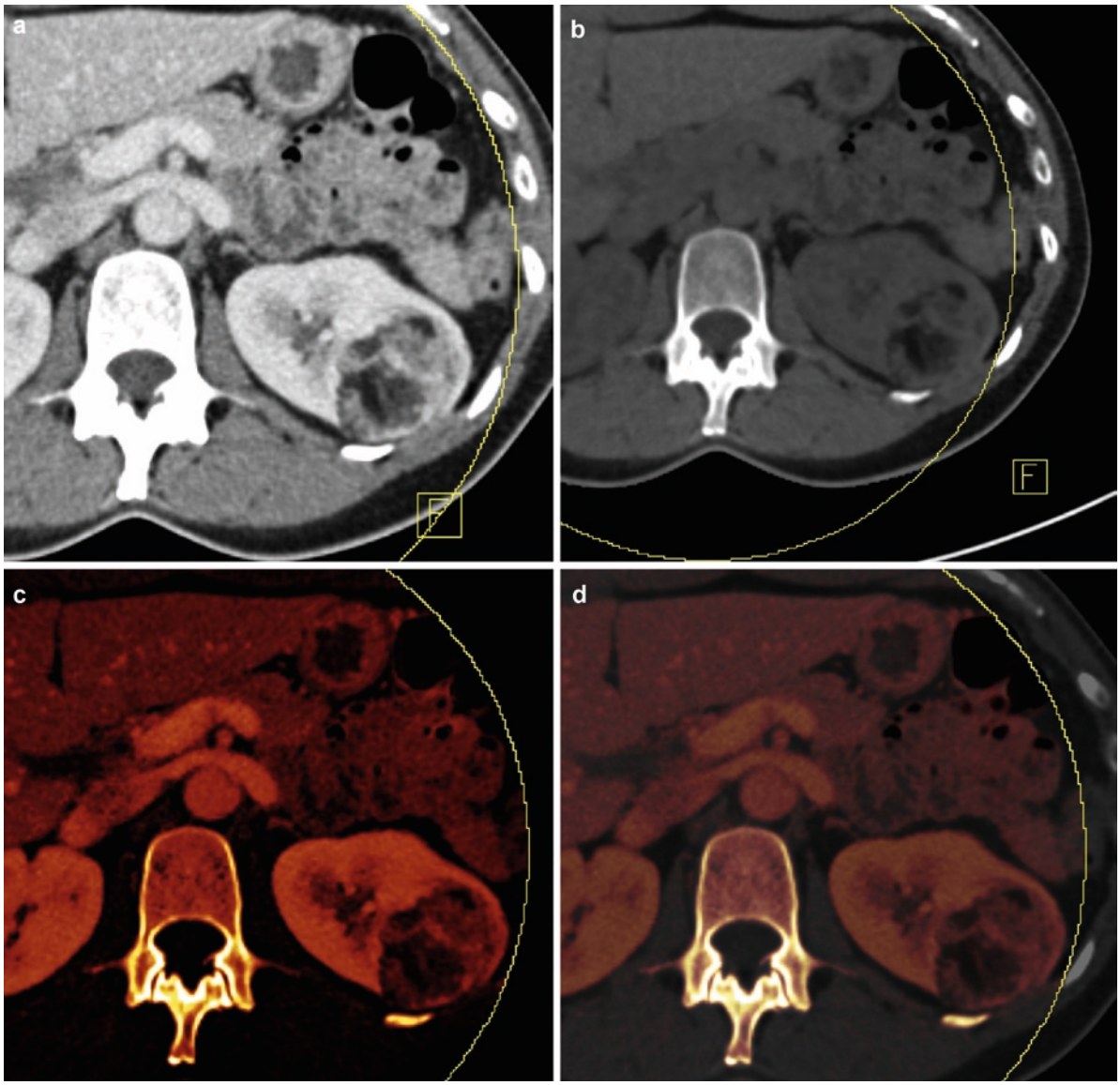

Fig. 2 Images derived from a nephrographic phase dual-energy CT scan in a patient with a fat-containing, well-defined mass on the posterolateral aspect of the left kidney most consistent with an angiomyelolipoma (AML). The weighted average image (**a**) contains information on both the high and low kVp tube and approximates a standard 120 kVp single energy image. Image (**b**) represents the virtual nonenhanced (VNE) image from which iodine has been subtracted; (**c**) shows an iodine-only image; and (**d**) shows a superimposition of (**c**) onto (**b**), allowing for simultaneous visualization of enhancement and high-resolution anatomical information

of CT numbers on both VNE and contrast-enhanced images. Also, a so-called "overlay" value will be displayed which represents the average enhancement in HU, see Fig. 3. We defined a minimum enhancement of 15 HU to indicate malignancy.

In the second reading session, nonenhanced and weighted average nephrographic phase contrast-enhanced images were used, thereby simulating a standard biphasic renal mass examination on a scanner without dual-energy capabilities. Again, masses had to be characterized as malignant or benign, and enhancement of masses was measured as delta of the density on TNE and contrast-enhanced images.

DECT and simulated SECT performance for correct characterization of both benign and malignant renal masses were calculated; we also assessed the

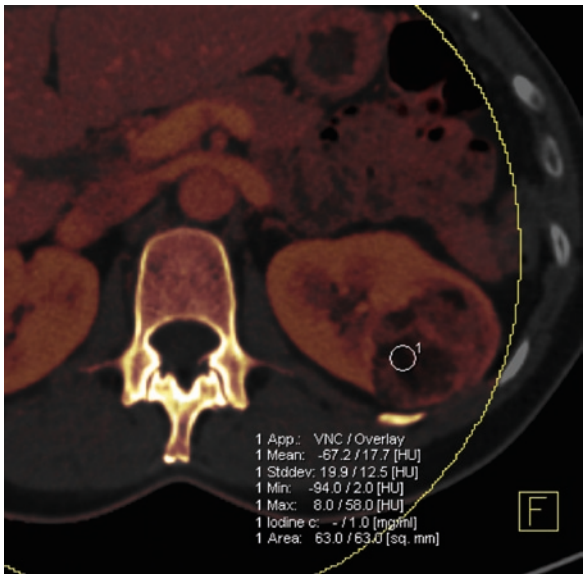

Fig. 3 Same patient as in Fig. 2. Color-coded iodine map superimposed onto VNE image, both derived from the same nephrographic phase DECT acquisition, with circular ROI for measurement of CT numbers. Within the fatty component of the AML, VNE density is −67.2 HU, while enhancement ("overlay") is 17.7 HU

capability of both paradigms to exclude renal pathology in the 37 patients who had no renal mass.

In our study population, histopathology showed malignancy in 99 of 202 (49.0%) patients; while DECT identified 95 of 99 (96.0%); the dual-phase protocol correctly characterized 96 of 99 (97.0%) of these patients, $p > 0.05$. Both DECT and SECT were 95.1% specific for the absence of malignancy (98 of 103 patients).

Malignant tumors showed a mean contrast enhancement of 88.4 ± 37.4 HU (range, 18–168 HU). An example of the two reading paradigms in a patient with a stage T4 TCC of the right kidney is shown in Fig. 4.

Sixty-six patients had benign renal masses, and 18 of these patients underwent resection, while 48 were followed by cross-sectional imaging. Benign masses were enhanced by an average of 5.1 ± 5.0 HU (0–15 HU). In 37 patients, no mass could be found at CT. In 21 cases, anatomical normal variants (dromedary hump, $n = 15$; persistent fetal lobulation, $n = 6$) were detected; 16 patients had normal kidneys at DECT (Fig. 5).

DECT allows for fast image interpretation in patients with renal masses: readers took an average of 3.5 ± 1.0 (range, 1.6–7.2) minutes to interpret biphasic examinations, while the dual-energy single-phase approach allowed interpretation in 2.2 ± 0.8 (range, 1.0–5.8) minutes, $p < 0.0001$.

Mean effective radiation exposure was 4.67 ± 1.35 (1.83–8.60) mSv for the nonenhanced acquisition; 4.95 ± 1.65 (2.28–10.52) mSv for the dual-energy acquisition; and 9.17 ± 2.60 (3.29–15.80) mSv for the biphasic protocol. On the basis of these values, a single-phase dual-energy renal mass protocol would lead to a 48.9 ± 7.0% dose reduction over the dual-phase protocol.

3 Discussion

Study results show that DECT allows for time-efficient and accurate characterization of renal masses. It is widely accepted that at least two CT acquisitions are needed for accurate renal mass detection and characterization, namely a non-contrast and one contrast-enhanced phase (Israel and Bosniak 2008). DECT provides the unique ability to reconstruct VNE images from which iodine has been subtracted, thereby obviating the need for TNE scanning. We could show that VNE images are a reasonable approximation of true non-contrast CT images, and that CT numbers measured on these images are accurate (Graser et al. 2009a, b). Furthermore, DECT provides direct visualization of iodine uptake within a mass in a color-coded fashion, which makes a reliable identification of enhancement without HU measurements possible. There is no significant difference in the diagnostic accuracy of a biphasic single-energy CT and a monophasic DECT approach in the characterization of benign and malignant renal masses. On the basis of our results, it can be recommended to change a renal mass examination protocol on a DSCT scanner to one single nephrographic phase dual-energy acquisition.

It has to be noted that on the first generation DECT scanner (DS), image noise can be high in large patients; this will lead to reduced Hounsfield unit stability due to beam hardening artifacts and may influence the decision about whether or not a renal mass is enhanced. Furthermore, the smaller (26 cm) size of the B detector may not cover the entire abdomen, and off-center positioning of the patient may be required in order to ensure complete coverage of renal pathology (Graser et al. 2009a, b). Therefore, we recommend that patients whose BMI is >30 should not undergo renal DECT on first generation scanners. Both issues have been

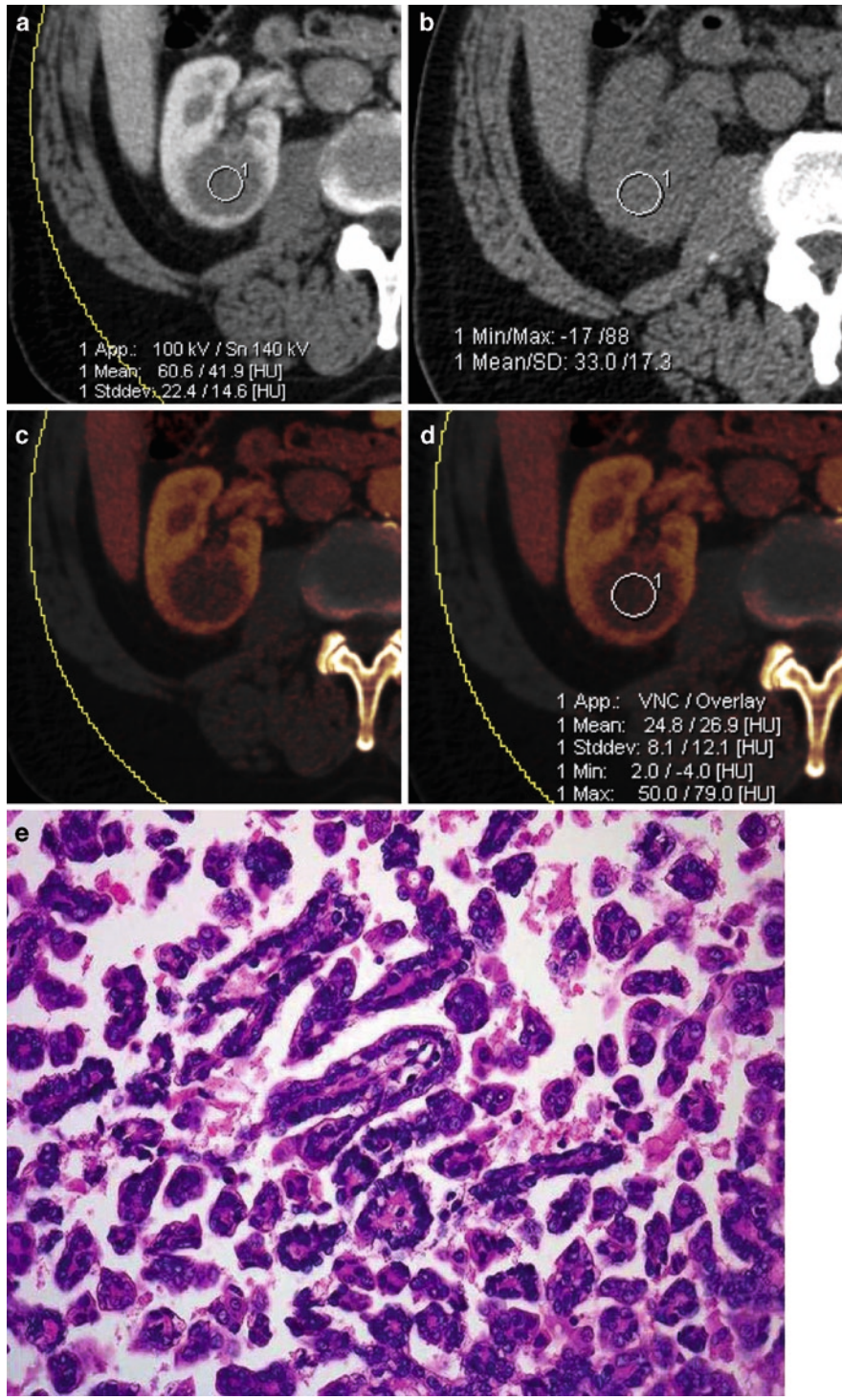

Fig. 4 Comparison of standard single-energy CT and dual-energy CT for renal mass characterization in a patient with a 3.5-cm enhancing intraparenchymal neoplasm on the right kidney. (**a**) and (**b**) show standard SECT workflow: the mass measures 60.6 HU at 100 kVp, and 41.9 HU at Sn140 kVp; before contrast (**b**), the density is 33 HU. Weighted average density is 53.5 HU, enhancement equals 20 HU. Dual-energy CT (**c**) immediately shows enhancement (orange color within the mass); measured VNE density is 25 HU, with an overlay (=enhancement) of 27 HU (**d**). Histopathology showed T3 transitional cell carcinoma (TCC) (**e**)

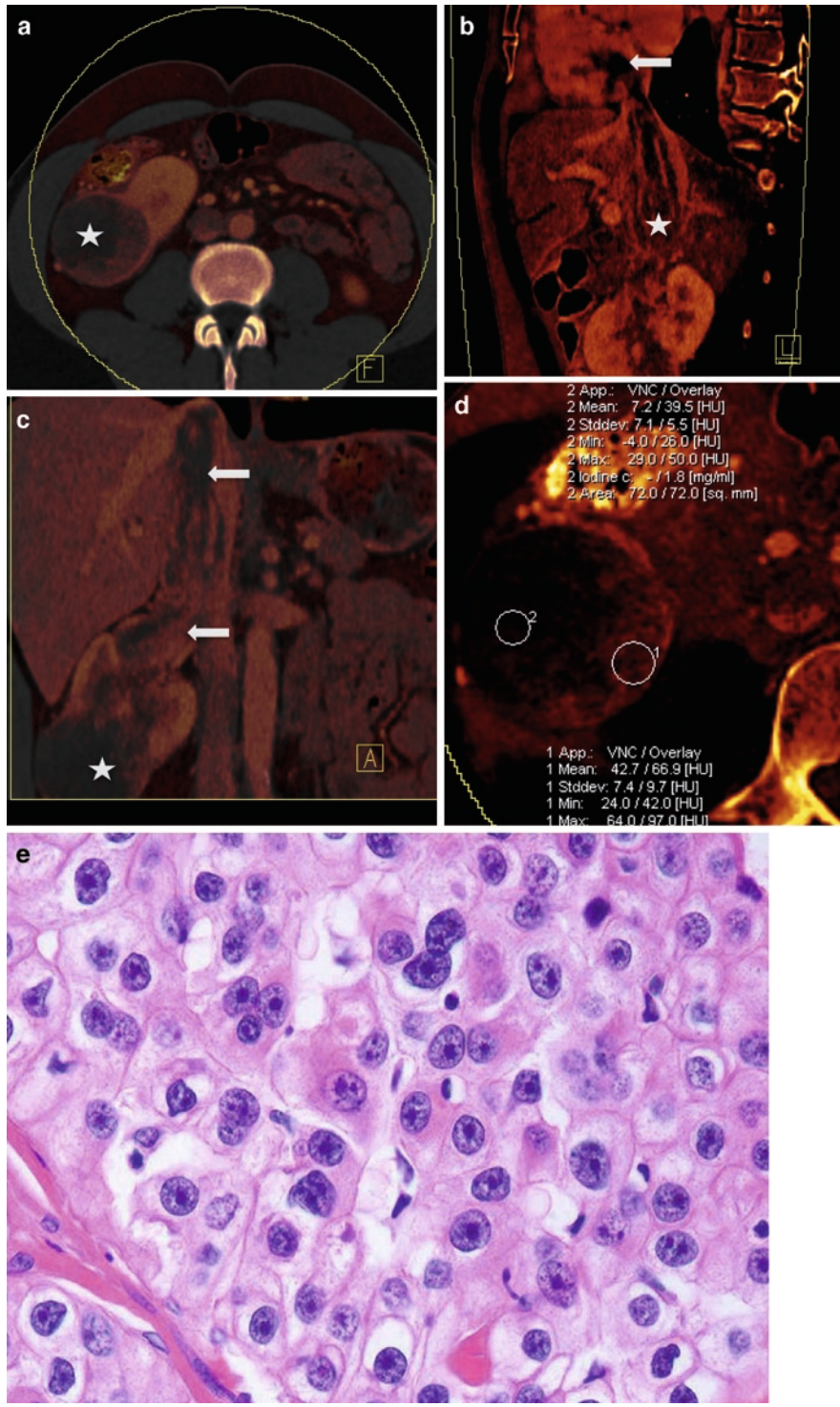

Fig. 5 A case of T3c clear cell renal cell cancer with large SVC tumor thrombus. (**a**) superimposition of color-coded iodine map and VNE image shows heterogeneously enhancing mass (*asterisk*) on right kidney; (**b**) coronal MPR demonstrates large SVC tumor thrombus (*arrows*); (**c**) oblique sagittal iodine only image shows that the thrombus (*asterisk*) contains large vessels and extends into the right atrium (*arrow*); (**d**) axial DECT image shows hypoattenuated lateral part of the mass and hyperenhancing rim-like medial portion (enhancement: VNE density, 7 vs. 43 HU). (**e**) Histopathology shows clear cell renal cell carcinoma

resolved with second generation DECT, as the scanner allows for use of Sn140/100 kVp tube kilovoltages for improved photon penetration and reduced image noise, and the smaller detector now covers 33 cm. We found the additional 7 cm in size to be sufficient for bilateral renal imaging and coverage of the entire abdomen in our patient population. Patients with a BMI of up to 35 might undergo DECT on this type of scanner.

Our results underline that DECT may be suitable to significantly reduce reading times in patients with renal masses. By means of direct visualization of enhancement, masses can be diagnosed as benign or malignant within one color-coded set of images, obviating the need for ROI placement and HU measurement on both pre- and postcontrast images. So far, DECT can only be interpreted on dedicated workstations with adequate postprocessing software; in the near future, PACS reading will also be available, helping to further speed up the diagnostic workflow.

Potential limitations of renal DECT include determination of enhancement within homogeneously hyperattenuating renal masses that contain hemorrhage or proteinaceous fluid. In high-density (>60 HU) lesions, virtual nonenhanced DECT images may show inaccurate CT numbers that are higher than TNE measurements. However, even in these lesions, the presence or absence of enhancement can be clearly determined. Further research is warranted to assess whether DECT may be able to reliably distinguish hemorrhagic cysts from high-density cystic renal cell carcinoma in the presence of protein-rich cyst contents.

In conclusion, DECT offers fast and reliable interpretation of abdominal CT scans performed for the assessment of renal masses. Our results show that a single nephrographic phase protocol may be suitable to replace biphasic scanning and at the same time preserve diagnostic accuracy using DECT. This approach significantly reduces reading times and cuts radiation exposure by almost 50%.

References

Birnbaum BA, Jacobs JE et al (1996) Multiphasic renal CT: comparison of renal mass enhancement during the corticomedullary and nephrographic phases. Radiology 200(3): 753–758

Birnbaum BA, Hindman N et al (2007) Renal cyst pseudoenhancement: influence of multidetector CT reconstruction algorithm and scanner type in phantom model. Radiology 244(3):767–775

Bosniak MA, Rofsky NM (1996) Problems in the detection and characterization of small renal masses. Radiology 200(1): 286–287

Chandarana H, Godoy MC et al (2008) Abdominal aorta: evaluation with dual-source dual-energy multidetector CT after endovascular repair of aneurysms–initial observations. Radiology 249(2):692–700

Graser A, Wintersperger BJ et al (2006) Dose reduction and image quality in MDCT colonography using tube current modulation. AJR Am J Roentgenol 187(3):695–701

Graser A, Johnson TR et al (2008) Dual energy CT characterization of urinary calculi: initial in vitro and clinical experience. Invest Radiol 43(2):112–119

Graser A, Johnson TR et al (2009a) Dual energy CT: preliminary observations and potential clinical applications in the abdomen. Eur Radiol 19:13–23

Graser A, Johnson TR et al (2009b) Dual-energy CT in patients suspected of having renal masses: can virtual nonenhanced images replace true nonenhanced images? Radiology 252:433–440

Israel GM, Bosniak MA (2005) How i do it: evaluating renal masses. Radiology 236(2):441–450

Israel GM, Bosniak MA (2008) Pitfalls in renal mass evaluation and how to avoid them. Radiographics 28(5):1325–1338

Johnson TR, Krauss B et al (2007) Material differentiation by dual energy CT: initial experience. Eur Radiol 17(6):1510–1517

Macari M, Spieler B et al (2010) Dual-source dual-energy MDCT of pancreatic adenocarcinoma: initial observations with data generated at 80 kVp and at simulated weighted-average 120 kVp. AJR Am J Roentgenol 194(1): W27–W32

Petersilka M, Bruder H et al (2008) Technical principles of dual source CT. Eur J Radiol 68(3):362–368

Vikram R, Ng CS et al (2009) Papillary renal cell carcinoma: radiologic-pathologic correlation and spectrum of disease. Radiographics 29(3):741–754, discussion 755-757

Pancreas

Ralf W. Bauer

Contents

Abstract

› Cross sectional imaging plays a paramount role in the diagnosis of pancreatic pathologies. However, detection of early stage pancreatic carcinoma may be challenging due to only very distinct alterations of morphology and contrast material uptake compared to normal pancreatic tissue. But accurate diagnosis in an early stage is vital in this disease. Acute necrotising pancreatitis represents another potentially life-threatening condition where the extend of necrotic areas has been shown to be directly related to mortality. As acute pancreatitis usually goes along with a general oedematous swelling of the organ, difficulties in detecting necrotic areas due to limited soft tissue contrast of CT may occur. Dual Energy CT with its potential to increase soft tissue contrast and display and quantify iodine distribution in different body tissues may be an important step towards superior diagnostic accuracy compared to regular Single Energy CT. This chapter intends to give a practical approach to Dual Energy CT imaging of the pancreas in front of current literature and clinical case presentations

1 Clinical Background

Pathologies of the pancreas frequently take a fatal course. Namely two conditions are to be mentioned which show both a high disease-related mortality and

R.W. Bauer
Department of Diagnostic and Interventional Radiology, Clinic of the Goethe University, Theodor-Stern-Kai 7, 60590 Frankfurt am Main, Germany
e-mail: ralfwbauer@aol.com

T.R.C. Johnson et al. (eds.), *Dual Energy CT in Clinical Practice*, Medical Radiology,
DOI: 10.1007/174_2010_42

are both difficult to assess due to sometimes only subtle morphological differences compared to the surrounding tissue: Pancreatic carcinoma and acute necrotizing pancreatitis. Pancreatic carcinoma ranks fifth in the list of cancer-related causes of death in adults after lung and colorectal cancer and the gender-specific carcinomas of the prostate and female breast (Goldstein et al. 2004). It typically shows no specific early symptoms, and therefore, more than 80% of the cases are diagnosed in an incurable locally advanced or metastasised inoperable stage (UICC stage III and IV) (Goldstein et al. 2004). Tumours located in the head or papillary region often present with painless jaundice as a first, but not early, symptom due to obstruction of the common bile duct. Tumours in the pancreatic body or tail do not show this typical symptom and cause mostly non-specific symptoms like fatigue, loss of weight, indigestion, or intestinal discomfort. General prognosis is bad with a median survival of approximately 6 months for all stages, while it increases to 20 months with a 5-year-survival rate of up to 15% after complete tumour removal (Goldstein et al. 2004). As complete surgical resection (R0) currently represents the only curative option for this disease, detection in an early stage is vital. Both CT and MRI play a paramount role for diagnosing pancreatic lesions. In daily practice, thin-section multi-slice CT is the method of choice because of its equal diagnostic accuracy for solid lesions, wider availability, faster acquisition time and lower costs (Delbeke and Pinson 2004; Francis 2007; Grenacher and Klauss 2009; Mehmet Erturk et al. 2006). On both, CT and MRI, adenocarcinomas of the pancreas typically present as low-signal solid or cystic lesion with delayed contrast material uptake compared to normal pancreatic tissue. However, even if cross-sectional imaging is performed early, diagnosis of small carcinomas can be difficult due to only very faint changes of the tumour compared to surrounding normal pancreas like loss of lobulation, regional thickening, or slight alteration in density. If a tumour is present, CT plays an important role to give the surgeon information about resectability by visualizing vascular infiltration (portal vein, superior mesenteric artery and vein, celiac trunk with branches), penetration of surrounding organs, presence of lymphatic and hepatic metastases and signs of peritoneal carcinosis (Delbeke and Pinson 2004; Francis 2007; Grenacher and Klauss 2009).

Different to pancreatic carcinoma, acute pancreatitis is usually diagnosed by typical clinical presentation, patient history and laboratory tests (elevated pancreatic enzyme levels like lipase, amylase, etc.). However, CT is frequently used to confirm diagnosis, to determine disease severity and to assess complications. The CT severity index (CTSI), according to Balthazar, is based on radiological findings such as the presence of fluid collection and necrosis and has been shown to have actually a higher prognostic value in terms of prediction of mortality than have scores based on clinical findings only (Alhajeri and Erwin 2008; Balthazar et al. 1990; Chatzicostas et al. 2003; Leung et al. 2005). One important complication in the course of acute pancreatitis is the development of necrosis, which's extend has been shown to be directly related to mortality (Alhajeri and Erwin 2008; Balthazar et al. 1990; Chatzicostas et al. 2003; Leung et al. 2005). Areas of necrosis would typically appear as hypodense areas with lower or no perfusion. The delineation of such necrotic areas in an early stage can sometimes be difficult due to a general oedematous swelling of the pancreas, and therefore, generally reduced attenuation.

On the other hand, CT helps characterizing a variety of cystic pancreatic lesions like pseudocyst, micro- and macrocystic adenoma or intraductal papillary-mucinous neoplasia (IPMN) by imaging of the wall of the cyst and its relation to the pancreatic duct. Further, CT reliably enables detection of calcifications and its distribution pattern and helps to differentiate between chronic pancreatitis and various cystic lesions that may also show calcification. To reliably differentiate between slight calcifications and contrast material and to quantify the enhancement of a lesion, however, a non-enhanced baseline scan is usually required which exposes the patient to increased radiation burden.

Dual Energy CT based on its physical background may improve early detection of pancreatic malignancies, facilitate improved and time-saving post-processing for tumour staging or reduce overall radiation burden. The basis of that is material differentiation based on spectral behaviour at the high and low tube voltage, and therefore, calculation of virtual non-enhanced images as well as the increased contrast of iodine-enhanced scans at low kV (Graser et al. 2009a; Johnson et al. 2007). Initial observations with Dual Energy CT of the upper abdomen or in patients with pancreatic adenocarcinoma have shown a significant rise in achievable contrast-to-noise ratio (CNR) (Marin et al. 2010) and better lesion conspicuity compared to virtual, composed 120 kV images (Macari et al. 2010).

In the following chapter, we would like to outline a practical approach to Dual Energy CT imaging of pancreatic pathologies with the background of current literature based on clinical cases from our department.

2 Physical Background

Dual Energy CT imaging of the pancreas is largely based on iodine enhancement and separation for increasing the contrast between pathology and normal pancreatic tissue. The low-kV image series acquired with every Dual Energy scan gains prominence in this regard.

For abdominal imaging, the additional hardening of the 140 kV spectrum by the introduction of a tin filter in the second generation of Dual Source CT (Somatom Definition Flash, Siemens) has been an important step. The mean spectra from the low and high kV tube are separated clearly with fewer overlap of quanta of equal energies (keV). This enables especially better iodine separation with quantitative algorithms. As a consequence of this, 100 kV instead of 80 kV as low tube voltage may now be preferably used for abdominal imaging. The 100 kV spectrum is more penetrable with direct impact on improved image quality of the gray scale images.

Dedicated Dual Energy post-processing software provided by different vendors (syngo Dual Energy, Siemens; Volume Dual Energy/GSI Viewer, General Electric) is based on three material decomposition (MD) algorithms that differentiate between fat, soft tissue, iodine and calcium as described earlier in this book in detail. Early studies on evaluation of kidney tumours have shown that the HU values are almost identical to that of real native scans and that this technique has potential to replace baseline native scans, and therefore, reduce overall patient dose (Graser et al. 2009b). On the other hand, one can quantify iodine-based enhancement (CT density in HU and iodine content in mgI/mg tissue) by placing region of interest cursors and calculate colour-coded steady-state perfusion maps of iodine distribution in organs and tissue. To highlight differences in perfusion is important for the detection of usually hypoperfused pancreatic carcinoma and regularly perfused tissue between areas of necrosis in acute pancreatitis.

3 Scan Protocol

For selective imaging of the pancreas, plain drinking water is generally used as negative oral contrast material for the upper gastrointestinal tract. Patients should drink at least 1.5 L of water prior to the examination. Immediately before the scan starts, the patient, while already being on the CT table, should drink another 0.25–0.5 L (one big cup). The patient is positioned centrally on the table. As the pancreas is usually situated around the midline of the body, there should not be a problem with including the organ in its whole length even with a reduced field of view of 26 cm (B-detector of the Siemens Somatom Definition). The patient is routinely scanned in supine position. However, some institutions may prefer a 45° right lateral position. If there are no contraindications (e.g. known allergy, closed-angle glaucoma, ileus, tachyarrhythmia, hypertrophic prostate with urinary retention, myasthenia gravis, etc.), 40 mg *N*-butylscopolaminbromide (Buscopan, Boehringer-Ingelheim) are administered intravenously to relax smooth musculature of the intestine and to allow for pooling water in the stomach and duodenum. As an alternative, one may also use glucagon.

For imaging of pancreatic lesions, dual-phase protocols with arterial and hepatobiliary venous phase are widely used. The scan range should cover the whole liver in *z*-axis extension. For Dual Energy imaging with a Siemens Somatom Definition scanner, tube potentials are set to 140 and 80 kV on system A and B, respectively. In abdominal CT imaging in general, expected noise is fairly high. In addition, Dual Source Dual Energy imaging produces more cross-scattered radiation than a single source scanner. To gain a higher signal and reduce image noise, a thick detector collimation of 14 × 1.2 mm is chosen, gantry rotation time is set to 0.5 s and pitch to 0.55. Quality reference tube current-time product values are set to 96–110 mAs on the 140 kV and 404–467 mAs on the 80 kV tube (tube current ratio of 1:4.25). Automated tube current modulation (CAREdose 4D, Siemens) is turned on. With the second generation of Dual Source Dual Energy CT (Somatom Definition Flash, Siemens), some technical disadvantages have been solved. First, there is no major restriction of the field of view of the second detector anymore, since FOV size was increased by 25% (from 26 to 32 cm). Second, increased tube power (100 kW) and additional hardening of the spectrum of

Table 1 *Scan protocols*, recommended scanner settings for Dual Energy CT imaging of the pancreas are summarized for the Siemens Somatom Definition and the second-generation Dual Source scanner, Definition Flash

Parameter	Definition	Definition Flash
Tube potential		
A tube	140 kV	100 kV
B tube	80 kV	140 kV + tin filter
Tube current		
A tube	96–110 mAs	230–300 mAs
B tube	404–467 mAs	178–232 mAs
Tube current modulation	On	On
Collimation	14 × 1.2 mm	32 × 0.6 mm
Pitch	0.55	0.6
Rotation time	0.5 s	0.5 s

the 140 kV tube with a tin filter (140SN) allow for setting the tube potential on the second tube to 100 kV, and therefore, generating a more penetrable spectrum. In sum, cross-scattered radiation is reduced and a thin collimation (32 × 0.6 mm) with the advantage of improved spatial resolution, if required, can routinely be used. An overview on scan protocols is given in Table 1.

4 Contrast Material Injection

The use of low-osmolar non-ionic iodinated contrast materials with a concentration of 350–400 mg iodine per millilitre may be preferred over low-concentration contrast material as the total injection volume remains low, a sharp bolus geometry allows for better separation of different arterial and venous phases and parenchymal enhancement improves (Heiken et al. 1995; Cademartiri et al. 2002).We routinely aim at an iodine dose of 0.5 g per kg body weight, i.e. 1.2 mL/kg with contrast material with a concentration of 400 mgI/mL (iomeprol, Imeron 400, Bracco Imaging). This results in a total contrast material volume of 90 mL for a 75-kg adult patient (72 mL for a 60-kg, 108 mL for a 90-kg patient). Depending on the size of the intravenous line, the contrast material followed by a 40-mL NaCl chaser bolus is automatically injected with a double-syringe power injector (Injektron CT2, Medtron) at a flow rate of 3 mL (20 gauge) or 4 mL (18 gauge).

For arterial phase imaging, we use the bolus-tracking technique. A region of interest is placed in the abdominal aorta at the level of the celiac trunk. An enhancement threshold of +100 HU to trigger scan start is used. Depending on suspected pathology, it may be advisable to use two different arterial phases: (1) A regular arterial phase with a scan delay of 15 s after trigger threshold is reached, if there is suspected neuroendocrine tumour; (2) A late arterial phase or pancreatographic phase with a scan delay of 25 s after trigger threshold is reached, if there is primarily suspected pancreatic adenocarcinoma, pancreatitis or other pathologies. Eighty seconds after the start of contrast material injection, the venous scan in hepatobiliary phase is acquired.

5 Post-Processing

Reconstruction and archiving of axial 1.5 mm thin slices with a position increment of 1 mm and a medium-soft kernel (D30f) for the low (80 or 100 kV) and high kV (140 kV with or without Sn filter) image series have shown to be practical. Additionally, a mixed image series with a similar image impression like a regular 120 kV scan is reconstructed (so-called M_0.3 series), which combines 70% of the information of the 140 kV and 30% of the 80 kV series. These thin slice series allow for additional 3D reconstructions. Routinely, these are coronal images with 3 mm section width, and if necessary, further reconstructions in different planes such as the curved multiplanar reformations (MPR) along the pancreatic duct. Here, one may especially make use of the higher image contrast of the low-kV series that may be beneficial in detecting only faint differences in attenuation between a lesion and healthy pancreatic tissue (Macari et al. 2010). However, in some cases, iodine contrast in the 80 kV images may be so high that diagnosis is impaired; in this case blending of high and low-kV information in a ratio of 50:50% may be more beneficial (Fig. 2). As low-kV images typically show higher noise, MPRs with 3 mm slice thickness are recommended to compensate for this.

Moving on from gray scale image interpretation to dedicated Dual Energy post-processing software algorithms (syngo Dual Energy, Siemens), there are largely

two helpful applications for imaging the pancreas: LiverVNC for iodine quantification and Body-Bone-Removal for direct angiographic visualization. With LiverVNC, the iodine content of tissues is quantified and colour-coded. Therefore, faint differences in contrast material uptake that might have been missed on gray scale images are highlighted. A variety of different colour-code templates is available; however, utilizing a colour scale from shades of blue to red coding for low to high iodine content ("PET Rainbow" template) has shown best acceptance in our routine use. To emphasize the differences in iodine content even more, it is recommended to normalize the algorithm to an area with healthy pancreatic tissue using a normalization circle ROI tool. The colour-map may be superimposed on virtual non-enhanced or regular gray scale MIP (maximum intensity projection) or MPRs. The latter option may be preferred as MPR images show full morphological information. Colour overlay and gray scale image can be blended in steps of 1% from a pure colour to a pure gray scale image. However, usually we use a fused image with 60% colour overlay and 40% gray scale MPR to start evaluation with. To reduce image noise, again at least 3 mm or even thicker MPRs are recommended. This will improve distinguishing between areas of different iodine content. In addition, one may use ROI tools to compare mean unenhanced tissue density, mean iodine enhancement in HU and mean iodine content in mgI/mg tissue (the latter available with the software version Siemens syngo VA30 or higher) between two or more areas of pancreatic tissue with different appearance. Finally, by subtracting the iodine signal from the dataset, virtual non-enhanced images can be calculated to show the presence of calcifications and give baseline CT numbers. Similar post-processing options are available for Dual Energy data acquired with rapid kV-switching (GSI Viewer, General Electric). Utilizing MD, image series are available in which iodine information is either highlighted or subtracted, and iodine uptake can be quantified and colour-coded.

With Body-Bone-Removal (syngo Dual Energy, Siemens), the algorithm will automatically remove bony structures from the dataset based on different spectral behaviour of iodine and calcium and will create a rotatable thick slab MIP. This gives an excellent overview about vascular invasion or compression caused by pancreatic mass. In addition, one may save the dataset after bone-removal as a DICOM file series to the local patient browser or PACS and load it into any other post-processing software for curved centreline vessel analysis or for creating volume rendering images (VRT) to highlight anatomical information for surgeons.

6 Diagnostic Evaluation

As referenced above, early detection of pancreatic carcinoma is vital as surgical resection is currently the only curative treatment option. Also, clinical symptoms with early stages are lacking or unspecific. In the first case (Fig. 1), a 67-year-old female patient presented with a history of recurring intestinal discomfort, recurring indigestion and slight insignificant loss of weight over a period of approximately 6 months. Oesophago-gastro-duodenoscopy was normal. Blood tests were normal. A test for helicobacter pylori infection was negative. Finally, she was referred to CT to exclude a variety of differential diagnoses. On the first view, arterial and venous abdominal DECT scans were normal except for a suspicious group of lymph nodes around the celiac trunk and the superior mesenteric artery (1a). A close research of the pancreas on the virtual 120 kV images of the venous phase (1b) revealed a faint thickening and a minimally increased contrast enhancement. On the 80 kV series, due to the higher inherent contrast, these changes come out better (1c). The Dual Energy iodine distribution analysis reveals a slight hyperdensity in the suspicious area in gray scale mode (1d). However, when iodine distribution is colour-coded, the hyperenhancing area in the pancreatic body can be clearly delineated (1e). The iodine enhancement was quantified by drawing regions of interest around the lesion and the normally appearing head and tail (1f). While the native CT values (i.e. VNC values) do not differ between the ROIs, the lesion shows a clearly increased iodine enhancement (i.e. overlay) of 60 HU compared to 30–40 HU of the head and tail region. Explorative laparoscopy showed diffuse peritoneal carcinosis and histopathology revealed pancreatic adenocarcinoma. This case impressively shows the potential of Dual Energy CT to detect very discrete changes in contrast by iodine distribution analysis in a lesion that can easily be overlooked, if there is no "eye-catcher" like the suspicious group of lymph nodes.

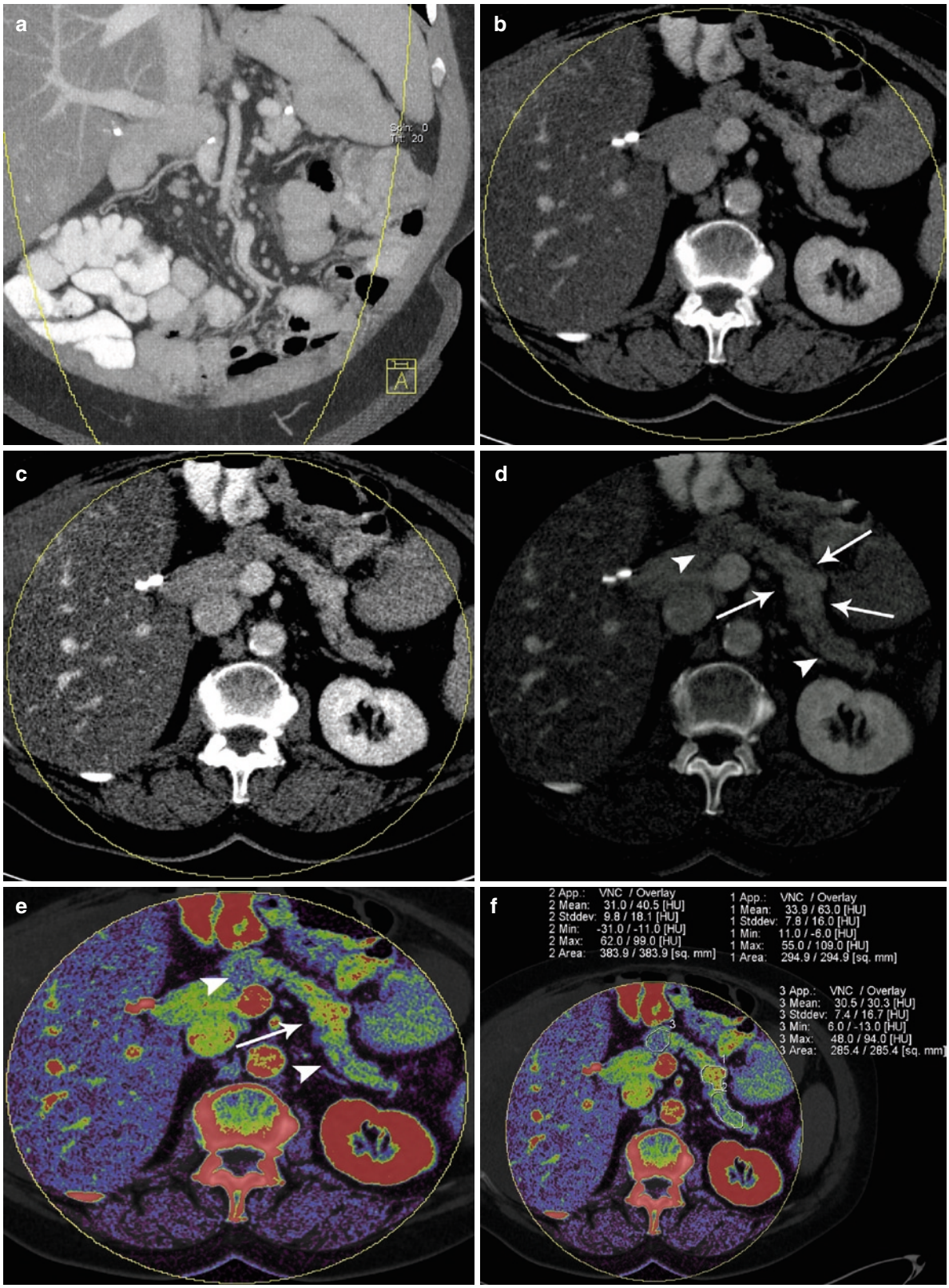
a
b
c
d
e
f
2 App.: VNC / Overlay
2 Mean: 31.0 / 40.5 [HU]
2 Stddev: 9.8 / 18.1 [HU]
2 Min: -31.0 / -11.0 [HU]
2 Max: 62.0 / 99.0 [HU]
2 Area: 383.9 / 383.9 [sq. mm]
1 App.: VNC / Overlay
1 Mean: 33.9 / 63.0 [HU]
1 Stddev: 7.8 / 16.0 [HU]
1 Min: 11.0 / -6.0 [HU]
1 Max: 55.0 / 109.0 [HU]
1 Area: 294.9 / 294.9 [sq. mm]
3 App.: VNC / Overlay
3 Mean: 30.5 / 30.3 [HU]
3 Stddev: 7.4 / 16.7 [HU]
3 Min: 6.0 / -13.0 [HU]
3 Max: 48.0 / 94.0 [HU]
3 Area: 285.4 / 285.4 [sq. mm]

In the second case (Fig. 2), a 56-year-old female patient with loss of weight, fatigue and recurrent diffuse upper abdominal pain was referred for CT with suspected pancreatic carcinoma. DECT revealed a big hypodense tumour in the pancreatic head with infiltration into the surrounding mesenterium as well as lymph nodes around the aorta (2a). Images 2a and 2b provide the coronal view of the process at 80 kV (2b) and as 50:50% mixture (2c) of 140 kV and 80 kV image information (M_0.5). While the contrast of the iodine signal especially in the vessels and the regular perfused healthy part of the pancreatic head in the 80 kV image is so high that image details actually get lost, the M_0.5 image provides still very high contrast with preserved image detail about tumour borders and perivascular infiltration. If iodine distribution is colour-coded (2d), one can easily assess the superior mesenteric artery and the deep descending splenic artery as red dots being completely surrounded by tumour tissue with very low iodine uptake (dark blue). However, the vessel lumen does not seem altered. Healthy pancreatic tissue shows a green colour and the borders to the tumour tissue are clearly delineated. Besides encasing of the arteries, the tumour infiltrated the superior mesenteric vein and occluded it. The Body-Bone-Removal algorithm was applied. The suppressed calcium information in the data set allows for VRT reconstructions that do not need further post-processing like manually removing ribs or the spine (2e): Although completely surrounded by the tumour mass, the mesenteric artery and the branches of the celiac trunk are not stenosed. The splenic vein (VL) and the portal vein (VP) are filled with contrast, while there is no inflow from the superior mesenteric vein (arrow head) to the venous confluens. With the comprehensive use of Dual Energy "direct angio" tools and iodine distribution analysis, the local extend and unresectability of this pancreatic carcinoma could exactly be assessed by demonstrating periarterial infiltration leaving this patient for palliative gemcitabine chemotherapy only.

In the third case (Fig. 3), a 39-year-old female patient with year-long Crohn's disease and status post multiple abdominal operations because of stenoses and fistulae presented again to the emergency department with acute onset of abdominal pain. Plane film X-ray revealed free intraabdominal gas. Emergency laparatomy was performed. Surgeons found segmental inflammation in the transverse colon with a ruptured fistula to the pancreatic space. However, exploration of the retroperitoneal space did not show signs of pancreatic necrosis. Three days after surgery, the patient developed signs of pancreatitis with typical pain and continuously rising enzyme levels. DECT of the abdomen was performed. Iodine distribution maps show areas of significantly reduced iodine content (i.e. blue colour) between the pancreatic head and body and in the transition from body to tail (3a and b). There is an island of regularly perfused (i.e. green colour) tissue in the pancreatic tail. In sum, less than 30% of the pancreas showed signs of necrosis. Oedema was only mild. The resulting CTSI score was calculated to be 4, going along with an increased clinical likelihood of severe complications. Two drainages were still in situ after laparatomy 3 days earlier (red stripes). Colour-coding iodine distribution can be a helpful tool in differentiating from hypoperfused necrotic and hypodense oedematous areas in acute pancreatitis. This may help to grade the area of necrosis and, therefore, predict patient outcome more exactly.

7 Scientific Evidence

In their recent publication, Macari et al. (2010) presented initial observation with Dual Source Dual Energy CT in 15 patients with pancreatic adenocarcinoma. The 80 kV image series were compared with the virtual, composed 120 kV image series. The attenuation difference between normal pancreatic tissue and tumour was

Fig. 1 Sixty-seven-year-old female patient with a history of recurring indigestion and intestinal discomfort over a period of approximately 6 months. (**a**) Oblique maximum intensity projection of the situs with multiple mesenteric lymph nodes. Faint thickening and increased iodine uptake of the pancreatic body. (**b**) Virtual 120 kV image (M_0.3). (**c**) 80 kV series. (**d**) Iodine-weighted gray scale image. (**e**) Colour-coded iodine distribution. (**f**) Iodine quantification. Note an increased iodine uptake (**d, e**) in the corpus (*arrows*) compared to the caput and cauda region (*arrows heads*). On region of interest measurements (**f**), the suspicious area in the corpus shows an enhancement of 63 HU (i.e. "overlay") compared to only 30-41 HU of the pancreatic tissue of the caput and cauda region, while for virtual non-enhanced (i.e. "VNC") density values no substantial difference is seen (range: 31-34 HU)

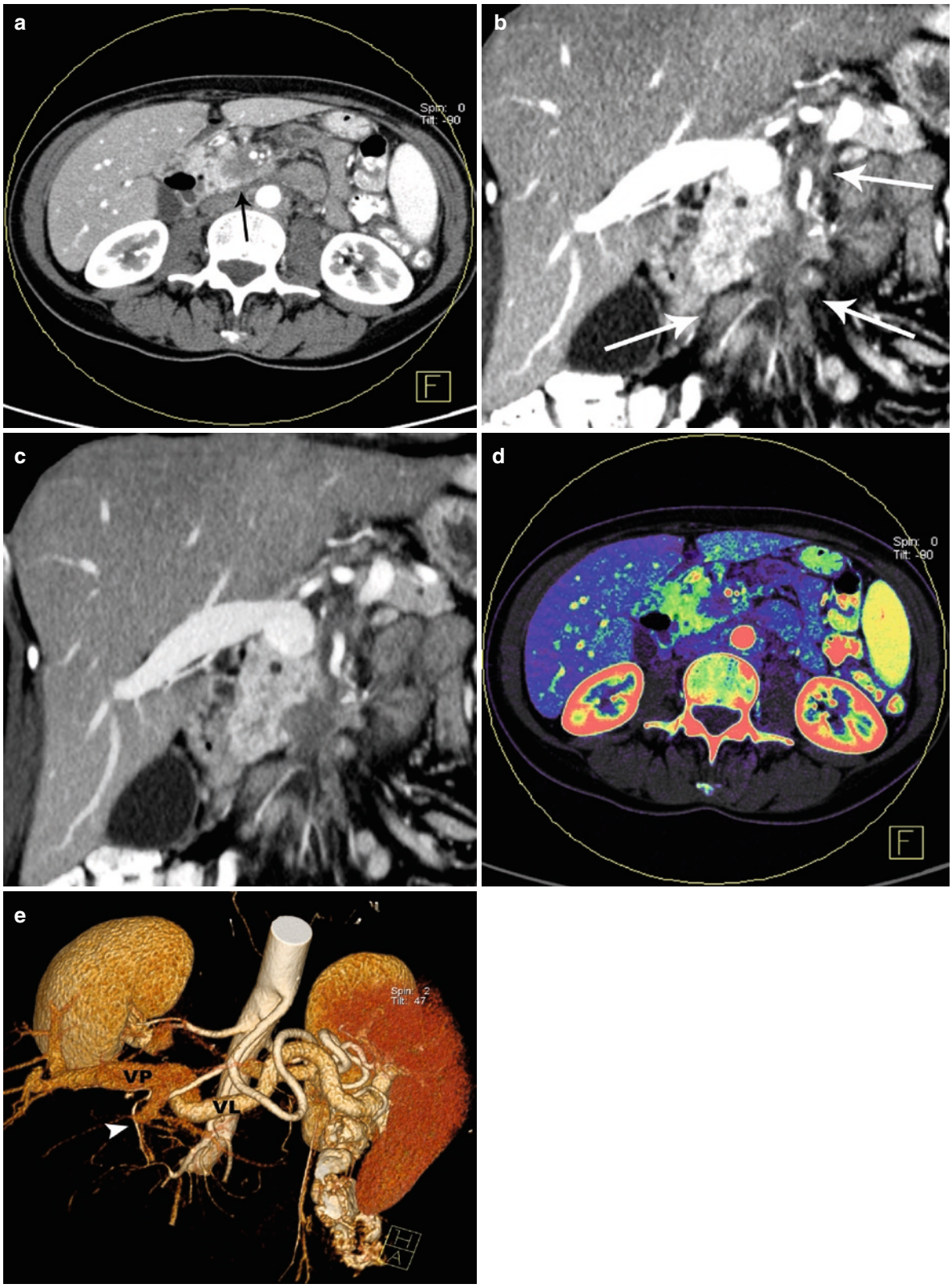
a
Spin: 0
Tilt: -90
F
b
c
d
Spin: 0
Tilt: -90
F
e
Spin: 2
Tilt: 47
VP
VL
H
A

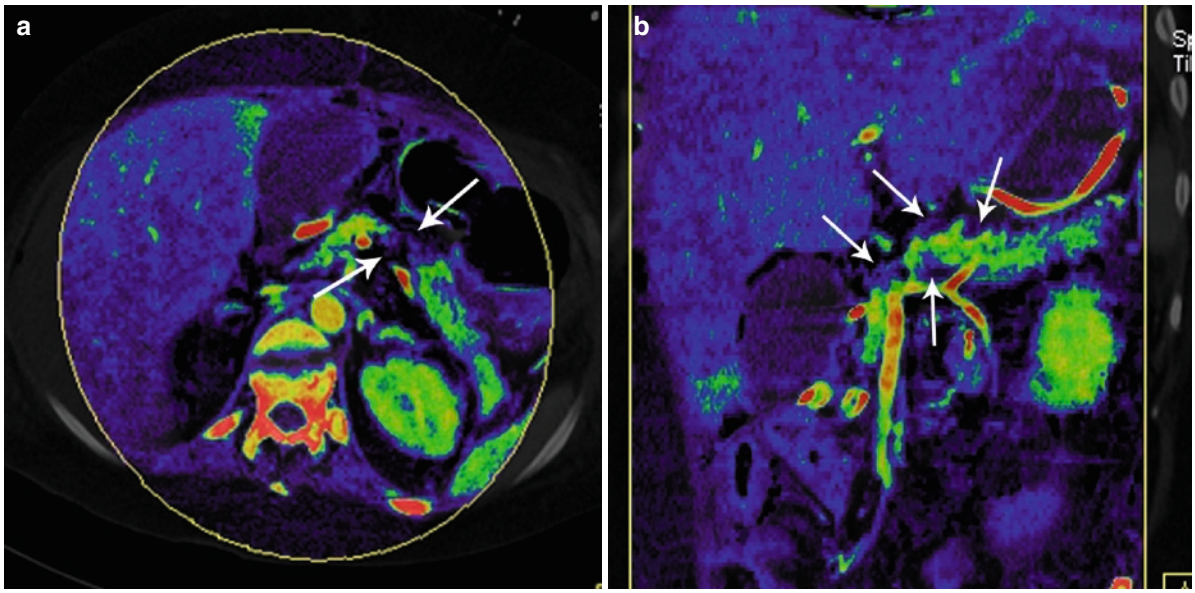

Fig. 3 Thirty-seven-year-old female patient with acute necrotizing pancreatitis. Note an area with reduced iodine uptake in the transition from caput to corpus (*arrow*). (**a**) Colour-coded iodine distribution map, paraxial view. (**b**) Paracoronal view

significantly ($p=0.00006$) increased for the low-kV images (83 ± 30 HU) compared to the composed 120 kV images (49 ± 23 HU). Also, CNR was significantly higher in the 80 kV images than in the composed images (4.25 ± 2.03 vs. 3.31 ± 2.10; $p=0.00147$). On subjective rating of lesion conspicuity, radiologists preferred the 80 kV images, but with a lower rating for subjective image quality. The major reason for the latter is the inherently increased noise and the greater susceptibility for beam hardening that comes with low-kV imaging. Setting very high tube current values would be the typical answer to this problem. However, patient dose is directly related to the amount of X-ray quanta the body is exposed to. New ways of handling and reconstructing CT image data have become robust for clinical use in recent years: namely, iterative reconstruction algorithms which statistically eliminate image noise and therefore may facilitate (a) further improved image quality with regular dose scans or (b) reduced dose scans with preserved image quality. First experiences with adaptive statistical iterative reconstruction (ASIR) have been recently described for Dual Energy CT with rapid kV-switching during arterial hepatic phase (Marin et al. 2010). Marin et al. found a significant reduction of image noise from 20.4 ± 1 HU at 80 kV to 15.6 ± 1 HU after applying ASIR. Likewise, CNR increased from 17.2 ± 2 at 80 kV to 22.3 ± 3 at 80 kV with iterative reconstruction. Vice versa, assuming CNR was kept constant, ASIR would allow for an up to 43% reduction of dose.

For further Dual Energy applications in the abdomen, Graser et al. (2009b) used DECT for the evaluation of renal masses. They found no significant difference for CT values of virtual non-enhanced and true non-

Fig. 2 Fifty-six-year-old female patient with loss of weight, fatigue, and recurrent diffuse upper abdominal pain. Locally advanced carcinoma in the pancreatic head (UICC stadium III) with 360° surrounding of the superior mesenteric artery and splenic artery and invasion of the superior mesenteric vein. (**a**) Virtual 120 kV axial image showing the big hypodense mass in the pancreatic head (*arrow*). (**b**) Coronal reformation of the 80 kV series, note a diffuse infiltration along the mesenterium with encasing of the superior mesenteric artery and branches (*arrow*). (**c**) Same projection as (**b**), but with a 50%:50% mixture of 80 and 140 kV image information to reduce excessive vascular iodine contrast of the 80 kV series. (**d**) Colour-coded iodine distribution in axial view with the tumour appearing as dark blue area with significantly reduced iodine uptake compared to a regular iodine uptake of the healthy pancreatic tissue shown in light green and yellow. (**e**) Volume-rendered image (VRT) pointing out occlusion of the superior mesenteric vein (*arrow head*). VP = portal vein; VL = splenic vein

enhanced baseline images. They concluded that a native baseline scan could be avoided for Dual Energy CT renal imaging resulting in a significantly reduced radiation exposure. Likewise, this may present a viable way for Dual Energy CT imaging of the pancreas and liver. Although there is a general concern about elevated radiation exposure with Dual Energy CT compared to single source single energy CT, we did not find that problem when comparing between our regular scan protocol for the Dual Source scanner (Somatom Definition, Siemens) when used in single source mode (120 kV, 260 mAs, 24×1.2 mm collimation) and our above outlined Dual Energy protocol. In two cohorts with each 90 patients that did not differ significantly in terms of age, gender and abdominal diameters, mean CTDIvol for the single source mode was 13.2±4.3 mGy, while for DECT it was 11.6±3.8 mGy, and therefore, significantly lower ($p=0.006$; Wilcoxon-Mann-Whitney-U test). Considering the growing discussion about CT's disproportionate share to public radiation exposure, the acceptance of Dual Energy CT with its yet under-explored diagnostic potential in pancreatic imaging as well as in many fields will directly be affected by this topic.

From our clinical experience with the presented cases and in front of the current literature, we believe that DECT, especially with its recent technical improvements, represents an imaging modality with big potential to improve early detection of pancreatic carcinoma and severity assessment of acute necrotizing pancreatitis.

References

Goldstein D, Carroll S, Apte M, Keogh G (2004) Modern management of pancreatic carcinoma. Intern Med J 34(8):475–481

Delbeke D, Pinson CW (2004) Pancreatic tumors: role of imaging in the diagnosis, staging, and treatment. J Hepatobiliary Pancreat Surg 11(1):4–10

Francis IR (2007) Pancreatic adenocarcinoma: diagnosis and staging using multidetector-row computed tomography (MDCT) and magnetic resonance imaging (MRI). Cancer Imaging, 7 Spec No A:S160–S165

Grenacher L, Klauss M (2009) Computed tomography of pancreatic tumors. Radiologe 49(2):107–123

Mehmet Erturk S, Ichikawa T, Sou H et al (2006) Pancreatic adenocarcinoma: MDCT versus MRI in the detection and assessment of locoregional extension. J Comput Assist Tomogr 30(4):583–590

Alhajeri A, Erwin S (2008) Acute pancreatitis: value and impact of CT severity index. Abdom Imaging 33(1):18–20

Balthazar EJ, Robinson DL, Megibow AJ, Ranson JH (1990) Acute pancreatitis: value of CT in establishing prognosis. Radiology 174(2):331–336

Chatzicostas C, Roussomoustakaki M, Vardas E, Romanos J, Kouroumalis EA (2003) Balthazar computed tomography severity index is superior to Ranson criteria and APACHE II and III scoring systems in predicting acute pancreatitis outcome. J Clin Gastroenterol 36(3):253–260

Leung TK, Lee CM, Lin SY et al (2005) Balthazar computed tomography severity index is superior to Ranson criteria and APACHE II scoring system in predicting acute pancreatitis outcome. World J Gastroenterol 11(38):6049–6052

Graser A, Johnson TR, Chandarana H, Macari M (2009a) Dual energy CT: preliminary observations and potential clinical applications in the abdomen. Eur Radiol 19(1):13–23

Johnson TR, Krauss B, Sedlmair M et al (2007) Material differentiation by dual energy CT: initial experience. Eur Radiol 17(6):1510–1517

Marin D, Nelson RC, Schindera ST et al (2010) Low-tube-voltage, high-tube-current multidetector abdominal CT: improved image quality and decreased radiation dose with adaptive statistical iterative reconstruction algorithm – initial clinical experience. Radiology 254(1):145–153

Macari M, Spieler B, Kim D et al (2010) Dual-Source Dual-Energy MDCT of pancreatic adenocarcinoma: initial observations with data generated at 80 kVp and at simulated weighted-average 120 kVp. AJR Am J Roentgenol 194:W27–W32

Graser A, Johnson TR, Hecht EM et al (2009b) Dual-energy CT in patients suspected of having renal masses: can virtual nonenhanced images replace true nonenhanced images? Radiology 252(2):433–440

Heiken JP, Brink JA, McClennan BL, Sagel SS, Crowe TM, Gaines MV (1995) Dynamic incremental CT: effect of volume and concentration of contrast material and patient weight on hepatic enhancement. Radiology 195:353–357

Cademartiri F, van der Lugt A, Luccichenti G, Pavone P, Krestin GP (2002) Parameters affecting bolus geometry in CTA: a review. J Comput Assist Tomogr 26(4):598–607

Kidney Stones

Andrew N. Primak, Terri J. Vrtiska, Mingliang Qu,
and Cynthia H. McCollough

Contents

Abstract

› Although state-of-the-art CT provides accurate sub millimeter details of the size and location of renal stones, current routine clinical image analysis does not differentiate stone composition. This is particularly important in the case of uric acid (UA) stones (~10% of cases), since urinary alkalinization can be prescribed to dissolve UA stones. Therefore, simple and reliable differentiation of UA vs. non-UA stone composition could potentially allow patients with UA stones to avoid invasive interventional urinary procedures for stone removal or external shock wave lithotripsy. This chapter describes a novel Dual-Energy CT (DECT) technique for renal stone differentiation, which is based on the difference in X-ray attenuation properties at high and low kV between UA- and non-UA-containing stones. The technique has been implemented on modern Dual-Source CT scanners which allow simultaneous Dual-Energy acquisition with high spatial resolution and immediate postprocessing using commercial algorithm available on the system. Principles of DECT imaging, acquisition parameters and postprocessing details are discussed. Diagnostic evaluation of three clinical cases is provided together with a summary of the results of all known validation studies performed both in vitro and in vivo. The reported accuracy and sensitivity of the UA vs. non-UA differentiation using DECT varied from 88 to 100%. Further improvement is expected with the second generation of Dual-Source scanners due to increased spectral separation.

A.N. Primak (✉)
Siemens Medical Solutions USA, 51 Valley Stream Parkway, Malvern, PA 19355, USA
e-mail: andrew.primak@siemens.com

T.J. Vrtiska, M. Qu, and C.H. McCollough
Department of Radiology, Mayo Clinic, 200 First St. SW, Rochester, MN 55905, USA

T.R.C. Johnson et al. (eds.), *Dual Energy CT in Clinical Practice*, Medical Radiology,
DOI: 10.1007/174_2010_33

1 Clinical Background

The formation of kidney stones affects 12% of men and 5% of women in industrialized countries by age 70, including 900,000 persons in the United States each year (National Institutes of Health 1990) resulting in estimated annual medical cost of $2.1 billion based on insurance claims (Pearle et al. 2005). However, the mechanisms by which renal calculi arise are poorly understood and precise noninvasive imaging tools to stratify patients into treatment groups based on the composition and quantity of the stone burden have yet to be developed.

State-of-the-art unenhanced CT provides accurate sub millimeter details of the size and location of renal stones (Dillman et al. 2007; Vrtiska 2005; Williams et al. 2004) and has become the imaging method of choice for diagnosing *the presence* of ureteral stone disease. However, current routine clinical CT image analysis does not differentiate stone composition. This is particularly important in the case of uric acid (UA) stones (~10% of cases), since urinary alkalinization can be prescribed to dissolve UA stones and could thereby be initiated at presentation rather than following lengthy metabolic work-up including exams such as 24-h urine collections and blood tests to evaluate UA levels. Therefore, simple and reliable differentiation of UA vs. non-UA stone composition could potentially allow patients with UA stones to avoid invasive interventional urinary procedures for stone removal or external shock wave lithotripsy, which are expensive and might result in renal hemorrhage, fibrosis, and/or hypertension (Evan et al. 1998; Lemann et al. 1991; Lingeman et al. 1990).

Previous attempts to predict stone composition using spiral CT were based on the analysis of CT attenuation values. Several in vitro and in vivo studies have shown that this approach can discriminate UA from non-UA stones (Mitcheson et al. 1983; Mostafavi et al. 1998; Nakada et al. 2000; Motley et al. 2001; Joseph et al. 2002; Pareek et al. 2003; Sheir et al. 2005). Combining the analysis of CT attenuation values with visual assessment of stone morphology using a wide window setting (e.g., bone window), substantially improves the accuracy of stone characterization (Williams et al. 2002). Bellin et al. (2004) reported in vitro prediction of stone composition with 64–81% accuracy, while Zarse et al. (2004) demonstrated that high resolution spiral CT yields unique attenuation values for common types of stones, if proper window settings are used to localize homogeneous regions within the stones.

Unfortunately, the known single-energy CT approaches to predict stone composition are not robust or reliable enough to be used as a routine clinical application. In this chapter, we describe Dual-Energy CT (DECT) imaging as a promising novel technique for kidney stone differentiation.

2 Physical Background

The principle of DECT imaging is that the attenuation coefficient for any material is very dependent upon the effective atomic number (Z_{eff}) of the material and the energy of the X-rays interacting with the material (Alvarez and Macovski 1976). The chemical formulas for common urinary stone types are listed in Table 1. Since UA-containing stones are composed only of light chemical elements (H, C, N, O), they have significantly smaller Z_{eff} and absorb X-rays differently at any given energy compared to other (non-UA-containing) stone types, whose composition includes heavy elements (P, Ca, S). DECT imaging exploits this difference in the X-ray attenuation behavior to discriminate stones of different composition.

Table 1 Common urinary stone types

Stone type	Chemical formula
UA stones	
Uric acid	$C_5H_4N_4O_3$
Uric acid dihydrate	$C_5H_4N_4O_3{\cdot}2H_2O$
Ammonium urate	$C_5H_3N_4O_3NH_4$
Non-UA stones	
Calcium oxalate monohydrate	$CaC_2O_4{\cdot}H_2O$
Calcium oxalate dihydrate	$CaC_2O_4{\cdot}2H_2O$
Calcium hydroxyapatite	$Ca_{10}(PO_4)_6(OH)_2$
Carbonate apatite	$Ca_{10}(PO_4,CO_3)_6(OH,CO_3)_2$
Calcium phosphate	$Ca_3(PO_4)_2$
Brushite	$CaHPO_4{\cdot}2H_2O$
Struvite	$MgNH_4PO_4{\cdot}6H_2O$
Cystine	$C_6H_{12}N_2O_4S_2$
2,8-dihydroxyadenine[a]	$C_5H_5N_5O_2$

[a]This rare stone is the only non-UA stone composed entirely of light chemical elements and, hence, cannot be differentiated from the UA stones using DECT imaging

Several studies (Mitcheson et al. 1983; Mostafavi et al. 1998; Sheir et al. 2005; Grosjean et al. 2008) utilized the difference between attenuation values of stones obtained from multiple single-energy scans acquired at different kV values, $\Delta HU = HU^{stone}_{Low\ kV} - HU^{stone}_{High\ kV}$, in order to improve the accuracy of stone discrimination. The other parameters which can be used as the DE stone differentiation metrics include the CT number ratio, $R = HU^{stone}_{Low\ kV} / HU^{stone}_{High\ kV}$ (Matlaga et al. 2008; Boll et al. 2009), the Dual-Energy ratio, $DE_{ratio} = (HU^{stone}_{Low\ kV} - HU^{urine}_{Low\ kV})/(HU^{stone}_{High\ kV} - HU^{urine}_{High\ kV})$ (Primak et al. 2009) and the DE index, $DEI = (HU^{stone}_{Low\ kV} - HU^{stone}_{High\ kV})/(HU^{stone}_{Low\ kV} + HU^{stone}_{High\ kV} + 2000)$ (Graser et al. 2008; Stolzmann et al. 2009).

To understand which metric is the most appropriate for stone differentiation, let us recall that the attenuation for a stone of given composition linearly depends on the stone density ρ_{stone} (varies with porosity)

$$HU^{stone}_{Low\ kV,\ High\ kV} = k^{stone}_{Low\ kV,\ High\ kV}\rho_{stone} + HU^{urine}_{Low\ kV,\ High\ kV}.$$

Here, $k^{stone}_{Low\ kV,\ High\ kV}$ are the composition-specific slopes of the linear CT number vs. density curves and we take into account that an in vivo renal stone has its pores filled with urine and, hence, its attenuation should asymptotically approach the attenuation of urine as the stone density decreases to zero. Using the ρ_{stone}-dependences of HU values at high- and low-kV, we can write down the stone DECT metrics as

$$\begin{aligned}\Delta HU &= (k^{stone}_{Low\ kV} - k^{stone}_{High\ kV})\rho_{stone} + (HU^{urine}_{Low\ kV} - HU^{urine}_{High\ kV})\\ &\approx (k^{stone}_{Low\ kV} - k^{stone}_{High\ kV})\rho_{stone} = f(\rho_{stone}),\end{aligned}$$

$$\begin{aligned}R &= (k^{stone}_{Low\ kV}\rho_{stone} + HU^{urine}_{Low\ kV}) / (k^{stone}_{High\ kV}\rho_{stone} + HU^{urine}_{High\ kV})\\ &\approx k^{stone}_{Low\ kV} / k^{stone}_{High\ kV} \neq f(\rho_{stone}),\end{aligned}$$

$$DE_{ratio} = k^{stone}_{Low\ kV} / k^{stone}_{High\ kV} \neq f(\rho_{stone}),$$

$$\begin{aligned}DEI &= \frac{(k^{stone}_{Low\ kV} - k^{stone}_{High\ kV})\rho_{stone} + HU^{urine}_{Low\ kV} - HU^{urine}_{High\ kV}}{(k^{stone}_{Low\ kV} + k^{stone}_{High\ kV})\rho_{stone} + HU^{urine}_{Low\ kV} + HU^{urine}_{High\ kV} + 2000}\\ &\approx \frac{DE_{ratio} - 1}{DE_{ratio} + 1 + \dfrac{2000}{k^{stone}_{High\ kV}\rho_{stone}}} = f(\rho_{stone}).\end{aligned}$$

The most appropriate DECT metric should depend only on stone composition and be independent of stone density (porosity). The only metric which truly satisfies this criterion is the DE_{ratio}. The CT number ratio R is approximately independent of ρ_{stone} when $HU^{stone}_{Low\ kV,\ High\ kV} >> HU^{urine}_{Low\ kV,\ High\ kV}$. The ΔHU and DEI parameters can be simplified using an approximation $HU^{urine}_{Low\ kV} \approx HU^{urine}_{High\ kV} << 1000$ to clearly reveal their functional dependence on ρ_{stone}. Thus, we conclude that the DE_{ratio} should be used as the proper metric for stone differentiation with DECT imaging.

A recently introduced second generation Dual-Source CT scanner (Definition Flash, Siemens Healthcare, Forchheim, Germany) features an additional tin filter for the high energy X-ray tube resulting in a better spectral separation compared to the original Dual-Source scanner (Definition). The larger spectral separation increases the difference between the DE ratios of two materials (Primak et al. 2009) (e.g., UA and non-UA stones) and should improve the kidney stone differentiation using DECT. It also allows for the use of 100 kV for the low energy portion of a DECT scan providing much more X-ray power (and, hence, less noise) necessary for adequate DECT imaging of large patients.

3 Scan Protocol

The scan protocols for the first (Definition) and second (Definition Flash) generations of Dual-Source CT scanners are described in Table 2. A Definition scanner has only one DE mode (140/80 kV for Tube A/Tube B) which has limited power resource at 80 kV. Therefore, a relatively low pitch of 0.7 and a thicker (1.2 mm) detector collimation are recommended. DECT imaging of large patients (lateral width >36 cm) on Definition could result in suboptimal algorithm performance due to inadequate noise level at 80 kV and should be avoided. A special care needs to be taken to center the patient so the region of interest is located within the limited 26-cm DE field-of-view (FOV).

A Definition Flash scanner has three DE modes (140/80 kV, 80/Sn140 and 100/Sn140 kV) where "Sn" denotes the tin filter. The mode without the tin filter is provided mostly for a direct comparison to the Definition. The default DE mode is the 100/Sn140 kV because it has a little better spectral separation and much more power available at low-kV compared to the DE mode on the Definition allowing DE imaging of patients with lateral width up to 45 cm. For small patients (lateral width ≤32 cm) who can be imaged using 80 kV with an adequate noise level, the use of the 80/Sn140 kV mode is recommended due to a better spectral separation.

Table 2 Scan parameters for DECT imaging of kidney stones using first and second generation Dual-Source scanners

Scan parameters	Definition	Definition Flash	Definition Flash
Patient lateral dimension L (cm)	$L \leq 36$[a]	$L \leq 32$	$32 < L < 45$[a]
Scan range	Kidneys only or kidneys through pelvis	Kidneys only or kidneys through pelvis	Kidneys only or kidneys through pelvis
Scan direction	Cranio-caudal	Cranio-caudal	Cranio-caudal
Scan time (s)	~6–20	~6–20	~6–20
Tube voltage A/B	140/80 kV	80/Sn140 kV	100/Sn140 kV
Dose modulation	CARE Dose4D	CARE Dose4D	CARE Dose4D
Quality reference mAs A/B	80/340	400/216	240/185
$CTDI_{vol}$ (mGy)	~15[b]	~18[b]	~18[b]
Rotation time (s)	0.5	0.5	0.5
Pitch	0.7	0.6	0.6
Detector collimation (mm)	14 × 1.2	32 × 0.6	32 × 0.6
Reconstruction slice width (mm)	1.5	1	1
Reconstruction increment	1	0.8	0.8
Reconstruction kernel	D30f	D30f	D30f
Ratio for weighted-average images	0.3	0.5	0.5

[a]Patients with greater lateral size should not be scanned using the DE protocol
[b]Since dose modulation is used, $CTDI_{vol}$ varies with patient size and body habitus. The given values approximately correspond to an adult weighting 70–80 kg

The Flash has a significantly larger (33 cm) DE FOV that makes centering patients much less of an issue.

4 Postprocessing

Each reconstruction job for a DECT scan produces three image data sets, the original high- and low-energy images and a combined (linearly mixed) or "weighted-average" data set generated according to equation

$$\text{Weighted-average image} = \text{Low-kV image} \times C_{ratio} + \text{High-kV image} \times \left(1 - C_{ratio}\right).$$

The combined images utilize the full dose of a DECT scan, while the composition ratio, C_{ratio}, is chosen so these images could better approximate the conventional single-energy 120 kV images and, hence, could substitute them for a diagnostic evaluation (Yu et al. 2009; Behrendt et al. 2009).

The recommended reconstruction parameters for the DECT images are 1.5-mm slice thickness with 1.0 mm increment and a medium smooth DE specific (non edge enhancing) D30f kernel. In case if the 0.6 mm collimation was used during acquisition (could be beneficial for differentiation of small (≤2 mm) stones), the images should be reconstructed at 1.0 mm slice thickness with 0.8 mm increment. A 20–30% overlap is necessary to improve the image quality of 3D rendering and multiplanar reformations. The reconstructed high- and low-kV images can be immediately postprocessed on a workstation equipped with commercially available DE software (Kidney Stones, Syngo DE, Siemens Healthcare). The processing time is minimal and typically does not take longer than 2–3 min.

According to the algorithm utilized by the DE software tool, a kidney stone can be considered as a mixture of a hypothetical "pure" stone with no pores (such a stone would have a very high density and unrealistically high CT numbers) and the material that fills the pores ("urine"). In a plot of the CT numbers at 80 kV vs. the CT numbers at 140 kV, a real stone has to lie somewhere (depending on its porosity) on a line segment between the "urine" and the "pure" stone data points (Fig. 1). The slope of this line segment is equal

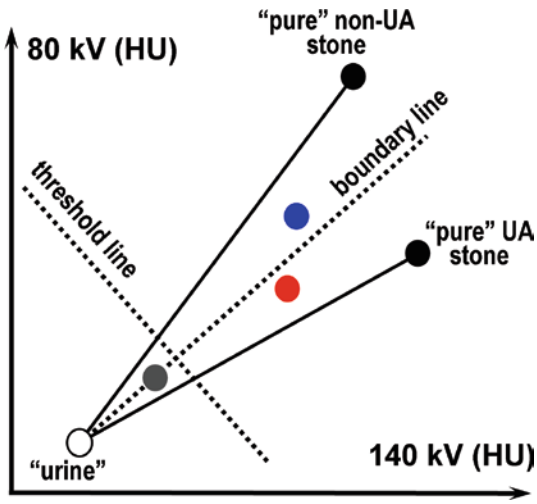

Fig. 1 A simplified pictorial description of how the commercial postprocessing DE algorithm differentiates UA and non-UA kidney stones

to DE_{ratio} described in Sect. 2. Since DE_{ratio} depends only on the stone composition and is independent of the stone porosity (density), the slopes of different stone types can be determined using stones of known composition. Since UA stones are made of light chemical elements, their slope is quite different from the slopes of other (non-UA) stones, which have heavier atoms. As the slopes of non-UA stones are relatively close to each other and might overlap when error bars are taken into account, they are, for simplicity, represented in Fig. 1 by a single average slope corresponding to all non-UA stones. Figure 1 also provides a simplified description of how the Dual-Energy algorithm works. If a data point corresponding to a stone with unknown composition falls below the angle bisector (boundary line) dividing the angle between the UA and non-UA line segments, the algorithm will characterize such stone as a UA stone and assign it a predefined color code (red in Fig. 1). If an unknown data point falls above the boundary line, the corresponding stone will be identified as a non-UA stone and assigned a different predefined color code (blue in Fig. 1).

The described DE algorithm is limited and cannot discriminate different non-UA stone types. The discriminating power of the DECT technique could be improved if the high- and low-energy spectra were better separated (Primak et al. 2009). A better spectral separation would result in a larger angle between the UA and non-UA line segments in Fig. 1. Another limiting factor is noise which increases error bars for the data points representing the stones in the DECT number plot. The data points for stones with relatively small attenuation (e.g., caused by large partial volume effect (Williams et al. 2001)) will be located close to the boundary line and might have error bars which extend beyond this line. Such stones cannot be confidently classified as a UA or non-UA stone. Therefore, the noise level will determine the threshold line shown in Fig. 1 perpendicular to the boundary line. Stones whose data points fall below the threshold line cannot be properly evaluated by the algorithm and will be assigned no color.

A stone with a mixed (red/blue) color could either represent a stone of mixed (UA/non-UA) composition or a misclassification caused by an artifact or excessive noise. Since bones are calcified structures, they will be colored in blue (the same as calcified plaque). The presence of red-colored regions in the bone would indicate a significant artifact which affected the accuracy of the CT numbers in the original high- and low-kV images and, hence, compromised the performance of the DE algorithm.

Some fine-tuning of the algorithm performance can be achieved by adjusting the parameters in the user dialog box (Fig. 2). The user can set the exact CT numbers of urine at high- and low-kV and change the minimum and maximum threshold HU values. The voxels with HU values below or above these thresholds are not processed by the algorithm. The parameter called Ratio defines the slope of the boundary line in the low-kV vs. High-kV CT number plot that separates UA from non-UA stones (see Fig. 1). This parameter depends on the spectral characteristics at high- and low-kV, and hence, varies among the DE modes available on Definition and Definition Flash scanners. Changing the ratio can have a drastic effect on the accuracy of the UA vs. non-UA discrimination and should be done with extra care. One example when adjusting the Ratio could be of potential value is given in (Graser et al. 2008). In this study, the two struvite stones and the cystine stone showed red and blue pixels. When the Ratio parameter was adjusted the calculi turned uniform in color indicating their homogeneous composition. On the other hand, the stones with mixed (UA and calcified) composition, which displayed red pixels within the blue stones, remained inhomogeneous in color even after the Ratio was adjusted.

Another important parameter is Range. It defines the size of the cluster of neighboring voxels which

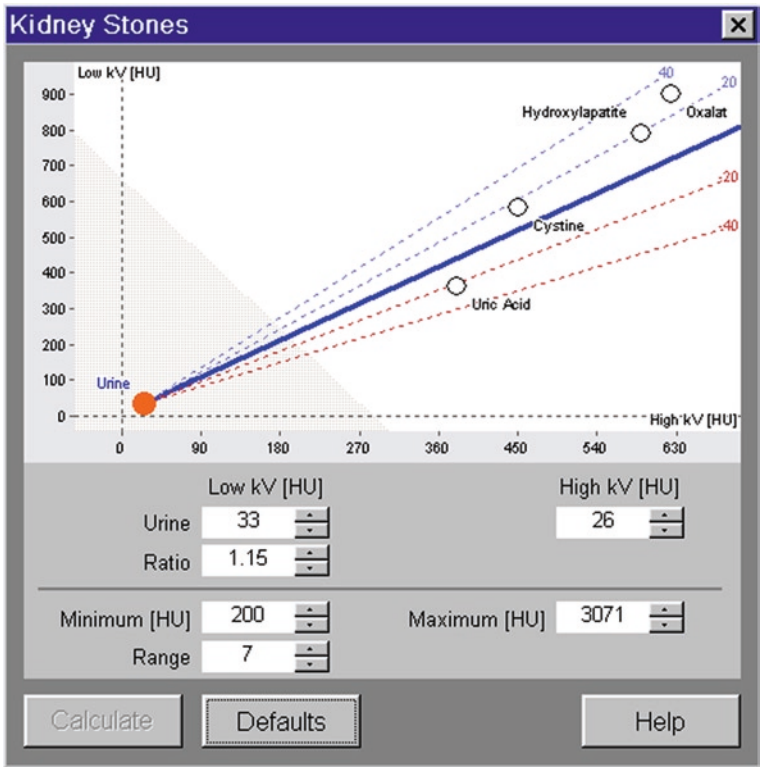

Fig. 2 User dialog box for the commercial DE software (Kidney Stones, Syngo DE, Siemens Healthcare) used for kidney stone differentiation

are averaged out during postprocessing in order to suppress noise and improve the algorithm performance. Excessive smoothing can effectively reduce the CT numbers of the periphery voxels (similar to partial volume effect) and, hence, compromise evaluation of very small stones causing a relatively large number of the stone voxels to fall below the threshold line (see Fig. 1). Therefore, reducing the Range parameter from its relatively large default value (range = 7) might turn a noncolored small stone into a colored one resulting in a proper differentiation.

As we have already mentioned, the automatic postprocessing can only differentiate UA from non-UA (red vs. blue) stones. Additional information about the stones can be acquired with further manual processing. The CT numbers at high- and low-kV can be obtained by placing a region-of-interest (ROI) within the stone and the stone size (dimensions) can be measured using the digital ruler. We should note that these measurements are strongly dependant on the window and level settings at which the images are displayed. This is especially important for the HU attenuation values since the size and location of the ROI within the stone will determine at what degree these values are affected by the partial volume effect between the stone and its surroundings (soft tissue and fat). The manual CT number measurements can be used in an attempt to further differentiate the stones within the non-UA group (e.g., cystine from calcified stones). However, the accuracy of such an additional discrimination is questionable and, in spite of some supporting evidence (Matlaga et al. 2008; Graser et al. 2008) more validation is needed.

5 Diagnostic Evaluation

The interpretation of the unenhanced DECT for renal stone composition requires the traditional review of the size, number and distribution of stones including exclusion of any complication of stone disease such as obstruction or perinephric urinoma. The addition of the color-coded DE postprocessed images provides supplemental information indicating the likely stone composition as non-UA stone disease (likely calcium based stones, blue color), UA stone disease (red color)

or indeterminate (no color). Below we describe three clinical cases. The first two were studied using the Definition (first generation DSCT), while the third case was done on the Definition Flash (second generation DSCT). All cases were done using the protocols described in Table 2.

Case 1: 72 year-old male who has passed 20–30 stones over the past four decades. Current CT evaluation demonstrates bilateral intrarenal calculi (Fig. 3a, b) which have increased in size when compared to a CT scan from 3 years ago. DECT characterization (Fig. 3c) with blue color-coding indicates that the stone material is non-UA in composition. The patient had analysis of the stone material in the past which was shown to be consistent with calcium oxalate. Review of the current CT and laboratory information by the patient's nephrologist was consistent with calcium oxalate stone material with an increase in the stone size due to urinary supersaturation due to low urine volume and improved fluid consumption was advised.

Case 2: 70 year-old male with a right ureteral stent placement for obstructing ureteral calculus. Scout CT imaging demonstrates the right ureteral stent (Fig. 4a) without visible radio-opaque stone material. Additional history includes myelofibrosis with diffuse sclerosis throughout the visible skeleton and splenomegaly (Fig. 4b). Myelofibrosis often results in an overproduction of UA due to increased cell breakdown and turnover. Coronal CT images (Fig. 4b, c) demonstrate a right intrarenal calculus. DECT characterization with red color-coding (Fig. 4c) confirms that the stone material is UA in composition. The patient was treated with doubling of dose of sodium bicarbonate and the addition of allopurinol to lower the UA production.

Case 3: 42-year-old female with a 20 year history of recurrent nephrolithiasis, medullary sponge kidney and hypocitraturia. The surgical history included a gastric bypass procedure. CT evaluation demonstrates multiple bilateral intrarenal kidneys stones with the largest measuring 7 mm. DECT characterization (Fig. 5) indicated blue color-coding consistent with non-UA composition. Kidney stone analysis concluded the stones are composed of 100% calcium oxalate monohydrate. The large attenuation (lateral abdominal size is ~39 cm) would preclude this patient from having a DECT exam on the first generation DSCT scanner.

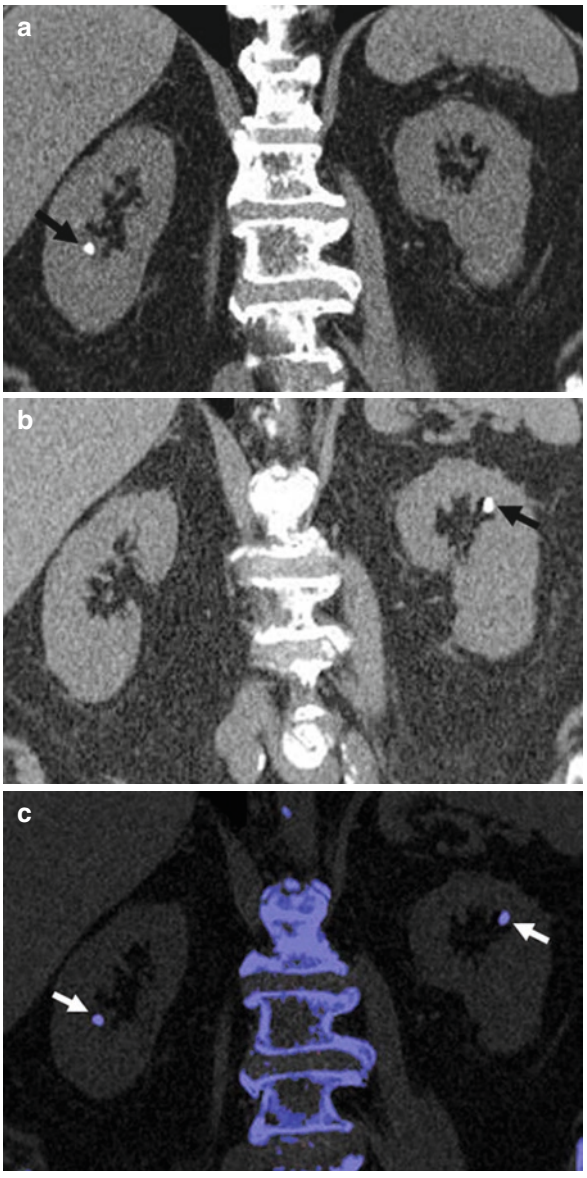

Fig. 3 First generation DSCT evaluation of 72 year-old male with a known history of stone disease demonstrates bilateral intrarenal calculi (*arrows* in **a**, **b**) which have increased in size when compared to a CT scan from 3 years ago. DECT characterization (**c**) with *blue* color-coding indicates that the stone material is non-uric acid (UA) in composition. The patient had analysis of the stone material in the past which was shown to be consistent with calcium oxalate

6 Scientific Evidence

To date, we are aware of seven peer-reviewed publications (Matlaga et al. 2008; Boll et al. 2009; Graser et al. 2008; Stolzmann et al. 2008, 2009; Thomas et al. 2009;

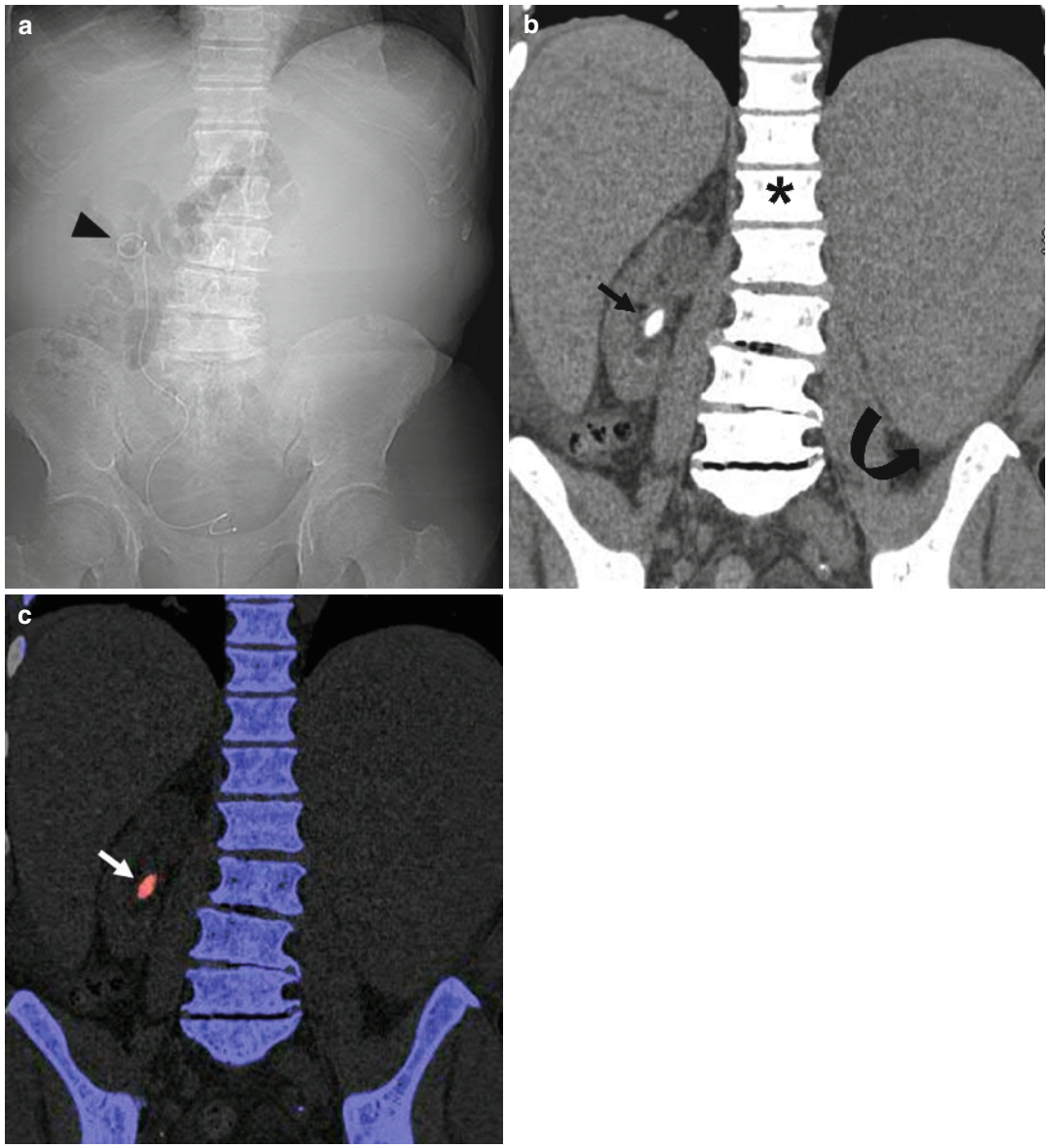

Fig. 4 First generation DSCT evaluation of 70 year-old male with a stent placement for obstructing ureteral calculus. Scout CT imaging demonstrates the right ureteral stent (**a**, *arrowhead*) without visible radio-opaque stone material. Additional history includes myelofibrosis with diffuse sclerosis throughout the visible skeleton (**b**, *asterisk*) and splenomegaly (**b**, *curved arrow*). Myelofibrosis often results in an overproduction of UA due to increased cell breakdown and turnover. Coronal CT images (**b**, **c**) demonstrate a right intrarenal calculus (*arrows*). DECT characterization with red color-coding (**c**) confirms that the stone material is UA in composition

Primak et al. 2007) devoted to the use of Dual-Source DECT imaging for kidney stone differentiation. The majority of these studies were done in vitro using different types of renal phantoms and ex vivo human stones. As to in vivo validation, there have been only three reports so far, one small feasibility study on 20 patients (Graser et al. 2008), one retrospective study of 51 consecutive patients scanned using a low dose DE renal stone protocol (Thomas et al. 2009) and one prospective clinical trial which involved 180 patients with suspected urinary stone disease (Stolzmann et al. 2009). All but two studies utilized the commercially available algorithm described in Sect. 4. Table 3 summarizes the important features of all seven manuscripts.

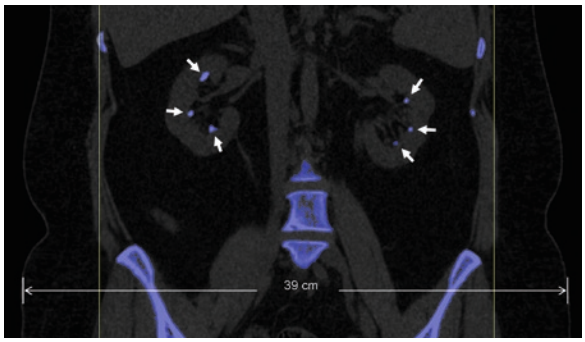

Fig. 5 Second generation DSCT evaluation of 42-year-old female with a 20 year history of recurrent nephrolithiasis, medullary sponge kidney and hypocitraturia demonstrates multiple bilateral intrarenal kidney stones (*arrows*). DECT characterization indicated blue color-coding consistent with non-UA composition. Kidney stone analysis concluded the stones are composed of 100% calcium oxalate monohydrate. The large attenuation (39 cm lateral dimension) would preclude this patient from having a DECT exam on the first generation DSCT scanner. The *yellow vertical bars* indicate the scan volume where the DE postprocessing was applied

Primak et al. (2007) used forty human urinary stones of different composition and size, carefully characterized with Fourier transform infrared (FTIR) microspectroscopy and micro CT. The stones were hydrated to make sure all pores were filled with water and inserted in four bivalved porcine kidneys (10 stones each kidney). The kidneys with stones were placed in a 30 cm water tank anterior to a cadaver spine in order to create realistic scattering and attenuation conditions. To take into account variable patient attenuation, three patient sizes were simulated. For the medium and large phantom sizes, the DE algorithm correctly identified all 40 stones as either UA or non-UA, regardless of the detector collimation, demonstrating 100% accuracy and 100% sensitivity. For the extra-large phantom size and the 0.6 mm collimation (the noisiest data set), 3 stones could not be classified, resulting in 93% accuracy (37/40) and 94% sensitivity (15/16). One small UA stone was not color-coded and two cystine stones were assigned both colors. For the extra-large phantom size and the 1.2 mm collimation, the DE algorithm failed to identify two small UA stones demonstrating 95% accuracy (38/40) and 88% sensitivity. In summary, all stones >3 mm were correctly identified under all conditions.

Another in vitro study reported by Stolzmann et al. (2008) also used 40 human renal stones collected during surgical and endoscopic procedures. The stone composition was determined prior to DECT using crystallography as the reference standard. The stones were embedded in fat ($20 \times 15 \times 8$ cm^3) representing the fatty tissue and the phantom was fully submerged in a water tank ($35 \times 35 \times 25$ cm^3) to simulate normal human attenuation. The commercial DE software correctly identified all but one stone as UA- or non-UA-containing. Only one small (2 mm) UA stone could not be evaluated resulting in 98% (39/40) accuracy and 93% (13/14) sensitivity. When the attenuation values of this stone (determined using a manual ROI measurement to be 70 and 64 HU at 140 and 80 kV, respectively) were manually plotted in the 80 vs. 140 kV CT number plot, the data point fell below the boundary line indicating a UA-containing stone.

To date, the only study designed to prospectively evaluate the diagnostic performance of DECT imaging for kidney stone differentiation in a large group of patients is the clinical trial reported by Stolzmann et al. (2009). This study enrolled 180 consecutive patients with suspected urinary stone disease. The disease was detected in 110/180 patients and stones or their fragments were sampled in 53/110 patients using urinary straining or surgical and endoscopic interventions. The composition of the sampled stones was analyzed by crystallography used as the reference standard. The overall image quality of weighted-average images was assessed on a 4-point scale (4 = inacceptable, 3 = marginally to fairly acceptable, 2 = acceptable and 1 = very acceptable) by two blinded and independent readers. In the 53 patients with sampled stones, DECT detected a total of 84 calculi, with 20 patients having more than one stone. In the 20 patients with more than one stone, DECT showed no difference in the UA vs. non-UA characterization for multiple stones from the same patient. Therefore, stone differentiation was performed on a per-patient basis. The commercial DE software correctly differentiated UA- vs. non-UA-containing stones in 51/53 patients. One small (2 mm) non-UA stone was not evaluated (no color) and one mixed stone (3 mm) with 20% of UA content was misclassified as a non-UA stone resulting in 98% (51/53) accuracy and 89% (8/9) sensitivity. The additional DEI analysis of stone composition based on manual ROI measurements of stone attenuation at high- and low-kV was also performed but showed poorer performance compared to the commercial DE algorithm. The study demonstrated (with high inter-observer agreements) that weighted-average DECT images have acceptable

Table 3 Study details of the published manuscripts devoted to the use of Dual-Source DECT imaging for kidney stone differentiation

Study details	Primak et al. (2007)	Stolzmann et al. (2008)	Graser et al. (2008)		Matlaga et al. (2009)	Thomas et al. (2009)	Boll et al. (2010)	Stolzmann et al. (2009)
In vitro or in vivo	In vitro	In vitro	In vitro	In vivo	In vitro	In vivo	In vitro	In vivo
Anthropomorphic phantom (yes or no)	Y	N	N	–	Y	–	Y	–
Total number of stones/patients	40	40	24	20	26	28	50	53
Total number of UA-containing stones/patients	16	14	8	7	8	3	8	9
Number of mixed UA/non-UA stones/patients	0	6	4	3	0	1	1	2
Stone size range/mean size (mm)	2–7	2–7/4.5	1.5–9/3.5	1–15	4.19;5.57;4.71[a]	2–12/5	10–6,720 mm^{3}[b]	1–12
Dose modulation (CARE Dose4D) (yes or no)	Y	N	Y	Y	N	Y	N	Y
Tube currents 140/80 kV (ref mAs or eff mAs)	100/425	95/400	76/342	76/342	110/468	46/210	118/499	90/350
$CTDI_{vol}$ (mGy)	13.7–21.9	No info	No info	8.8–16.8	No info	4.95–12.09	22.4	No info
Detector collimation (mm)	0.6 (1.2)	2×32×0.6	14×1.2	14×1.2	2×32×0.6	2×32×0.6	2×32×0.6	2×32×0.6
Slice thickness (mm)	1.0 (1.5)	2.0	2.0	2.0	1.5	1.0	1.5	1.5
Reconstruction increment (mm)	0.8 (1.0)	1.5	1.5	1.5	0.7	0.7	1.0	1.0
Reconstruction kernel	D30f	D30f	D20f	D20f	no info	D30f	no info	D20f
Reference standard	FTIR, micro CT	Crystallography	Chemical analysis	Chemical analysis	FTIR, chemical analysis	Infrared spectroscopy	FTIR	Crystallography
Analysis by commercial DE software (yes or NO)	Y	Y	Y	N	N	Y	N	Y

DE metrics used for stone differentiation	DE_{ratio}	DE_{ratio}	DE_{ratio}	DEI	ΔHU, *R*	DE_{ratio}	$DECT_{slope} = 1/R$	DE_{ratio}, DEI
Accuracy of the UA vs. non-UA differentiation (%)	93–100[c]	98	100/88[d]	100[e]	100	93[e]	98	98[e], 89[e]
Sensitivity of the UA vs. non-UA differentiation (%)	88–100[c]	93	100/100[d]	100[e]	100	100[e]	88	89[e], 74[e]

[a]The three values correspond to the mean sizes of CaOx, CaP and UA groups of stones, respectively
[b]Only volumes of stones were provided in this manuscript
[c]The range of values covers six different acquisitions (three phantom sizes × two collimations)
[d]The two values correspond to the results obtained with and without adjusting the range parameter
[e]These values were calculated on per patient basis

quality for diagnostic imaging of the urinary tract and the diagnosis of kidney stone disease. Only one exam had the overall image quality rated with score ≥3 by both readers, and the conspicuity and margins of each stone were rated by both readers as being acceptably delineated (score 1 or 2) for all 53 patients.

All the studies we described so far utilized the commercial postprocessing algorithm. The in vitro experiments by Matlaga et al. (2008) and Boll et al. (2009) attempted to overcome the limit of the commercial DE software and go beyond a simple UA vs. non-UA differentiation. The study by Matlaga et al. (2008) used the ΔHU and R parameters (see Sect. 2) obtained from manual ROI measurements to discriminate the three groups of stones: calcium oxalate (CaOx, 10 stones), calcium phosphate (CaP, 8 stones) and UA (8 stones). They showed that statistically significant differences existed between the CaP ($R=1.51–1.53$) and CaOx ($R=1.44$) groups, as well as between each of calcium-based group and the UA group ($R=1.04–1.09$). We should note, however, that the R values for the CaOx and CaP stones are too close to each other making a reliable in vivo differentiation of these two stone types using DECT extremely difficult. In addition, it is quite common for calcified calculi to have both CaOx and CaP components heterogeneously mixed within a stone complicating the matter even further.

The study by Boll et al. (2009) used the $1/R$ parameter (named $\mathrm{DECT}_{\mathrm{slope}}$) and the voxel-by-voxel postprocessing algorithm developed in-house to distinguish the five groups of stones: UA-containing (8 stones), cystine (4 stones), struvite (3 stones), CaOx/CaP (29 stones) and brushite-based (6 stones). The algorithm generated the specific identifier U_{slope} (unfortunately, no details were provided on how it was generated) which allowed separating the five groups of stones based on the ranges of the U_{slope} values: UA ($U_{\mathrm{slope}}=77–80$, one outlier), cystine ($U_{\mathrm{slope}}=70–71$), struvite ($U_{\mathrm{slope}}=56–60$), CaOx/CaP ($U_{\mathrm{slope}}=17–59$) and brushite-based ($U_{\mathrm{slope}}=4–15$). One mixed UA-containing (UA/CaOx) stone had the U_{slope} value below the cystine range and, hence, was treated as false-negative when calculating the UA vs. non-UA accuracy and sensitivity for Table 3. We should note, however, that the ranges of the U_{slope} values overlap for the struvite and CaOx/CaP groups and almost overlap for the CaOx/CaP and brushite groups. Therefore, being on a conservative side, it is safer to assume that a reliable in vivo differentiation can probably be achieved only for the three groups of stones: UA, cystine and the rest (calcified stones, struvite, etc.). An example of the "UA vs. cystine vs. calcified stones" differentiation using the DEI metric was also given in (Graser et al. 2008). Since the $\mathrm{DECT}_{\mathrm{slope}}$ algorithm uses essentially the same metric as the commercial DE software ($\mathrm{DECT}_{\mathrm{slope}}=1/R\approx 1/\mathrm{DE}_{\mathrm{ratio}}$) and both algorithms work on a voxel-by-voxel-basis, it is reasonable to assume that the commercial DE algorithm can be improved to identify cystine stones within the non-UA group of stones.

In summary, all publications discussed in this section provide a great deal of evidence that Dual-Source DECT imaging can be reliably used in clinical settings to differentiate between UA- and non-UA-containing stones with high degree of accuracy and sensitivity. In all studies analyzed by the commercial DE software, only five stones were misclassified and three small (<3 mm) stones missed (not classified). All large (≥3 mm) pure UA stones were correctly classified as UA stones in all studies. Moreover, none of non-UA stones were misclassified as pure UA stones potentially resulting in wrong treatment regime (the only exception was a rare 2,8-dihydroxyadenine stone in (Thomas et al. 2009)). The accuracy and sensitivity of the DECT technique should further improve with the use of the second-generation Dual-Source CT scanner due to its better spectral separation.

References

Alvarez RE, Macovski A (1976) Energy-selective reconstructions in X-ray computerized tomography. Phys Med Biol 21:733–744

Behrendt FF, Schmidt B, Plumhans C et al (2009) Image fusion in dual energy computed tomography: effect on contrast enhancement, signal-to-noise ratio and image quality in computed tomography angiography. Invest Radiol 44:1–6

Bellin MF, Renard-Penna R, Conort P et al (2004) Helical CT evaluation of the chemical composition of urinary tract calculi with a discriminant analysis of CT-attenuation values and density. Eur Radiol 14:2134–2140

Boll DT, Patil NA, Paulson EK et al (2009) Renal stone assessment with dual-energy multidetector CT and advanced postprocessing techniques: improved characterization of renal stone composition–pilot study. Radiology 250:813–820

Dillman JR, Caoili EM, Cohan RH (2007) Multi-detector CT urography: a one-stop renal and urinary tract imaging modality. Abdom Imaging 32:519–529

Evan AP, Willis LR, Lingeman JE et al (1998) Renal trauma and the risk of long-term complications in shock wave lithotripsy. Nephron 78:1–8

Graser A, Johnson TR, Bader M et al (2008) Dual energy CT characterization of urinary calculi: initial in vitro and clinical experience. Invest Radiol 43:112–119

Grosjean R, Sauer B, Guerra RM et al (2008) Characterization of human renal stones with MDCT: advantage of dual energy and limitations due to respiratory motion. Am J Roentgenol 190:720–728

National Institutes of Health (1990) National Kidney and Urological Diseases Advisory Board long range plan: window on the 21st century. In: NIH Publication 90–583. United States Department of Health and Human Services, Washington

Joseph P, Mandal AK, Singh SK et al (2002) Computerized tomography attenuation value of renal calculus: can it predict successful fragmentation of the calculus by extracorporeal shock wave lithotripsy? A preliminary study. J Urol 167:1968–1971

Lemann J Jr, Taylor AJ, Collier BD et al (1991) Kidney hematoma due to extracorporeal shock wave lithotripsy causing transient renin mediated hypertension. J Urol 145:1238–1241

Lingeman JE, Woods JR, Toth PD (1990) Blood pressure changes following extracorporeal shock wave lithotripsy and other forms of treatment for nephrolithiasis. JAMA 263:1789–1794

Matlaga BR, Kawamoto S, Fishman E (2008) Dual source computed tomography: a novel technique to determine stone composition. Urology 72:1164–1168

Mitcheson HD, Zamenhof RG, Bankoff MS et al (1983) Determination of the chemical composition of urinary calculi by computerized tomography. J Urol 130:814–819

Mostafavi MR, Ernst RD, Saltzman B (1998) Accurate determination of chemical composition of urinary calculi by spiral computerized tomography. J Urol 159:673–675

Motley G, Dalrymple N, Keesling C et al (2001) Hounsfield unit density in the determination of urinary stone composition. Urology 58:170–173

Nakada SY, Hoff DG, Attai S et al (2000) Determination of stone composition by noncontrast spiral computed tomography in the clinical setting. Urology 55:816–819

Pareek G, Armenakas NA, Fracchia JA (2003) Hounsfield units on computerized tomography predict stone-free rates after extracorporeal shock wave lithotripsy. J Urol 169:1679–1681

Pearle MS, Calhoun EA, Curhan GC (2005) Urologic diseases in America project: urolithiasis. J Urol 173:848–857

Primak AN, Fletcher JG, Vrtiska TJ et al (2007) Noninvasive differentiation of uric acid versus non-uric acid kidney stones using dual-energy CT. Acad Radiol 14:1441–1447

Primak AN, Ramirez Giraldo JC, Liu X et al (2009) Improved dual-energy material discrimination for dual-source CT by means of additional spectral filtration. Med Phys 36: 1359–1369

Sheir KZ, Mansour O, Madbouly K et al (2005) Determination of the chemical composition of urinary calculi by noncontrast spiral computerized tomography. Urol Res 33:99–104

Stolzmann P, Scheffel H, Rentsch K et al (2008) Dual-energy computed tomography for the differentiation of uric acid stones: ex vivo performance evaluation. Urol Res 36: 133–138

Stolzmann P, Kozomara M, Chuck N et al (2009) In vivo identification of uric acid stones with dual-energy CT: diagnostic performance evaluation in patients. Abdom Imaging. doi:10.1007/s00261-009-9569-9

Thomas C, Patschan O, Ketelsen D et al (2009) Dual-energy CT for the characterization of urinary calculi: In vitro and in vivo evaluation of a low-dose scanning protocol. Eur Radiol 19:1553–1559

Vrtiska TJ (2005) Quantitation of stone burden: imaging advances. Urol Res 33:398–402

Williams JC Jr, Saw KC, Monga AG et al (2001) Correction of helical CT attenuation values with wide beam collimation: in vitro test with urinary calculi. Acad Radiol 8:478–483

Williams JC Jr, Paterson RF, Kopecky KK et al (2002) High resolution detection of internal structure of renal calculi by helical computerized tomography. J Urol 167:322–326

Williams JC Jr, Kim SC, Zarse CA et al (2004) Progress in the use of helical CT for imaging urinary calculi. J Endourol 18:937–941

Yu L, Primak AN, Liu X et al (2009) Image quality optimization and evaluation of linearly mixed images in dual-source, dual-energy CT. Med Phys 36:1019–1024

Zarse CA, McAteer JA, Tann M et al (2004) Helical computed tomography accurately reports urinary stone composition using attenuation values: in vitro verification using high-resolution micro-computed tomography calibrated to Fourier transform infrared microspectroscopy. Urology 63: 828–833

Part VI

Extremities

Tendons and Ligaments

Susanne Jochum

Contents

Abstract

- The imaging of tendons and ligaments was the domain of MRI and ultrasound, so far. The dual-energy CT offers a new imaging method to visualize tendons and ligaments.
- Tendons of the hand and wrist but also of the foot, talocrural region and Achilles tendon could be demonstrated by dual-enery CT. Not only normal tendons can be shown, it is reported that even lesions can be depicted.
- The visualization of ligaments at the knee with dual-energy CT is possible. The significance of this new method has to be shown. At the moment it seems to be an interesting alternative in patients with MRI contraindications. The results of depiction of the tendons and ligaments in the shoulder with dual-energy CT are not promising yet.

1 Introduction

The imaging of tendons and ligaments was the domain of the MRI and ultrasound, so far. With the development of dual-energy CT there are new possibilities of imaging of these structures, because of the good delineation of collagen versus the surrounding structures like fat and bone. The tissue differentiation is possible, because of the different exhibition of Houndsfield values at the different tube voltages (Petersilka et al. 2008).

The use of dual-energy CT in the depiction of tendons especially of the hand and feet is reviewed. Dual-energy CT seems promising in the imaging of the knee

S. Jochum
Institute of Radiology, Westpfalz Clinic, Hellmut-Hartert-Strasse 1, 67655 Kaiserslautern, Germany and
Department of Clinical Radiology and Nuclear Medicine, University Medical Center Mannheim,
Medical Faculty Mannheim of the University of Heidelberg, Theodor-Kutzer-Ufer 1-3, 68167 Mannheim, Germany
e-mail: s.jochum@gmx.de

T.R.C. Johnson et al. (eds.), *Dual Energy CT in Clinical Practice*, Medical Radiology,
DOI: 10.1007/174_2010_54

showing ligamental structures very well, but the use in trauma patients is not evaluated yet.

2 Tendons and ligaments

2.1 Tendons

Injuries of the tendons are often caused by sport and work activities. Some tendons like the extensor pollicis longus tendon are highly vulnerable structures due to their superficial location at the dorsum of the forearm and wrist. There are many reasons for injuries of the tendons like fractures, stab wounds, but also spontaneous ruptures in patients with rheumatic diseases, steroid administration or repetitive stress (Santiago et al. 2008).

The diagnostic work-up of the tendons is usually performed by clinical examination, ultrasound and magnetic resonance imaging (MRI). CT was made in cases, when MRI is not possible like obese patients (Santiago et al. 2008), but there are also studies using three-dimensional CT imaging to evaluate the extensor tendons in the hand and wrist (Sunagawa et al. 2005) or depict extensor tendon rupture in rheumatic wrists (Abe et al. 2010). MRI is considered the imaging modality of choice to display tendons but it is not helpful in patients with internal or external fixation. On MRI it is hard to depict an individual tendon along its entire course or depict all tendons in a short period of scanning time (Abe et al. 2010).

The accuracy of ultrasound depends extremely on the examiner, but it has the highest spatial resolution. It cannot be used in patients with surgical wounds or open lacerations in the area of interest (Sunagawa et al. 2005). In many cases therefore no diagnostic imaging is performed at all, and only the clinical experience leads to subsequent early surgical exploration (Deng et al. 2009).

Dual-energy CT offers a new imaging method to visualize tendons, but there is only initial experience in visualizing hand and foot tendons by this technique, yet. Along with the general advantages of CT, namely the three-dimensional visualization of structures by the volume rendering technique, the relationship of the tendons to the bony structures can be displayed helping the surgeons to plan the operation. The advantage of dual-energy CT versus the ultrasound hereby, is the better delineation of the bony structures and the soft tissue.

As an examination protocol, the following parameter setting are proposed: tube A: 140 kV, 40 mAs and tube B 80 kV, 170 mAs in the hand and 56/234 mAs in the feet. Collimation 0.6 mm. Slice thickness 2 mm with a reconstruction increment of 0.75 mm and a rotation time of 1.0 s. Image postprocessing is usually performed with a multimodality workplace (i.e., MMWP Siemens Medical Solutions, Forchheim, Germany) using the Dual-Energy mode. The tendons can be highlighted because of the different attenuation of the collagen versus the bony and fatty structures. It is helpful to create multiplanar reconstructions (MPR) as well as volume rendered images (VRT). In a study of 20 patients with suspected tendon disease, the weighted CT dose index (CTDI vol) of the dual-energy CT ranged between 5.45 and 7.80 mGy with an average of 6.56 mGy (Deng et al. 2009).

It is reported that most tendons such as the flexor pollicis longus tendon, flexor digitorum superficialis/profundus tendon, Achilles tendon, extensor hallucis longus tendon and extensor digitorum longus tendon could be demonstrated by dual-energy CT with their profile, insertion, continuity, soft tissue and skeletal structure: (Fig. 1). Tendons in the anterior talocrural region, posterior talocrural region and dorsum of the foot were displayed better than those in the sole of foot, while tendons in the palm of the hand were better seen than those in the

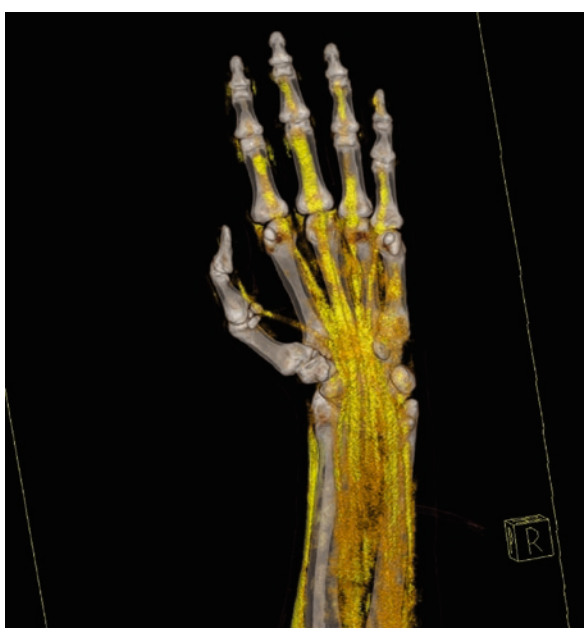

Fig. 1 Palmar view of the flexor tendons of the forearm and hand. The delineation of the tendons versus the bone using the dual-energy postprocessing mode is very good

dorsum of the hand (Deng et al. 2009). Not only normal tendons can be shown with dual-energy CT. Deng reported of lesions of the tendons like circuitry, atrophy, adherence, compression, overlength and thickening. An unsolved problem is the identification of thinner tendons such as the distal end of the extensor digitorum tendon and the extensor pollicis longus tendon. Also the peroneus longus tendon in the sole of the foot was not displayed satisfactorily (Deng et al. 2009).

There are no studies available yet, which compare the different imaging methods like dual-energy CT, MRI and ultrasound with regard to the accuracy for the detection of injuries and diseases of the tendons.

2.2 Ligaments

2.2.1 Knee

For the diagnostic work-up of injuries of the knee, especially the ACL, MRI is the gold standard. In conventional X-ray, the ACL itself cannot be depicted. Only indirect signs like swelling of the surrounding soft tissue or fractures of the intercondylar eminence or Segond's fractures might be seen (Wischer et al. 2001). Ultrasound is a highly sensitive instrument for the diagnosis of traumatic rupture of the ACL (Ptasznik et al. 1995), but it depends on the experience of the examiner.

CT so far only played a small role in the diagnostic assessment of the knee, especially the ACL. Only with CT arthrography an adequate visualization was possible.

The sensitivity and specificity of CT arthrography for the diagnosis of anterior cruciate ligament abnormalities were 87.5–100% and 93.3–96.7%, respectively (Lee et al. 2004).

Dual energy CT opens up new possibilities in the diagnosis of the ligamental structures (Johnson et al. 2007; Sun et al. 2008) without invasive methods like air or intraarticular contrast media injection. An examination protocol for ligaments in the knee is similar to the one of the tendons above using the "dual-energy program knee" with a tube voltage of 140 and 80 kV (56 and 234 mAs), collimation of 0.6 mm, pitch 0.7 and a reconstruction increment of 0.75 mm with a rotation time of 1 s. For the examination of the knee, a CTDI vol of 4.70–6.26 mGy is reported (Sun et al. 2008), our own results range between 5.27 and 7.12 mGy. The image post-processing includes multiplanar reconstruction (MPR) and volume rendering technique (VRT) using the dual-energy postprocessing application "tendon."

An initial qualitative study of dual-energy CT for the knee ligaments shows, that the patellar ligament, the fibular collateral ligament, the anterior and posterior cruciate ligament were displayed clearly (Figs. 2 and 4),

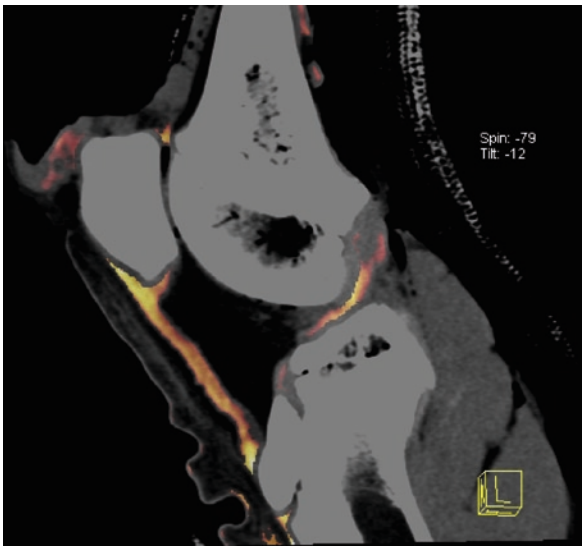

Fig. 2 Good depiction of the anterior cruciate ligament and patella ligament in an animal model (swine), sagittal view

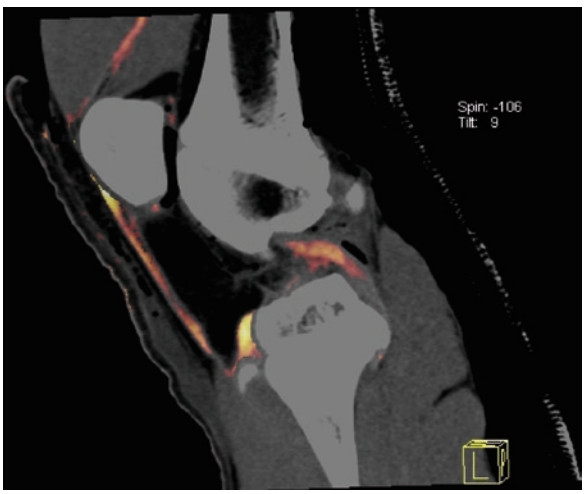

Fig. 3 Good depiction of the patella ligament and the posterior cruciate ligament in the swine model. Regard the incomplete depiction of the anterior cruciate ligament at the dorsal apical part representing a proven complete rupture of this ligament (Sagittal view)

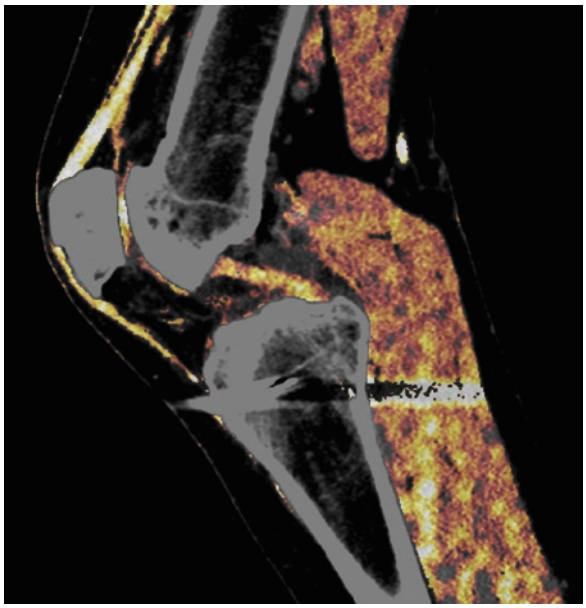

Fig. 4 Sagittal view with a good depiction of the dorsal cruciate ligament in a patient. The basal artifact in the tibia is caused by metal fixation after reconstruction of the anterior cruciate ligament with an autograft

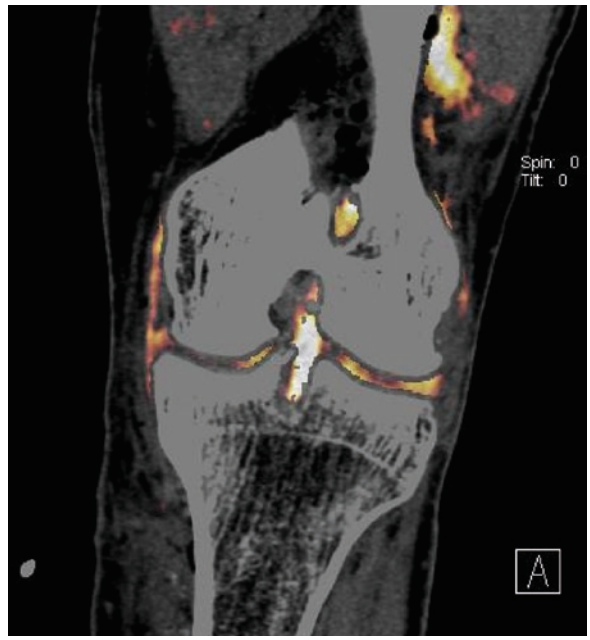

Fig. 5 ACL autograft reconstruction with a good delineation in dual-energy CT, coronal view

whereas the tibial collateral ligament, the transversal ligaments and the posterior ligament were poorly shown (Sun et al. 2008).

Our own results in a swine model show a good depiction of the anterior cruciate ligament, but the sensitivity for depiction of injuries like incomplete or complete ruptures is lower than for MRI (Fig. 3). Dual-energy CT may become an alternative method in imaging of patients with MRI contraindications like pacemaker or claustrophobia. A further promising application may be the postoperative imaging of autografts for ACL reconstruction, because the utilized tendons are very well suited for depiction by dual-energy CT (own results). However, there are no publicized studies yet (Figs. 5 and 6).

2.2.2 Shoulder

Despite the clinical experience with dual-energy CT for several years, there are no published studies available yet. Our own results are not promising with regard to the depiction of tendons and ligaments in the

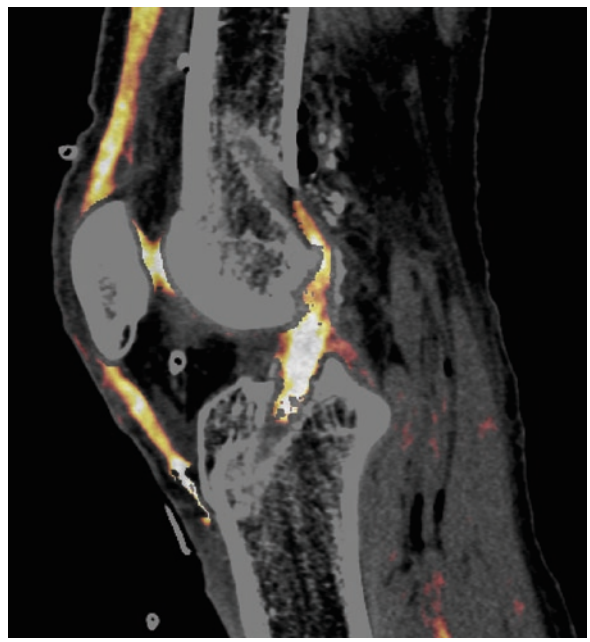

Fig. 6 ACL autograft reconstruction with a good delineation in dual-energy CT, sagittal view. The circular structures within the knee and on the skin surface are drainages

shoulder, so it might be speculated that MRI remains the gold standard for this joint.

References

Abe A, Ishikawa H, Murasawa A, Nakazono K (2010) Extensor tendon rupture and three-dimensional computed tomography imaging of the rheumatoid wrist. Skeletal Radiol 39:325–331

Deng K, Sun C, Liu C, Ma R (2009) Initial experience with visualizing hand and foot tendons by dual-energy computed tomography. Clin Imaging 33:384–389

Johnson TR, Krauss B, Sedlmair M et al (2007) Material differentiation by dual energy CT: initial experience. Eur Radiol 17:1510–1517

Lee W, Kim HS, Kim SJ, Kim HH, Chung JW, Kang HS, Hong SH, Choi J (2004) CT arthrography and virtual arthroscopy in the diagnosis of the anterior cruciate ligament and meniscal abnormalities of the knee joint. Korean J Radiol 5(1):47–54

Petersilka M, Bruder H, Krauss B, Stierstorfer K, Flohr TG (2008) Technical principles of dual source CT. Eur J Radiol 68:362–368

Ptasznik R, Feller J, Bartlett J, Fitt G, Mitchell A, Hennessy O (1995) The value of sonography in the diagnosis of traumatic rupture of the anterior cruciate ligament of the knee. AJR Am J Roentgenol 164:1461–1463

Santiago FR, Plazas PG, Fernandez JM (2008) Sonography findings in tears of the extensor pollicis longus tendon and correlation with CT, MRI and surgical findings. Eur J Radiol 66:112–116

Sun C, Miao F, Wang XM et al (2008) An initial qualitative study of dual-energy CT in the knee ligaments. Surg Radiol Anat 30:443–447

Sunagawa T, Ishida O, Ishiburo M, Suzuki O, Yasunaga Y, Ochi M (2005) Three-dimensional computed tomography imaging: its applicability in the evaluation of extensor tendons in the hand and wrist. J Comput Assist Tomogr 29:94–98

Wischer TK, Bredella MA, Bongartz G (2001) Bildgebung des vorderen Kreuzbandes. Arthroskopie 14:114–118

Gout

Savvas Nicolaou, Steven John Co, and Daniel James Hou

Contents

Abstract

- This chapter explores the technique of dual energy computed tomography (DECT) and the current and future clinical use of DECT in the diagnosis and management of gouty arthropathy.
- Gout is a common type of crystalline arthropathy of metabolic origin. Both the incidence and prevalence of gout appear to be increasing worldwide. It is triggered by the crystallization of monosodium urate (MSU) within joints which is characterized by intermittent attacks of inflammation. Gout causes significant pain, activity limitation and can be a substantial cause of morbidity. The definitive diagnosis of gout requires microscopic analysis of fluid aspirated from the joint; however, many physicians diagnose and manage gout without confirming the diagnosis with joint aspirate crystal analysis. There is limited clinical utility among the current imaging modalities used to identify and monitor gout including X-rays, ultrasound, conventional computed tomography, and magnetic resonance imaging which all lack specificity for gout. Dual energy CT can accurately characterize MSU deposition and can improve clinical diagnoses of unclear arthropathies. DECT has the potential to be a problem-solving tool that can be utilized to diagnose the presence of gout in challenging clinical presentations and potentially obviating the need for arthrocentesis.
- DECT has the potential to revolutionize the diagnosis and management of gout.

S. Nicolaou (✉), S. J. Co, and D.J. Hou
Vancouver General Hospital, 895 West 12th Avenue,
Vancouver, BC, V5Z 1M9, Canada
e-mail: savvas.nicolaou@vch.ca

T.R.C. Johnson et al. (eds.), *Dual Energy CT in Clinical Practice*, Medical Radiology,
DOI: 10.1007/174_2010_34

1 Clinical Background

Gout is a common type of crystalline arthropathy of metabolic origin. Both the incidence and prevalence of gout appear to be increasing worldwide (Lawrence et al. 2008). It is triggered by the crystallization of monosodium urate (MSU) within joints which is characterized by intermittent attacks of inflammation. It is often associated with hyperuricemia and it is believed that the persistence of hyperuricemia can lead to the development of tophaceous disease and chronic gouty polyarthropathy (Dalbeth and Haskard 2005). Gout causes significant pain, activity limitation and can be a substantial cause of morbidity. Chronic tophaceous deposits can lead to deformity, disability, and ultimately joint destruction. Gout can occur at any joint throughout the body but common sites include the foot, heel, ankle, knee, hand, wrist, fingers and elbows. In addition, it is also believed to be strongly associated with metabolic syndrome, myocardial infarction, insulin resistance, stroke, and premature death (Choi et al. 2007; Choi and Ford 2007; Choi and Curhan 2007; Kim et al. 2009). As a result, gout is a significant economic strain in society due to both direct medical costs and indirect medical cost (Brook et al. 2006; Kleinman et al. 2007; Mould-Quevedo et al. 2008; Wu et al. 2008). An estimated $27 million is spent each year on new acute cases (Kramer et al. 2003; Kim et al. 2003).

The definitive diagnosis of gout requires polarized light microscopic analysis of fluid aspirated from the involved joint demonstrating needle-shaped, strongly negatively birefringent MSU crystals. Nonetheless, in clinical practice only 11% of patients undergo arthrocentesis and the vast majority of cases of gout are diagnosed on clinical grounds (Underwood 2006). However, other diseases can mimic or coexist with gout. These include rheumatoid arthritis, erosive osteoarthritis, psoriasis, tophi coexisting in Heberden's nodes and calcium pyrophosphate dihydrate (CPPD) deposition arthropathy. To date, there is no established imaging tool to facilitate the diagnosis and follow up of gout patients.

There is limited clinical utility among the current imaging modalities used to identify and monitor gout including X-rays, ultrasound, conventional computed tomography, and magnetic resonance imaging (Thiele and Schlesinger 2007; Perez-Ruiz and Naredo 2007; Schumacher et al. 2006; Dalbeth et al. 2007a, b; Gerster et al. 1996). Plain radiographs appear normal until late in the disease and are not sensitive in their diagnosis of gout. Ultrasound has a poor sensitivity and specificity for gout as a diagnostic modality. Furthermore, visualization of tophi as echogenic nodules results in posterior acoustic shadows which further limits imaging structures posterior to the tophus (Fig. 1) (Thiele and Schlesinger 2007). Studies have

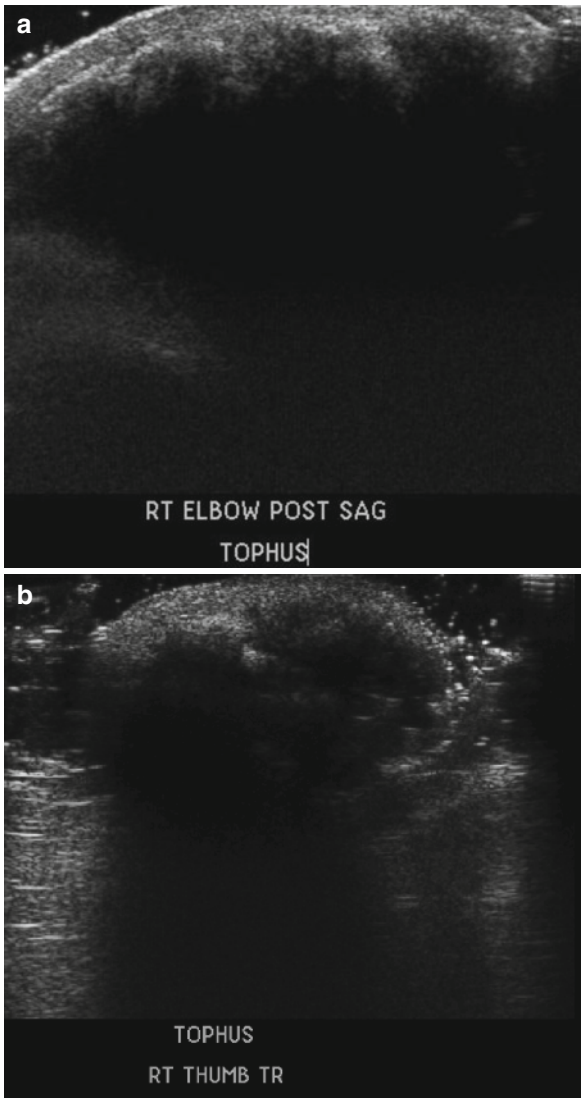

Fig. 1 (**a**) Sagittal sonogram of the posterior aspect of the elbow. Severe acoustic shadowing artifact produced by the tophus which completely obscures the elbow joint. (**b**) Sagittal sonogram of the first interphalangeal joint. The joint is completely obscured by acoustic shadowing resulting from the tophus. The appearance of the tophus in both cases is nonspecific and a rheumatoid nodule would give a similar appearance

shown MR imaging to be non-specific in the diagnosis of gout with variable imaging appearances of tophi from low to intermediate signal on T1- and T2-weighted imaging, respectively (Fig. 2a–d) (Schumacher et al. 2006). Although conventional CT has been reported to be superior to both MRI and ultrasonography in the detection of intra-articular tophi and erosions (Dalbeth and McQueen 2009; Gerster et al. 2002), none of these modalities can accurately confirm the presence of MSU deposition. Thus, a highly accurate noninvasive imaging tool to confirm the presence of gout would be desirable.

Dual energy computed tomography (DECT) has the potential to revolutionize the diagnosis and management of gout (Fig. 3a–d). This CT scanner simultaneously uses two X-ray tubes at two different energy

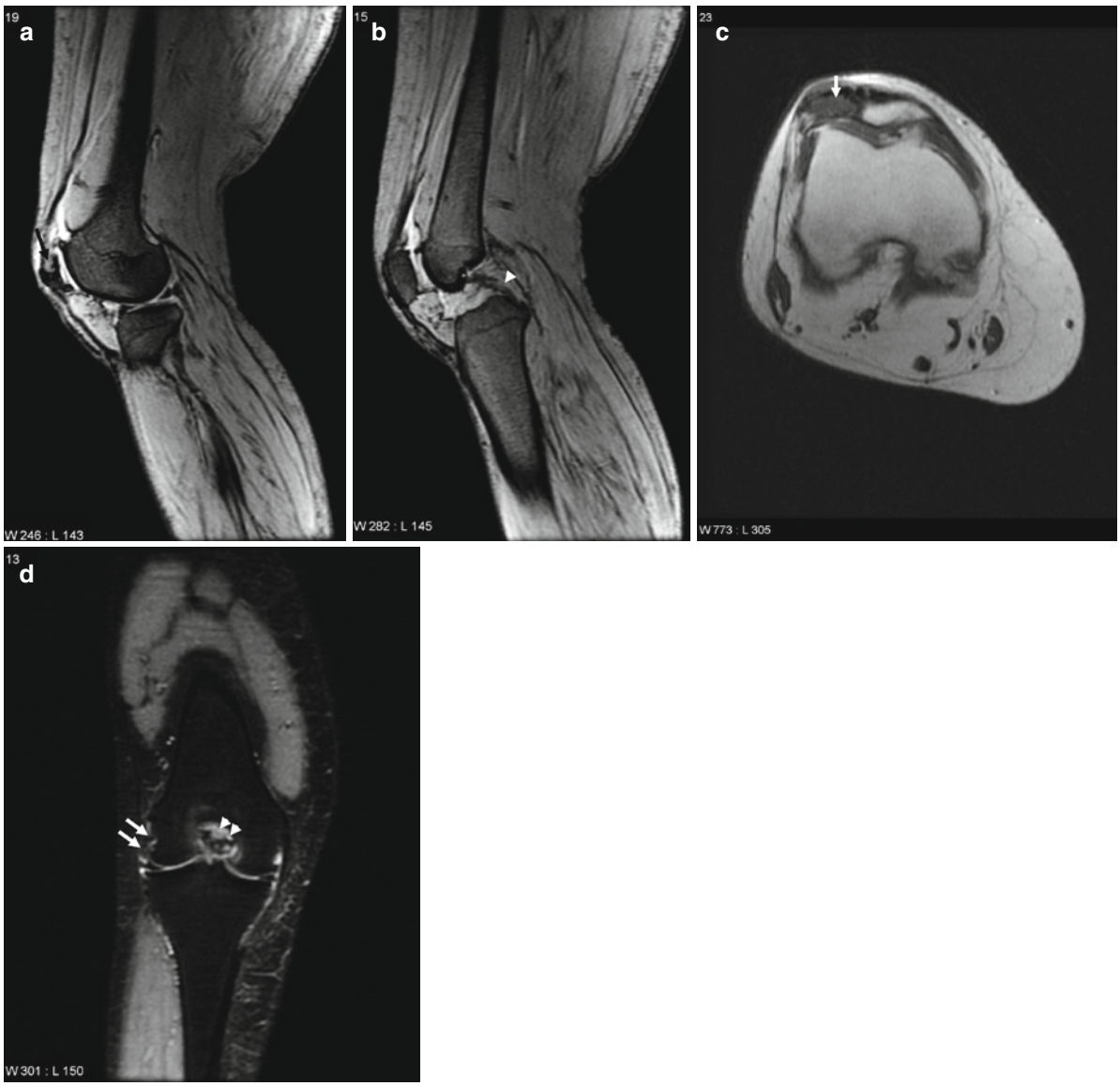

Fig. 2 (**a**) & **b**) Sagittal MPGR's reveals non-specific high signal mass with associated erosion and thickening of the PCL (arrowhead) and within the patella (arrow). **c**) Axial T1-weighted image reveals a non-specific medium signal mass with resulting erosion along the patella (arrow). **d**) Coronal FSE T2 with Fat sat reveals non-specific heterogeneous signal changes along the intercondylar region (double arrowheads) as well as along the popliteal tendon (double arrows)

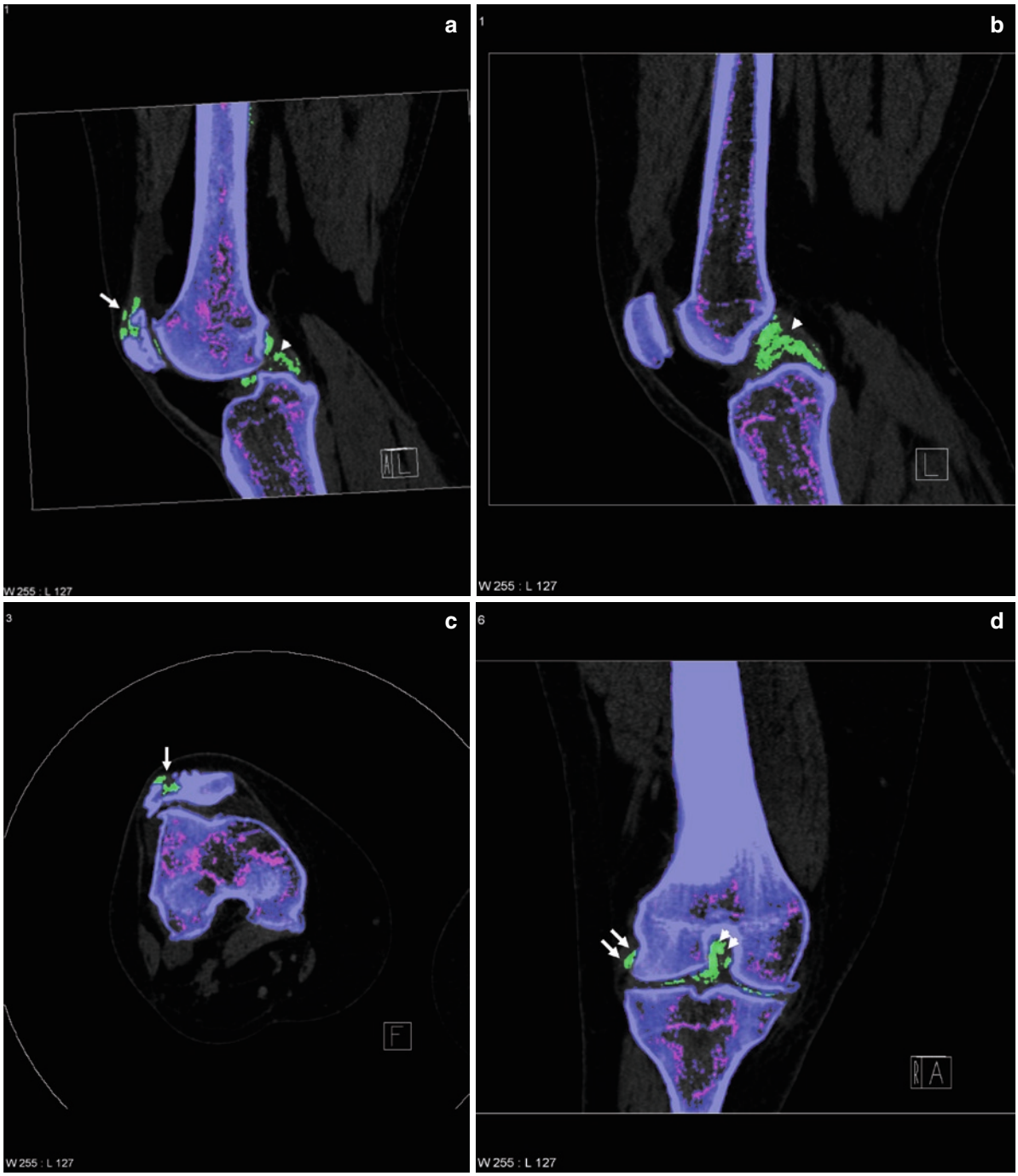

Fig. 3 (**a**-**d**) DECT reformatted two-material decomposition algorithm images of the patient in Figure 2 which confirms the presence of monosodium urate (MSU) deposition along the patella (arrow), PCL (arrowhead), popliteal tendon (double arrows), and intercondylar region (double arrowheads)

levels (80 and 140 kVp) to create two different data sets. A material decomposition algorithm is able to differentiate materials based on their chemical composition which enables easy classification of the scanned tissue. This allows accurate and specific characterization of MSU from calcium.

2 Physical Background

The DECT system (DefinitionR scanner, Siemens Medical Solutions, Forchheim, Germany) is equipped with two X-ray tubes rather than one. Scans performed on the dual source scanner acquire data at two different energy levels simultaneously. The dual energy principle is based on the photoelectric effect, which is strongly energy dependant, and CT numbers vary considerably with material composed of high atomic numbers that can be differentiated further by applying different energy spectra and analyzing the differential attenuation. Based on this principle of differential attenuation at 80 and 140 kV, one can calculate a value know as the Dual Energy Index. Materials with high positive values, such as iodine and bone, attenuate more at 80 kV than at 140 kV. Materials such as fat and bile attenuate more at 140 kV than at 80 kV and have a negative value. Thus, each material has its own specific Dual Energy Index and in principle can be characterized with DECT.

3 Scan Protocol

3.1 Gout Protocol: Upper Extremity (Wrists) Siemens Definition Dual Source Scanner

3.1.1 Patient Position

Patient should be positioned head first in a prone position. Forearms and wrists are positioned forward of the patient's head with hands in a neutral position on a radiolucent sponge for support of the palms and digits. Palms are placed with the dorsum facing up (palms down), in a relaxed dorsiflexion position. Patient's head should be positioned on a pillow to alleviate strain on the head position.

3.1.2 Scan Range

Scan in a craniocaudal direction, proximally 5 cm from the wrist joint to the distal end of the phalanges (including distal soft tissue). Both wrists are scanned axially in one acquisition.

3.2 Gout Protocol: Lower Extremity (Ankles) Siemens Definition Dual Source Scanner

3.2.1 Patient Position

Patient should be positioned feet first in a supine position, with the knees bent, approximately in a 90° position, with the feet in a firm plantarflexion position. A knee bolster is recommended to support the position of the knees.

3.2.2 Scan Range

Scan is acquired in a craniocaudal direction starting proximally 5 cm from the ankle joint to the distal end of the phalanges (including distal soft tissue). Both ankles are scanned axially in one acquisition.

3.3 Technical Factors

Scanning protocol of DECT for gout includes images of both hands, wrists, elbows, knees, ankles and feet. Scanning parameters were as follows: tube A: 140 kV, 55 mA, tube B: 80 kV, 243 mA, collimation 0.6 mm reconstructed to 0.75 mm transverse thick slices obtained at 80 kV and 140 kV (Table 1). The dose was maintained the same as single source CT by altering the mAs on the 80 and 140 kvp to equal single source CT doses. The baseline value of MSU of 80 kV was chosen to be 50 HU and at 140 kV, 50 HU. Best results were obtained by setting the dual energy index param-

Table 1 Dual Energy CT Scanning Parameters for Gout

Protocol	mAs (Tube A) kV 140	mAs (Tube B) kV 80	Kernel D	Kernel B	Collimation	Pitch
DE gout upper	100	425	D30 0.75 mm×0.5 mm	B20 2 mm×1.5 mm	64 mm×0.6 mm	0.55
DE gout lower	120	400	D30 0.75 mm×0.5 mm	B20 2 mm×1.5 mm	64 mm×0.6 mm	0.55

eter ratio to 1.28. The range of values for the calculation was set between 125 and 3,000.

4 Post-Processing

After the images are obtained, the two different data sets are loaded into the post processing application "SyngoR DUAL ENERGY" on a multi modality CT Worksplace, SW-Version VA20 (Siemens Medical Solutions, Forchheim, Germany). The data sets are further processed utilizing the two material decomposition algorithm.

This two material decomposition application allows visualization of MSU (gout), calcium (bone), and contrast agent at the same time with different color coded disc schemes. The two-material decomposition algorithm is based on the physical principle that the attenuation of photons depends on the atomic number and energy of the photons. Material with a high atomic number (calcium) has a higher change in attenuation than material with a low-atomic-number (MSU). This difference in attenuation directly translates into a difference in CT values. Compared to single energy threshold-based techniques for material separation, the huge benefit of DECT is that the ratio or change in CT values is independent of density or concentration of the tissue.

As seen in Fig. 4, the attenuation of MSU differs greatly from that of the bone (including the trabecular bone which has similar attenuation to iodine). If iodine contrast is given, the attenuation of the tissue mixtures is represented by the pink line. The blue line separates MSU voxels from soft tissues, bone, and iodine. When the calculation is complete, three materials are displayed in different colors in the result image: bone in blue, MSU in green, and iodine or trabecular bone in pink (Fig. 5).

Practical tips for interrogating regions of interest to determine the presence of MSU include: (1) Increasing the ratio to 1.32, (2) Decreasing the range to 3. Employing this technique makes questionable areas of MSU deposition more discernable and increases the confidence of diagnosis. This will increase the sensitivity of detecting MSU at the expense of decreasing specificity.

It should be noted that image artifacts can exist which can lead to erroneous identification of MSU deposition if not appreciated. Image artifacts can be found to occur at certain sites including on the skin, within and around nail beds, and along flexor tendons of the feet and hands and along peroneal tendons (Fig. 6a). As well, metallic materials can also result in artifacts mimicking MSU deposits which is of particular concern in patients with arthroplasties (Fig. 6b). Practical tips would be to (1) recognize the common locations of artifacts, (2) increasing the minimum value (HU) of interrogation to 140, (3) increasing the range to 6–7.

5 Diagnostic Evaluation

The definitive diagnosis of gout is based on the detection of needle-shaped negatively birefringent MSU crystals under polarized light following joint fluid aspiration. Although accurate, joint fluid aspiration is invasive and can be technically demanding; challenges include variations in human anatomy and subcutaneous fat, thickened synovial membranes resulting from chronic synovitis, and hyperviscous fluid due to chronic effusion (Nicolaou et al. 2010). In addition, occasional joint aspirations prove to be indeterminate further complicating the diagnosis. As well, although rare, the complication of septic arthritis following joint aspiration is also possible (Nicolaou et al. 2010). Many physicians

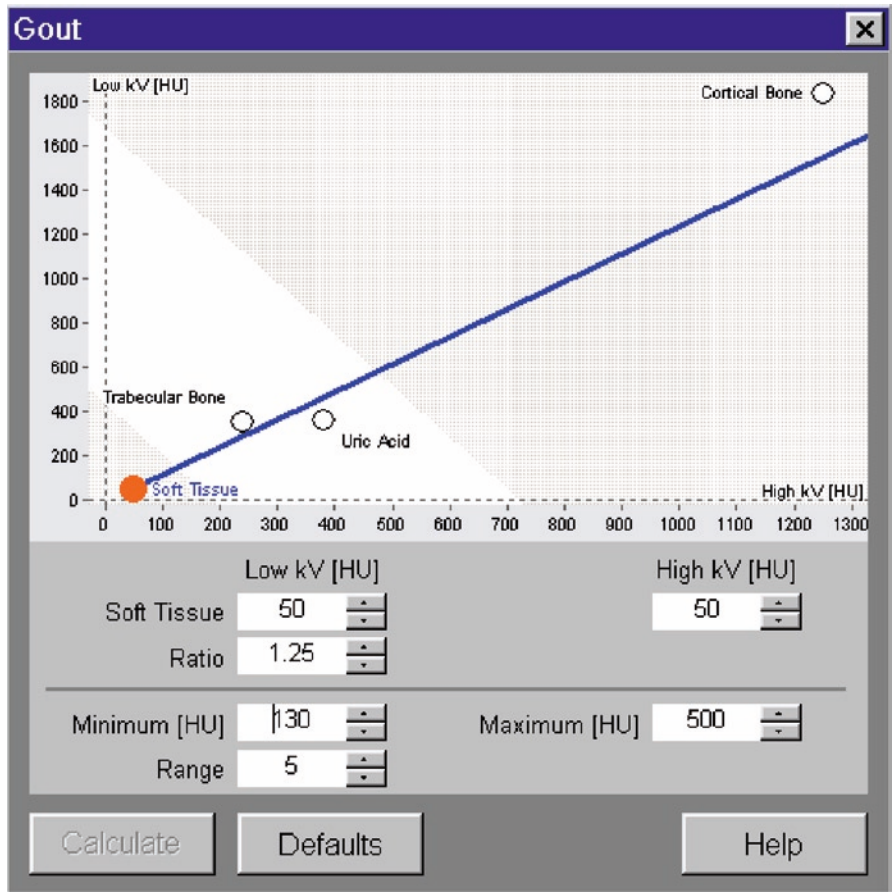

Fig. 4 Syngo® Siemens Dual energy software tool for analysis of gout demonstrating the differential Dual Energy Indices (DEIs) between trabecular bone, uric acid and cortical bone

diagnose and manage gout without confirming the diagnosis with joint aspirate crystal analysis. Currently, only 11% of suspected gout cases are diagnosed through joint aspiration and the majority of cases are diagnosed clinically (Underwood 2006). Therefore, physicians often rely on clinical criteria, including the ACR, New York, and Rome criteria which when compared to crystal identification are neither very sensitive nor specific (Malik et al. 2009). However, at times, the clinical picture of gout can be confused with septic arthritis, osteomyelitis, trauma, pseudogout (CPPD), rheumatoid arthritis (RA), psoriatic arthritis, and osteoarthritis (OA) (Malik et al. 2009). As a result, there has been escalating interest in using a less invasive technique to confirm the diagnosis of gout.

Conventional CT has been reported to be superior to both MRI and ultrasonography in the detection of intra-articular tophi and erosions (Dalbeth et al. 2007a; Gerster et al. 1996; Gerster et al. 2002); however, these findings are not specific to gout as it does not accurately confirm the presence of MSU deposition.

DECT can accurately characterize MSU deposition and can improve clinical diagnoses of unclear arthropathies. DECT can serve as a problem solving tool and help differentiate gout from similar presenting arthropathies.

5.1 Case 1

A 70 year old gentleman presented to the Emergency Department with diffuse swelling and erythema of his right hand but no history of trauma. Given the severity of pain and swelling, there was clinical concern of osteomyelitis vs. gouty arthropathy. Serum urate levels were mildly increased. Plain film radiography was initially ordered which showed soft tissue swelling

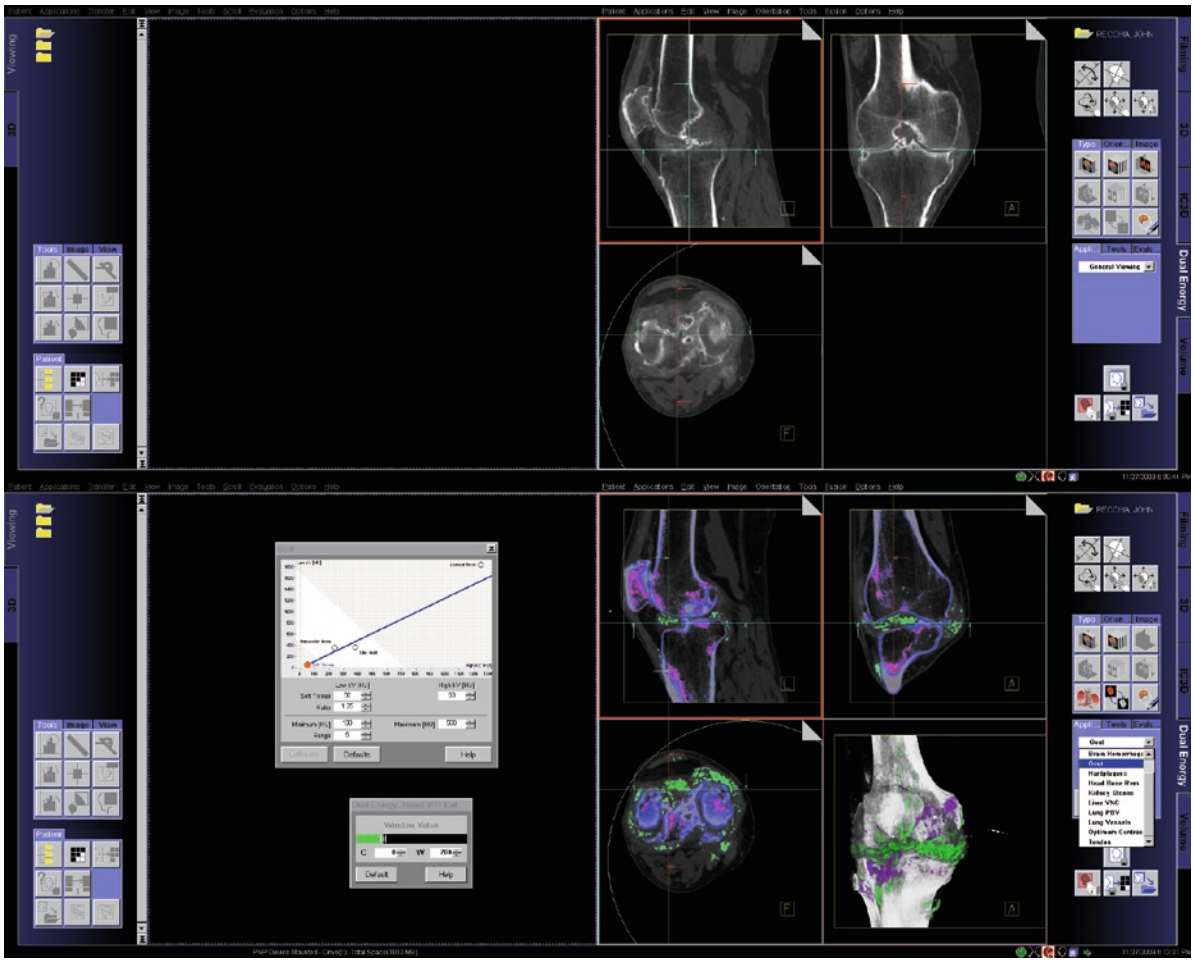

Fig. 5 DECT with gout algorithm. Screen shot from a dual energy workstation showing the gout algorithm applied to the images. Calcium is a heavy, high atomic number element which has high attenuation of the low kV beam. Therefore, bone attenuation lies above the *blue line* and is color coded *blue*. MSU is composed of C, H, N, O. Therefore it has a relatively low atomic number per unit area and it attenuates the High kV beam to a greater extent. It will lie below the *blue line* and will be color coded *green*. Iodine or trabecular bone appears *pink*. The slope of the *blue line* was adjusted to separate the differential attenuation of uric acid vs. calcium

overlying the right second DIP joint with periarticular erosive changes and joint space narrowing. (Fig. 7a). A DECT scan was subsequently performed which revealed MSU deposits surrounding the second DIP but also of the first PIP, consistent with gouty arthropathy and tophus formation rather than osteomyelitis (Fig. 7b, c) This patient was treated with anti-inflammatory medications and subsequently urate lowering therapy and improved clinically.

This case highlights how the acute presentation of gout can mimic multiple pathologies and how DECT can be utilized to be an invaluable tool in the evaluation of diagnostically challenging cases.

5.2 Case 2

A 72 year old gentleman was seen in the Emergency Department with a similar presentation to the case above: diffuse swelling and erythema of his feet but no history of trauma. The clinical concern was of osteomyelitis vs. septic arthritis. A plain radiograph and a single source CT scan was performed which initially raised the possibility of gout (Fig. 8a, b). A DECT scan was subsequently performed which did not demonstrate any abnormal MSU deposits, but did have findings to suggest osteomyelitis or an aggressive lesion such as a neoplasm (Fig. 8c, d). An ultrasound

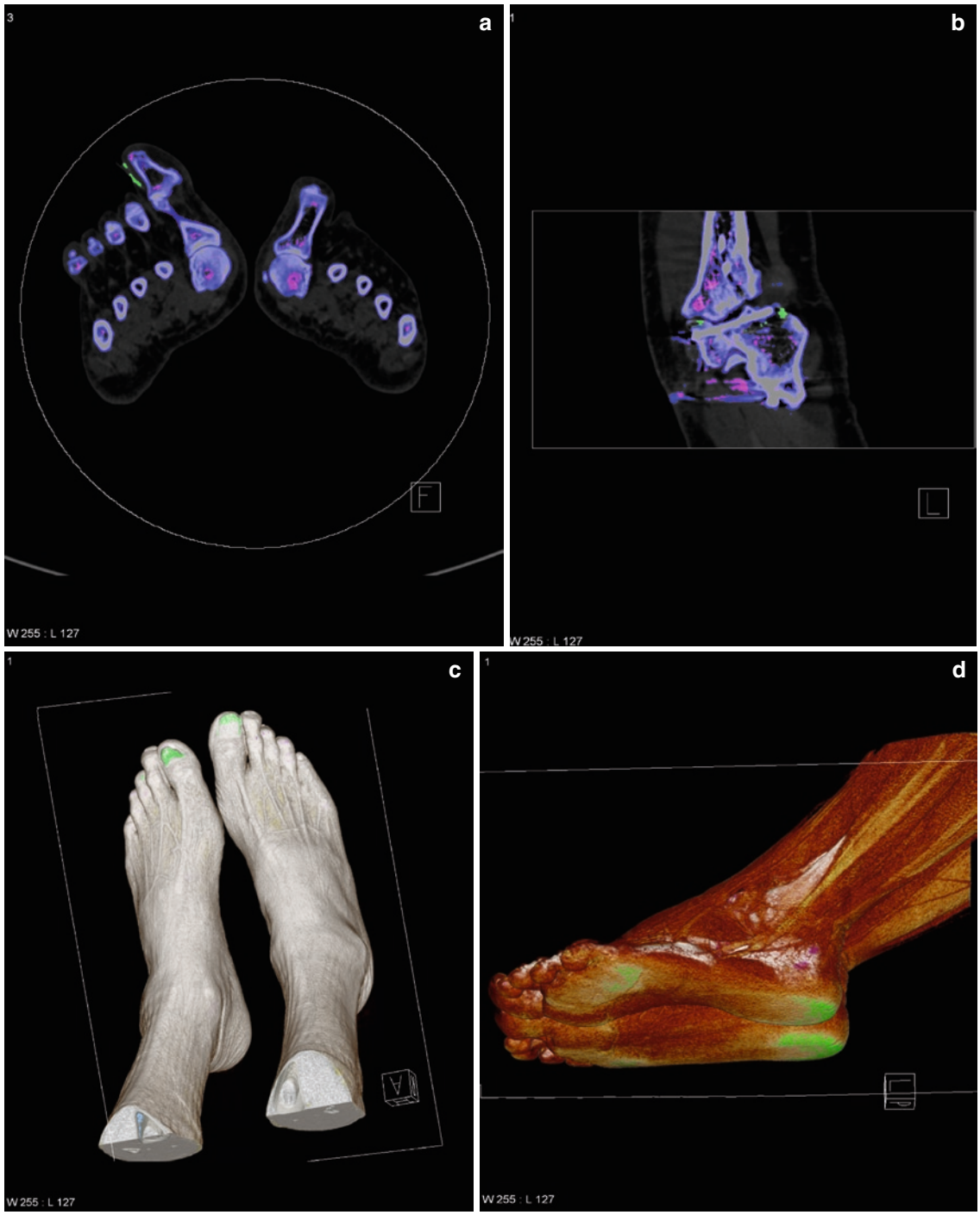

Fig. 6 (**a**) Coronal reformatted DECT demonstrating green artifact mimicking a MSU deposit at the nailbed of the *right first* big toe. (**b**) *Green* artifact is seen surrounding the surgical screw, also mimicking monosodium urate deposits (**c**) Artifact green nail beds are common artifact and has the same attenuation as uric acid but is easily recognized as an artifact with VRT images. (**d**) the skin along the sole of the feet is green simulating uric acid again easily recognized on VRT imaging as artifact and should not to be confused with uric acid deposits

Fig. 7 70 year old man who presented with cellulitis and pain in his right hand. Scans were ordered to rule out osteomyelitis. (**a**) Radiograph – demonstrates a destructive process centered along the second DIP. (**b**) 3D volume rendered, coronal reformatted DECT: surrounding the second DIP are MSU deposits (color coded – *red*) consistent with tophaceous gout without evidence of osteomyelitis. (**c**) Sagittal reformatted DECT through the area in question: MSU deposits (color coded – *green*) are again demonstrated along the second DIP

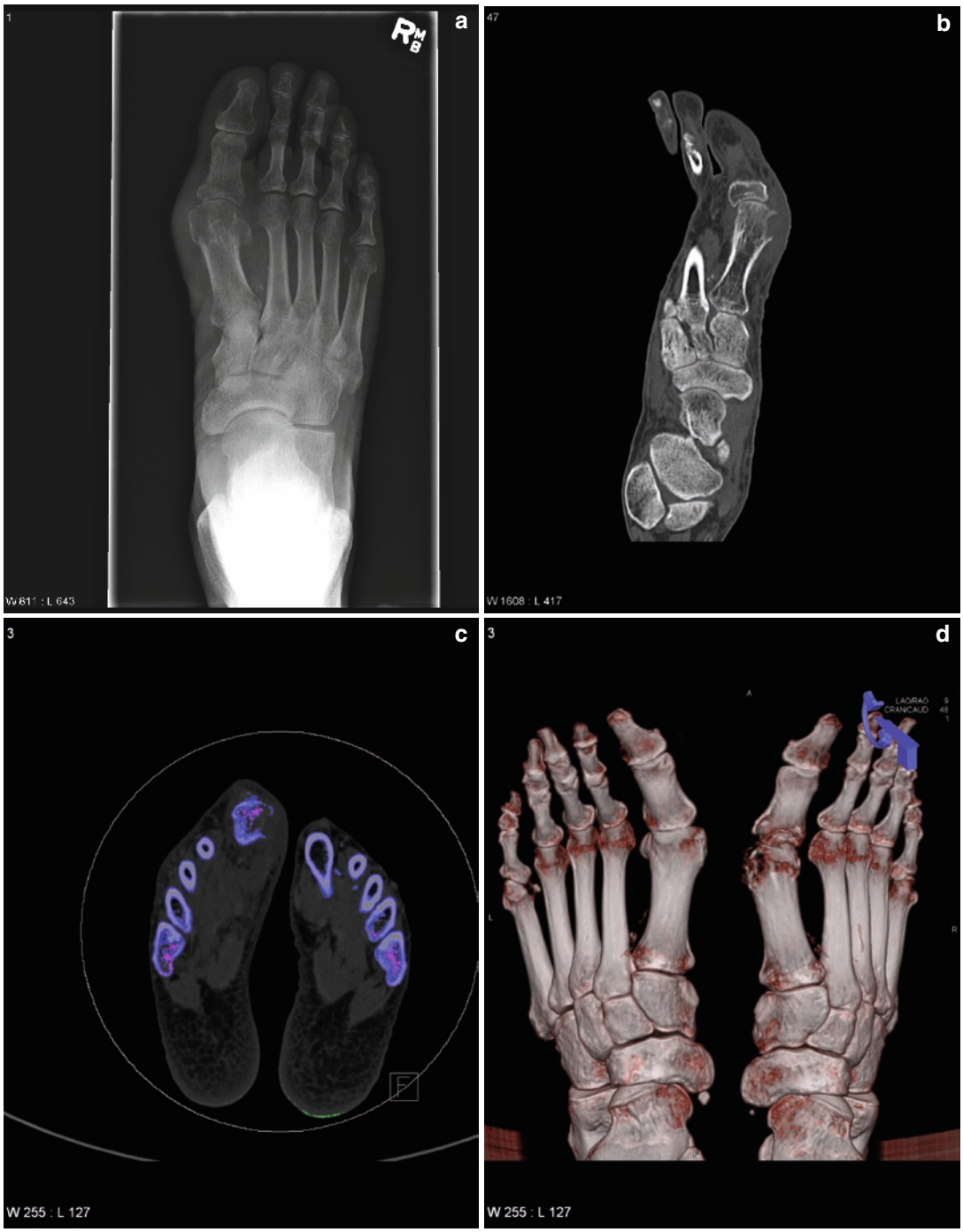

Fig. 8 72 year old man who presented with cellulitis and pain in his feet. Scans were ordered to rule out osteomyelitis vs. septic arthritis. (**a**) AP Plain Radiograph right foot reveals a lucent region involving the medial aspect of the right MT head with overlying soft tissue swelling and associated periosteal reaction. (**b**) 1 mm Single Source CT coronal reformat view of the right foot which reveals a well defined erosion of the right first MT head with overhanging edges. (**c**) DECT coronal reformatted two material decomposition algorithm through the distal interphalangeal joint of the first toe which demonstrates no abnormal MSU deposition, which points against the diagnosis of gout and more in keeping with an aggressive reaction such as osteomyelitis or neoplasm. (**d**) 3D volume rendered, coronal reformatted DECT of both feet demonstrates no tophus present in contrast to (**e**) coronal VRT with aspiration proven monosodium urate tophi of the first metatarsalphalangeal joint with a pressure erosion

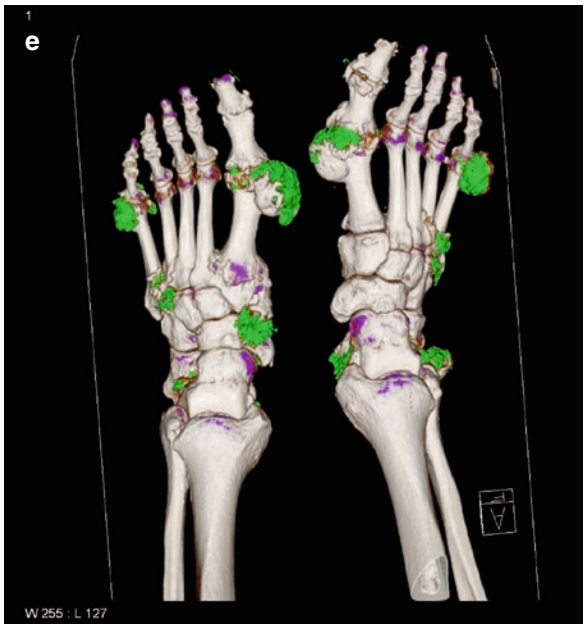

Fig. 8 (continued)

guided aspiration was also performed which did not show MSU crystals.

This case once again reinforces how DECT can be utilized to help with diagnostically challenging cases.

DECT is useful in noninvasively detecting MSU deposits in anatomic regions which are challenging to assess clinically. This can improve diagnostic dilemmas as intraarticular tophi can be easily differentiated from a torn meniscus or a loose ossific body that can cause locking of the knee.

5.3 Case 3

A 53 year old gentleman presented to a rheumatologist with a locking and painful right knee. Clinical examination found overlying the right knee. The patient had a limited range of motion of the knee with the differential suggesting either a torn ligament, torn meniscus, or loose intraarticular body. A MRI was ordered which demonstrated a prepatellar soft tissue mass of intermediate signal intensity with anterior patellar bone erosion with thickening of the posterior cruciate ligament and low signal material along the posterior aspect of the joint (Fig. 9a). Subsequent DECT examination demonstrated MSU deposits on the posterior cruciate ligament, and proximal attachment of the patella with erosion of the patella (Fig. 9b, c). This patient was put on urate lowering therapy and a follow-up scan demonstrated a decrease in the size of the tophus.

As highlighted through these cases, DECT has the potential to be a problem-solving tool that can be utilized to diagnose the presence of gout in challenging clinical presentations and potentially obviating the need for arthrocentesis. It should be of note that gout can also co-exist with other arthropathies, and thus the presence or lack of MSU deposition in a joint can help guide management of clinically challenging cases. DECT also has the capability to detect subclinical cases of gout which allows for early treatment not only aimed at preventing articular, bony, ligamentous, and tendon damage. Furthermore, its utility to accurately delineate the anatomic distribution of the disease has future potentials to help better understand the disease process of gout. Future advances include undertaking volume measurements of MSU deposition which can be used to assess disease progression and response to therapy over time (Fig. 10)

6 Scientific Evidence

Initial studies in material differentiation utilizing DECT were focused on renal calculi characterization. Graser et al. studied 24 renal calculi of known composition and also 20 consecutive patients with known or suspected uroliths. These patients received DECT scans prior to mechanical extraction of their stones which were correlated with the chemical analyses of stones after mechanical extraction (Graser et al. 2008). This in vitro and in vivo study demonstrated that differentiation of MSU from other calculi was possible. Stolzmann et al. scanned 40 stones with known compositions via DECT and subsequently concluded that the sensitivity, specificity, positive predictive value, and negative predictive value for the detection of MSU containing calculi was 100% (Stolzmann et al. 2008).

This concept of detecting MSU in the kidneys was serendipitously expanded to detecting MSU deposits in other body parts, specifically, for gout. An initial case report confirmed the feasibility to identify uric acid and contrast enhancement in gout tophi with active inflammation (Johnson et al. 2007).

Choi et al. studied the utilization of DECT for the diagnosis of gout in 20 consecutive patients with

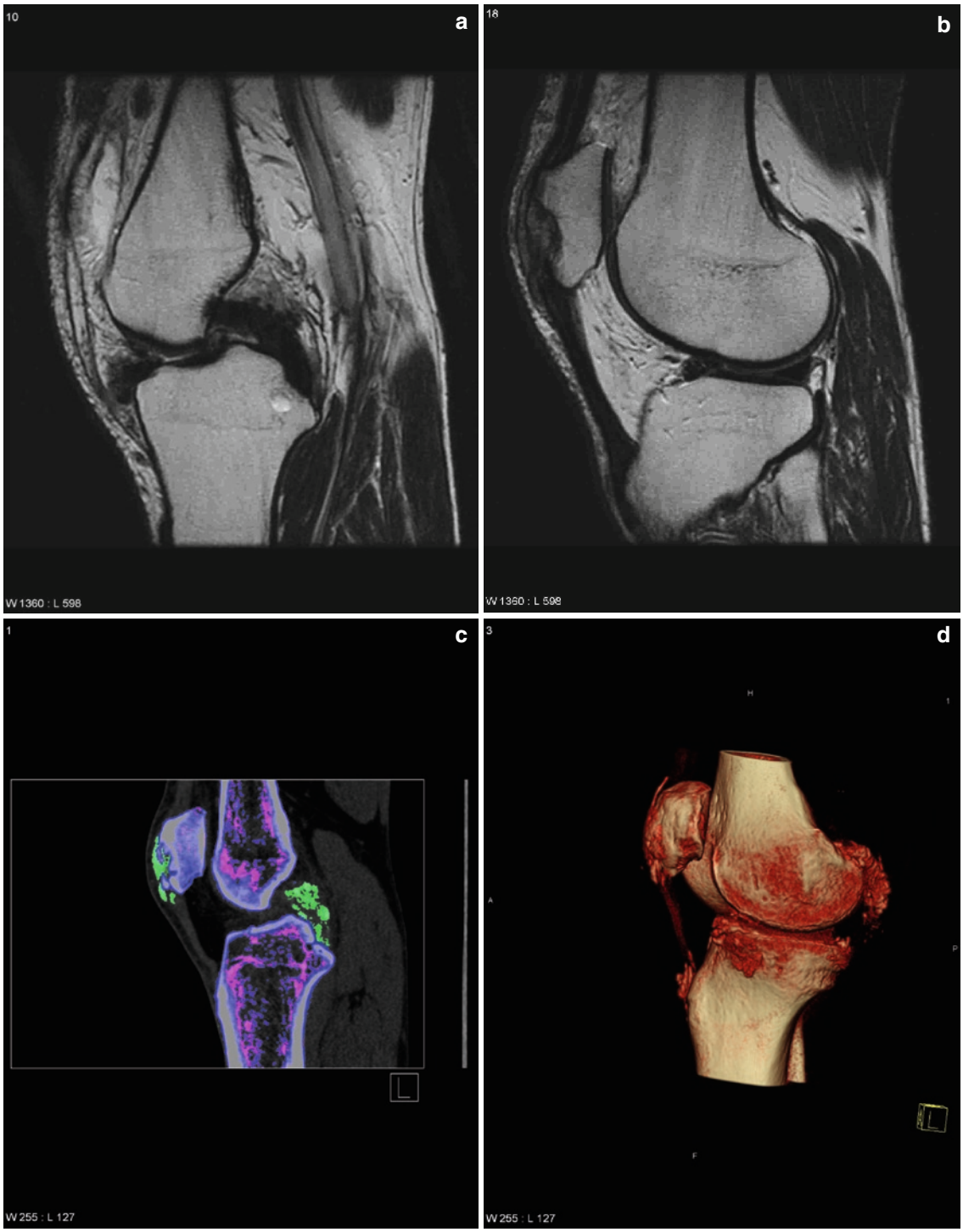

Fig. 9 53 year old man who presented with right knee pain and locking knee. (**a**) MRI Oblique Sagittal FSE T2 Weighted Image: thickening of the posterior cruciate ligament with low signal material along the anterior aspect of the joint. (**b**) MRI oblique sagittal FSE T2 Weighted Image: anterior prepatellar soft tissue mass of intermediate signal intensity with anterior patellar bone erosion. (**c**) Sagittal reformatted image, DECT: MSU deposits on the posterior cruciate ligament, and proximal attachment of the patella with erosion of the patella. (**d**) 3D volume rendered, coronal reformatted DECT: MSU deposits are again demonstrated along the posterior cruciate ligament and proximal attachment of patella

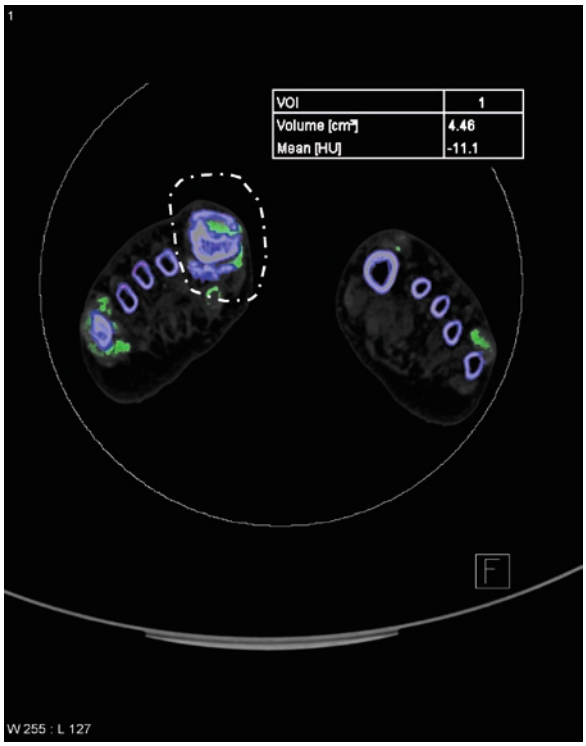

Fig. 10 DECT showing volume measurements of the tophi on the first IP joint. Volume within this selected region on interest produces a MSU volume of 4.46 cm^3. Sequential volume measurements can be calculated to compare disease progression and to monitor response to treatment

tophaceous gout and 10 control patients with other arthritic conditions and found that all 20 patients with gout showed MSU deposits on their DECT scans whereas none of the 10 controls showed urate deposits (Choi et al. 2009). Furthermore, Artmann et al. acquired DECT examinations of 71 regions from 41 patients and found that DECT allowed for specific and quantitative visualization of urate deposits in peripheral regions (Artmann et al. 2010). Nicolaou et al. have also found DECT to be useful to diagnose gout in diagnostically difficult cases (Nicolaou et al. 2010).

Studies from our institution have also given insight into the distribution of disease of gout. What was revealed has not been classically described in imaging literature is the predilection for the superficial/deep hand flexor tendons, cruciate and collateral knee ligaments, knee extensor mechanism, and within the midfoot tarsal articulations. In fact, DECT was shown to be more efficacious in identifying the presence of gout (MSU crystal deposition) in comparison to clinical assessment.

Future directions include the use of DECT as a non-invasive method of assessing response to treatment through volume calculations, which can be used to identify subclinical gout, to provide important insight into disease pathogenesis, disease complications and prognosis, and to allow monitoring of disease over time the response to treatment.

References

Artmann A, Ratzenbock M, Noszian I, Trieb K (2010) [Dual energy CT--a new perspective in the diagnosis of gout]. Rofo 182:261–266

Brook RA, Kleinman NL, Patel PA et al (2006) The economic burden of gout on an employed population. Curr Med Res Opin 22:1381–1389

Choi HK, Curhan G (2007) Independent impact of gout on mortality and risk for coronary heart disease. [see comment]. Circulation 116:894–900

Choi HK, Ford ES (2007) Prevalence of the metabolic syndrome in individuals with hyperuricemia. Am J Med 120:442–447

Choi HK, Ford ES, Li C, Curhan G (2007) Prevalence of the metabolic syndrome in patients with gout: the Third National Health and Nutrition Examination Survey. Arthritis Rheum 57:109–115

Choi HK, Al-Arfaj AM, Eftekhari A et al (2009) Dual energy computed tomography in tophaceous gout. Ann Rheum Dis 68:1609–1612

Dalbeth N, Haskard DO (2005) Mechanisms of inflammation in gout. Rheumatology 44:1090–1096

Dalbeth N, McQueen FM (2009) Use of imaging to evaluate gout and other crystal deposition disorders. Curr Opin Rheumatol 21:124–131

Dalbeth N, Clark B, Gregory K, Sheehan T, McQueen F (2007a) Clinical images: three-dimensional computed tomography imaging of tophaceous gout. Arthritis Rheum 56:29

Dalbeth N, Clark B, McQueen F, Doyle A, Taylor W (2007b) Validation of a radiographic damage index in chronic gout. Arthritis Rheum 57:1067–1073

Gerster JC, Landry M, Duvoisin B, Rappoport G (1996) Computed tomography of the knee joint as an indicator of intraarticular tophi in gout. Arthritis Rheum 39:1406–1409

Gerster JC, Landry M, Dufresne L, Meuwly JY (2002) Imaging of tophaceous gout: computed tomography provides specific images compared with magnetic resonance imaging and ultrasonography. Ann Rheum Dis 61:52–54

Graser A, Johnson TR, Bader M et al (2008) Dual energy CT characterization of urinary calculi: initial in vitro and clinical experience. Investig Radiol 43:112–119

Johnson TR, Weckbach S, Kellner H, Reiser MF, Becker CR (2007) Clinical image: dual-energy computed tomographic molecular imaging of gout. Arthritis Rheum 56:2809

Kim KY, Ralph SH, Hunsche E, Wertheimer AI, Kong SX (2003) A literature review of the epidemiology and treatment of acute gout. Clin Ther 25:1593–1617

Kim SY, Guevara JP, Kim KM, Choi HK, Heitjan DF, Albert DA (2009) Hyperuricemia and risk of stroke: a systematic review and meta-analysis. Arthritis Rheum 61:885–892

Kleinman NL, Brook RA, Patel PA et al (2007) The impact of gout on work absence and productivity. Value Health 10: 231–237

Kramer HJ, Choi HK, Atkinson K, Stampfer M, Curhan GC (2003) The association between gout and nephrolithiasis in men: The Health Professionals' Follow-Up Study. Kidney Int 64:1022–1026

Lawrence RC, Felson DT, Helmick CG et al (2008) Estimates of the prevalence of arthritis and other rheumatic conditions in the United States. Part II. Arthritis Rheum 58:26–35

Malik A, Schumacher HR, Dinnella JE, Clayburne GM (2009) Clinical diagnostic criteria for gout: comparison with the gold standard of synovial fluid crystal analysis. J Clin Rheumatol 15:22–24

Mould-Quevedo J, Pelaez-Ballestas I, Vazquez-Mellado J et al (2008) El costo de las principales enfermedades reumaticas inflamatorias desde la perspectiva del paciente en Mexico. Gac Méd Méx 144:225–231

Nicolaou S, Yong-Hing C, Galea-Soler et al (2010). Dual energy computed tomography as a potential new diagnostic tool in the management of gout in the acute setting. American Journal of Roentgenology 194:1072–1078

Perez-Ruiz F, Naredo E (2007) Imaging modalities and monitoring measures of gout. Curr Opin Rheumatol 19:128–133

Schumacher HR Jr, Becker MA, Edwards NL et al (2006) Magnetic resonance imaging in the quantitative assessment of gouty tophi. [erratum appears in Int J Clin Pract. 2006;60(5):630]. Int J Clin Pract 60:408–414

Stolzmann P, Scheffel H, Rentsch K et al (2008) Dual-energy computed tomography for the differentiation of uric acid stones: ex vivo performance evaluation. Urol Res 36:133–138

Thiele RG, Schlesinger N (2007) Diagnosis of gout by ultrasound. Rheumatology 46:1116–1121

Underwood M (2006) Diagnosis and management of gout. BMJ 332:1315–1319

Wu EQ, Patel PA, Yu AP et al (2008) Disease-related and all-cause health care costs of elderly patients with gout. J Manage Care Pharm 14:164–175

Index